FABRICATION AND CHARACTERIZATION OF HIGHLY ORDERED POROUS ANODIC OXIDE AND NANOWIRES

A thesis submitted to The University of Manchester
Faculty of Engineering and Physical Sciences
for the Degree of Doctor of Philosophy

2010

Guanjie Liu

School of Materials
Corrosion and Protection Centre

Table of Contents

List of Figures

List of Tables

Declaration

No portion of the work referred to in this thesis has been submitted in support of an application for another degree or qualification of this or any other university or other institution of learning.

2010

Guanjie Liu

Acknowledgements

I would like to express my heartfelt appreciation and gratitude to my supervisors, Dr. X.Zhou and Professor. G.E.Thompson for their invaluable guidance and great support throughout every stage of my graduate studies.

It has been a great pleasure to work and interact with all the staff and students in Corrosion and Protection Centre. My appreciation goes to the members in Light metal group.

I would like to express my gratitude to my parents for their love and encouragement, and for supporting me in many ways throughout my study. Finally, a very special thank is given to my Husband, Dr. Wei Guo who has been with me every step of the way, for his love and support.

Abstract

Porous anodic films with highly ordered pores were successfully fabricated with multi-steps anodizing. The degree of pore ordering was quantitatively assessed by obtaining the pore distribution regularity based on fast Fourier transform (FFT) of scanning electron micrographs of the resultant porous anodic films. It is revealed that the degree of pore ordering in anodic films increases with increased number of repeated steps of anodizing. Anodizing conditions, i.e. anodizing voltage and the electrolyte concentration, are found to have significant effects on pore ordering. The best regularity was recorded on the porous anodic films formed at 30 V in 0.3 M oxalic acid and 40 V in 0.4 M oxalic acid. Further, anodic oxide films, with pores arranged in hexagonal or square patterns, were obtained by anodizing of aluminium with corresponding pre-patterns induced by optic grating impressions under selected anodizing voltages. Additionally, anodic film templates were successfully fabricated using optimised procedures with selective removal of the aluminium substrate and the barrier oxide layer.

Nickel nanowires were produced by electrodeposition using anodic film templates. The current density-time response reveals three growth stages of nickel nanowires during electrodeposition. The electrodeposition current efficiency varied with the variation of electrodeposition parameters, mainly due to side reactions i.e. hydrogen evolution. The process temperature and applied voltage have a significant influence on the growth rate of nickel nanowires. Further, the structure of the resultant nickel nanowires depends on the process temperature. At a process temperature of 3°C, single crystal nanowires grew preferentially along [110] orientation. However, polycrystalline nanowires were obtained at an increased temperature of 37°C due to the increased surface diffusion rate of nickel adatoms. Optical limiting assessment of the nickel nanowires revealed significant non-linear scattering in the wavelength range of 532 to 1064 nm, suggesting potential applications in the fields of ultrahigh-density magnetic recording, ultrafast optical switching and microwave devices.

Manganese oxide nanowires were also fabricated via the anodic film template route in a mixed solution of 0.1 M manganese acetate and 0.1 M Na_2SO_4. The resultant nanowires

exhibit an amorphous structure with short range ordering. A high population of fine crystalline particles, with an average diameter of 3~5 nm, was revealed within the nanowires. The crystalline particles were determined as ε-MnO_2 with a hexagonal structure. Further, a high specific capacitance of 220 F g^{-1} was recorded on the electrode fabricated from the deposited manganese oxide nanowire array in a cyclic voltammetry measurement at a scan rate of 5 mV s^{-1} from 0 to 1 V (SCE) in 0.1 M Na_2SO_4 solution at 25°C , indicating excellent capacitive properties.

Copyright Statement

Chapter 1

Introduction

Recently, one dimensional nanostructures, including nanowires, nanorods and nanotubes of metallic and semiconductor materials, have drawn intensive research interest because of their unique properties, which are interesting from the view point of different applications, such as high density storage media, functional nanostructures exhibiting quantum size effect, highly sensitive chemical sensors, nano electronic devices and functional bio-chemical membranes.

Numerous methods for preparing one dimensional nanostructures have been developed, ranging from lithographic techniques to chemical methods [1]. Template synthesis, i.e. synthesizing the desired material within the pores of templates, was extensively used. Porous anodic films formed by anodizing have been intensively investigated as templates to produce one dimensional nanostructures. Research on the formation of nanostructures via porous anodic oxide template route intensified in the mid-1990s, when porous anodic films with well ordered pores were achieved by two steps anodizing [2].

However, it still remains challenge to form porous anodic film with long range pore order. Further, by far the self-ordering mechanism during porous anodic film formation has not been fully understood, although several rational mechanisms have been suggested, among which the stress-assisted material flow model together with the field-assisted oxide dissolution model are commonly accepted [3-5]. For the fabrication of metallic and semiconductor nanowires via anodic film template, challenges remain with efficient template fabrication, control of the diameter, length,

morphology, composition, structure of individual nanowire and the arrangement of nanowire arrays.

The objectives of this thesis are to form porous anodic film with long range pore order, to advance the understanding of pore ordering during anodizing, to optimize the fabrication procedure for anodic film template, to fabricate relatively large area arrays of nickel nanowire and manganese oxide nanowire with controlled diameter, length, morphology, composition and structure, and to evaluate their physical and electrochemical properties, therefore their potential applications.

Chapter 2 presents a literature review, including the fundamental researches on porous anodic film formation, the current developments of highly ordered porous anodic film fabrication, properties and applications of one dimensional nanostructures, and the fabrication techniques of one dimensional nanostructures. Chapter 3 presents the experimental procedures employed in the present work, including the materials selection, specimen preparations, anodizing and nanowire fabrication procedures, as well as characterization methods. Chapter 4 discusses the formation procedures and mechanisms of highly ordered anodic oxide films. Optimum anodizing conditions, including anodizing time, anodizing steps, anodizing voltage and the electrolyte concentrations, are suggested. Chapter 5 describes the fabrication procedure for highly ordered porous anodic oxide films on pre-patterned aluminium substrate and their characteristics. In Chapter 6 describes the electrodeposition of nickel nanowires within porous film templates. The influence of electrodeposition parameters on the properties of nickel nanowire, the optical-limiting properties and applications of the nickel nanowire are discussed. Chapter 7 describes the fabrication procedure for manganese oxide nanowire arrays. The influence of deposition conditions on the properties of manganese oxide nanowire arrays is evaluated. Chapter 8 summarizes the main findings and suggests possible future works.

Chapter 2

Literature Review

2.1 Introduction

A great amount of metals including pure aluminium, Niobium (Nb), Zirconium (Zr), and Tungsten (W) etc. are prone to oxidation under ambient condition and develop a thin amorphous and inert oxide on metal surface [6]. Under typical atmospheric conditions, a native oxide film naturally forms on aluminium. The native oxide layer is non-uniform, thin and non-coherent. Nevertheless, the native oxide film provides corrosion protection at a certain level [6].

Anodizing aluminium is a hard fixture in the mind of the light metal industry. By capitalizing on the natural phenomenon of anodic oxide film formation on aluminium in a production environment, the anodizing process has become synonymous with surface protection and durability of aluminium substrates. Anodizing can be viewed as a controlled oxidation of the aluminium surface to yield a uniform, continuous protective oxide film. Its uniquely self assembling, highly ordered, columnar nanoscale structure has been extensively studied, yet the mechanism of anodic oxidation on aluminium is still not fully established, though there are agreed mechanism [7].

Porous anodic oxide film with parallel pores have been known as honeycomb-like hexagonal structure that has short-distance ordering (in several tens to hundreds of square nanometers) but long-distance disordering of pore arrangement [8]. It was Masuda and Fukuda who ignited an explosion of highly ordered porous anodic oxide research when they produced an oxide film with excellent regularity for the first time [2]. They reported that a highly ordered porous anodic oxide film could be obtained by two steps anodizing

on pure aluminium using a 0.3 M oxalic acid solution under constant voltage of 40 V at 0°C. To achieve a highly ordered pore arrangement over a large area, many studies have so far described a variety of pre-treatments or pre-patterning techniques.

This has opened a wide range of applications of porous anodic oxide films, particularly as a template to form nanowires, nanotubes, nanodots and composites for catalysis, emitters, rechargeable batteries, magnetic storage devices, etc [9]. The highly hexagonally ordered pores in porous anodic oxide film have also been found to be extremely useful to exploit and study magnetic interactions, dielectric properties, and optical interference [10]. The other useful properties are photo- and electro-luminescence, and transparency with absorption wavelengths higher than corundum [11]. The ordered porous anodic oxide film, by itself, has been commercially used as a membrane filters that are suitable for use in a wide range of specialized applications, including HPLC mobile phase filtration and degassing, ultra cleaning of solvents, gravimetric analysis and liposome extrusion.

This chapter presents a review of the current development of highly ordered porous anodic oxide films formation, applications of one dimensional nanostructure, and the one dimensional nanostructure fabrication by template synthesis with porous anodic oxide films.

2.2 Anodized films on aluminum

2.2.1 Classification of alumina anodic films

Two types of anodic oxide film on aluminium can be produced when aluminium is made the anode in an electrolytic cell by varying the electrolyte and other film forming conditions [12], as illustrated in Figure 2.1.

One type of films is highly uniform in thickness and relatively compact, which are specified as barrier type films. Barrier type films normally forms in electrolytes in which the oxide films are completely insoluable. Examples of this type of electrolyte include neutral solutions such as boric acid solution, ammonium borate or tartrate solutions (pH 5-7), ammonium tetraborate in ethylene glycol, and several organic electrolytes including citric, malic, and glycollic acids. In strong acidic solutions completely barrier type films do not form, thus the specifying of neutral or pH value 5-7 aqueous solutions for some electrolytes is important.

A relatively regular porous anodic film normally develops in acid electrolytes or selected alkaline electrolytes, instead of barrier type films. The pores of cylindrical section pass normally to the macroscopic aluminum surface but are separated from it by a relatively compact barrier layer of scalloped appearance. Normally, in the previous electrolytes porous anodic oxide film is slightly soluble. There are numerous examples of this electrolyte in which porous anodic film could be produced, with sulfuric, phosphoric, chromic, and oxalic acids at almost any concentration being the most commercially important.

2.2.2 Mechanism of anodic oxide films formation

Under specific conditions, i.e. the aluminium is set as the anode in electrolytes of certain concentration when direct current electricity is applied on the electrolytic cell, aluminium metal is converted into oxide through the following electrochemical reaction：

Anode:

$$Al - 3e^- \rightarrow Al^{3+}$$

$$2Al^{3+} + 3O^{2-} \rightarrow \quad Al_2O_3; \quad q = -1675.7 \text{ kj.mol}^{-1}$$

$$2\ Al + 6\ OH^- \rightarrow Al_2O_3 + 3\ H_2O + 6\ e^- \qquad (1)$$

Cathode:

$$2\ H_2O + 2\ e \rightarrow H_2 + 2\ OH^-$$

$$2\ H^+ + 2\ e \rightarrow H_2 \qquad (2)$$

Under applied electricity field, the Al^{3+} ions escaped from metal lattice and transport to anodic oxide layers through the metal anode/oxide interface, and then continue to move outwards. Meanwhile, the O^{2-} that formed at the position of electrolyte/oxide interface is moving inwards with the oppisite direction, until when both of them meet each other to form anodic oxide (Al_2O_3).

2.2.3 Composition and structure of anodic films on aluminum

A number of workers have investigated the composition and structure of anodic oxide films. In the work of investigating barrier type oxide films, Verwey [13] found that the composition was crystalline γ'-Al_2O_3. γ'- $A1_2O_3$ is regarded as an intermediate case between amorphous and *c*rystalline γ- $A1_2O_3$**.** The distinction between crystalline γ-$A1_2O_3$ and crystalline γ'- $A1_2O_3$ is different arrangement of cations in the structure, both having the same oxygen lattice.

Early electron diffraction study of films formed in a wide variety of electrolytes found the composition of the anodic oxide films to be amorphous. The structures tended to be less random when the films were formed at high temperatures. This was explained by Taylor [14] as due to an increase in the crystalline proportion of the film, which was also favored by increasing film thickness, high formation voltages, dilute electrolytes, and ac current. The increase in the crystalline γ-$A1_2O_3$ proportion with increasing thickness was confirmed by Stirland [15] using a dissolution technique involving the measurement of the oxide solubility in a mixture of phosphoric and chromic acids. Below 100 V formation voltages, barrier type films were found to be amorphous. Above 100 V the film was again amorphous but crystalline γ-$A1_2O_3$ was also detected.

Franklin [16] reported the presence of at least three types of oxide in the investigation of films prepared in boric acid-borax electrolyte: (a) a hydrated oxide at the oxide/electrolyte interface, (b) occurrence of irregular patches of crystalline γ-$A1_2O_3$, and (c) amorphous oxide constituting the majority of the film. The complexity of these films increases as the formation voltage increases, which could be due to an increase in film crystallinity.

Trillat and Tertain investigated films formed in 20 % aqueous solution of sulfuric acid and reported that: outer layer consisting of a mixture of boehmite, AlO(OH), and crystalline γ-$A1_2O_3$ and an inner layer of amorphous the presence of boehmite resulting from the incorporation of water, leading to a gradual formation of monohydrate from amorphous oxide. The results of Trillat and Franklin indicate that even in boric acid borax electrolytes some degree of porous oxide film is formed.

2.2.4 Main early researches on formation of porous anodic film on aluminum

Anodic oxide film for aluminum has been explored since the early 1900s, and widely used as tableware, kettle, car body and other commodities.

In the early days of porous anodic film research, Keller [17] reported details on cell structure and anodizing voltage dependence of the cell size. They defined a model of hexagonally close packed cells of oxide, each of which contains a single six-direction star shape nanohole. The solvent action by the electrolyte causes the dissolve of anodic films, which finally lead to the porous microstructure of anodic film. **Theoretically,** a cylindrical cell with a roughly hemispherical end and a central cylindrical pore was formed. While as the triangular pillars of metal with concave surfaces between each group of three contacting cylinders were converted to anodic oxide, the metal would be consumed equally from each face under the influence of the current from the pores. When all metal pillars were consumed in this way, the oxide layer would be continuous and the cells would have the form of hexagonal shape rather than cylinders. In this case, because of the localized current flow, heating and solvent action within each cell, the centre pore would be in a six point star shape instead of cylindrical.

The metal toward the junction of three adjoining cells would be under the influence of current from the pores in these cells and should be converted to oxide more rapidly by virtue of the higher current density resulting from the overlapping current fields. Consequently, the front of a single cell in a close-packed array will have a larger radius of curvature than that of a single isolated cell, and the cell front will have the shape of a spherical section somewhat less than a hemisphere.

In late nineteen seventies, Wood and O'Sullivan managed to observe the barrier layer and porous structure of oxide films formed in phosphoric acid at high anodizing voltage with electron microscopy [8, 18, 19], which largely confirmed the geometrical model by Keller in principle but not in some crucial details, thereby various important developments and corrections to Keller's work had been made. They did not find the regularity of close-packed cells from their observation, and the pore in the centre of each cell showed an almost perfect circular shape (Figure 2.3) instead of six pointed star shape in Keller's model.

In 1986, K.Wada [20] from Japan investigated the microstructure of porous anodic films on aluminium formed in sulphuric acid solution. Their transmission electron microscopy revealed a multilayer or higher order structure in the former films. In contrast to the fibrous colloidal structure in the cells and barrier layer in the conventional films anodized in a sulphuric acid solution at 15 V, a network structure is formed in the cells and barrier layer in the hard films prepared at higher voltage of 25 V. The microstructure changes according to the anodizing conditions.

A new model for the films formed in sulphuric acid was presented, i.e. the cell walls were constructed with five layers and the fracture of the films occured at the centre of the cell walls, i.e. at the boundary layer (IC in Figure 2.4) between the two centre barrier layers (CB in Figure 2.4). Centre barrier layer (4 to 6 nm in thickness) composed of high crystalline oxide was found in a layer at the bottom of the pore, and the thickness of barrier layer was independent on the applied voltage of the anodizing. Increase in

thickness of the barrier layer due to applied voltage was governed by that of the outer barrier layer.

The fundamental aspects of anodic oxide films were investigated with the basic theories established. Although there still exists plenty of unconfirmed aspects i.e. the exact mechanism of porous anodic oxide film formation, these early researches still show important influences and did great contribution to the field of light metal electrochemistry.

2.3 Barrier type anodic alumina oxide films formation

Barrier type films on aluminum formed generally, but not exclusively, in near neutral aqueous electrolytes [7]. The barrier type films are considered to provide the fundamental aspects for understanding the development of porous anodic oxide film. For constant current anodizing, the voltage-time behavior in Figure 2.5 reveals an initial voltage surge of about 2.0 V, indicating the prior presence of an air formed film in thickness of 2.5 nm on the electropolished aluminum surface. Further, the voltage rises linearly with time as the relatively compact film thickens uniformly with time. The driving force for film growth is high field ionic conduction, which may be simply expressed as

$$I = \mathrm{A}\exp(\mathrm{B}E) \qquad (3)$$

Where I is the current density (typically in the mA range), A and B are temperature dependent constants, and E is the field strength (the ratio of the potential drop across the anodic oxide film to the film thickness). Clearly, films grown at constant current density develop at constant field strength, of the order of $10^6 - 10^7$ V cm^{-1}. Further, the reciprocal of the field strength for anodizing of aluminum reveals that the film thickens at a constant rate. In order to maintain the constant field strength, the voltage must increase as the film thickens.

The field also provides highly uniform film growth, with the developing film smoothing the roughness of the initial aluminum surface. Uniform film thickening is terminated

eventually by dielectric breakdown, with visible sparking observed frequently over the anodic film surface.

Through the inert marker experiments, the locations of film growth are defined [21]. A transmission electron micrograph of cross section of a barrier type film, the typical barrier type film shows relatively flat metal/oxide and oxide/electrolyte interfaces and appears generally featureless in section upon initial examination in the transmission electron microscope, a typical characteristic of amorphous anodic oxide films, as shown in Figure 2.6.

During the investigation of barrier type films formation with inert marker experiments, a critical current density may be defined for many electrolytes at which point the directly measured cation transport number approaches zero. No solid oxide growth is observed above the marker layer, which stays close to the oxide/electrolyte interface, and no pore formation is evident. Analysis of the electrolyte after anodizing reveals the presence of Al^{3+} ions which indicates an apparent cation transport number equivalent to that directly measured under conditions of high current efficiency when converted to equivalent anodic oxide film thickness. Thus, during oxide growth both $A1^{3+}$ and O^{2-}/OH^{-} are mobile. Further, the extent of film formation at the film/electrolyte interface depends on the specific anodizing conditions. At the critical current density, little or no oxide film formation is evident at that interface.

In order to gain further insight into the traces of outwardly mobile $A1^{3+}$ ions, anodizing was carried out at current densities below critical current density, where no solid oxide formation at the oxide/electrolyte interface is feasible (Figure 2.7 (a)*).* Thus, if a uniform oxide dissolution proceeds during anodizing at relatively low current efficiency, the original oxide film material containing the marker layer is expected to be completely lost to the electrolyte (Figure 2.7 (b))**.** It is worth noted that the presence of the marker layer is always close to the oxide/electrolyte interface, although it is lost in local regions owing to undermining of the film material by pore initiation by field-assisted dissolution at preferred sites (Figure 2.7 (c)).

When aluminium is anodized in a near neutral solution, the dissolution of oxide is very slow. The thickness of the oxide layer will continuously increase. On the other hand, the electric field strength can be written as E = U/d. For a constant applied voltage U to the oxide layer, the electric field strength E in the oxide layer is inversely proportional to the thickness of the oxide layer, d. Therefore, E will drop when the thickness of the oxide layer increases, reducing the migration rate of the anions. The oxidation process will eventually stop when d approaches a critical value, $d_{C,}$ depending on the anodizing conditions, while the corresponding electric field strength (E_C) is merely too weak to drive the oxygen containing anions through the oxide barrier layer.

In a near neutral electrolyte, wherever the thickness of the oxide layer is smaller than d_C, the field strength $E > E_C$, and the migration of anions will continue to thicken the oxide layer. Finally, a uniform thickness of d_C and therefore constant electric field strength is established in the whole barrier layer.

2.4 Porous anodic films formation

2.4.1 Pore initiation during porous anodic oxide formation

2.4.1.1 Prerequisite for pore initiation: surface roughness and corrosions

Corrosion of aluminum takes place during anodizing in an acidic electrolyte even when no electric field is applied. During the very early stage of anodizing, the dissolution rate in the whole surface area is normally not even. Defects such as impurities, dislocation, grain boundaries, or nonmetallic inclusions in the underlying metal all have the chances to cause a faster dissolution rate.

As illustrated before, when Al^{3+} cations are ejected from the oxide surface driven by an applied field, cation vacancies can arise and accumulate to form high density voids in the oxide film, which can also help the propagation of pores. As shown in Zixue Su' s work [22], a non-pretreated aluminum foil was dipped in a fresh 0.3 M oxalic acid for 20 h without any applied electric field. High density pores from tens of nanometers to several hundred nanometers in diameter can be found over the whole surface as shown in Figure

2.8 (a). When a voltage of 40 V was applied, pores with a high population density with a rather uniform size could be observed after only 90 s and the ordering of the pores increased with the anodizing time (Figure 2.8 b–d).

On the other hand, aluminum forms a thin oxide layer in air and this layer is normally rough on a nanometer scale. A large number of defects in the layer can act as pore initiation sites and an applied voltage can increase the pore number and growth rate rapidly. This assumption was supported by Hebert and co-workers [23] in their studies.

It is reported that films on electropolished aluminum thicken non-uniformly because of local crack-heal events at the pre-existing metal ridges [24]. Electropolish is a process of improving micro-smoothness and micro-topology by anodic dissolving of the substrate in an electrolyte with an external source of electricity. It also causes redistribution of current and its concentration into the thin film regions between ridges. The local film surfaces in these areas exhibit appreciable hemispherical curvatures of varying radii; also, with further increase in voltage, the ridges become wider, due to persistent crack-heal events, increasing the curvature of the film/electrolyte interface in the thin film regions. The increasing curvature increases the field in the previous thinner film regions to a level where the field-assisted dissolution rate is equal to the rate of thickening of the oxide at the metal/film interface due to inward migration of O^{2-} regions of locally thinner film material of increased curvature between the protuberances develop major pores earlier than regions of reduced curvature.

In conclusion, not only the defects of aluminum surface facilitate the initiation of regular pores of anodic oxide, but also the pretreatments as electropolishing and scratching have great impacts during the initial state of pore initiation.

2.4.1.2 Prerequisite of pore initiation: dissolution

The anodic oxide film develops simultaneously and only at the oxide/electrolyte and metal/oxide interfaces by Al^{3+} egress and O^{2-}/OH^{-} ingress under the high field, i.e. no growth of film occurs within the film. Variation of dissolution rate closely related to the

non-uniform electric field over the aluminum surface plays an important rule for the pore initiation of anodic oxide film.

The current distribution is non-uniform during the "nuclei" process with initial concentration at the thickening regions, but eventual concentration at the thin areas which are the precursors of the steady state pores. In Figure 2.9, by rapidly transforming into the situation with a scalloped pore base, the film then actually penetrating more into the metal in these locations. As the voltage rises, the pore and cell diameters increase and so a smaller number of major pores eventually propagate, certain of the incipient pores ceasing to function, and any very large ones would not grow much and might even decrease in size.

Even under constant current anodizing when the field should be constant all over the surface, some local variations due to structural and impurity effects in the metal or the pre-existing air-formed film seem possible. Thus, although there appear to be too many 'nuclei' for them to be related to substrate dislocations, the microstructure of metal substrate is involved because the main pores and cells develop most rapidly along the metal grain boundaries. Local thickening could be due to easier entry of ions into the film at defective sites or to easier transport through the film. This would be due to greater structural imperfection of the film or possibly to greater impurity at the regions. Due to current concentration at the developing major pores, it eventually is greater than the field across the film.

As shown in Figure 2.10, after the concentration of current in the initially thin oxide regions, just a single major pore (Figure 2.10 a) and then two adjacent pores (Figure 2-10 b) are seen developing. The lines representing the easiest current paths through the barrier layer may also be considered as the lines of force of the electric field. The configuration of these lines shows that, although the field is constant across the flat parts of the barrier layer, at the curved pore base it increases in passing from WX to YZ. At the pore bases the local field in the vicinity of the pore base YZ, which is the field assisting dissolution, is greater than the average field between YZ an WX which determines film growth, as

suggested by Hoar [25]. Thus, the rate of dissolution near YZ is assisted by the field to a greater extent than is growth, and also more than elsewhere on the outer film surface, so that the pore can be propagated and becomes surrounded by a cell. During this period, when only occasional major pores have initiated, the rest of the film surface is still passing current, but the true current density at the major pore base is greater than elsewhere because the increased oxide dissolution here results in a lower barrier layer thickness, and also the pore is drawing current from the larger area of the cell base. This explains the self-sustaining nature of pores. Other locally thin areas can only develop into pores if they can compete with already established pores for current. The distribution of current lines in Figure 2.10 shows that a high forming voltage, producing a thicker barrier layer and cell wall, will require greater pore separation and fewer pores than a low voltage. It is expected that an approximately close-packed distribution will be arrived at and that this will be more regular beneath the surface than upon it, because the latter represents the initial non-steady state situation. The rate of spread of pores will depend upon the dissolving ability of the electrolyte under the field.

Even though the barrier layers stay essentially constant in thickness with anodizing time, it follows that film dissolution at the pore bases must be much faster at higher electric field. This is a strong indication that field-assisted dissolution of the oxide is occurring at the pore bases, as suggested by Hoar [25], since the solution conditions are nominally identical in each case.

The development of penetration paths and, ultimately, pores arises from the concentration of the field beneath and closely adjacent to them. The concentration of electric field and hence the current results in the so-called field-assisted dissolution of the film.

2.4.2 Steady-state porous anodic film formation

The steady state evolution of the porous structure results from the balance between two competing processes across the barrier layer: Oxide formation at the metal-oxide interface and field-assisted oxide dissolution at the oxide-electrolyte interface. This

balance results in a barrier layer of constant thickness that is displaced into the aluminium substrate as anodizing proceeds [12].

It was suggested that oxidation and dissolution proceed by the following mechanisms:
1) The growth of aluminum oxide, either at the interface between aluminum and alumina or within the barrier layer due to the counter migration of Al^{3+} ions and OH^{-} and O^{2-} ions;

2) The dissolution of aluminum oxide at the interface between the alumina film and solution.

For the initially developed relatively uniform barrier type film, a uniform potential distribution is revealed across the film section. However, with the development of penetration paths, the potential lines remain relatively uniformly separated within the compact region of film but, immediately beneath the paths, the potential lines are concentrated, indicating a local increase in field strength, enhancing their development through field-assisted dissolution; field-assisted dissolution effectively polarizes the Al-O bonds, allowing more ready Al^{3+} dissolution than in the absence of the field. The eventual development of the penetration paths into the readily recognized pores arises, which is assisted by the relatively strong lateral component of the field beneath the tip of the penetration path, resulting in its lateral expansion to develop an embryo pore with the characteristic inversely funneled sectional appearance [26].

As a consequence of pore development, the electric field and ionic current become concentrated in the barrier layer beneath the major pores. This implies continued ingress of $O2^{-}/OH^{-}$ ions to form solid film at the metal/film interface and corresponding Al^{3+} ejection at the pore base/electrolyte interface as well as field-assisted dissolution of Al^{3+} ions, unlike the relatively low field strength regions between developing pores. Consequently, in the regions of current concentration, a localized scalloping of the metal/film interface occurs. This trend continues until the scalloped regions merge. Thus, the steady state anodic film morphology is created.

For the steady state film displayed in the schematic diagram of Figure 2.11, the average field across the barrier layer dictates the film growth, with the locally increased field at the pore base/electrolyte interface influencing field at the pore base/electrolyte interface influencing field assisted dissolution. Calculations by Xu [24] suggest an average field strength of 8×106 $V.cm^{-1}$ and a local increased field strength of 2×107 $V.cm^{-1}$. Clearly, for steady state film growth, there is a dynamic equilibrium between film growth at the metal/film interface and field-assisted dissolution at the pore base-electrolyte interface.

Under steady-state conditions, when the voltage does not change with time, the resultant anodic film parameters remain unchanged. This results from a self-adjusting situation, where any tendency for the pore diameter to increase or decrease is checked by a consequent increase or decrease in the radius of curvature of the pore base. Thus, in essence, film formation occurs at a constant rate, being determined by the average field. It is balanced by field-assisted dissolution, at a rate determined by the local field, related to the radius of curvature of the pore base.

Observations of porous anodic film surfaces and cell-base patterns in the metal after oxide stripping reveal a greater pore population density at the surface. This arises from incipient pores which develop initially but are surplus to the requirement of the field and crease to function. For normal growth conditions, the steady-state pores are cylindrical in section and remain unchanged in diameter with anodizing time. Close to the film surface, such pores are inversely funneled, reflecting their initial development. Under certain situations, normally funneled pores may develop, particularly when the influence of chemical dissolution on the oxide is enhanced, i.e. by anodizing at sufficiently high temperature.

2.4.3 Controlling factors on film parameters

It is known that the major anodic film parameters, such as barrier layer thickness and pore and cell diameters, are directly dependent upon the steady state voltage. However, for controlled morphology and composition film formation, more precise understanding

on controlling factors on film parameters is needed.

During the initial development of anodic oxide films at constant current density, the voltage rises progressively, so the pore diameter increases proportionately. Meanwhile, a proportion of the numerous, random, incipient pores nucleated on the outer film surface must be eliminated as the remainder take up their equilibrium distribution and size *[18]*.

Figure 2.12 shows schematically how the anodizing voltage determined the pore parameters. There are three possible cases, in which the pore base has different radii of curvature. Initially it is assumed to be constant voltage anodizing, and that the barrier-layer thickness, b, and the solid angle, w, remain constant as the pore diameter varies. It is assumed that r2 is the equilibrium pore base radius of curvature under the conditions.

Since the same current is passing through all of the surfaces, the extent of the field increases when passing from cell base to the pore is measured approximately in three cases by the ratio of the cell base area to pore base area, thus:

$$\frac{(r_1+b)^2}{r_1^2}; \quad \frac{(r_2+b)^2}{r_2^2} \quad \text{and} \quad \frac{(r_3+b)^2}{r_3^2}.$$

As the radius of curvature increases, any enhancement of the field assisting dissolution at the pore base due to convergence of the lines of force there decreases and the field approaches the average field through the barrier layer, which is the same everywhere. Basically, film formation occurs at a constant rate in all situations determined by the average field. It is balanced by field-assisted dissolution, whose rate is determined by the local field, i.e. by the radius of curvature of the pore base. A self-adjusting situation predominates, any tendency for the pore diameter to become too large or too small being checked by a consequent increase or decrease in the radius of curvature of the pore base. The constant pore and cell sizes, proportional to cell voltage, are a consequence of the equilibrium barrier-layer thickness and pore base radius of curvature established.

At constant voltage anodizing, slight variations in barrier layer thickness may occur during the establishment of the steady-state period. While at constant current density, relatively large changes can occur in the barrier-layer thickness reflected in the measured voltages. The initial rise is dominated by barrier layer growth. The drop from the maximum corresponds to the initial pores having a low radius of curvature, giving a high rate of field-assisted dissolution. As the pore base radius of curvature increases with the growth of the pore diameter, the dissolution at the pore bases slows down and the rate of voltage decrease declines until the pores and barrier layer have reached their equilibrium dimensions [18].

In practice, the pore and cells remain constant interpore distances of the spheres of which they respectively form parts. Based on consideration of the field at the intersection points of two adjacent cells for the three different cases of Figure 2.13, in which the barrier layer is of constant thickness but the proportions of the appropriate spheres occupied by the cell and pore bases vary. The un-oxidized metal close to points A in Figure 2.13 is acted upon by two components of the field, each component trying to pull the metal into different cells. In Figure 2.13 a, where the pore and cell bases are almost hemispheres, these two fields almost cancel each other out and so there is virtually no net field acting to pull ions through the oxide towards or away from the pore base. In the absence of moving ions there is less tendency for field-assisted dissolution to propagate the pores sideways and enlarge. As we move to Figure 2.13 b and c, however, the horizontal components of the field cancel out as before but the vertical components reinforce, causing film growth and balancing field-assisted dissolution to promote barrier layer and pore propagation into the metal. Therefore, if the segment becomes too small, the appropriate component of the field causes lateral spread of the pore, whereas if it is too large penetration into the barrier layer predominates.

Therefore it is clear why a constant angle θ of $\cos^{-1}$ 0.71 should be obtained for the limited range of voltages under a given set of anodizing conditions, requiring a direct relationship between cell-wall thickness and barrier-layer thickness.

The size and geometrical arrangement of the well ordered porous anodic oxide is constrained by the self-organization anodizing conditions that is determined by the acid species. Shingubara [27] quantified the regularity of the pore arrays, in the case of oxalic acid electrolyte, as a function of anodizing voltage and acid concentration.

The anodizing voltage that gives a well ordered anodic pore array is found to be dependent on the acid species. Reported typical dimensions of the pore arrays under self organization conditions are summarized in Table 2.1. The cell diameter under self-organization conditions were stated to be 500, 90 and 50–60 nm for phosphoric acid (anodizing voltage 195 V), oxalic acid (40 V) and sulfuric acid (25–27 V), respectively by conventional anodizing. Pore diameters immediately after anodizing are listed in the table; additional diluted phosphorous acid etching can increase these values, i.e., widen the pores.

For ordered pore arrays, the dependence of interpore distance on the anodizing voltage are compared in Figure 2.14 for the three types of electrolyte [4]. The samples anodized under voltage ranges of 19–160 V show interpore distances from 50 to 400 nm. It can be found that, for phosphoric acid, the pore distances are a little bit larger than the fitting values, while for oxalic and sulfuric acids they are a little bit smaller. Similar electrolyte dependence was also found for disordered pore arrays [28]. All these mean that the morphology has a similar formation mechanism for both ordered and disordered pore arrangements.

In conclusion, the pore arrangements, the interpore distance in porous anodic oxide film has the dependence on the anodizing voltage, the electrolyte, and its concentration, and that the anodic voltage has a major effect on both pore diameter and interpore distance.

2.5 Self-ordering of porous anodic oxide films

Except for the pre-patterning methods for an aluminium substrate such as an imprinting process, highly ordered self-organizing porous anodic oxide can be obtained only in three types of electrolyte at individually specified self-ordering voltages, *i.e.*, sulphuric acid at

25 V, oxalic acid at 40 V [2], and phosphoric acid at 195 V, giving 63 nm, 100 nm, and 500 nm pore intervals, [29-31] respectively. Although massive researches have been focusing on this, the mechanism has not been fully confirmed. However, several rational explanations have been suggested, and relevant factors that are normally taken into consideration are discussed in following paragraphs.

2.5.1 Mechanical stress and volume expansion during anodizing

When aluminum is oxidized to oxide, the volume expands by roughly a factor of 2 since the atomic density of aluminum in alumina is a factor of 2 lower than in metallic aluminum [32]. The oxidation takes place at the metal/ oxide interface, which leads to compressive stresses in the layer. However, the material can only expand in the vertical direction, therefore the existing pore walls are pushed upwards [33].

On the other hand, during steady state pore growth of porous anodic oxide film, pores grow perpendicular to the surface with equilibrium of field-enhanced oxide dissolution at the oxide/electrolyte interface and oxide growth at the metal/oxide interface. Al^{3+} ions are mobile in the oxide under the electric field and some of the Al^{3+} ions reaching the oxide/electrolyte interface are ejected into the electrolyte without contributing to the oxide formation [12]. Moreover, the hydration reaction of the oxide layer takes place at the oxide/ electrolyte interface leading to dissolution and thinning of the oxide layer. As a result, under the usual experimental conditions, the expansion of aluminum during anodizing leads to less than twice the original volume, but strongly depends on experimental conditions like the electrolyte concentration or anodizing voltage [34].

A possible origin of forces between neighboring pores is therefore the mechanical stress which is associated with the expansion during oxide formation at the metal/oxide interface. Since the oxidation takes place at the entire pore bottom simultaneously, the material can only expand in the vertical direction, so that the existing pore walls are pushed upwards.

In the electrolytes, it was found that optimal conditions for the growth of ordered

structures are accompanied by a moderate expansion of the aluminum, whereas no ordered domains can be observed in the cases of contraction or very strong volume expansion. The mechanical stress, which is associated with the expansion of the aluminum during oxide formation should be the cause of repulsive forces between neighboring pores during the oxidation process, which lead to self-organized formation of hexagonal pore arrays [33].

2.5.2 Porosity of porous anodic oxide film

The porosity of porous anodic oxide film is an evaluated parameter when investigating the self-ordered mechanism during anodizing of aluminum. Nielsch's [32] group has analyzed in detail the cell structure of the self-ordered porous film obtained from three different electrolytes using transmission electron microscopy as shown in Figure 2.15. A constant ratio of the radius of the pores r to the interpore spacing D_{int} (r/D_{int}) was obtained when neglecting the scale. The porosity of a hexagonal structure is given by

$$P = \frac{2\pi}{\sqrt{3}}\left(\frac{r}{D_{int}}\right)^2$$

By calculation the optimum porosity P with the constant value of $r/D_{int,}$ the optimum porosity is around 10%. This corresponds to a volume expansion of alumina to aluminum of about 1.2. The observation of the 10% porosity rule strongly supports the mechanical stress explanation for the self-ordered mechanism, which is actually a balance of formation and dissolution of porous anodic oxide morphologically stable from the view point of mechanical stress.

2.5.3 Electric field strength during self-ordered anodizing

The high field theory suggests that logarithm of current density has a linear relationship with electric field strength. Ono [35] have investigated the self-ordering behaviour of porous anodic oxide formed in three major acid electrolytes by focusing on the current density during oxide growth and the effect of the ratio of pore diameter to cell diameter. It was reported that the theory was applicable to the porous film growth and confirmed

the linear relationship between logarithm of current density and the ratio of pore diameter d_{pore} to cell diameter d_{cell}. This suggests that the d_{pore} /d_{cell} ratio is controlled by the electric field strength E at the barrier layer and the ratio decreased with increasing E. Therefore, it is assumed that self-ordering proceeds in the film with a low d_{pore} /d_{cell} ratio formed under a high electric field.

The porosity of self-ordered anodic film lowered markedly and converged to 0.1 regardless of the electrolyte type, as shown in Figure 2.16, which corresponded to a d_{pore} /d_{cell} ratio of 0.3, when the voltage approached the individual self-ordering voltage accompanying the exponential current increase. Thus, the mechanism of self-ordering is assumed to be closely related to the high electric field strength at the barrier layer during anodic film growth, rather than to the individual self-ordering voltage itself.

Thus it is indicated that high current density, i.e high electric field at the barrier layer of porous anodic oxide is the most important factor that determined the self-ordering of pore arrangement. All other factors such as aluminum ions, concentration of electrolyte and temperature could be explicable by that they lead to keep high current density anodizing without occurring local events such as burning which interrupt the uniform film growth.

In shingubara's work [36], the SEM images of pores in anodic oxide films are analyzed by fast Fourier transformation (FFT) when varying experimental parameters such as temperature, concentration of electrolyte (here oxalic acid specifically) and voltage. Figure 2.17 shows comparisons of pores at various concentrations of oxalic acid and their FFT images. In the case of irregular pore arrangements obtained in 0.05 M oxalic acid electrolyte, the FFT image exhibited a ring structure; while with an increase of oxalic electrolyte concentration to 0.15 M and 0.5 M, the order of pore arrangement improved and the ring split into six spots which reflected six-hold symmetry. The spatial order of holes, $1/\sigma$, is compared by evaluating the ratio of the spot intensity I and its full-width half maximum σ of FFT images. $1/\sigma$ is shown as a function of the oxalic acid concentration in Figure 2.18. The highest order of two-dimensional array of pores was obtained at 0.5 M. This illustrates the influence of electrolyte concentration on ordering

degree of pores.

2.6 Highly ordered porous oxide formation with pre-pattern method

Alternative methods for achieving well ordered porous anodic oxide have been developed to avoid two steps anodizing which is time consuming and sacrifice a thick anodic layer, that is the oxide layer removed after long period first steps anodizing. Some techniques which focused on pore nucleation have been developed on the basis of the formation of pre-structures acting as seeds for the electrochemical pore growth [37].

The pre-pattern can be effectively fabricated using E-beam lithography, focused-ion beam lithography, and nano-imprint lithography so that single direction ordered porous anodic oxide can be prepared over a large area. Nano-imprint lithography has several advantages in terms of efficiency in preparing highly ordered porous anodic oxide. In Masuda's novel work [2], a SiC nano-imprint master stamp was fabricated by using a sequence of lithographic device fabrication processes, and the advantage of this method is that the stamp can be reused for several times, so that greatly enhances the productive efficiency.

If the thickness for the sacrificial layer is limited to a few micro meters, as in the case for a thin aluminium film prepared through vacuum deposition, nano-imprint lithography is required for the preparation of ordered porous anodic oxide [38, 39]. Moreover, it was demonstrated that successive nano-imprint lithography processes can create complicated patterns which cannot be easily fabricated by conventional lithography [40].

Although the merits of nano-imprint pore nucleation are well known, the construction of a master stamp requires complicated nanofabrication techniques.

2.6.1 Pre-patterning using mold or stamp

To achieve highly ordered porous anodic oxide films, Masuda also invented a pre-patterning process [41], using a textured SiC mold to produce ordered patterns on aluminium by a mechanical indentation prior to anodizing. The shallow concaves on

aluminium induced the pore initiation during anodizing and led to an ideally ordered pore arrangement within the stamped areas. They prepared periodic concave regions on the aluminium surface by pressing it using a SiC mold with an array of periodic convex surfaces. Figure 2.19 schematizes the pre-patterning process. The SiC mold was fabricated by conventional lithography. A long-range-ordered channel array in an area of millimetres could be obtained by this method. This method is very effective for fabricating a photonic band crystal. However, the density and hence the fineness of the pore arrays is limited by the electron beam lithography and dry etching of the SiC mold. A cell size that is finer than 50 nm would be too difficult to fabricate in large area.

Recently, some modified pre-texturing methods, such as pre-patterning on aluminium by optical diffraction grating [42], atomic force microscope scanning probe [43], focused ion beam, and polystyrene beads, have been also attempted, to perform direct or mold-less patterning on aluminium exclusive of the expensive SiC master fabrication.

2.6.2 Pre-patterning with nano-indentation

Alternative pre-patterning technique using scanning probe microscope nano indentation was proposed [43]. The schematics of nano-indentation are shown in Figure 2.20. By using a nano-indentation apparatus equipped with a scanning probe microscope, periodic ordered pore arrays of porous anodic films can be guided and then formed during anodizing with the desired pore intervals by changing the intervals of the concaves by nano-indentation with the scanning probe microscope.

The indentation of Al was made using the nano-indentation apparatus attached to a scanning probe microscope. A three-sided pyramidal diamond tip with an angle of 142.3º was used as an indenter. The atomic force microscopic (AFM) image was obtained with the same tip. The indentation load is usually 25 to 40 μN.

Figure 2.21 (a) shows the AFM view of the surface of aluminium after nano-indentation. It can be observed that almost uniformly sized concaves were formed in an ordered array after the nano-indentation. The shape of the concave was inversed pyramidal, which

corresponded to the tip used for the nano-indentation. The figure on the right side shows an SEM micrograph of the porous anodic film after anodizing in 0.2 M phosphoric acid under a constant voltage of 160 V for 20 minutes. From Figure 2.21, it is observed that each concave initiated pore development and guided the growth of the highly ordered pores, whereas the pore arrangement in an untreated area was disordered.

An indenting strength of around 4×10^{-5} N was sufficient to control the initiation of pore formation by nano-indentation. The effect of indentation interval on the regularity of pores at anodizing voltage of 40 V is shown in Figure 2.22. At a 55 nm interval (Figure 2.22 a), pores were connected to each other, and at a 110 nm interval (Figure 2.22d), additional holes formed at random between the holes whose positions were controlled by indentation. Ordered arrays of pores were formed at 65 and 80 nm intervals. Thus, controllability of pores depends on both anodizing voltage and indentation interval [44].

2.6.3 Pre-pattering using optic grating

One of the alternative method to do nano-indentation using optic grating was elaborated by Irmantas Mikulskas [42]. The main motivation of using optic grating is to avoid using expensive way of electro beam lithography or nano-indentation. Meanwhile, large dimension of well arranged textures can be obtained easily using this way compared to the other methods.

A regular groove mesh on the surface of the aluminum substrate was formed by mechanically pressing it with a commercially available optical diffraction grating. The surface morphology of the grating was shown in Figure 2.23 (a). After the pressing procedure, parallel grooves (d =833 nm) spacing were formed on the substrate surface (Figure 2.23 (b)). In order to support the growth of cells in a triangular lattice configuration, two-step press-in procedure were used, which means a second press was performed by rotating 60º around the axis perpendicular to the surface after the first press (shown in Figure 2.23 c). The subsequent anodizing was performed for 3 h at a constant voltage of 200 V at room temperature in very dilute (1:600 v/v H_3PO_4/water) electrolyte. The voltage and electrolyte concentration were chosen so as to produce a cell size of 481

nm, suitable for a close packed array matching the pressed-in pattern period. However, a critical problem with optic grating is the minimum limit of cell distance constrains further application.

2.6.4 Pre-texturing using chemical particles

Chemical particles with uniform size and shape have also been used to be pre-texturing methods for fabricating highly ordered porous anodic films [45].

Figure 2.24 schematically illustrates the procedure for the fabrication of highly ordered porous anodic films using self-organized polystyrene particle arrays. The polystyrene particles with a submicron-scale diameter were self organized to be ordered arrays on a glass plate. Then, pure aluminum were vapor deposited onto the top of the well arranged polystyrene particles. After the removal of glass substrate and polystyrene particles, anodizing was performed on the aluminum with embossed textures by the particles. Anodizing was initiated at the concaves of the aluminium surface. Employment of the self-organized particle array to produce highly ordered porous anodic films with a submicron-scale channel structure was shown to be feasible in Figure 2.24.

2.6.5 Hard Anodizing

The so-called “hard anodizing”(HA) process, which was invented in the early 1960s, was characterized by the use of sulphuric acid at relatively low temperatures and high current densities, and has been widely used for various industrial applications such as surface finishing of aluminium cookware, automobile engineering, textile machinery etc. by taking advantage of the high-speed oxide growth [46].

When the anodizing process is carried out outside the traditional self-ordering regimes, the degrees of spatial ordering decrease drastically. Applied voltages higher than the optimum value required to maintain stable anodizing in a given electrolyte always result in ‘breakdown’ or ‘burning’ of the anodic film caused by catastrophic flow of electric current. These process limitations reduce the potential applications of porous anodic films.

Efforts have been made to explore new self-ordering regimes in a wider range of *D*int [35, 47, 48] [49]. Shingubara used a 1:1 oxalic/sulphuric acid mixture in anodic oxidation to obtain self-ordered pore arrays with *D*int = 73 nm. Ono *et al.* found that domains of highly-ordered pore arrays occur in porous alumina film formed during breakdown. Chu [48] reported the fabrication of self-ordered AAO in sulphuric acid solution under high anodizing potentials and current densities of up to 70 V and 200 $mAcm^{-2}$, far from the MA regime (H_2SO_4: 25V and 2–4$mAcm^{-2}$) but similar to the anodizing conditions for HA. They named this process 'high-field anodizing' and used an 'aged sulphuric solution'.

The Lee's[50] group reported a new self-ordering regime of porous anodic films that was found during HA of aluminium substrates using oxalic acid and applying potentials of 100–150 V, which are more than three times higher than the voltage (40 V) used in conventional oxalic acid anodizing.

An oxide layer (thickness >400 nm) was formed on the surface of the aluminium substrate by anodizing an aluminium substrate under normal conditions (i.e. 40V in oxalic acid) before carrying out the HA process to suppress breakdown effects. Subsequently, the anodizing voltage was slowly increased to a target formation voltage (100–150 V) for HA at a rate of 0.5–0.9 V s^{-1} and the HA will be continued under a constant potential. The HA is accompanied by a large evolution of heat, which is effectively removed using an appropriate electrochemical setup in the experiment.

Figure 2.25 shows the relationship between *D*int and the anodizing voltage for HA with self-ordering voltages and the corresponding *D*int that have been reported for conventional anodizing processes are also plotted for comparison.

This HA process establishes a new self-ordering regime in the ranges of *D*int = 200–300 nm, filling the gap that has not been achieved by conventional anodizing processes. On the basis of the newly found self-ordering behaviors, the fabrication of porous anodic

film templates with periodically modulated diameters of pores, whose three-dimensional (3D) pore structures have the potential for a broad range of nanotechnology applications, such as 3D photonic crystals, meta-materials, microfluidics and for the template-based synthesis of multifunctional nanowires and nanotubes with modulated diameters.

2.7 One dimensional nanostructure fabrication

One dimensional nanostructure can be defined as those in which, the free mean path of charge carriers is larger than the available lengths in two spatial dimensions so that, the carriers are confined for transport phenomena only in one dimension as it happens in nanowires and nanotubes.

In general, nanotubes are defined as hollow nanowires with submicrometric wall thicknesses independently of the material on which they were made. Currently both types of nanostructures, nanowires and nanotubes, can be made of multiple materials including metals, semiconductors, insulators and also bioactive materials.

For nanostructure materials, at least one of its phases is in the nanometer size range, usually defined as 1–100 nm. Nanostructure materials exhibit electronic and optical properties somewhat different from the same bulk materials because of their quantum tunable electronic properties, which emerge as a function of size, the so-called quantum size effect. Since the discovery of carbon nanotubes by Iijima [51], there has been tremendous interest in both the preparation and property of nanostructure materials formed from various materials such as metal sulfides and oxides.

Currently, various kinds of nanostructures including nanowires, nanotubes and nanodots have been fabricated using porous anodic oxide templates. All these types of nanostructures can be made of multiple materials including metals, semiconductors, insulators and also bioactive materials etc. according to their **peculiar** properties.

2.7.1 Magnetic properties

Magnetic nanowire/nanotube arrays have recently aroused considerable interest in terms of perpendicular magnetic recording. The magnetic nanowires/nanotubes that are introduced into the pores of anodic oxide templates by electrodeposition are potentially capable of producing bit densities more than 100 G bit in^{-2}.

The nanowires/nanotubes may consist of a single magnetic element [52, 53] or a magnetic alloy [54, 55]. The magnetic properties of nanowires/nanotubes have been extensively investigated with particular emphasis on three areas, namely, the factors that determine the effective easy axis of the nanowires/nanotubes [56, 57], magnetization reversal processes within the array [58] and magnetic interactions between wires [23, 59] respectively. The magnetic nanowire/nanotube arrays exhibit a coercive field when the magnetic field is applied parallel to the long axis [60]. It has also been reported that the squareness of the hysteresis loop can be increased from 30% up to nearly 100% by decreasing the wire diameter. Studies also have been performed on the composition [58], magneto-optical [9] and annealing temperature [55] dependent properties. Magnetic nanowires [9] arrays based on porous anodic oxide present in principle an attractive potential medium because when deposited the wires comprise a highly ordered pattern of reasonably magnetically isolated units.

Figures 2.26 [61] shows the variation of squareness of the hysteresis loop as a function of the applied magnetic field (H) parallel and perpendicular to the wire axes for different nanowire diameters. For Co nanowire arrays, a gradual increase of coercivity is observed with increasing aspect ratio (length (l)/ diameter (d)), but little change is observed when diameter is larger than 50 nm. This is mainly due to large crystal grains extending transversally across the full wire diameter and longitudinally over several micrometers. Even more, when electrodeposited, Co is proved to adopt a rather good quality hexagonal compact structure with a preferential texture which depends on the diameter of the wires. Therefore for diameters smaller than 50 nm, the *c*-axis is preferentially oriented parallel to the revolution axis of the wires, whereas for diameters larger than 50 nm it is aligned within 10^{o} of the normal to the wire axis. The magnetic properties of the nanowires could be modified by simply changing their diameter, which will change coercivity,

magnetization, remanance and squareness of the hysteresis loop.

The total magnetic anisotropy of these nanowires was found to be significantly influenced by the magnetic anisotropy, form of the nanowires and the demagnetization fields between the nanowires. The magnetic nanowires of Fe, Co, Ni show much enhanced magnetic coercivity than that of their bulk counterpart. The coercivity is strongly influenced by annealing of the wire at different temperatures, the aspect ratio and the wire diameter. Figures 2.27 (a) and (b) show coercivity of the magnetic Fe, Co and Ni nanowires with their diameters at room temperature and at zero temperature.

Chen's group studied the magnetic properties of Fe–Co alloy nanowire arrays fabricated by electrodeposition, and found that their coercivity increases with increase in the spontaneous magnetization of the nanowires [58]. The coercivities *Hc* and remanence *Mr /Ms*, which were measured with the applied field perpendicular to the substrate, which is the easy axis are stated in Table 2.2 for the series of Fe–Co nanowire arrays. The magnitude of *Mr /Ms* is about 0.9. The coercivity increases with increasing Co content from 0 to about 30 at.%, and then decreases with continued increase of the Co content. The Slater–Pauling curve predicts that the spontaneous magnetization *Ms* of Fe–Co alloy increases with Co content and then decreases with Co content above 30 at.% in bulk states. In this case, the wires are nanoscaled and the imperfections may decrease *Ms* as well as the shape anisotropy of the nanowires compared with bulk state materials. But for the nanowires fabricated under the same conditions and having the same diameter, the influence of imperfections can be expected to be the same. Following this, it is concluded that the coercivity *Hc* of the nanowire increases with the increase of its spontaneous magnetization *Ms*.

Another important aspect is the interactions on parallel nanowire arrays, which are based on magnetostatic effects that are relevant when the line separation (s) is less than the line width (w). The main effect of line interaction is the reduction of the coercive field (or the effective anisotropy) with decreased line separation for fields applied along the line (Figure 2.28). This result is consistent with the intuitive dipole picture discussed earlier.

The interaction field due to the neighboring lines will be such that it helps the switching, thus reduced coercivities are expected.

For longitudinal fields, it has been reported that the magnetization of the lines tends to align antiferro-magnetically [62], as would be expected for a system of parallel dipoles with 90° bond angle. For perpendicular fields, the effect of the dipolar coupling is to reduce the saturation field, as compared to isolated lines (Figure 2.28). This is caused by the magnetic charges created along the edges of the lines, which induce a field in the same direction as the applied field. Hence, the effective demagnetizing field is reduced [62, 63].

2.7.1.1 Applications

The most attractive potential applications of nanowires/nanotubes are in the magnetic information storage medium, especially the magnetic nanowire arrays which may have potential in future applications as high-density storage media. Studies have shown that ordered arrays of magnetic nanowire arrays possess the capability of storing 1012 bits/in^2 of information per square inch of area. The small diameter, single domain nanowires of Ni, Co fabricated into the pores of porous anodic alumina has been found to be most suitable for the above purpose. The high aspect ratio of the nanowires results in enhanced coercivity and suppresses the onset of the 'superparamagnetic limit', which is considered to be very important for preventing the loss of magnetically recorded information between the nanowires. Suitable separation between the nanowires is maintained to avoid the inter-wire interaction and magnetic dipolar coupling. It has been found that nanowires can be used to fabricate stable magnetic medium with packing density > 1011 wires/cm^2.

2.7.2 Electrical transport properties

Electron transport properties of nanowires are important for electrical and electronic applications as well as for understanding the unique one-dimensional carrier transport mechanism. Researches have shown that the wire diameter, wire surface condition, chemical composition, crystal structure and its quality, crystallographic orientation and the wire axis etc. are important parameters to influence the electron transport mechanism

of nanowires.

It was reported that nanowires exhibit both ballistic and diffusive type electron transport mechanism, which depends upon the wire length and diameter. Ballistic type transport phenomena is associated with predominant carrier flow without scattering which is due to the fact that the carrier mean free path is longer than that of the wire length.

Ballistic type transport mechanism is normally observed at the contact junction of nanowires and other external circuits [64, 65], where the conductance is quantized into an integral multiple of $2e^2/h$, called the universal conductance unit (e the electronic charge and h the Plank's constant) [66].

In the case of ballistic type transport in metallic nanowires, the conductance quantization phenomena takes place because of the fact that the nanowire diameter becomes comparable to the electron Fermi wavelength of that metal [67]. As compared to the ballistic transport mechanism, in diffusive type conduction mechanism, the carrier mean free path is smaller than that of the wire length. Therefore, various types of scattering affect the carriers and the carrier transport mechanism of nanowires becomes quite similar to that of bulk counterpart.

The electron transport mechanism of the metallic/semi-conducting nanowires can be obtained by considering three parameters: wire diameter (d), carrier mean free path (lc) and the de Broglie wavelength of electron (λe). Earlier studies have shown that when the wire diameter (d) is larger than the carrier mean free path (lc) and the de Broglie wavelength of electron (λe) i.e. $d >> lc$ and $d >> \lambda e$, the electron transport mechanism of nanowires remains similar to that of bulk counterpart. However, if the wire diameter (d) becomes smaller or comparable to that of the carrier mean free path (lc) and much larger than the de Broglie wavelength of electron (λe) i.e. $d \leq lc$ and $d >> \lambda e$, the electron transport mechanism of nanowires follows the classical laws of physics.

On the other hand, when the carrier mean free path (lc) and the de Broglie wave length of

electron (λe) both become comparable to the wire diameter i.e. d ≤ lc and d = λe, the phenomena of quantum confinement occurs in nanowires which includes significant change in the density of electron states. Studies show that the electronic density of states (DOSs) of nanowires is strongly diameter dependent.

The conductance of nanowires strongly depends on their crystalline structure. In the case of perfect crystalline Si nanowires having four atoms per unit cell, generally three conductance channels are found [10]. One or two-atom defect, either by addition or removal of one or two atoms may disrupt the number of such conductance channel and may cause variation in the conductance. Variation in conductance due to the above reason is shown in Figure 2.29, where conductance is plotted as a function of energy for perfect Si nanowires and single atom addition defect nanowires.

2.7.2.1 Applications

Nanowires possess the potential for use in numerous electronic applications. Junctions of semiconductor nanowires such as GaAs and GaP have shown good rectifying characteristics[68]. Several semiconductor devices such as junction diodes[69, 70], memory cells and switches [71], transistors, FETs, LEDs [68, 72] and inverter [73] etc have already been fabricated using nanowire junctions.

The basic building blocks of semiconductor devices can be used to fabricate complex IC chips of much reduced dimension. It has been found that these junction devices exhibit transport and current rectifying properties similar to their parent counterpart. Several attempts have been made to fabricate nanowire diode and it has been demonstrated that the crossings of phosphorus (n) and boron (p) doped Si nanowires form p–n junction diodes.

The field effect transistors (FET) made of nanowires exhibit remarkably modified conductance behavior and they are very attractive because of their morphological advantages. The operational speed of FETs made of nanowires is much faster compared to that of bulk FETs.

In contrast to the crossing of two distinctive nanowires, several heterogeneous junctions can be formed inside single superlattice nanowire, by varying the materials compositions along the wire axes or perpendicular to the wire axes. Nanowire junctions can also perform certain logical operations and can be used as logic gates[72]. The electroluminescence (EL) properties of nanowires can be employed for different opto-electronic applications[71].

2.7.3 Thermoelectric properties

The efficiency of thermoelectric energy conversion devices is a function of thermoelectric figure of merit *ZT* where *T* is the temperature and Z is defined as $Z = S^2\sigma/\kappa$. In the expression of *Z*, *S* is Seebeck coefficient, σ is the electrical conductivity and $\kappa = \kappa e + \kappa l$ is the thermal conductivity, which includes contribution from carriers (κe) and from lattice (κl). Large values of *ZT* require high *S*, high σ and low κ. It is very difficult to increase *Z* in bulk thermoelectric materials. Specifically, an increase in *S* normally leads to a decrease in σ due to carrier density considerations and an increase in σ implies an increase in the carrier contribution to κ as given by the Wiedemann-Franz law. In fact, the thermoelectric figure of merit *ZT* in bulk materials has been approaching the limit; the best bulk thermoelectric materials are alloys of bismuth (Bi) and tellurium (Te) such as $Bi_{0.5}Sb_{1.5}Te_3$, with $ZT \approx 1.0$ at 300K. It is believed that a *ZT* value exceeding 3 is needed in order for a thermoelectric cooler to compete with a vapor compression cooling unit such as a chlorofluorocarbon (CFC)-based refrigerator [74]. Low dimensional materials systems like nanowires may have significantly improved *ZT* compared with their bulk counterparts and thus meet this requirement, as shown in a number of theoretical investigations on different nanowires [75-77].

Some nanowires exhibit interesting thermoelectric properties when they are composed of promising thermoelectric materials such as Bi or $Bi_{1-x}Sb_x$ alloys. The unique electronic band structure and diameter dependent variation in electron density of state make nanowires promising materials for various thermo-electronic applications [78].

Because of the low effective masses and large anisotropy of the constant energy surfaces

of these materials, quantum confinement effects at 77K are predicted for wire diameters as large as 50 nm. These effects have been verified experimentally by transport measurements.

Metal nanowires exhibit many fold increase in Seebeck coefficient due to their enhanced density of electronic states at the one-dimensional sub-band edges, which is attributed to the quantum confinement effect. The thermopower of the metallic nanowires also increases because of the enhanced electronic density of state near the Fermi energy level. Studies have shown that the Seebeck coefficient and thermopower of metallic nanowires are significantly influenced by the wire diameter and the alloy phase concentration. It is also observed that the thermal conductivity of nanowires is influenced by the wire diameter. The variations of thermal conductivity (k) as a function of temperature for Si nanowires of different diameters are shown in Figure 2.30 [79].

It has been reported [80] that in Sb and Si doped Bi nanowires, the thermo power can be increased by decreasing the wire diameter. A similar phenomenon has also been observed in the case of alumina doped Zn nanowires[80]. Bi nanowires also exhibit significant temperature (T) dependence of resistance, R(T), and the phenomena is strongly influenced by the variation of diameter of the nanowires[81]. Here it should be noted that the Bi nanowires exhibit quantum confinement effect below certain critical diameter (48 nm) and the semimetallic phase of Bi transforms into the semiconducting phase[80] [75, 81]. This implies that at higher temperature, the semimetallic phase transformation of Bi nanowires is possible only by reducing the wire diameter. The crystalline structure of the material is also an important factor, which influences the quantum size effect of nanowires.

Investigations have also clearly shown that the electronic wave function becomes more localized with the reduction of diameter of the nanowires [80]. This phenomenon is considered to be the key factor that causes nanowires to exhibit interesting thermoelectric properties.

2.7.3.1 Applications

The figure of merit for a thermoelectric material, *ZT*, is proportional to its electrical conductivity and the square of the thermopower, and is inversely proportional to the thermal conductivity. The best commercially available thermoelectrics have a figure of merit of ZT ~ 1, corresponding to an energy conversion efficiency of about 10% of the Carnot value. Whereas this relatively low efficiency limits thermoelectrics to niche applications, a significant increase in efficiency would have substantial economic impact. For instance, an effective thermoelectric may be used to partially recycle waste heat from the exhausts of car engines, potentially leading to significantly improved gas mileage. Thermoelectrics can also be used for silent refrigerators that have no compressor or refigerant.

The incorporation of nanometer-scale features into bulk materials has led to recent improvements in thermoelectric performance. These nanostructures decrease the thermal conductivity without detrimental effects on the electrical conductivity and thermopower of a material. In this way nanostructure materials can achi
eve significantly higher *ZT* values than their unstructured bulk counterparts. The enhanced thermo power and manifold increase in the Seebeck coefficient of nanowires make them very attractive for thermoelectric cooling system and energy conversion devices [79].

2.7.4 Chemical properties

Nanowires also exhibit interesting chemical properties mainly because of their enhanced surface to volume ratio, high aspect ratio, large curvature at the nanowire tips and huge number of surface atoms. The high chemical reactivity, interesting electrical and electronic properties of nanowires make them very attractive for sensor devices applications.

Chemical and biological sensors made of nanowires as sensing probe exhibit enhanced sensitivity and fast responsivity compared to the conventional sensors, as they need less electrical power to work. It is believed that the capability of providing real space-time

distribution of a particular species will be improved significantly if arrays of nanowires are used in the sensing probe. These types of nanowire sensors can also estimate the real concentration of a particular substance quickly. It should be noted that functioning of nanowire-based sensors is based on the principle of change in electrical conductivity, which arises due to the adsorption of the molecules that are required to be detected.

2.7.4.1 Applications:

Nanowires are promising material for sensors because their sensitivity enhanced by their small dimensions. Nanowire-based light sensors can detect just a few photons. But to be applicable in practical devices, the sensors have to be integrated with electronics that can amplify and process such small signals.

X.T.Zhou reported chemical sensitivity of silicon nanowires [82]. Upon exposure to ammonia gas and water vapor, the electrical resistance of the HF-etched relative to non-etched silicon nanowires sample was found to dramatically decrease even at room temperature. This phenomenon serves as the basis for a new kind of sensor based on silicon nanowires. The sensor, made by a bundle of etched silicon nanowires, is simple and exhibits a fast response, high sensitivity and reversibility.

2.7.5 Optical properties

The optical properties of nanowires have been studied extensively by employing different optical characterization and analytical techniques.

The complex dielectric function ($\varepsilon 1 + \varepsilon 2$) of the nanowires which are embedded in the template material are deduced with the effective medium theories[83] by considering the nanowires and the matrix to act as one single material. The refractive index (n) and the absorption coefficient (k) of the medium are related to $\varepsilon 1$ and $\varepsilon 2$, respectively for the composite medium.

Metallic nanowires exhibit interesting plasmon absorption effect. Research has shown that the energy of the surface plasmon band is sensitive to various factors such as particle

size, shape, composition, surrounding media and inter-particle interactions [84, 85]. Information about plasmon frequency, donor atom concentration and carrier concentration of nanowires can be obtained by analyzing the infrared (IR) spectra of the nanowires.

The photoluminescence (PL) spectroscopic studies on semiconducting nanowires (InP, CdS, ZnO nanowires)[86] have shown that the PL energy peak and band gap increases with the decrease of the wire diameter. The above phenomena confirm the effect of quantum confinement in nanowires when the wire diameter is reduced.

Fluorescence study of nanowires provides vivid information about the band gap, quantum confinement effect, strain in nanowires, oxygen vacancies, electron effective masses and Fermi energies[68]. The band gap and temperature variation of band gap of the nanowires can be determined from the complex refractive index measurements[87], which are considered to be important parameters for selection of materials for particular photonic applications..

The number of subbands of the nanowires can be measured with the help of magneto-optic techniques. The determination of the number of subbands in nanowires is very important for determining the electron transport properties in them [88].

Nanowire arrays exhibit non-linear optical properties, which make them very attractive for application as photonic material. The sharp increase in the energy of the absorption peak with the decrease of the wire diameter is attributed to quantum confinement effect[75] and the occurrence of the blue shift.

2.7.5.1 Applications

Uniform morphology and interesting optical properties of nanowires have raised their potential for various optical applications. The n–p junction of nanowires has been found to be capable of light emission, by virtue of their photoluminescence (PL) or electroluminescence (EL) properties. The use of p–n junction nanowires has been

contemplated for laser applications. It has been established that ZnO nanowires of wire diameter smaller than the wavelength of emitted light exhibits lasing actions[89] at lower threshold energy compared to their bulk counterpart. This has been attributed to the exciton confinement effect in the laser action, which decreases the threshold lasing energy in nanowires. This effect has been observed in small diameter ZnO (385 nm diameter) and GaN nanowires [89].

The n–p junction nanowires or superlattice nanowires with p–n junctions can also be used as light emitting diodes [10, 71]. Nanowires made of various metal segments like Ag, Au, Ni, Pd etc can be used as barcode tags for different optical read outs.

2.8 Synthesis of nanowires via porous film template

There exist a lot of published papers and reviews on the synthesis of these one dimensional nanostructures including numerous methods. Generally speaking, two basic strategies, top–down, bottom–up and even their combination have been the fundamental modes for fabrication.

In the top–down approach highly ordered nano-lines can be obtained by expensive techniques such as, electron beam lithography (EBL) [90], which nowadays does not rise the required industrial performance. Other alternative is the production of moulds by nano-imprint lithography which could produce features characteristic in fine arrange like 25 nm [91] or less. On the other hand, with the bottom–up approach by self-assembly of molecules is possible to form nanowires at low costs although it could be very difficult to get them well arranged and patterned [92]. Up to date, everything seems indicative that the feasible and best solutions to fabricate functional nanowires and their arrays will be achieved by the joint use of both synthesis routes.

Among them, template synthetic method, using a highly ordered porous anodic oxide template, has attracted a good deal of research interest. At present, ordered porous anodic oxide is widely used to prepare nanosize materials due to its remarkable hardness, uniform pore size, high pore density together with its potentially low cost and relative

ease of their preparation.

For example, over the last few years semiconductor nanowires have been grown within the pores of anodic oxide films so that highly ordered nanowire arrays can be obtained with very attractive Photoluminescence properties. Using similar procedures ZnO nanowire arrays and ZnO-based magnetic semiconductors nanowire arrays have been prepared [93]. Further, anodizing techniques are also increasingly being used to create, in general, ordered porous structures which, can lately be used as templates to grow functional nanowires of different species by using mainly self-assembling process and electroplating techniques.

Compared with other nano-pore templates such as polythene, the porous anodic oxide has a much higher pore density (1011 pores/cm^2), which allows one to fabricate a large number of nanowires at one time. Another interesting feature of the porous anodic oxide template is that the chemistry of the pore walls can be altered via reaction with silane compounds.

Using the anodic oxide templates, nanowires of various metals, semiconductors and conducting polymers, have been fabricated. These nanostructures can be deposited into the pores by either electrochemical deposition or other methods, such as chemical vapor deposition (CVD) [94], chemical polymerization [95], or by sol–gel chemistry [96].

Methods that involve direct pore filling of the anodic oxide template are considered to be straight forward and versatile techniques for synthesizing nanowires. Highlights of some of the pore filling techniques that have gained reasonable popularity are described below.

2.8.1 Pressure injection:

Low melting point metals and semiconductors are melted and injected into the pores of anodic oxide template by applying high pressure in this technique. The material that has infiltrated into the pores is allowed to solidify and form nanowires. The nanowires were finally extracted by dissolving the anodic oxide template chemically. Nanowires of Bi, Sn,

In, Al, Te, Se, GaSb and Bi_2Te_3 have been reportedly fabricated by this technique [97, 98].

2.8.2 Vapor deposition:

Physical and chemical vapor deposition techniques are often employed to fabricate nanowires. Chemical vapor deposition involves the formation of nanostructures from the gas phase at elevated temperatures, usually onto a solid substrate or catalyst. Carbon nanotubes could be formed by chemical vapor deposition process. Bi nanowires in anodic oxide template have been synthesized by introducing Bi vapor into the pores of the anodic oxide template, which is then solidified by cooling [81]. Compound semiconductor nanowires of GaN have also been reportedly synthesized in anodic oxide template by gas phase reaction between Ga_2O vapor and ammonia [99].

2.8.3 Vapor-liquid–solid (VLS) method:

This method involves absorption of source material from the gaseous phase into a liquid droplet that acts as a catalyst. Primarily a liquid alloy is formed which becomes supersaturated and precipitates out the source material by nucleation. The precipitate acts as a preferred site for further deposition and growth of the material at the interface of the liquid droplet, favoring growth of the precipitate into nanowire by suppressing further nucleation on the same catalyst. It has been shown that the diameter of the nanowire depends on the diameter of the liquid alloy droplet. Recently, porous alumina membrane has been used as an alternative to control nanowire diameter in the VLS process [100]. Defect free Si nanowires with diameters in the range of 4–5 nm and lengths of several microns were synthesized by using a supercritical fluid solution phase approach where alkanethiol coated Au nanocrystal (2.5 nm in diameter) were used as seeds to direct the one dimensional crystallization of Si in a solvent heated and pressurized above its critical point [101]. The reaction pressure controls the orientation of the nanowires.

2.8.4 Electroless deposition

Electroless deposition occurs in solutions with complex chemistry without an applied

electric potential with the assistance of template. Deposition occurs spontaneously and sometimes auto-catalytically on surfaces, conducting or non-conducting.

2.8.5 Pulsed laser deposition:

Recently, pulsed laser deposition (PLD) technique is being used to deposit materials on top of the porous anodic oxide template. The material deposited inside the pores is shaped into nanowires and the material that is deposited in the nonporous region that separate adjacent pores, assume different morphologies depending on the nature of the surface. It has been reported that ordered arrays of ZnO nanodots with an average diameter of 60 nm and a periodicity of 100 nm were fabricated by PLD using AAO template. Controlling the oxygen pressure used in PLD photoluminescence (PL) at 380 nm is observed from the ZnO nanodots [102].

2.8.6 Chemical conversion:

Synthesis of nanowires by chemical reaction in the pores of anodic oxide template is another important approach. Initially nanowires of the constituent element is prepared, which is then reacted with chemicals containing the desired element to form the final product.

Ag_2Se nanowires were synthesized by reacting crystalline Se nanowires with aqueous $AgNO_3$ at room temperature[103]. ZnO nanowires were prepared by oxidizing metallic zinc nanowires that were prepared by electrodeposition in the pores of anodic oxide template prior to their oxidation in air at 300°C for 35 h. The free standing ZnO nanowires were extracted from the template by selective dissolutions [104].

Hollow nanotubes of MoS_2 with 50 nm external diameters were prepared by filling the pores of the anodic oxide template with a mixture of molecular precursors, $(NH_4)2MoS_4$ and $(NH_4)_2Mo_3S_{13}$. The filled template was then heated at an elevated temperature to thermally decompose the precursor into MoS_2[105].

2.8.7 Colloidal dispersion filling:

Oxide nanowires, nanorods and nanotubes can be synthesized easily by filling the template with colloidal dispersions. The colloidal dispersion was generally prepared through the sol–gel technique. The porous template was placed in a stable sol for appropriate length of time to drive the sol into the pores by capillary force. The filled template is then withdrawn from the sol and dried prior to firing for densification of the sol–gel derived nanowires, nanorods or nanotubes [96] .

2.8.8 Electrodeposition

Despite of the fact that all the above mentioned techniques are advantageously used for the deposition of nanostructure materials into the pores of anodic oxide template, electrodeposition or electrochemical deposition is regarded as one of the most popular methods of pore filling with conducting metals to obtain continuous arrays of nanowires with large aspect ratios. Electrochemical deposition route is easy, low-cost as well as less skill dependent compared to other techniques mentioned above. Structural analysis shows that the electrodeposited metal nanowires tend to be densely packed, continuous and highly crystalline. Moreover, by simply monitoring the total amount of passing charge one can precisely control the aspect ratios of the nanowires.

To use anodic oxide film for the electrodeposition of one dimensional nanostructures, the pores have to be filled with a conducting or semiconducting material. The anodic oxide film possesses a thick barrier layer. Therefore, the electrodeposition of a metallic or semiconducting material on an insulating and rather thick barrier layer at the pore tips of anodic oxide film is not straightforward. High potentials are required for the tunneling of the electrons through the barrier layer. Electrodeposition by direct current (DC) is very unstable and uniform filling of the pores cannot be achieved. This is due to a cathodic side reaction, which leads to a partial removal of the barrier oxide, formation of holes in the barrier layer, and local deposition in single pores.

Two different methods have been developed to obtain uniform and complete filling of pores by electrodeposition. In the first method, a direct current is used for the electrodeposition. Therefore, the anodic oxide film needs to be detached from the

aluminum substrate by chemically removing the aluminium in saturated $HgCl_2$ solution. Subsequently, the barrier layer is removed from aluminium substrate by a chemical etching process (normally immersed in warm 5_{wt}% H_3PO_4 solution for 80 minutes). A thin metal film of silver or gold is sputtered on one side of the free standing anodic oxide film by evaporation technique [106]. This thin metal film supported film acts as the conductive electrode. The concept of transferring the anodic oxide template by detaching it from aluminium substrate is only applicable for that are thicker than 20 mm and stable enough to be handled. For most of the nanostructure applications mentioned above, a porous alumina thickness of only a few hundred nanometers is required.

Metallic nanowires of Cu [107], Ag [108], Au [109] and different transition metals such as Fe [110, 111], Co [52, 61], Ni [52] [112] and their alloys can be fabricated by the electrodeposition method by filling the pores of the anodic oxide template. Nanowires of different semiconductors, superlattice and superconductors such as Pb [113] can also be fabricated.

For direct electrodeposition into as-prepared anodic oxide template with barrier layer, A.C. electrodeposition technique is preferred because direct current can not pass through the barrier oxide layer [61]. Electrodeposition depends on different process parameters such as deposition current amplitude, frequency of current (voltage), and electrochemical bath temperature and pH value of the electrolyte [114]. In a.c. electro deposition the anodic oxide template acts like a ‘rectifier’ when alternating current (voltage) is applied between the template and other electrodes. A.C. electrodeposition is capable of high pore filling ratio [115, 116].

It has been reported that Fe nanowires are deposited into the pores of the template by using A.C. pulse. The electrolyte solution contains 120 g/l of $FeSO_4.7H_2O$; 45 g/l of H_3PO_3; 1 g/l of ascorbic acid and 2 ml/l of glycerin. The pH value of the solution was maintained at approximately 3 throughout the electrodeposition process. Similarly, Co nanowires were fabricated from $CoSO_4$ salt solution containing 400 g/l of $CoSO_4.7H_2O$ and 40 g/l of H_3BO_4 as electrolyte [106].

It has also been reported that by using highly concentrated electrolyte like 300 g/l $NiSO_4.6H_2O$ or 45 g/l $NiCl_2.6H_2O$ and 45 g of H_3BO_4 solution of pH 4~5 [115], Ni nanowires can be deposited into the pores of the anodic oxide template under a negative current pulse of –25 mA/cm^2 for a duration of 6 ms followed by a positive voltage pulse of +4 V for 2 ms only. Semiconductor nanowires of CdS [117] have been fabricated by electrodeposition method using the oxide template. It has been reported [118] that single crystal compound semiconductor nanowires of CdS, CdSe and CdTe can also be fabricated into the anodic oxide template by electrodeposition. Xu et al (2000) reported that Co–Cu superlattice nanowires can also be synthesized by varying the cathodic potential in the electrolyte solution containing two different metal ions. These nanowires contain periodic modulation of composition along the wire axes. After pore filling with required materials, the aluminium substrate was removed by $HgCl_2$ solution [119].

Nielsch performed [115] pulse direct current electrodeposition on undetached anodic oxide films, and obtained successful electrodeposited nickel nanowires by thinning the barrier layer to a dendrite structure using an constant current anodizing technique. In his work, hexagonally ordered porous anodic oxide film were prepared via a two-step anodizing process, and then further anodizing of twice 15 minutes using constant current conditions at 290 and 135 mA/cm^2. During this period, the thickness of the barrier layer and the anodizing potential both decrease. Finally, the anodizing potential reaches a value of 6±7 V, which corresponds with a barrier oxide thickness of less than 10 nm. By thinning the barrier layer homogeneously with the pores branch out, the anodic oxide film could be kept on the aluminum substrate for the whole process. Pulse electrodeposition is reliable for electrodeposition into high aspect materials and which can compensate for the slow diffusion-driven transport in the pores. Previously pulse electrodeposition was commonly used for the electrodeposition of thin metallic films. For the first time in nielsch's work, this technique was applied in combination with a highly ordered nanostructure template material.

2.9 Conclusion

In this chapter, current developments of fundamental understanding on formation of anodic oxide films were reviewed. Further, the controlling factors and mechanism of self-ordering arrangement of pores in anodic oxide films were discussed. The fabrication, properties and applications of nanowires along with their potential applications are described. The nanowires possess unique properties that applicable for electrical, thermoelectrical, optical, magnetic and sensor device applications. The fabrication of nanowires with porous anodic film template is reliable, simple and worth investigation.

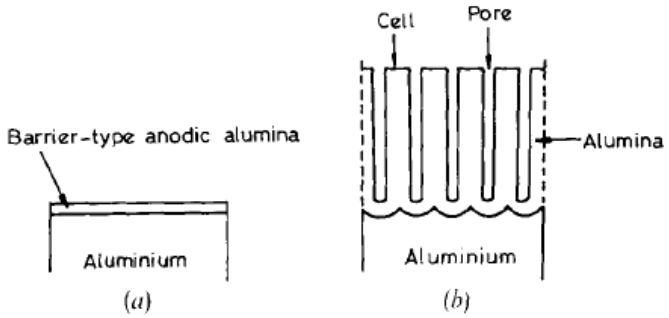

Figure 2.1 *Schematic illustrations of cross section of anodic films on aluminum: (a) barrier type anodic film, (b) porous type anodic film, revealing the barrier layer, pores and cells [15] .*

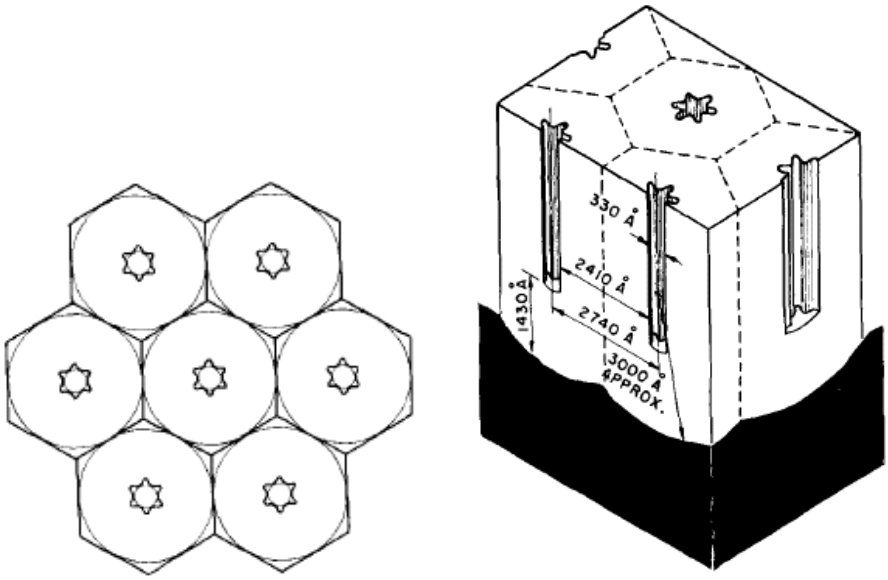

Figure 2.2 *Keller's cell model of anodic films (a)top view (b) 3-D view [20].*

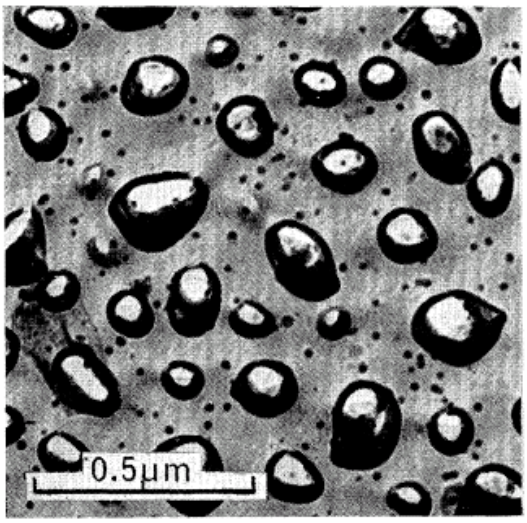

Figure 2.3 *Outer surface view of anodic films formed in phosphoric acid, 145 V [20]*

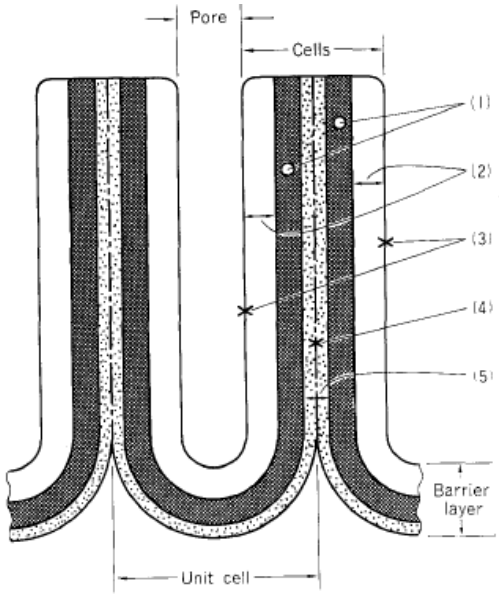

Figure 2.4 *multi-layer model of cross session of sulphuric acid alumina oxide film. (1) Centre barrier layer (CB); (2) Outer cell layer (OC); (3) Outer cell wall (OCW); (4) Centre of inner cell layer (CIC); (5) Inner cell layer (IC). [23]*

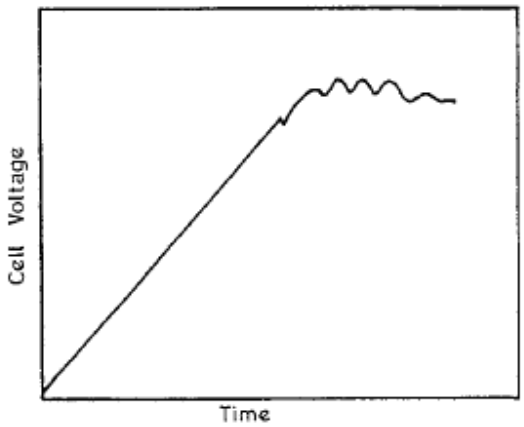

Figure 2.5 *diagram of voltage-time behavior during anodizing of Al at constant current density in neutral solution [10].*

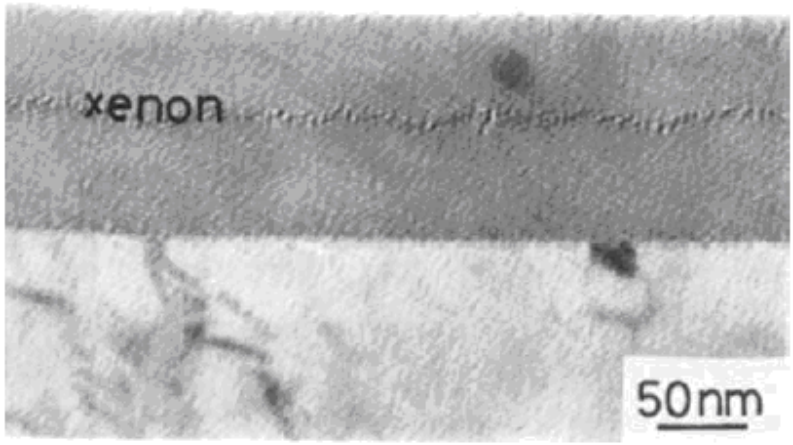

Figure 2.6 *TEM micrograph of cross session of Al substrate and anodic film, formed at a constant current density of 10A m^{-2} to 100 V in near-neutral potassium phosphate electrolyte at 298K. This reveals the xenon implant, originally retained within a relatively thin pre-formed anodic film [24].*

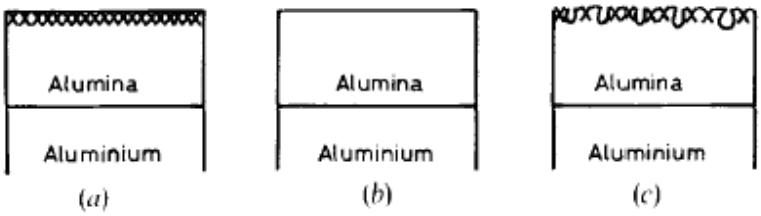

Figure 2.7 Schematic illustration of cross sessions of barrier type films formed at various current densities in chromate electrolyte: (a) films formed at critical current density; (b) film formed at a current density below critical density, when dissolution of the outer film regions is expected to remove the marker layer;(c) films formed at current density below current density, revealing location of the marker layer and pore initiation at preferred sites[8]

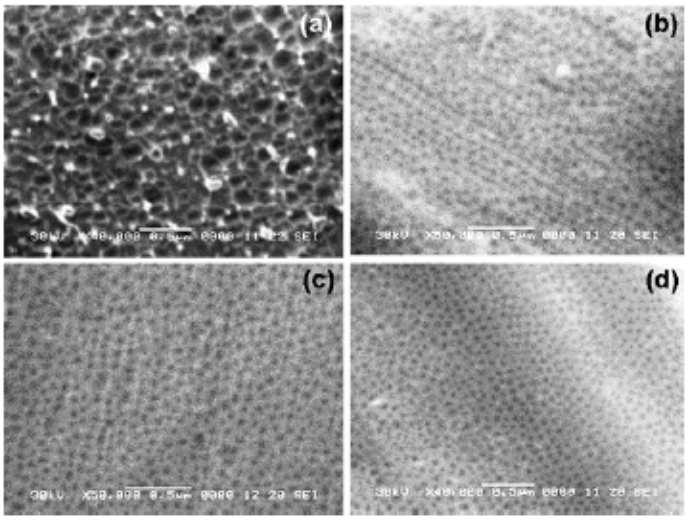

Figure 2.8 *SEM images of Al foil after dipping in 0.3 M oxalic acid for 20 h (a), base surfaces of aluminum substrate with alumina stripped away after anodizing at 40 V in 0.3 M oxalic acid for 30 s (b), 60 s (c), and 90 s (d) [25].*

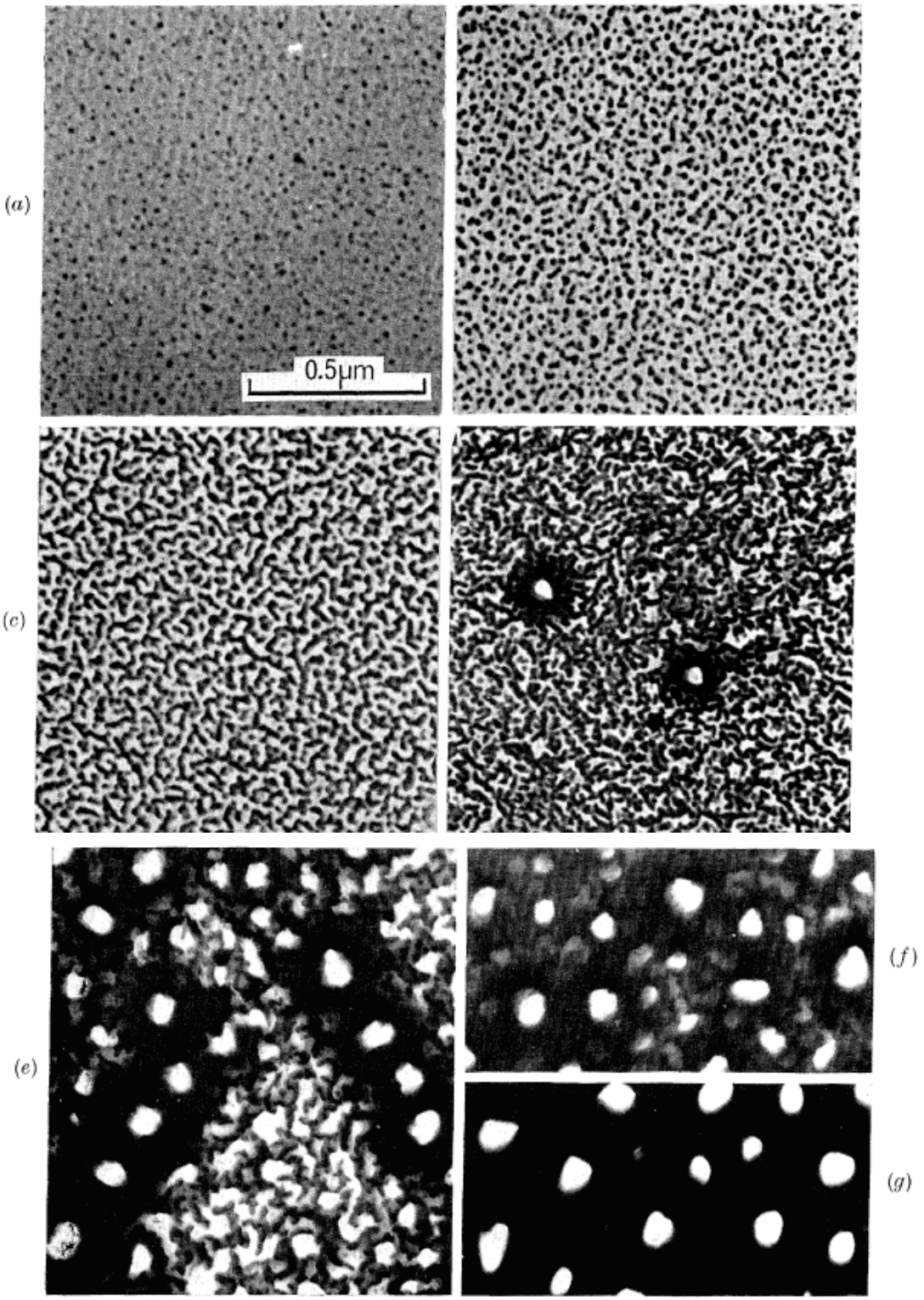

Figure 2.9 *TEM micrographs of films grown at 50 A m^{-2} in 0.4 M phosphoric acid at 25°C for (a)40 s (b)80 s (c) 120 s (d) 160 s (e) 200 s (f)280 s (g) 330 s showing "nuclei", incipient pores and major pore development. [21]*

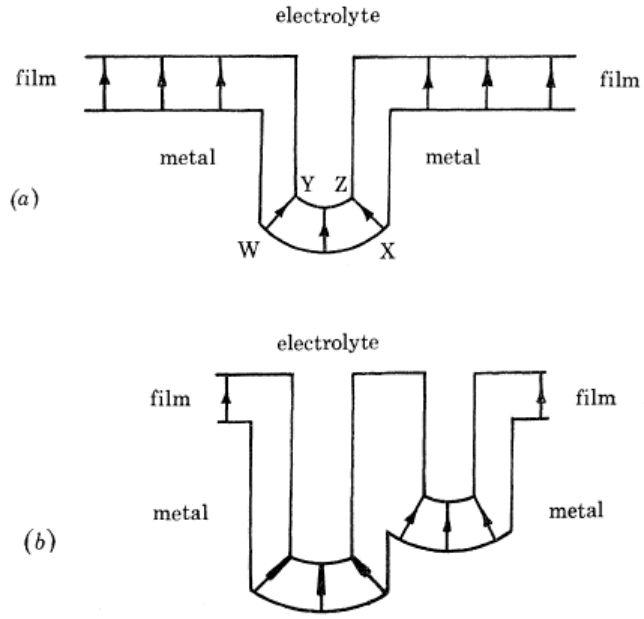

Figure 2.10 *Schematic representation of anodic film during initiation of the major pores: (a) single pore initiated, and (b) development of pore and cell distributions for adjacent cells at different stages of development, showing the current distributions.[21]*

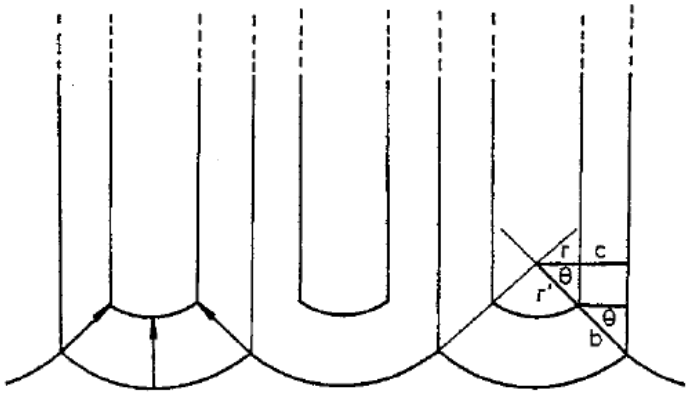

Figur 2.11 *Model of the steady-state porous anodic film [15].*

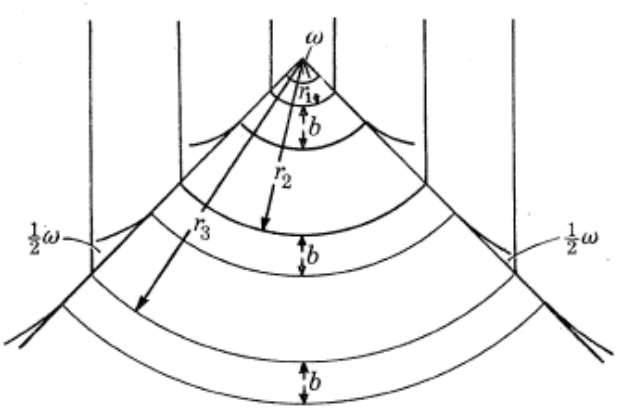

Figure 2.12 *Schematic representation of three possible pore base situations, r1,r2 and r3 representing the radii of curvature of the pore bases, b the constant barrier-layer thickness and w the solid angle subtended from the centre of curvature to pore bases. r2 is the steady-state radius of curvature under the prevailing anodizing conditions [21]*

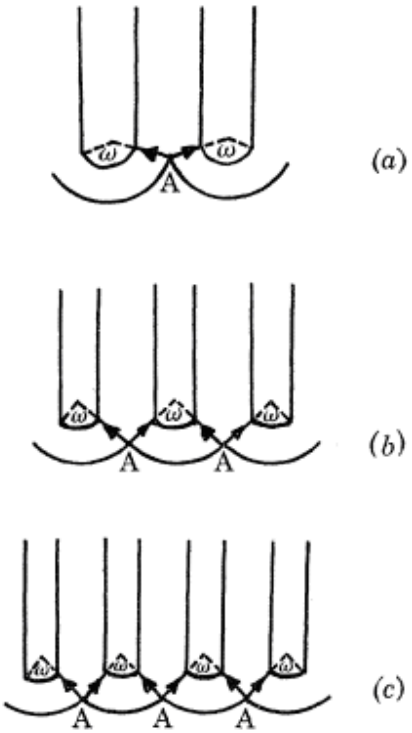

Figure 2.13 *Schematic representation of three possible situations at pore base, with three varied interpore distance and constant barrier layer thickness [21].*

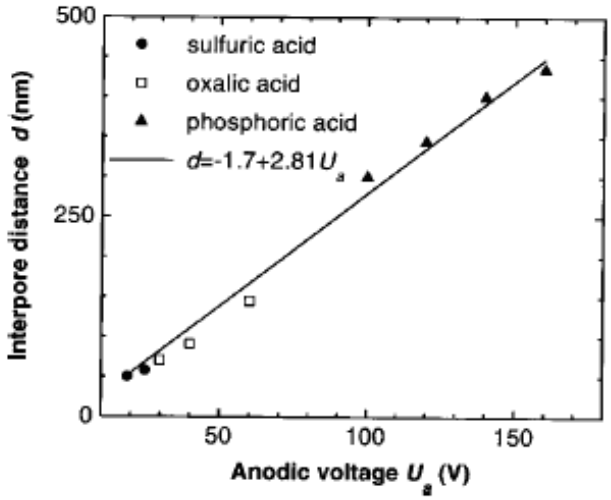

Figure 2.14 *Interpore distance (d) in self-organized porous anodic films vs anodizing voltage Ua for sulfuric, oxalic and phosphoric acid solutions. The solid line represents the relation d=-1.7+2.81Ua [4].*

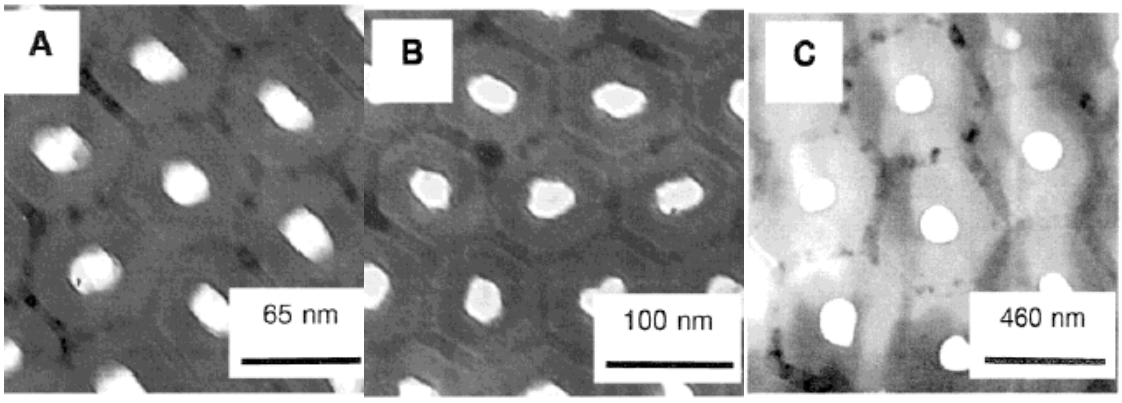

Figure 2.15 *Transmission electron micrographs of self-ordered porous anodic oxide fabricated at (a) 25 V in 1.7 wt % H_2SO_4, (b) 40 V in 2.7 wt % $(COOH)_2$, and (c) 195 V in 1 wt % H_3PO_4. [35]*

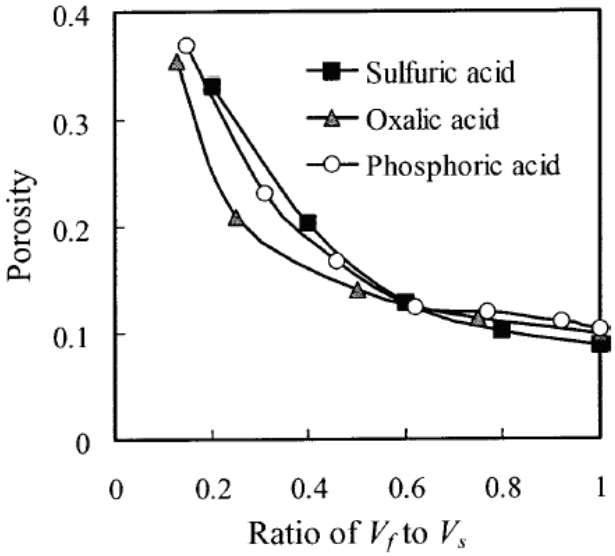

Figure 2.16 *porosity plotted as a function of ratio of formation voltage (V_i) to self-ordering voltage (Vs) [38]*

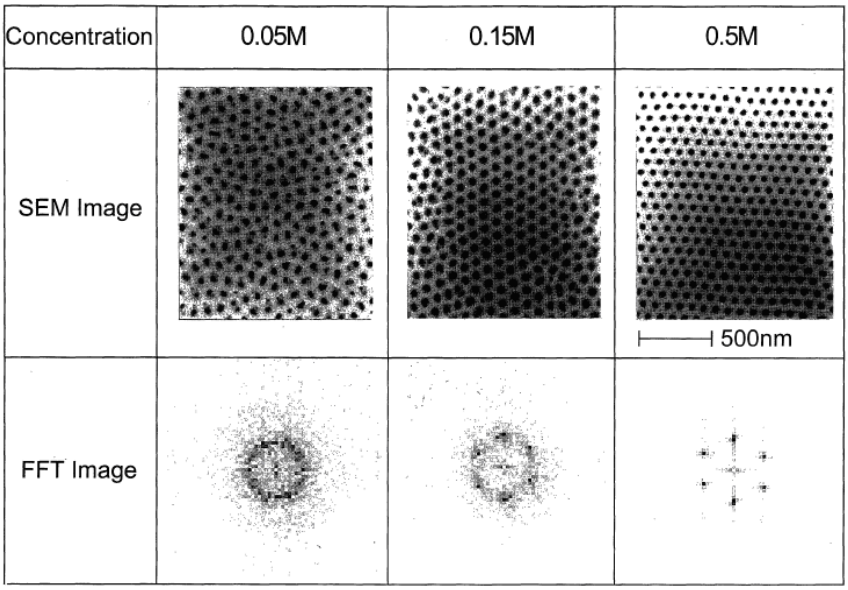

Figure 2.17 *Top view SEM photograph of Al_2O_3 obtained by two steps anodizing at various oxalic acid concentrations. the times of first and second anodizing are 20 h and 30 mins, respectively. The voltage is 40V and the temperature is 5 ^oC. [39]*

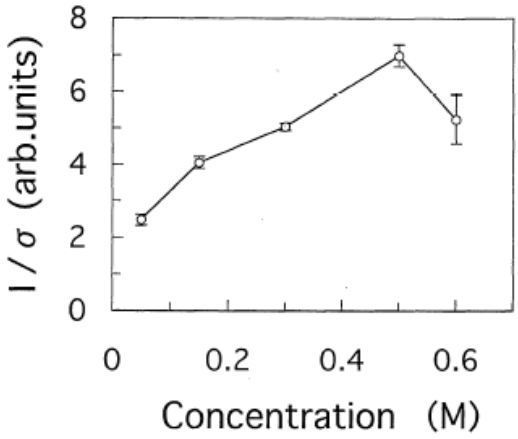

Figure 2.18 *The spatial order parameter 1/σ of the pore array is shown as function of the concentration of oxalic acid. Average value of 1/σare plotted in open circles and their standard deviations are shown in bar. [39]*

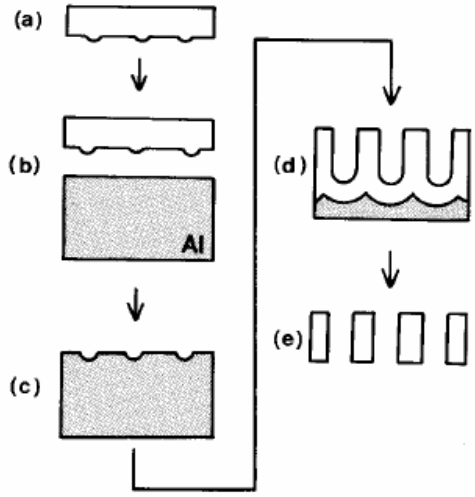

Figure 2.19 *Pre-patterning process using a SiC mold with an array of periodic convex surfaces [43].*

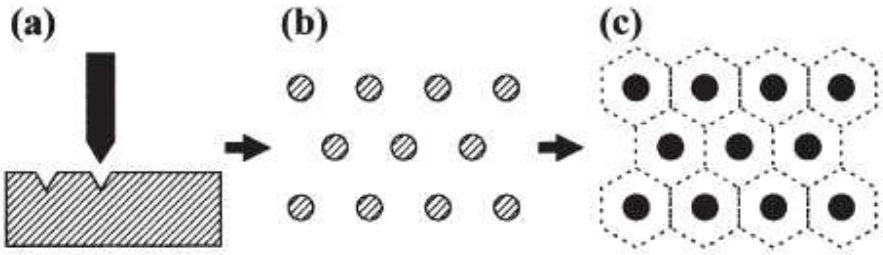

Figure 2.20 *Schematic of pre-patterning process using scanning probe microscope nano-indentation[45].*

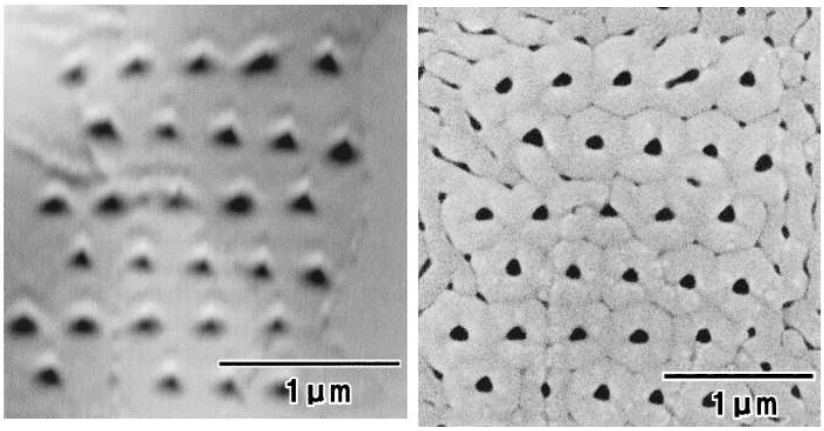

Figure 2.21 *a) AFM image of Al pre-patterned by indentation at 400 nm intervals. The indentation load was 40µN. b) SEM micrograph of the porous anodic film anodizing was carried out in 0.2 M phosphoric acid at 2 °C under the constant voltage of 160 V for 20 min [45].*

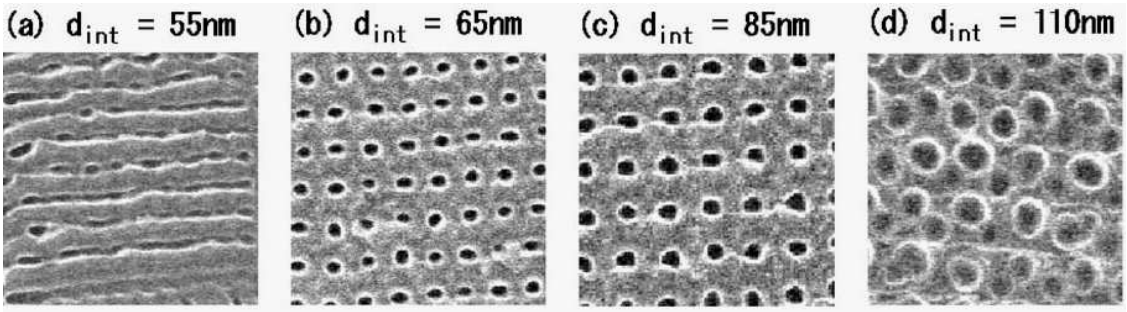

Figure 2.22 *Pore arrays formed by different indentation intervals and the subsequent anodizing: Al surfaces were nano-indented by different intervals from 55 to 110 nm, at the force of 4.16×10^{-5} N, and later they were anodized at 40 V, 1 min with 0.15 M oxalic acid [46].*

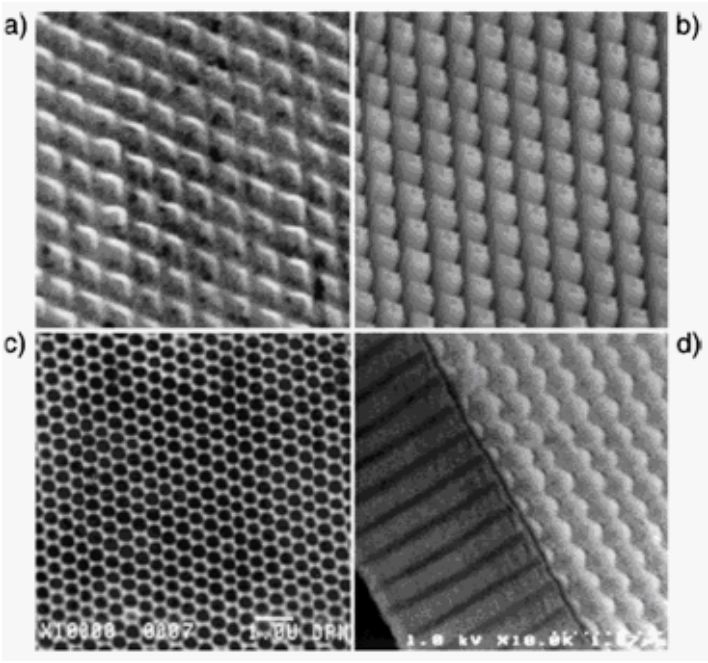

Figure 2.23 *High magnification micrographs of: a)aluminum substrate after press-in procedure; b)porous anodic film, bottom view; d)cleaved edge of porous anodic film from bottom side [44].*

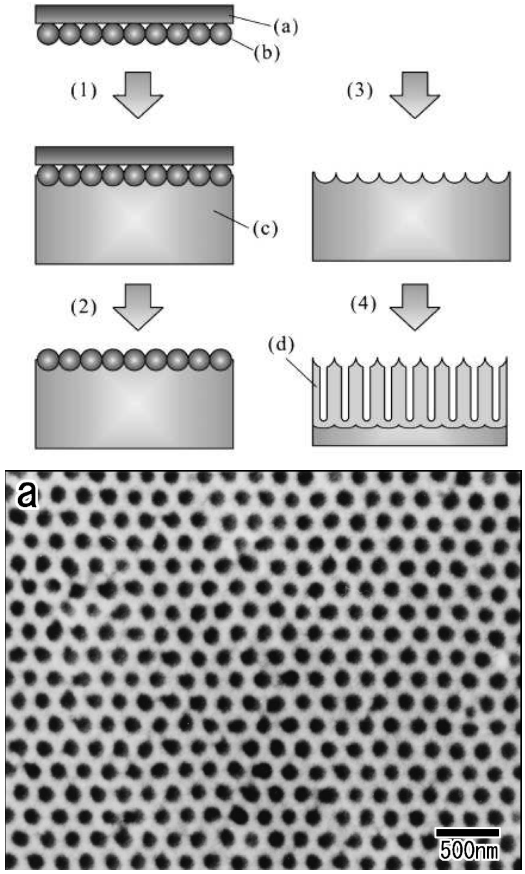

Figure 2.24 *a) Schematic of ordered porous anodic film formation with self-organized chemical particles pre-patterning process; b) SEM image of resultant highly ordered porous anodic films [47].*

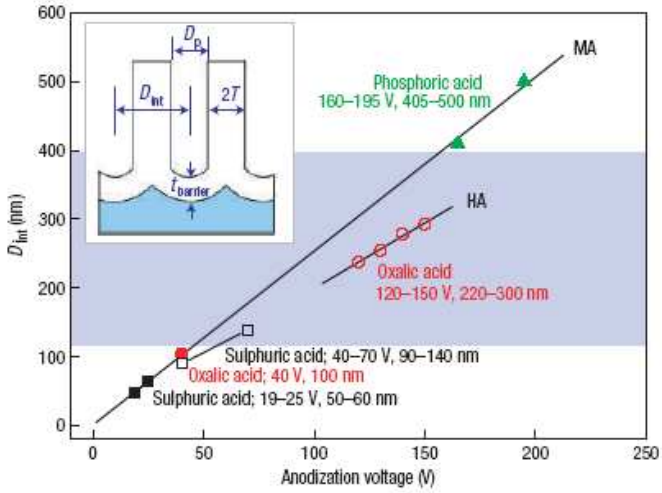

Figure 2.25 *Regime of self-ordering for oxalic acid anodizing for both conventional anodizing and hard anodizing [52].*

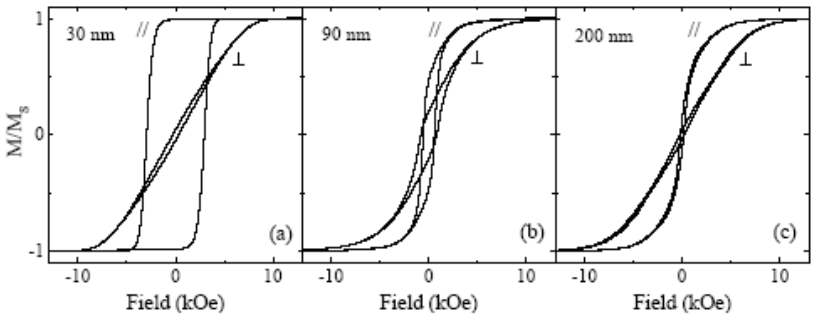

Figure 2.26 *Room temperature hysteresis loops measured on arrays of Co nanowires with the magnetic field applied parallel ( ) and perpendicular () to the wire axis. The nanowires have average diameters of (a) 30 nm, (b) 90 nm, (c) 200 nm [63].*

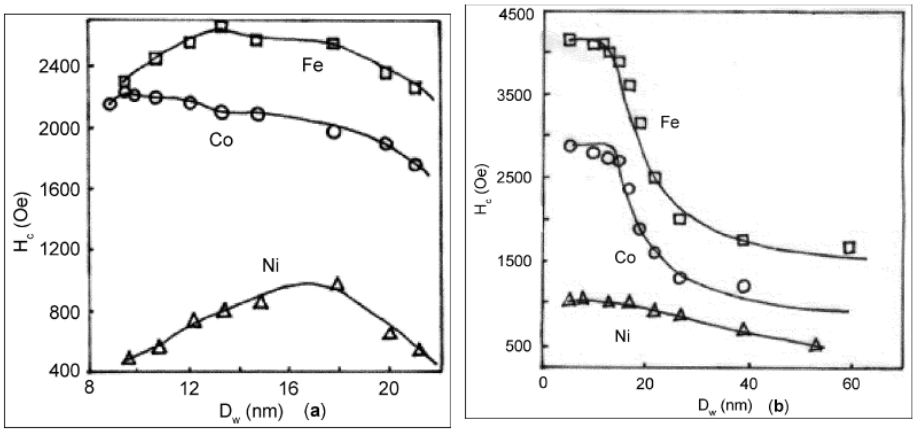

Figure 2.27 *Coercivity as a function of nanowire diameter (Dw) for magnetic nanowires of Fe. Co and Ni at (a) room temperature and (b) at zero-temperature [63]*

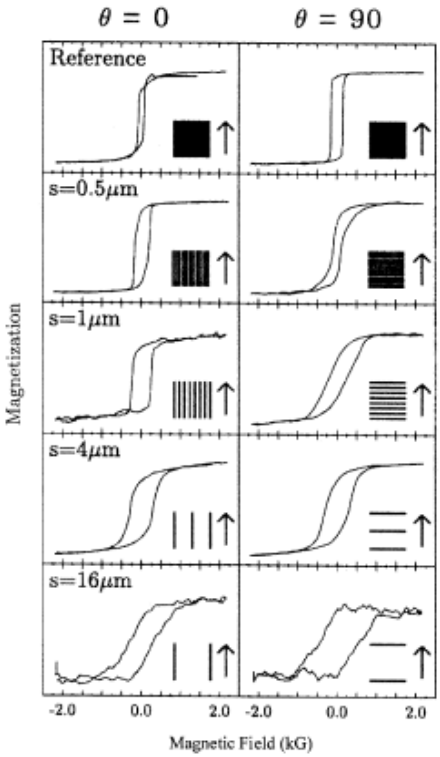

Figure 2.28 *The magnetization, as inferred from the magnetooptical kerr effect measurements on a range of Fe(001) gratings with wire width fixed at 0.5μm and variable separations s, for the field applied in-plane magnetic field parallel ($\theta=0^o$) and perpendicular ($\theta=90^o$) to the wires. The inserts show measurement direct schematically, with the arrow indicating the direction of applied magnetic field) [64].*

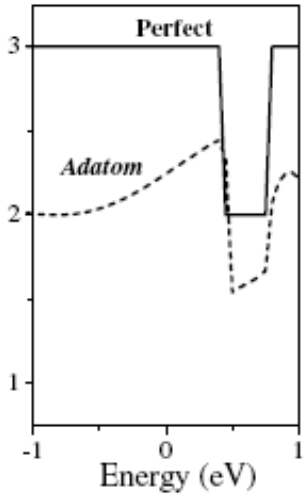

Figure 2.29 *Conductance, G(2e2/h) of silver nanowires with single-atom defects: A datom (dotted line) and for perfect nanowires (solid curve) [13]*

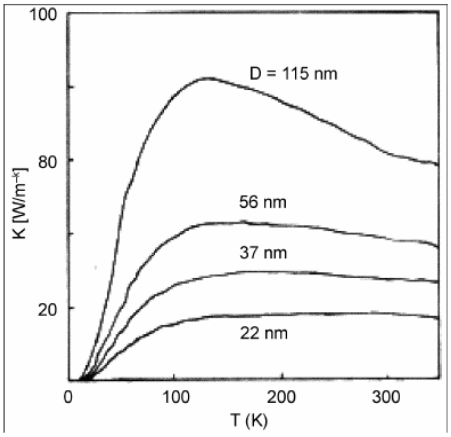

Figure 2.30 *Thermal Conductivity (k) as a function of temperature for Si nanowires of different diameters (D).*

Table 2.1 *Anodizing conditions for the self-ordered hexagonal pore arrangements in different electrolytes[4].*

Electrolyte (acid)	Concentration (M)	Voltage (V)	Temperature (°C)
Oxalic	0.3	40	3
Sulfuric	0.3	25	3
Phosphoric	0.1	195	3

Table 2.2 *Perpendicular coercivities（Hc）and remanence ratios Mr/Ms of the Fe-Co alloy nanowires with different proportions of Fe and Co [60]*

	Fe	$Co_{17}Fe_{83}$	$Co_{28}Fe_{72}$	$Co_{31}Fe_{69}$	$Co_{34}Fe_{66}$	$Co_{38}Fe_{62}$	$Co_{60}Fe_{40}$	Co
H_c (Oe)	2380	2412	2593	2856	2698	2444	2095	1968
M_r/M_s	0.90	0.89	0.88	0.91	0.91	0.90	0.93	0.91

Chapter 3

Experimental Procedure

3.1 Introduction

This chapter describes the experimental procedures related to the fabrication and characterization of highly ordered porous anodic oxide film template and one dimensional metal/metal oxide nanostructures, including materials selection, specimen preparations, anodizing and electrodeposition procedures, as well as characterization methods.

3.2 Formation of porous anodic oxide films

3.2.1 Specimen preparation

3.2.1.1 Material

In this work, 99.99% high purity aluminum foils is used for the formation of anodic films. The composition of the aluminum foil is as follows:

Al 99.99 wt%;

Cu 0.002 wt%;

Fe 0.005 wt%;

Si 0.003 wt%;

Foils of 0.1 mm thickness were cut into individual specimens of dimensions 20 × 30 mm.

3.2.1.2. Degreasing treatment

In order to remove lubricant and other contaminants from the surface, the specimens were initially agitated ultrasonically in acetone bath, and then rinsed with deionized water before dried in a stream of cold air.

3.2.1.3 Electropolishing

Electropolishing of aluminum is always performed as an important surface treatment prior to anodizing. Electropolishing is able to selectively reduce macroscopic heterogeneities, thus develop relatively smooth surfaces. Smooth surface is necessary for the formation of porous anodic films on pure aluminum substrate. Further, electropolishing give rise to fine nano-textures on the treated aluminium surfaces, which also facilitate pore nucleation at the initiation stage of anodizing.

A mixture of perchloric acid and ethanol in the proportion of 1:4 (vol) is used for electropolishing. Electropolishing was carried out at 20 V for 180 s at 5 ^{o}C using an aluminium sheet as counter electrode, in a fume cupboard with highly carefulness since perchloric acid is a strong oxidative and corrosive acid. Immediately after electropolishing, the specimens were rinsed in ethanol for 30 s first, then in deionized water for 30 s, and finally dried in a stream of cold air.

3.2.1.4 Annealing treatment of aluminum

Heat treatment of aluminum specimens, here specified as annealing treatment was carried out before electropolishing. Degreased aluminum specimens were annealed at 400°C for one hour. Grain size became significantly larger after heat treatment, since recrystallization and grain coarsening occur during annealing treatment [120]. The large grains favor self ordering process during the formation of porous anodic oxide films.

3.2.2 Anodizing processes

Masuda et al managed to fabricate porous anodic film with a highly ordered hexagonally arranged pore arrays for the first time using two-steps long period anodizing [2]. Since then extensive researches have been focused on pore ordering during anodic films formation. However, the precise formation mechanism of anodic films with highly ordered pore arrays has not been fully understood. Thus, in the

present work, self-ordering behaviors during porous anodic film formation is systematically investigated.

Figure 3.1 shows an anodizing set-up. The electrochemical cell is a two-electrode system, e.g., the aluminum foil surrounding the inner-wall of the beaker acting as a cathode and aluminum specimen acting as anode. The back side and the edges of aluminum specimens were covered with lacquer. The specimens were immersed into the electrolyte and connected by crocodile clamps. Anodizing is performed inside an anodizing station with an electric interlocking for the consideration of safety issues. A magnetic stirrer underneath the beaker is used to stir the electrolyte solution.

The power supply has a working range of 0-250 V (potentiostatic mode) or 0-10 A (galvanostatic mode). The process parameters were monitored by an in-situ computer system using home-made software, which records the variation of current through the anodizing process. Constant voltage anodizing was conducted throughout the work.

3.2.2.1 Multi-steps anodizing

Anodizing was conducted under the optimum anodizing conditions for self-ordered porous alumina films, i.e. constant voltage of 40 V in 0.3 M oxalic acid ($C_2O_2(OH)_2$) electrolyte and 25 V in 0.3 M sulphuric acid (H_2SO_4). Two steps, three steps and four steps anodizing were carried out with various anodizing time. The details will be discussed in Chapter 4. The temperature of the electrolyte was maintained at room temperature during anodizing using a water bath. The solution was stirred vigorously in order to accelerate the dispersion of the heat that was generated during anodizing.

For multi-steps anodizing, the oxide film formed in the previous steps was removed by chemical dissolution in a mixture of 0.2 M chromic acid and 0.35 M phosphoric acid at 80°C for an appropriate time depending on the thickness of the oxide films. Subsequent anodizing steps were carried out under the same conditions as the first step for different time period, which will be described later. For each step, the

anodizing current response was recorded against time.

3.2.2.2 Anodizing under varied voltages and electrolyte concentrations

Three oxalic acid concentrations of 0.2 M, 0.3 M and 0.4 M were used. Three anodizing voltages, i.e. 30 V, 40 V and 50 V, were employed respectively for each electrolyte concentration. Subsequently, the formed anodic films were chemically removed, and the second step anodizing was carried out for 1 h under the same conditions as that for the first step anodizing.

.

3.2.2.3 Anodizing of pre-patterned substrate

In addition to the self-ordering process for fabricating highly ordered porous anodic oxide films, various artificial methods have been studied extensively to facilitate ordering during anodic film formation. An optic grating is chosen in this work to investigate the effects of pre-patterning on the ordering of porous anodic films [121].

Pure aluminum specimens with a surface area of 1.0×1.0 cm^2 were used. The specimens were degreased and electropolished. A regular groove mesh on the surface of aluminum substrate was formed by mechanically impressing a commercially available optical diffraction grating (1200 lines per mm, blazing angle 26° 45′) with a working area of approximately 20 mm^2, using a surface micro-cracks tesing machine, shown in Figure 3.2. The profile of the grating is right-angle triangular, as shown in Figure 3.3 (a). The impressing generated parallel grooves, with approximately 833 nm spacing, on aluminum substrate surface as schematically illustrated in Figure 3.3 (b).

In order to facilitate the formation of ordered pores during anodizing, a two-steps impressing procedure was employed. After the first impressing step, a second impressing was performed by rotating the same grating to a certain angle (60° or 90°) around the axis perpendicular to the surface. Consequently, a close-packed rhomb or square shape textures was obtained respectively.

The impression of the pattern on aluminum surface after two impresses with optic grating is illustrated in Figure 3.3 (c) and (d). In the case when the optic grating was rotated for 60º for the second impressing, rhombus pattern is obtained over the aluminum substrate surface as shown in Figure 3.3 (c). While in the case of rotating the optic grating for 90°, square lattices are obtained, as shown in Figure 3.3 (d).

The pre-patterned specimens were then anodized for 1 h in a very dilute phosphoric acid (H_3PO_4) (1:300 v/v) electrolyte under constant voltages of 120 V, 160 V and 200 V respectively. For cooling the electrolyte, a water and ice cooling system is employed. The electrolyte was placed in an ice bath to control the temperature, which is necessary because burning and sparking often happens at room temperature due to local heating effects during anodizing in phosphoric acid.

3.3 Porous anodic oxide film template fabrication

3.3.1 Fabrication approach by PMMA replication

It is a common method to convert porous anodic films to through-hole template for nanoarrays fabrication. The critical step is to remove the barrier layer which blocks the pores of anodic films at one side. There are several approaches to turn the porous alumina oxide into through-hole nano-templates. The most commonly used approach is to apply PMMA (poly (methyl 2-methylpropenoate)) as a protective cover and support layer for anodic films.

The detail procedures for fabricating porous anodic oxide film templates are illustrated in Figure 3.4. Figure 3.4 (a), (b) and (c) schematically show a procedure for highly ordered porous anodic oxide film templates fabrication. After the oxide films were formed by anodizing, a thin layer of PMMA/acetone mixture is pasted onto surface of the oxide films surface, exposed in air for at least 24 hours to allow complete drying of PMMA coating, as shown in Figure 3.4 (d). PMMA poly (methyl 2-methylpropenoate) is a thermoplastic and transparent plastic. Chemically, it is the synthetic polymer of methyl methacrylate. To obtain the PMMA/ acetone mixture, 5g

PMMA powder and 20 ml acetone are mixed together with adequately shake, and then agitated in ultrasonic bath until a gel-like mixture with proper viscosity is obtained.

Afterwards, aluminum substrate was chemically removed by immersing the specimens in a mixed solution of 0.1 M $CuCl_2$ and 10% (vol) HCl at room temperature for 10-15 minutes, until aluminium substrate was completely removed and the specimens turned into transparent, as shown in Figure 3.4 (e).

The free standing porous anodic oxide films have hemispherical caps on bottom side, which is the barrier layer that formed during anodizing. The barrier layer was chemically removed by immersing the specimens into 5% H_3PO_4 at 30°C for 60 minutes. During the process, the PMMA does not only support the thin anodic films, but also prevent phosphoric acid solutions to penetrate into the pores in the films, thus preventing unnecessary thinning of the inner-wall of the pores.

Thereafter, a thin layer of gold was sputtered on one side of porous anodic oxide film templates, as shown in Figure 3.4 (f). The resultant gold layer is approximately 300 nm thickness.

PMMA film was then removed by immersing the specimens in warm acetone at approximately 30°C. Prior to the removal of PMMA, the gold coated side of the specimen was attached onto a glass substrate. This is to ensure that after the removal of PMMA film, the porous films could be smoothly attached onto surface of the glass substrate. Without the support of glass, the oxide film templates would be too fragile and thin to be handled.

The porous anodic oxide film is then successfully converted into a template. Finally, the film with glass substrate was immersed in acetone solution until the film was detached from glass substrate, then attached onto a copper foil with the side with gold coating to ensure electric conductivity.

3.3.2 Selectively removal of aluminum substrate

Although the PMMA replication approach is widely used for the fabrication of porous anodic film template, there are several drawbacks with it. First, the viscosity of PMMA is required in a certain region. If the PMMA mixture is over diluted, i.e. higher percent of acetone is added, there is a possibility that PMMA could sink into pores of anodic films. Although PMMA will be removed with acetone, there is still possibility to have residue in anodic films, which is not decided. If the PMMA mixture is over concentrated, there will be highly difficulty to spread PMMA over anodic films evenly. An alternative approach, which was successfully employed to produce through-hole anodic film template without PMMA, is described below and shown in Figure 3.5.

Highly ordered porous anodic oxide films were prepared in the same way as that described in 3.3.1, as illustrated in Figure 3.5 (a), (b) and (c). In Figure 3.5 (d), a lacquer coating is pasted on the edge of backside of the anodized specimens, leaving the middle area exposed. Afterwards, the aluminum substrate is chemically removed by immersing the specimens in an etching solution of 0.1 M $CuCl_2$ and 10% (vol) HCl at room temperature for 10-15 minutes. Since the metal on the edges is covered by lacquer coating and only the metal in the middle is exposed in the solution, thus the aluminum substrate is selectively removed from the middle of specimen's backside.

As the etching proceeds, aluminum becomes gradually thinned, and the specimen will become transparent when all aluminum is removed. The aluminum gets thinned fastest at the edge of exposed metal area on backside, which is surrounded by lacquer coating. Transparent area spreads as etching proceeds, and finally become a totally transparent window framed with remaining aluminum. The anodized films stay intact across this window, including the barrier layer. When taking the specimen out of etching solution, the best way is to keep the specimen perpendicular to the hydrous solution surface, and to move slowly. This is to avoid the thin anodic film being

destroyed by surface tension of hydrous solution.

The following procedures are similar to that described in 3.3.1, as shown in Figure 3.5 (f) and (e). Thin gold layer of approximately 300 nm thicknesses is sputtered at one side of the prepared specimens after barrier layer removal, and then attached to conductive copper substrate to form a template electrode ready for request nanostructure fabrication.

3.4 Nanowire fabrication

3.4.1 Electrodeposition of metal nanowires

Before applying the as prepared anodic film template as electrode, it was immersed in deionized water under ultrasonic agitation for two minutes. This step is important for achieve a homogeneous growth of nanowires over the working area, since the pores in anodic film templates can be thoroughly wetted by ultrasonic agitation.

Nickel nanowires were produced by direct current electrodeposition into the pores in the template. The composition of the electrolyte for the fabrication of nickel nanowires is listed below:

100 g/L $NiSO_4 \cdot 6H_2O$;
30 g/L $NiCl_2 \cdot 6H_2O$;
40 g/L H_3BO_3;

The pH value was adjusted to 2.5 with 1 M H_2SO_4. A pure nickel rod is immersed in the electrolyte opposite to alumina template electrode with a distance of approximately 2 cm as conductive electrode. A saturated calomel electrode (SCE) is used as reference electrode. Direct current electrodeposition was performed at various applied voltages of -0.8 V ~ -1.35 V, and at temperatures of 3°C, 17°C and 37 °C, respectively. Nickel nanowire arrays of various aspect ratios were fabricated by terminating the electrochemical process after different time intervals.

3.4.2 Manganese oxide nanowire fabrication

Manganese oxide nanowire arrays were fabricated using porous anodic oxide film templates via anodic deposition at room temperature. Electrolyte solution was composed of 0.1 M manganous acetate and 0.1 M sodium sulfate.

The working electrode was the through-pore anodic film templates, which was attached onto copper foils. A platinum stick electrode was used as counter electrode. An ACM analyzer was employed as power supply. The apparatus is monitored by an in-situ computer system, which controls the output of the ACM analyzer, and records the system responses through out the electrodeposition process. Both constant voltage/constant current electrodepositions were carried out. The experiment was conducted at positive potential versus the saturated calomel electrode (SCE) ranging from 0.4 V to 1.0 V.

After electrodeposition, all specimens were rinsed with deionized water and then blow dried in a stream of cold air.

3.5 Characterization

3.5.1 Specimen preparation for transmission electron microscopy

3.5.1.1 Ultramicrotomy

Microtome is an instrument used to mechanically cut biological materials into transparent thin sections for microscopic examination. Steel, glass, or diamond knives are used depending upon the materials being sliced and the desired thickness of the sections.

When applied to electron microscopy, this instrument is called ultramicrotome. After embedding specimens in epoxy resin, an ultramicrotome equipped with a glass or gem grade diamond knife is used to cut very thin sections (typically 15 to 100 nanometers). Sections are spread in water and then collected with a copper grid with or without

carbon films, and examined with transmission electron microscope. In the present work, ultramicrotome is employed to prepare anodic oxide film for the cross section examination.

3.5.1.2 Chemical dissolution

The electrodeposited manganese oxide nanowires were originally embedded in pores of anodic oxide film templates. To remove the anodic oxide films, the specimen was immersed in a small amount of 1 M NaOH solution for 1-2 hours at room temperature without stirring. Afterwards, the solution was adequately vibrated with sonic bath for at least 30 minutes to ensure well dispersion of nanowires in solution, and then the mixture went into centrifuge.

The centrifuge separates the solid nanowires from NaOH solution by rotating the mixture at a high speed. After several minutes of rotations, it could be seen that black deposits which is the nanowires gathered at bottom of the tube container. The solution was then removed by inhaled with a straw, and then filled in ethanol. The solution was shaken until the nanowires were well dispersed in ethanol. This procedure was repeated several times. Thereafter, the nanowires were collected with a copper grid coated with carbon film by dropping the mixtures of nanowires and ethanol onto the grid, and then left dried. The nanowires are ready for examination in transmission electron microscope.

3.5.2 Electron microscopy

3.5.2.1 Transmission electron microscopy

Transmission electron microscopy (TEM) is a technique that uses an electron beam to image a sample as the much smaller wavelength makes it possible to achieve a resolution significantly better than that with a light microscope. High energy electrons, incident on ultra-thin samples, allow for image resolutions that can reach of 0.5 Angstroms (10^{-10} m).

Briefly speaking, electron source generates electrons that travel through vacuum in the column of the microscope. Instead of glass lenses focusing the light in the light microscope, TEM uses electromagnetic lenses to focus the electrons into a very fine beam. The electron beam then travels through the specimen to be examined. Depending on the density of the material, some of the electrons are scattered or absorbed. At the bottom of the microscopes the unscattered electrons hit a fluorescent screen, which gives rise to a "shadow image" of the specimen with its different parts displayed in varied brightness based on their density. The image can be studied directly by the operator or recorded with a camera. Variations in the intensity of electron diffraction across a crystalline specimen, called “diffraction contrast,” is useful for making images of defects such as dislocations, interfaces, and second phase particles.

Although more time consuming than many other common analytical tools, the wealth of information available from TEM is impressive. Not only can one obtain outstanding image resolution, it is also possible to characterize crystallographic phase, crystallographic orientation (both by diffraction mode experiments), produce elemental maps (using X-ray), and images that highlight elemental contrast (dark field mode)—all from nm sized areas that can be precisely located. Compared to SEM, TEM has better spatial resolution, is capable of additional analytical measurements.

For TEM observations of nickel and manganese oxide nanowires, the porous anodic oxide film template was completely dissolved using the chemical dissolution method mentioned in 3.5.2.1. Information of morphology, chemical composition and crystal structures of nanowires are obtained.

3.5.2.2 HRTEM

High resolution transmission electron microscopy (HRTEM) is an imaging mode of the transmission electron microscopy (TEM) that allows the imaging of the

crystallographic structure of a sample at an atomic scale. Because of its high resolution, it is an invaluable tool to study nanoscale properties of crystalline material such as semiconductors and metals. At present, the highest resolution realized is 0.08 nm. At these small scales, individual atoms and crystal defect can be imaged. Since all crystal structures are three dimensional, it may be necessary to combine several views of the crystal, taken from different angles, into a three dimensional map. One of the difficulties with HRTEM is that image formation relies on phase-contrast. In Phase-contrast imaging, contrast is not necessarily intuitively interpretable as the image is influenced by strong aberrations of the imaging lenses in the microscope. One major aberration is caused by focus and astigmatism, which often can be estimated from the Fourier transform of the HRTEM image.

A Tecnai F30 high resolution TEM was employed to investigate the structure of electrodeposited manganese oxide nanowires. The specimen was prepared in the same way as that for conventional TEM.

3.5.2.3 Scanning electron microscopy

For Scanning electron microscopy (SEM), a focused electron beam is scanned across a sample surface and provides high-resolution and increased-depth-of-field images of the sample surface. A beam of electrons is produced at the top of the microscope by heating of a metallic filament. The electron beam follows a vertical path through the column of the microscope. It makes its way through electromagnetic lenses which focus and direct the beam down towards the sample. Once it hits the sample, other electrons (backscattered or secondary) are ejected from the sample. Detectors collect the secondary or backscattered electrons, and convert them to a signal that is sent to a viewing screen similar to the one in an ordinary television, producing an image.

Scanning electron microscopy is extensively used in this work for obtaining morphology details of porous anodic oxide. The formed porous anodic oxide films were characterized using a XL-Philips32 field emission scanning electron microscope

(FEG-SEM). Scanning electron microscope produces images of the sample's surface morphology, including pore size, pore arrangement and ordering degrees etc. All specimens are required to be conductive for SEM examination, thus the porous anodic oxide specimens are always carbon coated before SEM examination.

The histograms of pore diameter demonstrating the interpore distance distribution of produced pores were then derived based on SEM images. The orientation domains, within which pore arrangement is hexagonally aligned in one direction, were determined by firstly outlining the boundaries of adjacent domains on SEM micrographs, counting the number of pores for several domains, converting these numbers to areas, and finally the average domain area is obtained.

FFT (fast fourier transform) of average interpore distance and statistical standard deviation was performed based on SEM images for a quantitative evaluation of the ordering arrangement of pore arrays. FFT is a discrete fourier transform algorithm which reduces the number of computations need for N points from 2 N^2 to 2NlgN, where lg is the base-2 logarithm. If the function to be transformed is not harmonically related to the sampling frequency, the response of an FFT looks like a sinc function. In the present work, FFT was performed on SEM images of porous anodic films using a digitalmicrograph software incorporated with Tecnai high resolution transmission electron microscope.

The morphology of nickel and manganese oxide nanowire arrays was obtained using a field emission scanning electron microscope (FEG-SEM). For SEM observation of as-prepared nanowires, the porous anodic oxide films are partly dissolved by immersing the specimen in 0.1 M NaOH solution at room temperature for 10-30 minutes without stirring. The residual solution on specimen's surface was carefully rinsed with distilled water for several times, then dried in a steam of cold air.

3.5.2.4 Energy dispersive X-ray spectroscopy

Energy dispersive X-ray (EDX) spectroscopy is coupled with the applications including scanning electron microscopy and transmission electron microscopy. EDX provides elemental analysis on areas as small as nanometers in diameter. The impact of the electron beam on the sample produces X-rays that are characteristic of the elements in the specimens.

During the qualitative analysis, the X-ray energy values from the EDX spectrum are compared with known characteristic X-ray energy values to determine the presence of an element in the sample. Elements with atomic numbers ranging from that of beryllium to uranium can be detected. The minimum detection limits vary from approximately 0.1% to a few atomic percentages, depending on the element and the sample matrix.

Quantitative results can be obtained from the relative X-ray counts at the characteristic energy levels for the sample constituents. Semi-quantitative results are readily available without standards by using mathematical corrections based on the analysis parameters and sample composition. The accuracy of standardless analysis depends on the sample composition. Greater accuracy is obtained using known standards with similar structure and composition to that of the unknown sample.

For elemental mapping, characteristic X-ray intensity is measured relative to lateral position on the sample. Variations in X-ray intensity at any characteristic energy value indicate the relative concentration for the applicable element across the surface. One or more maps are recorded simultaneously using image brightness intensity as a function of the local relative concentration of the element(s) present. About 1 nm lateral resolution is possible.

During line profile analysis, **t**he SEM electron beam is scanned along a pre-selected line across the sample while X-rays are detected for discrete positions along the line.

Analysis of the X-ray energy spectrum at each position provides plots of the relative elemental concentration for each element versus position along the line.

Composition of nickel and manganese oxide nanowires was examined using energy dispersive X-ray spectroscopy incorporated with SEM and TEM.

3.5.3 X-ray diffraction

X-ray diffraction (XRD) is a powerful nondestructive technique for characterizing crystalline materials. It provides information on structures, phases, preferred crystal orientations (texture), and other structural parameters, such as average grain size, crystallinity, strain, and crystal defects. X-ray diffraction peaks are produced by constructive interference of a monochromatic beam of X-rays scattered at specific angles from each set of lattice planes in a sample. The peak intensities are determined by the atomic decoration within the lattice planes. Consequently, the X-ray diffraction pattern is the fingerprint of periodic atomic arrangements in a given material. An online search of a standard database for X-ray powder diffraction patterns enables quick phase identification for a large variety of crystalline samples. In the present work, the crystallinity of nickel nanowire arrays was examined with X-ray diffraction.

3.5.4 Atomic force microscopy

Atomic force microscopy (AFM) is a form of scanning probe microscopy (SPM) where a small probe is scanned across the sample to obtain information about the material's surface. The information gathered from the probe's interaction with the surface can be as simple as physical topography or as diverse as measurements of the material's physical, magnetic, or chemical properties. These data are collected as the probe is scanned in a raster pattern across the sample to form a map of the measured property relative to the X-Y position. Thus, the AFM microscopic image shows the variation in the measured property, e.g., height or magnetic domains, over the area imaged.

Unlike SEM which provides a two-dimensional projection or a two-dimensional image of a sample, AFM provides a true three-dimensional surface profile. Additionally, samples viewed by AFM do not require any special treatments (such as metal/carbon coatings for insulated samples) which would irreversibly change or damage the sample. While an electron microscope needs an expensive vacuum environment for proper operation, most AFM modes can work perfectly well in ambient air or even a liquid environment. However, AFM could not scan images as fast as SEM. It may require several minutes for a typical scan, while an SEM is capable of scanning at near real-time.

In the present work, a Vecco CP2 atomic force microscope (AFM) was also used to examine the surface topography of anodic films. The AFM data give information on depth of grooves on optic grating impressed aluminium surface, and also the true dimensions of porous structure in anodic films.

3.6 Electrochemical measurements

Electrochemical performance of the manganese oxide nanowire arrays was examined by cyclic voltammetry (CV) in a three-electrode cell in which the manganese oxide nanowire arrays was assembled as the working electrode. Cyclic voltammetry was carried in a 0.1 M Na_2SO_4 electrolyte. The potential was varied using an ACM analyzer in the range of 0–1.0 V (SCE) on manganese oxide nanowire arrays formed at different voltages, with a constant scan rate of 5 mV s^{-1} at room temperature.

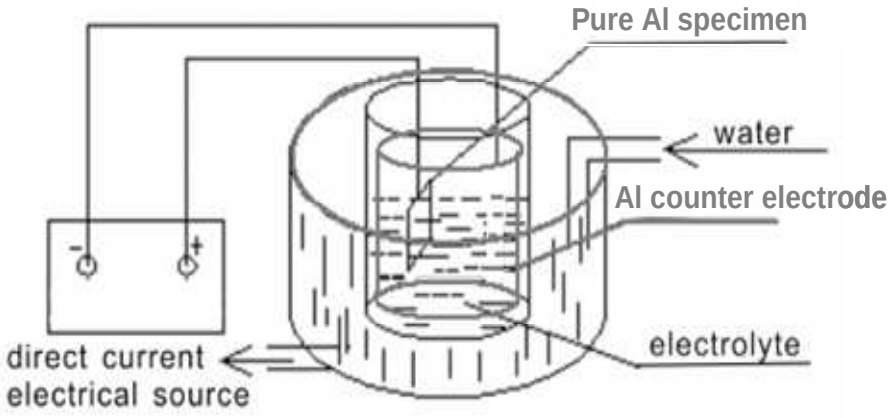

Figure 3.1 *Illustration of anodizing setup*

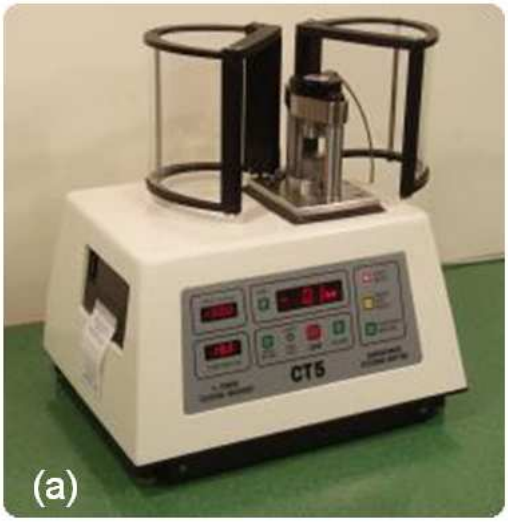

Figure 3.2 *Picture of surface micro-cracks testing machine, employed for optic grating press over aluminium substrate.*

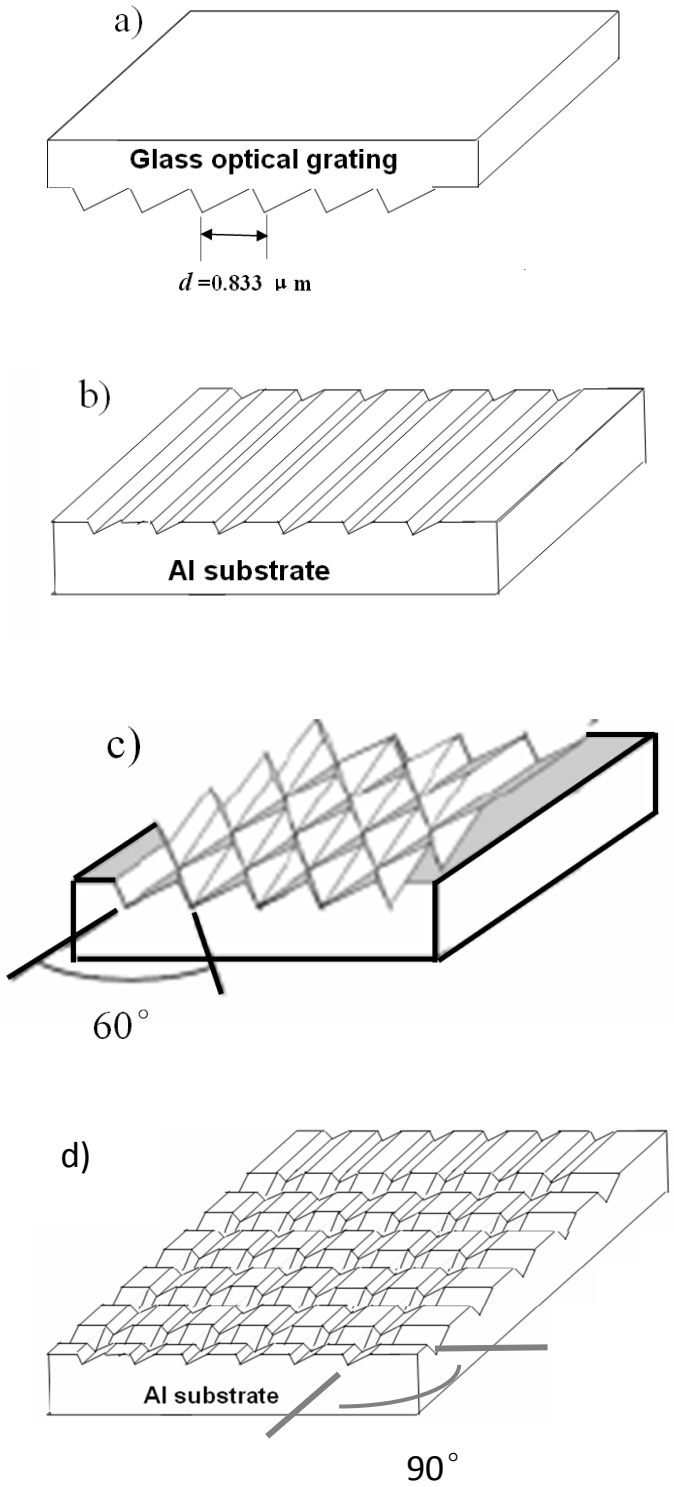

Figure 3.3 *Schematics of optic grating impress: a) features of optic grating; b) features on aluminum surface after one direction optic grating impress; c) features on aluminum surface after two optic grating presses at an angle of 60°, and d) Features on aluminum surface after two optic grating presses at an angle of 90°.*

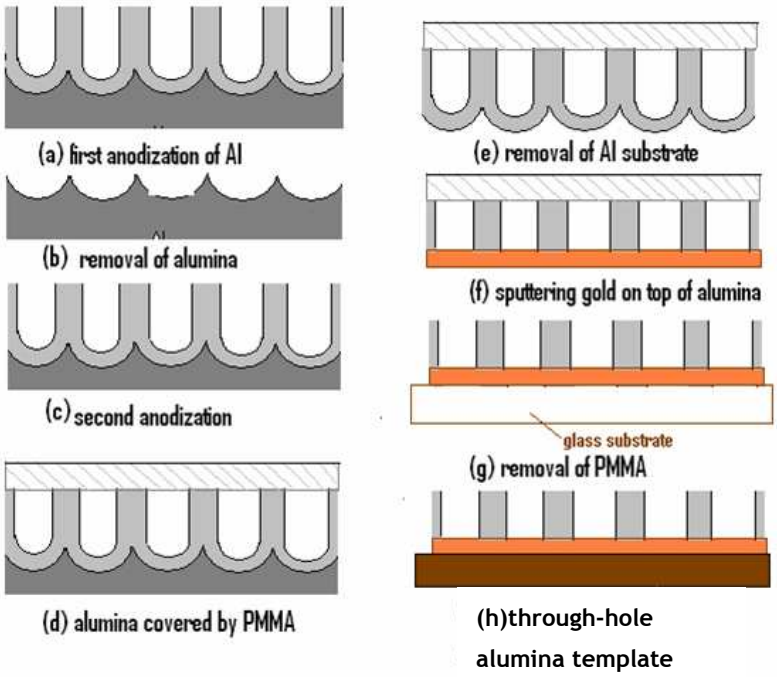

Figure 3.4 *Schematic showing procedures of fabricating anodic oxide template: (a) first anodizing for 20 h; (b) chemical removal of alumina; (c) second anodizing for 1 h; (d) cover the top side of anodic films with PMMA; (e) chemical removal of aluminum substrate; (f) sputtering Au on top of alumina; (g) removal of PMMA, and (h) Alumina template ready for electrodeposition*

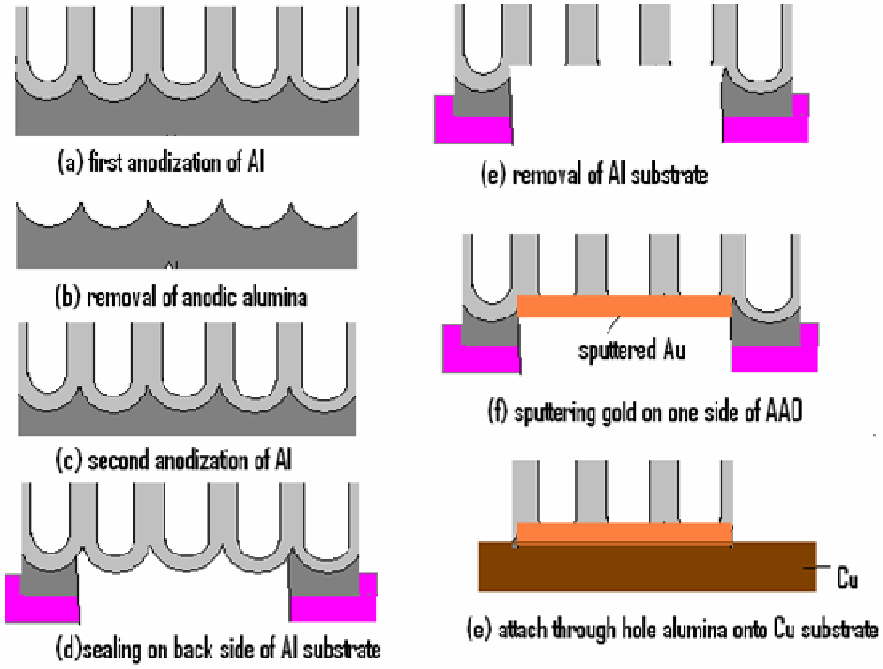

Figure 3.5 *Schematic showing procedures of fabricating anodic oxide template: (a) first anodizing for 20 h. (b) chemical removal of alumina; (c) second anodizing for 1 h; (d) cover the back side of specimen as a window shape with lacmat. (e) chemical removal of aluminum. (f) gold sputtered as substrate. and (e) alumina film attached onto Cu substrate.*

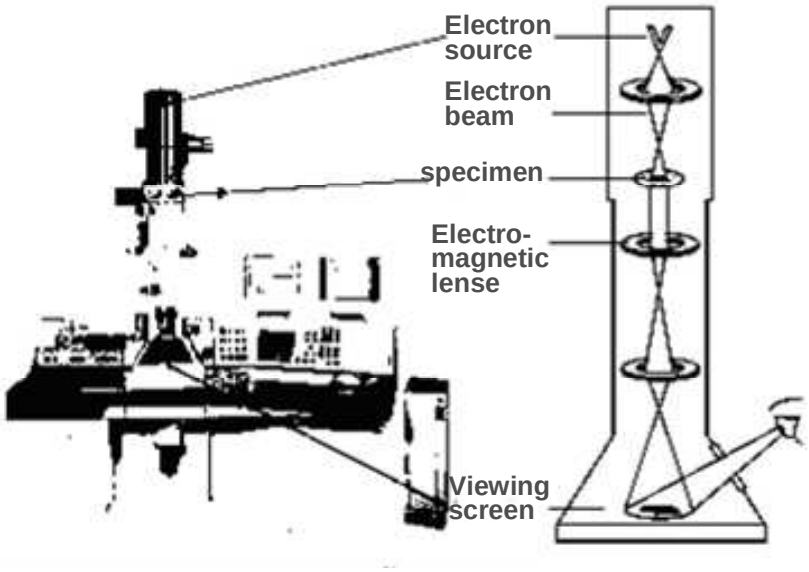

Figure 3.6 *Schematic of transmission electron microscope*

Figure 3.7 *Philips XL30 ESEM-FEG scanning electron microscope.*

Figure 3.8 *Image of Vecco CP2 atomic force microscope*

Chapter 4

Fabrication of Anodic Oxide Films with Highly Ordered Pores

4.1 Introduction

Various mechanisms have been proposed for self-organization of ordered pore arrangements during anodic oxide film formation. Jessensky [122] reported that the stress at the interface between the porous oxide and the aluminum substrate has a significant influence on the self-organization of ordered pores. He pointed out the effect of interfacial stress on the regularity of the pores. It was also reported that high current density employed for anodizing is a key factor for interpore distance that determines the self-ordering of the pore arrangement [123]. It was found that the formation of a ordered pore structure is sensitive to anodizing conditions [124]. The type of electrolyte (sulphuric acid, phosphoric acid or oxalic acid), applied voltage and anodizing temperature can affect pore distribution.

Most of the previous works on obtaining highly ordered anodic oxide films have been focused on processes with two-steps anodizing. It was revealed that as the duration for the first anodizing step increases, the sizes of orientation domains, within which all pores are aligned in the same orientation, become large [2, 4]. In this chapter, the aim is firstly to advance the understanding of the effects of multi-steps anodizing on the ordering of pores in anodic oxide films. In order to quantify the effect of each step, anodic films are formed by two-, three- and four-steps anodizing. The film growth mechanisms and film structures are also studied. Further, investigation on self-organization behavior during constant voltage anodizing was conducted. Effects of anodizing voltage and the concentration of electrolyte, on steady current density (i) and the morphology of porous anodic films were also investigated.

4.2 Current-time response during constant voltage anodizing

The current density transients during constant voltage anodizing of aluminum could provide information on pore initiation and steady state growth of porous anodic film. Figures 4.1 and 4.2 show the current density transients recorded for two-steps anodizing processes in sulphuric acid and oxalic acid respectively. Figure 4.1 illustrates the variation of anodizing current at a constant voltage of 40 V in 0.3 M oxalic acid at room temperature. Figure 4.2 displays the current variation in 0.3 M sulphuric acid at a constant voltage of 25 V at room temperature.

As revealed in Figures 4.1 and 4.2, the current density transients exhibit a peak within the initial five seconds after anodizing started. Current descends rapidly to a minimum value and then increases gradually to a stable and constant value until the end of anodizing. The shape of the current-time curves of the first anodizing step is similar to the shape recorded for the second anodizing step, but not identical. The occurrence of a minimum current density is observed in each step of anodizing. This minimum value occurs at approximately 17 seconds during first-step anodizing and approximately 10 seconds during second-step anodizing in 0.3 M oxalic acid, and approximately 15 seconds during first-step anodizing and approximately 10 seconds during second-step anodizing in 0.3 M sulphuric acid. Another significant difference is that longer durations of 120 s (oxalic acid) and 50 s (sulphuric acid) are needed for currents to gradually increase to a stable and constant value for the first-step anodizing, compared to that of 50 s (oxalic acid) and 25 s (sulphuric acid) respectively during the second-step anodizing.

To understand this phenomenon of current variation, the mechanism for film formation should be taken into consideration. During the initial stage immediately after voltage was applied, the resistance was low and thus the initial current was extremely high. Once anodizing started, a layer of dielectric compact oxide barrier

was formed rapidly on the surface of aluminum, which leads to the decreased current density after peak value.

Hoar and Yahalom [25] suggested that the current during barrier type film formation continued to decrease exponentially. Diggle [125] compared the current-time responses during barrier-type and porous-type oxide films formation by constant voltage anodizing. He found that in the current-time response during porous-type oxide film formation, before the current reached the minimum value, which is also observed in Figure 4.1, 4.2 and 4.3, the current transients is identical with the current for barrier-type film formation. After this point, the current for porous type anodic film formation gradually increased, reaching a stable and constant value. The increase of current density after the minimum value observed in Figure 4.1 and 4.2 is attributed to pore initiation**.** Pores start to initiate at the point of minimum current value. At the initial stage of anodizing before this point, only barrier type anodic film was formed. During the pore initiation stage, the film is thinned locally due to local dissolution [126]. Consequently, current density starts to increase slightly.

Therefore, the occurrence of minimum current density indicating the pore initiation gives information during the growth of porous anodic films. In previous works [25], it was stated that the current-time transients are dependent on the applied voltage and the electrolyte. The minimum current density occurs earlier with the increase of applied voltage and the decrease of pH of the electrolyte. Further, the value of the minimum current density increases with the increase of electric field strength. In Figure 4.1 and 4.2, the occurrence time of minimum current is earlier in second-step anodizing compared to that during the first-step anodizing.

This phenomenon could be explained by investigating the surface morphology of aluminum substrates. Before the first-step anodizing, the electropolished aluminum surface possesses fluctuant textures such as metal ridges in nanoscale [24]. Films

thickened non-uniformly, leading to redistribution of current which concentrated into the thin film regions between ridges. These are the precursors of the steady state pores. By rapidly transforming into scalloped pore base at these positions, the film then penetrates into the metal, thus the steady state porous anodic oxide formation is established.

After removing the anodic films formed during first step anodizing, the aluminum surface possesses hexagonal ordered scalloped hemispherical pattern textures, as shown in SEM images of Figure 4.6 (which will be discussed later). During the second-step anodizing, the current concentrated at the bottom of each curvature, where the resistance is lowest and electric field is the highest**.** Pores are initiated at these points that were already determined by these concave patterns, thus significantly accelerate the formation of hemispherical scalloped pore base, and finally accelerate the occurrence of pore initiation. Therefore, it could be deduced that the pore initiation is easier on the textured surface of aluminium substrate.

It is generally accepted that the increase of current density is a consequence of the rearrangement of pores occurring on the surface. The rearrangement process is a result of interaction of neighboring pores and leads to close packed pores on the surface. During the current increase period, with the electric-field-assisted dissolution [7], the oxide film dissolved partially at sites where pores are initiating, resulting in a gradually increasing current density. Finally, the growth and dissolution of the oxide film reached homeostasis, and the current density stays approximately constant. In Figure 4.1 and 4.2, current increase period was shortened in second step anodizing compared to that of the first step anodizing, indicating that the rearrangement of pores reaches the stable state sooner than that in first step anodizing.

Current-time responses of three-steps anodizing performed in 0.3 M oxalic acid under constant voltage of 40 V at room temperature is shown in Figure 4.3. It is evident that

the current transients of the first-step anodizing exhibit earliest occurrence of minimum current density and the longest increasing period from the minimum current density value to reach stable current density, which is consistent with the results in two-steps anodizing. This could also be attributed to the hexagonally ordered scalloped patterns on anodized aluminum surface. Only slight difference between the current transients of the second and the third anodizing steps could be observed, however. Further investigation on the effects of multi-steps anodizing over ordered porous anodic film is presented in sections below.

4.3 Morphology of highly ordered anodic oxide films

Figures 4.4 and 4.5 illustrate general morphology features of highly ordered anodic oxide films, as revealed by scanning electron microscopy (SEM) and atomic force microscopy (AFM) respectively.

Figure 4.4 shows the top surface features of films formed by four steps anodizing in 0.3 M oxalic acid under constant voltage of 40 V at room temperature. A perfectly arranged hexagonal cell array in a large area of several square micrometers is evident in Figure 4.4 (a). All pores are approximately circular. The cells and pores show a narrow range of sizes, approximately 90 nm and 25 nm diameters respectively. At an increased magnification view of Figure 4.4 (b), it is clearly evident that the hexagonally arranged pores are surrounded by six hexagonally arranged columns, which are interconnected to form a network of cell wall.

In Figure 4.5, AFM images confirm the surface features revealed in SEM images. Figure 4.5 (a) shows a larger area of the resultant oxide surface, with the correspondent three dimensional view of the surface being presented in Figure 4.5 (b). A relatively long range of hexagonally arranged pore array is evident. The single orientation of hexagonally arranged pore arrays is restricted within a certain domain, and different orientations of the pore arrays are observed within different domains.

The boundaries between the domains are outlined in Figure 4.5 (a). There are abnormal features along the boundaries, such as defects and distortion of pore shapes, as indicated by arrows in Figure 4.5 (a). Hexagonally arranged pore arrays of different orientation meet up along the boundaries.

AFM images of Figures 4.5 (c) and (d) present close view of the porous cells, showing hexagonally ordered columns of oxide structure. In Figure 4.5 (e) and (f), line scans reveal the surface profile of the porous anodic films. The profile along the cell walls of the hexagon cells, as illustrated by line E in Figure 4.5 (c), is displayed in Figure 4.5 (e). It is evident that there are double peaks for each cell. These double peaks confirmed the existence of six columnar hemispherical hills surrounding every hexagonal cell.

The surface morphology of aluminum substrate after the removal of porous oxide films is shown in Figure 4.6. A hexagonally arranged scalloped pattern is revealed over the entire surface. The hexagonally arranged cells surrounded by six hills could also be observed on aluminum substrate. This is similar feature to the morphology structures of anodic oxide films that were observed in Figure 4.5 (d).

Fiemings [127] stated that a breakdown of a planar growth interface causes the propagation of small cells with curved interfaces. Curved interface propagation has been found in various disparate systems. For instance, periodic cell structures exist in directional solidification [127]. Depending on the forces driving the instability, the interface can restabilize into curved shapes. Models of interface dynamics can be adopted to study the interface propagation in porous anodic film growth on aluminium, if the driving force for the instability can be identified. During the anodizing process in acid electrolyte, the electric field along the pore base surface is inhomogeneous [128], and the electrical fields across the pore walls are also unevenly distributed. The dissolution of aluminium and the growth of the oxide are controlled by the distributions of the electrical field. Under steady-state conditions, the curved interface

develops. Ordered pore cell can be obtained after only a few minutes during the second anodizing, in contrast with the tens of hours needed for regularity in first anodizing.

After stripping off the oxide film by chemically removing aluminum substrate in a mixed solution of $CuCl_2$ and 10% (vol) HCl, AFM was employed to investigate the morphology of the bottom side of the film. Hexagonally close packed hemispherical cell array is revealed in Figure 4.7, indicating that pores are closed up at the bottom side with barrier layer oxide immediately above the aluminum/film interface. The hemispherical cell arrays are orderly arranged in hexagonal patterns. This is the same arrangement as that observed on anodic film surface shown in Figure 4.4 and Figure 4.5. Figure 4.7 (c) displays the line scan on the bottom side of the film, revealing almost identical sizes and shapes of the porous cell.

Cross section view of porous anodic film formed by two-steps anodizing in 0.3 M oxalic acid at 40 V at room temperature is presented in Figure 4.8. It is evident that all the pores exhibit cylindrical morphology with identical pore diameter. Further, all pores are straight and parallel to each other. It was stated in previous works [3] that, the porous anodic films formed in one-step anodizing do not possess pores as uniform as that in the anodic films formed by two-steps anodizing. Those initially distorted and dendritic pores could be rearranged to the uniform straight cylindrical structure only after a long period anodizing. Therefore, it is essential to remove the anodic films initially formed in the first step anodizing to obtain porous anodic films with straight cylindrical structure.

4.4 Pore ordering of anodic oxide films during multi-steps anodizing

As for the pore ordering of anodic oxide films, there are basically two aspects of evaluation parameters: 1) single pore regularity; 2) spatial distribution of pore arrays.

By comparing the pore morphology and arrangements obtained by various combinations of anodizing conditions and durations, the dependence of the pore regularity and space distribution to the anodizing conditions was obtained.

Figure 4.9 shows the SEM micrographs of the top surfaces of the porous anodic oxide films, formed in 0.3 M oxalic acid electrolyte under constant voltage of 40 V at room temperature. In order to quantitatively evaluate the effects of the anodizing time and anodizing steps on the regularity of pore distribution, fast Fourier transform (FFT) of SEM images are inserted in each SEM images in Figure 4.9.

The FFT of the SEM images gives information about the periodicity of pore distributions in reciprocal space. The regularity in the pore distribution is reflected by the uniformity and spot intensity in FFT. For each anodizing condition, FFT is conducted first over a relatively large area of 20-30 μm^2 which covers several orientation domains, and then over a relatively small area of 1 μm^2. For the FFT over a relatively large area, it is evident that several orientation domains were introduced for most specimens. Therefore, the regularity of pores in anodic oxide films, including both orientation domains and interpore distance between adjacent pores is reflected in FFT. On the other hand, the FFT over a relatively small area gives exclusive information on uniformity of interpore distances between adjacent pores, since over a relatively small area, only one orientation domain was included for most specimens, thus the influence of orientation domains on FFT is excluded.

For films obtained by 6 hours one step anodizing (Figure 4.9), pore distribution is completely random, as revealed in Figure 4.9 a). The blurred intensity in FFT image, taken from an area of 5×8 μm^2, indicates little order in long distance pore distributions.

At an increased magnification, as shown by SEM image of Figure 4.9 b, pores exhibits irregular shapes, and the size of pore and cell do not appear uniform. FFT

taken from an area of approximately 3×2 μm^2 displays a highly blurred diffusion ring, indicating that pores are distributed irregularly, and the interpore distance between adjacent pores in films formed in one-step anodizing may vary significantly.

Figures 4.9 c-h display SEM images of anodic films obtained by two-steps anodizing with the following combination: anodizing for 12 hours for the first step and 4 minutes for the second step (Figure 4.8 c and d); 12 hours for the first step and 30 minutes for the second step (Figure 4.8 e and f); and 12 hours for the first step and 4 hours for the second step (Figure 4.8 g and h). It is evident that the porous cells are aligned hexagonally. The sizes of each cell are almost identical. It is observed that the hexagonally arranged pores are aligned in different orientation within various domains. These domains have irregular shapes and different sizes. When the duration for the second-step anodizing was changed from 4 minutes (Figure 4.9 c and d) to 30 minutes (Figure 4.9 e and f), similar regularity of pore distribution and orientation domain size were observed. When the second-step anodizing was extended to 4 hours (Figure 4.9 g and h), the regularity of pore distribution and domain size appears slightly improved.

FFT of SEM image of the anodic oxide films formed by two-steps anodizing (12 h for the first step and 4 minutes for the second step) over on an area of 5×7 μm^2 exhibits a clear ring structure, as shown in Figure 4.9 c. This is an indicator of slightly improved regularity than that for the films obtained by one-step anodizing. However, in the case of a perfectly arranged hexagonal pore arrays, a FFT pattern consisting of six individual spots on the edges of a hexagon is expected. The ring structure of FFT is associated with the shortage of hexagonally arranged pores over long range. Although pores are aligned hexagonally, they are orderly arranged in one orientation only within fairly limited areas.

SEM image from a relatively smaller area ($3.5 \times 2\ \mu m^2$) of the same sample in and the corresponding FFT image are shown in Figure 4.9 d）. The FFT consists of six blurred spots in hexagonal pattern, indicating improved ordered pore distribution and uniformity of interpore distances than that on films obtained by one-step anodizing.

Similar FFT obtained from the SEM image of the anodic oxide films produced by longer second step anodizing of 30 minutes and 4 hours respectively are shown in Figure 4.9 e to h. Rings are revealed in FFT over relative large area (Figure 4.9 e and g). Six hexagonally patterned blurred spots are revealed in FFT over relatively small area (Figure 4.9 f and h). The FFT data indicates that for porous anodic films formed by two-steps anodizing with up to 4 hours for the second step anodizing period, both regularity of pore distribution, i.e. the orientation domain sizes and uniformity of interpore distances are similar.

SEM images of the anodic films obtained by three-steps anodizing, with 12 hours, 4 hours and 4 minutes for the first, the second and the third step respectively, are shown in Figure 4.10. For three-steps anodizing, FFT over a relatively large area also exhibits a blurred ring pattern in Figure 4.10 a, indicating the orientation domain size is similar with films produced by two-steps anodizing. However, significant improvement of individual pore morphology uniformity is revealed in the SEM image, as shown in Figure 4.10 b. This is confirmed by the six-fold asymmetry clear spots in FFT over a small area. The spot in FFT appears obviously sharper than the films obtained by one-step and two-steps anodizing. Further, the second order of hexagonal spots is observed, confirming the improvement of pore ordering.

Figure 4.11 displays the SEM images obtained by four-steps anodizing with 12 hours, 4 hours, 30 minutes and 30 minutes for the first, the second, the third and the forth step respectively. Significantly improved pore distribution and uniformity of individual pores are evident. Further, domain size of single orientation aligned pores

appears increased for films formed with four-steps anodizing than one-steps, two-steps and three-steps anodizing.

It is clear that the regularity of pore distribution continuously increases with increasing anodizing steps. FFT of SEM images of porous anodic film produced with four-steps anodizing changed significantly from that for films formed with less anodizing steps. Even over an relatively large area of 5×7 μm^2, a hexagonally configured six individual spots is evident in Figure 4.11 a. Further, the second order that is actually a six-fold symmetry composed by twelve individual spots is also evident, indicating the almost perfectly hexagonally arranged pores over relative ly long range. The hexagonal lattice of FFT in Figure 4.11 b, which was obtained from SEM image of the same anodic films over a relatively small area (3×2.5 μm^2) is significantly clearer than that of the films produced with three-steps anodizing, indicating perfect uniformity of interpore distances.

Figure 4.12 shows the histograms of the distribution of the interpore distance between neighboring pores in anodic films, measured from the SEM images in Figure 4.9, 4.10 and 4.11. The histogram for the anodic films formed with one-step anodizing reveal a relatively wide distribution of interpore distance with a wide distribution from cells with interpore distances of 50 – 200 nm, as shown in Figure 4.12 (a). It generally reflects the irregularity of the pores in anodic films obtained with only one-step anodizing. There is a considerable change of interpore distance distribution for films formed with three- and four-steps anodizing, as shown in Figure 4.12 (c) and (d). The ranges of cell diameter narrow down with increased anodizing steps, indicating that pores tend to have better regularity in interpore distances. It is evident in Figure 4.12 that for the anodic film produced by three steps and four steps, improved ordering of size distribution can be achieved.

Profiles of FFT are presented in Figure 4.13. The full width at half peak maximum (FWHM) were calculated as the regularity ratio, $H/W_{1/2}$, where H is the maximum

intensity of peaks and W is the wide of the peak at half-maximum. $H/W_{1/2}$ is closely related to regularity of the nanostructure. The higher value of H means the higher intensity of the spot, and lower value of W means smaller spot size, both of them are corresponding to sharper spots. Thus, the value of $H/W_{1/2}$ is a reasonable and precise evaluation standard for the regularity of anodic pore distribution.

The average regularity ratio was calculated for all anodic films attained under related conditions, and then plotted in Figure 4.14, showing clearly the benefits of multi-steps anodizing for both pore distribution and individual pore regularity. The variation at Y axis represents the regularity variation. The upper curve is corresponding to the FFT over relatively large areas, and the lower curve is corresponding to the FFT over relatively small areas. Briefly, an increasing tendency with the increase of anodizing steps is observed in both curves, suggesting both the regularity of pore distribution and pore uniformity increases with the increase of anodizing steps.

The regularity ratios of the anodic films obtained by the two-steps anodizing (with second anodizing time of 30 minutes and 4 hours respectively) are compared. In the upper curve (labeled with A), which is corresponding to FFT of relatively large areas of SEM images, significant improvement of regularity is observed when the second anodizing time is prolonged from 30 minutes to 4 hours. In the lower curve (labeled with B) which is corresponding to FFT of relatively small areas of SEM images, the regularity values are almost identical. It means that the increase of anodizing time for the second step anodizing has a significant influence on the size of orientation domains, but little influence on the pore uniformity.

The orientation domains, figured out by the lines drawn on SEM images, are illustrated in Figure 4.15. By counting the number of pores within each domain, an average value could be obtained for each specimen. Further, the surface area of each pore is calculated as shown in Figure 4.16. The pores are ideally denoted as a hexagon. The interpore distance is fixed at 90 nm, since all anodic films were formed under the

same anodizing voltage of 40 V in 0.3 M oxalic acid in this section. The area of each anodic pore is described as:

$$S = \sqrt{3}\, d^2$$

In the equation, *d* is the interpore-distance between neighboring pores. By multiplying the average pore numbers of each domain with area of an individual pore, S, the average domain size is obtained. Therefore, the regularity of pore distribution over long range is quantitatively evaluated by comparison of domain sizes of different anodic films.

Measurements of the configured area reveal that the average domain size of anodic films produced by two-steps anodizing with the same first step anodizing times and the second anodizing step time of 4 minutes, 30 minutes and 4 hours are approximately 0.346, 0.293 and 0.467 μm^2, respectively. Average domain size increases from 0.297 μm^2 to 0.467 μm^2 when the second step anodizing time increases from 30 minutes to 4 hours, which is highly consistent with the regularity value in Figure 4.11. It is an exception that the domain size is 0.346 μm^2 when the second step anodizing time is 4 minutes, bigger than that of the anodic film produced with the second step anodizing time of 30 minutes. However, these two values are still in the same value range.

The average sizes of orientation domains for anodic films obtained by three-steps and four-steps anodizing are 1.578 and 1.719 μm^2, respectively. Increasingly larger domain sizes are obtained with further anodizing step being performed. The average domain size is consistent with the regularity ratio evaluated in Figure 4.11.

For anodic films formation, it was reported in previous researches [12] that the morphology and self-adjustment of pores were mainly governed by electric field enhanced electrochemical reactions in the electrolyte/oxide and oxide/metal interfaces.

During steady state stage of anodizing, porous anodic oxide film grows under an equilibrium of field-enhanced oxide dissolution at the oxide/ electrolyte interface, and the oxide formation at the metal/oxide interface by immigration of anions of O^{2-} and OH^- [7]. Since the current distribution over aluminium substrate is not uniform, the field-assisted oxide dissolution rate at the scalloped positions becomes slower than that at other positions. The fact that Al^{3+} ions are lost to the electrolyte has been shown to be a prerequisite for porous oxide growth [12].

To date, the most common accepted model for the self-adjustment of pores in anodic films is based on mechanical stress associated with expansion of aluminum during the oxide formation [4]. The atomic density of aluminum in alumina is by a factor of two lower than in metallic aluminum. Therefore, forces between neighboring pores originate probably from the mechanical stress which is associated with the expansion during oxide formation at the metal/oxide interface, and the volume expansion rate is determined by the extent of field-assisted oxide dissolution [3]. As the oxidation takes place at the entire pore bottom simultaneously, the material can only expand in the vertical direction, so that the existing pore walls are pushed upwards. Due to this repulsive force between neighboring pores, self-ordering process is established.

The initially formed oxide layers are pushed outwards as the oxide growth proceeds, thus locate at top surface of specimens, and the newly formed oxide layers locate at the metal/ oxide interface. Therefore, the irregularity of pore distribution in Figure 4.8 (a) actually represents the morphology conditions of initially formed oxide film layers. While after the removal of oxide layer formed during the first step anodizing, a hexagonally ordered scalloped hemispherical pattern is formed over the aluminum surface (as shown in SEM image of Figure 4.6). AFM investigation on the bottom topography of oxide films in Figure 4.7 reveals that the barrier layer cells are also hexagonally aligned, similar to the surface of aluminum substrate. This indicates that ordered pores evolve during the proceeding of oxide growth. Along the domain boundaries, it was stated that the pores gradually merged along the boundaries [129].

Pores gradually rearranged during the self-adjustment process, and the domains grew by alignments and mergers of pores at domain boundaries. Therefore, during one step anodizing, the domain size should be a function of time.

During the second-step anodizing, the anodic films formed over the scalloped patterned aluminum surface exhibit ordered pore structures ever since the initial period of the second step anodizing. This is confirmed by SEM image of the anodic films in Figure 4.9 (b), which was formed with a short period of second step anodizing. Further, significant improvement on regularity of pore distribution could be obtained by extending the second anodizing period to 4h. This is consistent with previous literature [30], where it was stated that longer anodizing duration allow improved regularity of the pore distribution.

However, previous literatures stated that prolonged anodizing time (>24 h) do not favor the increase of domain size [130]. There is an optimum anodizing time to obtain the largest domain size (average in several square micrometers), i.e. there exists a critical domain size that could not be exceeded in single step anodizing. This might be restrained by grain boundaries of aluminium substrate, which has not been clearly understood, however. In multi-steps anodizing, a restarted pore initiation and the following straight channel growth establishes a new equilibrium between oxide formation at metal/oxide interface and the dissolution at pore base at oxide/electrolyte interface.

During the early stage of anodizing [22], pores compete with each other since they have an interior tendency to enlarge their pore diameter and restrain the growth of their neighboring pores. When one pore grows relatively slower than the surrounding pores, the walls of two side pores will move towards the centre and the middle pore will reduce its pore size and its growth finally stops. When the pores are relatively too large, they may split into two or more normal sized pores. The reason for such pore splitting is probably the constant ratio of the dissolution rate of anodic oxide. Such

arrangements of pores are often observed at an early stage of pore growth in anodic oxide films, especially at the irregular positions on textured aluminium substrate. Here, the contribution of mechanical stress is notable when two pores growing in different directions touch each other. The repulsive force between pores help to form parallel channels. Hence, once one more anodizing step is conducted, more chances

are given to the pore self adjustments, especially the irregular pores along domain boundaries. Therefore, the time effect on improving pore ordering is evident. More precisely to say, it is the combination of prolonged anodizing times as well as repeating anodizing steps that creates enough chances for pores to resize and reorganize, thus resulting in an almost perfectly ordered porous structure.

4.5 Effects of anodizing conditions on the pore formation of porous anodic films

It was stated that the optimum anodizing condition to produce highly ordered porous anodic films in oxalic acid electrolyte is constant voltage of 40 V [2]. However, the mechanism for the self-organization of the pores is still worth further investigation. The effects of anodizing time and multi-steps were discussed previously. Therefore, the dependence of pore ordering and steady current density on anodizing conditions is worth investigation to gain further insights into the formation mechanism of highly ordered pore arrays. Thus, anodizing was performed under conditions near the optimum parameters, i.e. 0.2 M, 0.3 M and 0.4 M electrolyte concentration and 30 V, 40 V and 50 V anodizing voltages. The anodizing conditions are listed in Table 4.1. The recorded steady current densities are also listed for comparisons.

Figures 4.18, 4,19 and 4.20 show SEM images of the anodic oxide films. From these images, information about the pore and cell size variations, regularity of pore distributions and the size of orientation domains could be obtained. In Figures 4.18 a-c, for the films obtained under the voltage of 30 V with varied electrolyte concentrations, the pores exhibit irregular shapes. Little regularity of pore distribution could be observed. Further, the cell sizes are approximately 85 nm – 90 nm.

Figures 4.19 a-c show the anodic films formed at the voltage of 40 V. Almost perfectly ordered pore arrays are revealed. However, single orientation exists within area of domains. It is evident in Figures 4.20 b and c that defects such as nodules and irregular pores exist along the boundaries between the domains. The pores in anodic films produced in 0.2 M oxalic acid electrolyte at 40 V (Figure 4.19 a) show less regularity compared to others. The cell sizes are approximately 105 nm – 110 nm.

Figures 4.20 a-c show the SEM images of anodic films obtained at constant voltage of 50 V in oxalic acid electrolyte of various concentrations. The cells exhibit the largest size of approximately 120 nm to 125 nm compared to that in the films obtained in other conditions. However, the regularity of the anodic films has a significant fluctuation. Only the anodic film obtained by anodizing in 0.4 M oxalic acid at 50 V exhibit good regularity of pore distribution, as shown in Figure 4.20 c. Figures 4.20 a and b, obtained by anodizing at 50 V in oxalic acid of 0.3 M and 0.5 M respectively, show significant less regularity. Most of the pores are randomly distributed, while hexagonally aligned pores exist in limited area.

4.5.1 Effect of anodizing conditions on pore size in anodic films

The average pore diameter and interpore distance were measured based on the SEM images of Figures 4.18, 4.19 and 4.20. It is evident that when the anodizing voltage was increased from 30 V to 50 V, the cell size changes from 80 nm to 120 nm. The effects of the concentration of oxalic acid on pore diameter and interpore distance at different anodizing voltages are presented in Figure 4.21. It is revealed clearly that the pore diameter increases linearly with electrolyte concentration. However, the interpore distance does not alter under a given anodizing voltage. Meanwhile, both the interpore distance and pore diameter increase significantly when the anodizing voltage increases. The relationship between the pore diameter and the voltage is almost linear in a given electrolyte, this is consistent with the previous findings of linear relationship between anodizing voltage and cell sizes [36].

4.5.2 Effect of anodizing conditions on steady current density

Figure 4.22 shows the relationship between the steady current density and the anodizing voltage at various concentrations of oxalic acid electrolyte. The steady current density increases with the voltage at the selected electrolyte concentrations of

0.2 M, 0.3 M and 0.4 M. At the lower anodizing voltage, the effects of concentration of the oxalic acid on the steady current density is less significant, whereas it becomes more significant with the increase of the voltage. Further, the steady state current density has an enhanced increasing tendency as the anodizing voltage increases.

According to the model of porous anodic oxide film formation proposed by Wood [18], the thickness of barrier layer is approximately equal to a half of the thickness of inner wall, and the thickness of inner wall is determined by interpore distance (*D*) minus pore diameter (*d*). It can be figured as the following equation.

$$l = (D - d)/2 \tag{1}$$

Where *l* is the barrier layer thickness. During the anodizing process, an electric field is induced by the applied voltage. Since the aluminum substrate is conductive, the resistance is mostly distributed across the barrier layer. Therefore, the electric field intensity is determined by the anodizing voltage and barrier layer thickness.

The electric field intensity is given by

$$E = V/l \tag{2}$$

Where *V* is the voltage between the inner and outer surface of the barrier layer (equals to the anodizing voltage), *l* is the barrier layer thickness.

The current density in the circuit is determined by

$$Is = Aesp(BE) \tag{3}$$

Where *Is* is the current density. A and B are the coefficient related to temperature, E is determined by equation (2).

In a given electrolyte, both *D* and *d* increase with the increase of anodizing voltage in a linear relationship [4] and also presented in the present work, whereas the change of the barrier layer thickness is almost negligible. According to Equation (1) – (3), it can be deduced that the current density is approximately exponential with the voltage. This explains the curve tendency in Figure 4.22, in which current density increases more significantly at the higher end of anodizing voltage when the voltage is increasing. The high field theory also suggests that log of current density has a linear relationship with electric field strength, which is consistent with the results in present work [3].

4.5.3 Effect of anodizing conditions on the regularity of porous anodic films

FFT of SEM images over an area of approximately 10 μm^2 in Figure 4.23. As described in previous sessions, the regularity ratio $H/W_{1/2}$ is also employed. $H/W_{1/2}$ is calculated base on the pore distribution in Figure 4.23, and then plotted in Figure 4.24 to show the regularity variation with the change of anodizing conditions.

The regularity of porous anodic films varies with anodizing voltage and electrolyte concentration. The relationships are illustrated in Figure 4.24. When the regularity of anodic films is plotted versus anodizing voltage in Figure 4.24 a, interestingly, it is observed that the tendency of regularity increases when the voltage is increased at a

given electrolyte concentration, except for the electrolyte concentration of 0.2 M. The porous anodic films formed in 0.2 M oxalic acid exhibit the lowest regularities compared with that formed in the relatively high electrolyte concentration of 0.3 M and 0.4 M. Further, it is worth to note that the highest regularity was achieved at the electrolyte concentration of 0.3 M. Similar tendency is observed in Figure 4.24 b, when the regularity of porous anodic films is plotted versus electrolyte concentration. Generally, the porous anodic oxide films exhibit increased regularity with the increase of electrolyte concentration at a given anodizing voltage. However, when the anodizing voltage is reduced to 30 V, little regularity is observed. The highest regularity of porous anodic films is obtained at the anodizing voltage of 40 V in a given electrolyte concentration.

It could be summarized that ordered porous structure can only be formed within certain voltage and acid concentration regions (30–50 V, ≥0.3 M), as shown in Figures 5.1 s5, s6, s8 and s9. Within such voltage and electrolyte concentration windows, the current densities are $5.11E^{-5}$, $5.56E^{-5}$, $9.62E^{-5}$ and $9.64E^{-5}$ mA/cm^2 respectively. Interestingly, by examining the current density-voltage responses in Figure 4.24, it is revealed that the current densities for the highly ordered porous anodic film formation are all exceeding a critical current density value of approximately $4E^{-5}$ mA/cm^2. On the contrary, the porous anodic films formed at current densities lower than the critical value exhibit irregular pore arrangement. It is widely accepted that the anodic current density is associate with the growth rate of anodic films. Therefore, this observation may indicate that the formation of an ordered pore array is related to the growth rate of anodic films in a certain extent. However, due to the oxide dissolution at the oxide/electrolyte interface, the current efficiency for porous oxide formation is not 100%, but was yield with the ratio of aluminum which is transformed to oxide film to the total amount of oxidized aluminum [122]. Jessensky concluded that the current efficiency increases from 45% to 65% as the anodizing voltage increases from 30 V to 60 V. The current density obtained in the present work increases almost exponentially with the increase of

anodizing from 30 V to 50 V. Therefore, the growth rate of oxide film actually increases with the increase of anodizing voltage. This is mainly due to the increased migration velocity of the reactive cation and anion ions [122].

As described in previous sections, a common explanation for ordered porous anodic film formation is that the repulsive interaction between the pores, which are associated with the expansion of the aluminum during anodizing impulses the structural adjustment to form hexagonal ordered porous anodic films. Based on this, Li [4] reported that optimal conditions for the growth of ordered porous oxide films are accompanied by a moderate expansion of the aluminum. Further, Nielsch [130] extended the optimum conditions required for self-ordering of porous anodic films to a 10% porosity rule. It was found that [123] no regularity can be achieved in the cases of very weak or very strong volume expansion, i.e. too low or too high mechanical stress. A suitable stress will sustain the steady growth of anodic films with ordered pores. A higher stress might break the anodic oxide wall and release the local stress, while lower stress could not provide repulsive forces high enough for the self-arrangement of pores during films formation. This explains the irregularity of pores in anodic films formed at low voltage of 30 V, when the repulsive forces between neighbored pores might be too low to keep self-ordering arrangement.

For the formation of ordered porous anodic film at anodizing voltages of 40 V and 50 V, the optimum concentrations of oxalic acid is 0.3 M and 0.4 M respectively. The equilibrium of field-enhanced oxide dissolution at the oxide/ electrolyte interface, and the oxide formation at the metal/oxide interface [7] during steady state porous anodic oxide formation should also be considered. With the enhancement of anodizing voltage from 40 V to 50 V, the growth rate of the porous films increases. To keep the appropriate volume expansion, i.e. appropriate mechanical stress, the corresponding oxide dissolution rate should also be increased to be equilibrated. Therefore, it could be summarized that the equilibrium between a moderate growth rate and appropriate dissolution rate is essential for ordered porous oxide film formation. The increase of

electrolyte concentration could also accelerate the oxide dissolution rate, thus the concentration to obtain optimum self-ordering at 50 V is increased to be 0.4 M. While at a low voltage of 30 V, the film growth rate decreases due to lower migration velocity of reactive cation and anion ions, thus insufficient repulsive interactions between adjacent pores are generated, thus leading to completely random distributed pores in anodic films.

It can also be seen that the average size of orientation domains increases with the increase of acid concentration. For the same voltage, the higher the acid concentration (0.5 M) is, the larger the size of orientation domain and the higher the pore regularity is achieved. This trend could not be obviously observed for the anodic films obtained in 0.2 M oxalic acid. At lower concentration, there are not sufficient reactive H^+ ions for ion transport during migration through electrolyte/oxide interface, thus hinders the vertical pore growth rate. In this case, the repulsive stress between adjacent pores is not sufficient for pores to interact with each other, thus resulting in irregularity of pores as observed in SEM images.

4.6 Conclusion

1. Porous anodic films with highly ordered pores of approximately 90 nm in cell diameter were obtained in 0.3 M oxalic acid electrolyte at the voltage of 40 V. Each pore is surrounded by six hexagonally arranged columns.

2. In current density-time responses, the minimum current density, indicating the starts of pore initiation, occurs earlier during the second step anodizing compared to that in the first step anodizing, suggesting that the pore initiation during the second step anodizing was accelerated by the scalloped texture on the aluminum substrate introduced by previous step.

The steady current density during constant voltage anodizing increases nearly exponentially with the increase of anodizing voltage in the range of 30 V to 50 V in oxalic acid electrolyte.

3. With the constant voltage in the ranges of 40 V to 50 V for anodizing in oxalic acid electrolyte, anodic films with hexagonally arranged pores in could be obtained in selected electrolyte concentrations.

4. At relatively low anodizing voltages (i.e. 30 V) and low oxalic acid electrolyte concentration (i.e. 0.2 M), no regularity of pore distribution and interpore distances could be observed. The steady current density needs to exceed a critical current density value of approximately $4E^{-5}$ mA/cm^2 for the formation of anodic films with ordered pores. This is consistent with the mechanical stress theory. The repulsive interactions between the pores, which are associated with volume expansion during anodizing, should keep a sufficient value to impulse the self adjustment for ordered pore formation. Irregular distribution was achieved in the anodic films formed at relatively low anodizing voltages and low electrolyte concentration. The best regularity of pores in anodic oxide film was achieved in 0.3 M oxalic acid with an anodizing voltage of 40 V, and in 0.4 M oxalic acid with an anodizing voltage of 50 V.

5. The interpore distance in anodic films is varied linearly rely with anodizing voltage, regardless of electrolyte concentration. For a given anodizing voltage, the interpore distances remain constant, while the pore diameter increases nearly lineally with electrolyte concentration.

6. Quantitative characterization by fast fourier transform (FFT) was performed on the regularity of pores in anodic films formed by multi-steps anodizing with varied anodizing period. Significantly increased regularity of pore distribution and uniformity of interpore distances in anodic oxide films were observed with the

increased anodizing steps. Multi-steps anodizing, especially more than two-steps anodizing, can significantly improve the regularity of pores over long range. It is the combination of prolonged anodizing time and repeating anodizing steps that leads to sufficient self-adjustment and self-ordering, thus, resulting in ordered pore arrays.

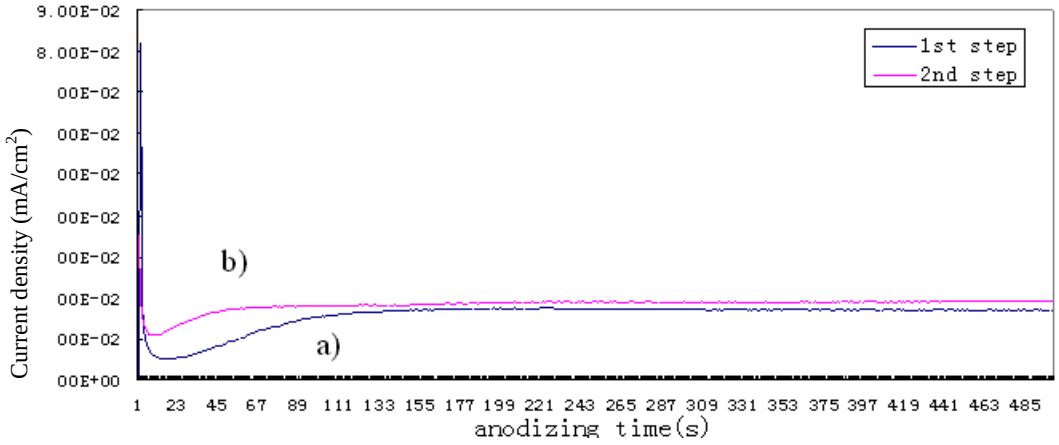

Figure 4.1 *Current transients during two steps constant voltage anodizing of aluminum in 0.3M oxalic acid at 40 V.*

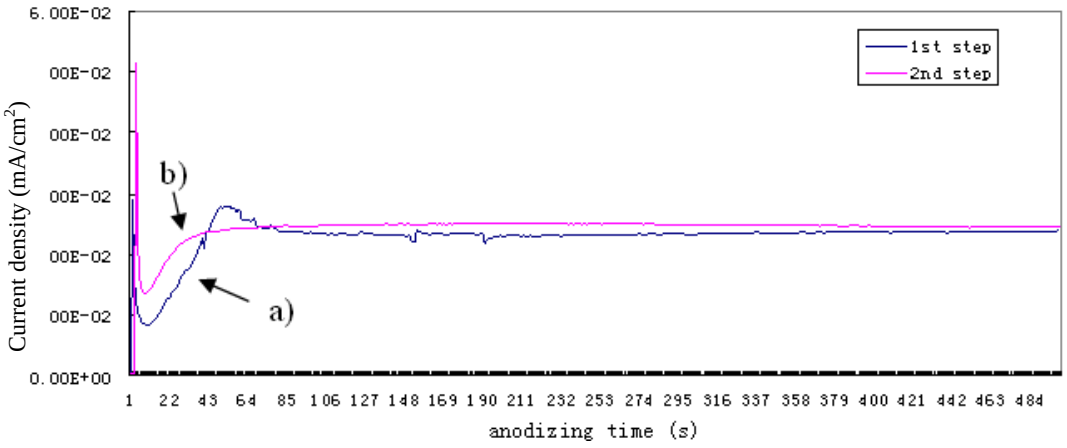

Figure 4.2 *Current transients during two steps constant voltage anodizing of aluminum in 0.3M sulphuric acid at 25 V.*

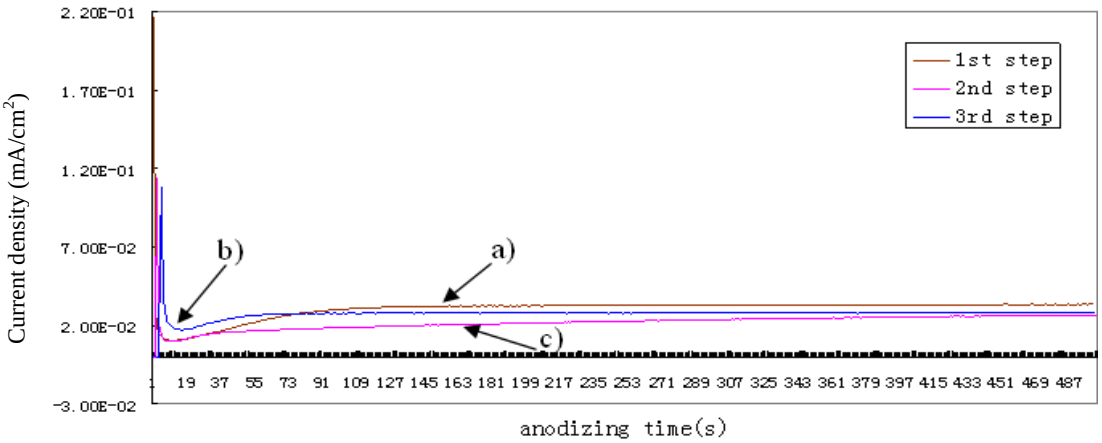

Figure 4.3 *Current transients during three steps constant voltage anodizing of aluminum in 0.3M oxalic acid at 40 V.*

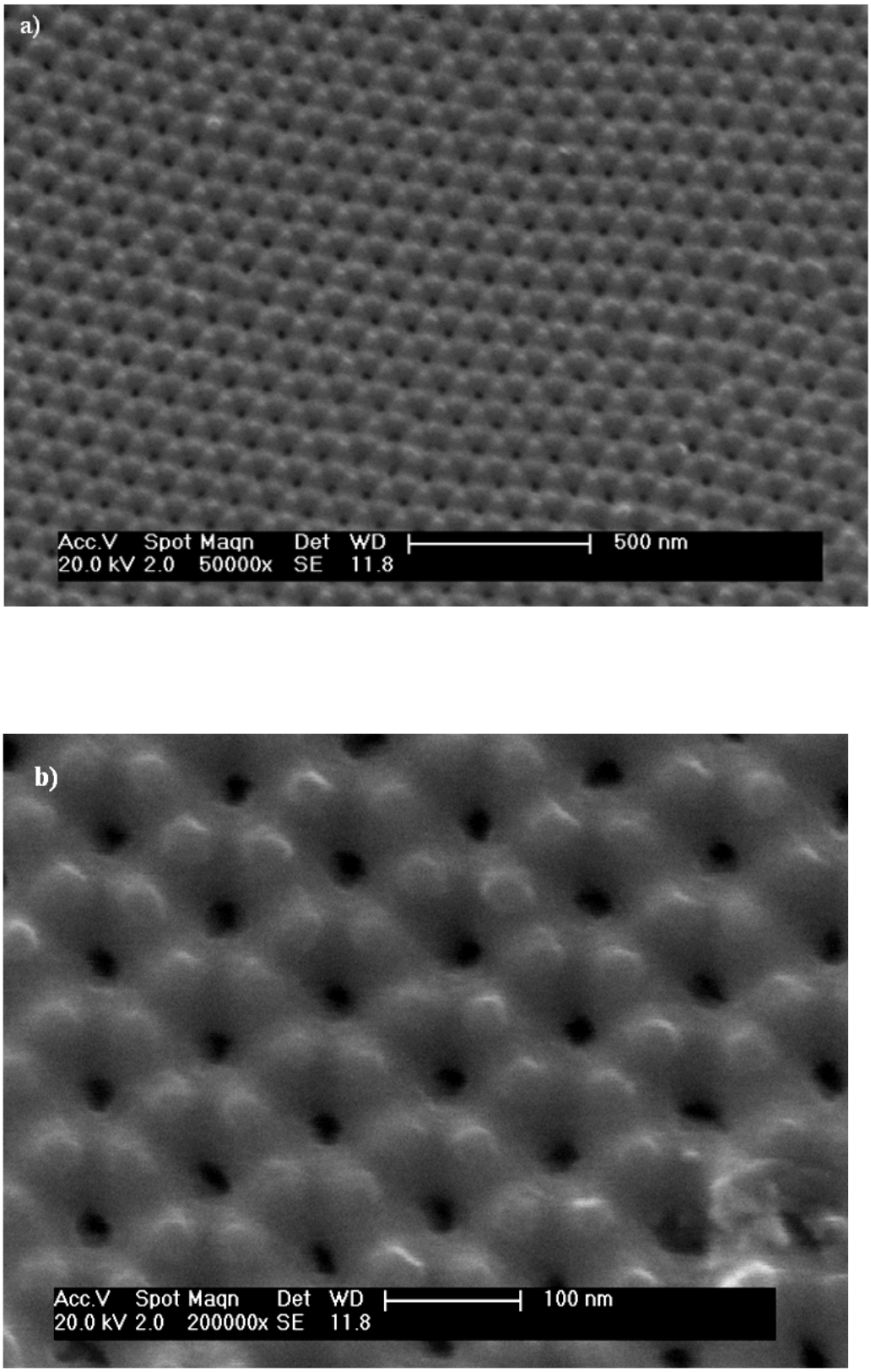

Figure 4.4 *Scanning electron micrographs of the top surface of anodic film formed by four steps anodizing: a) large area anodic films; b) increased magnification.*

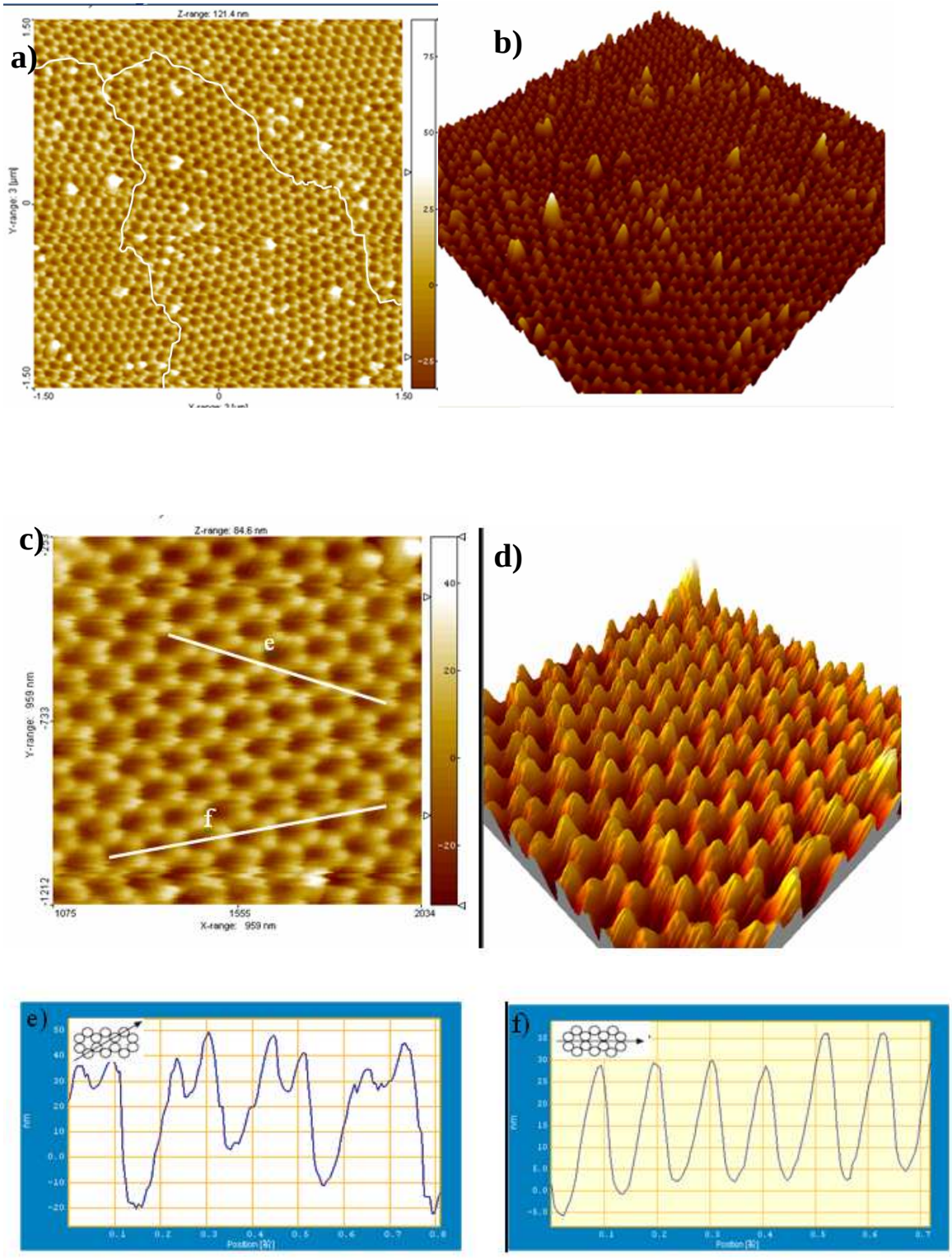

Figure 4.5 *Top surface morphology of anodic films formed: a) AFM image of a large area; b) corresponding 3D AFM image; c) increased magnification AFM image; d) corresponding 3D AFM image; e) and f) surface profiles obtained from AFM.*

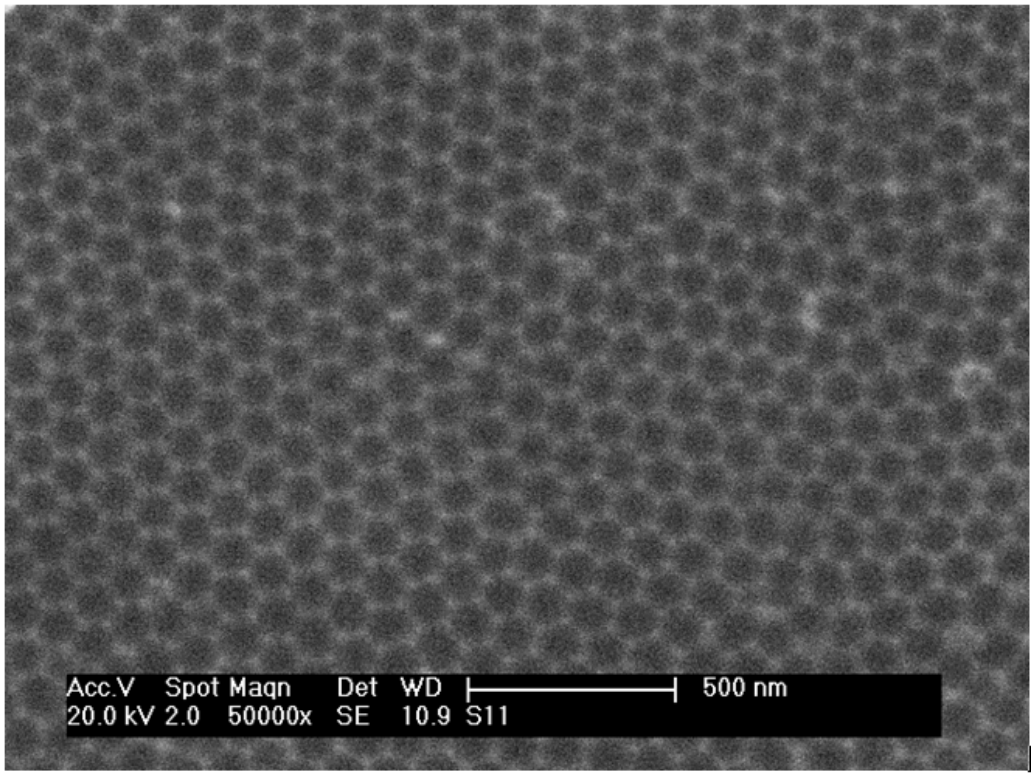

Figure 4.6 *SEM image of the aluminum substrate after removal of the oxide films*

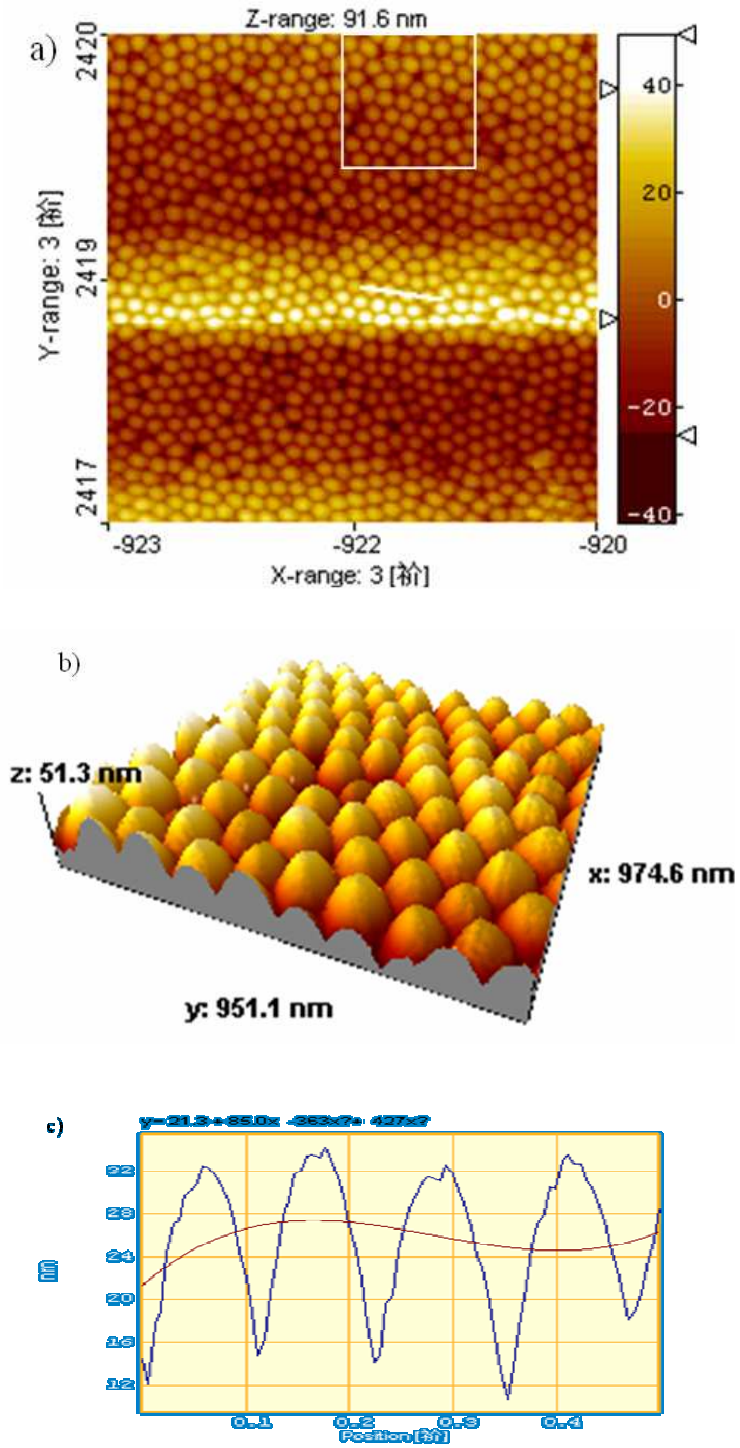

Figure 4.7 *Bottom view of stripped anodic oxide films: a) AFM image of barrier layer oxide films; b) three dimensional illustration of barrier layer oxide film morphology by AFM; c) line scan showing the aluminum/film interface profile.*

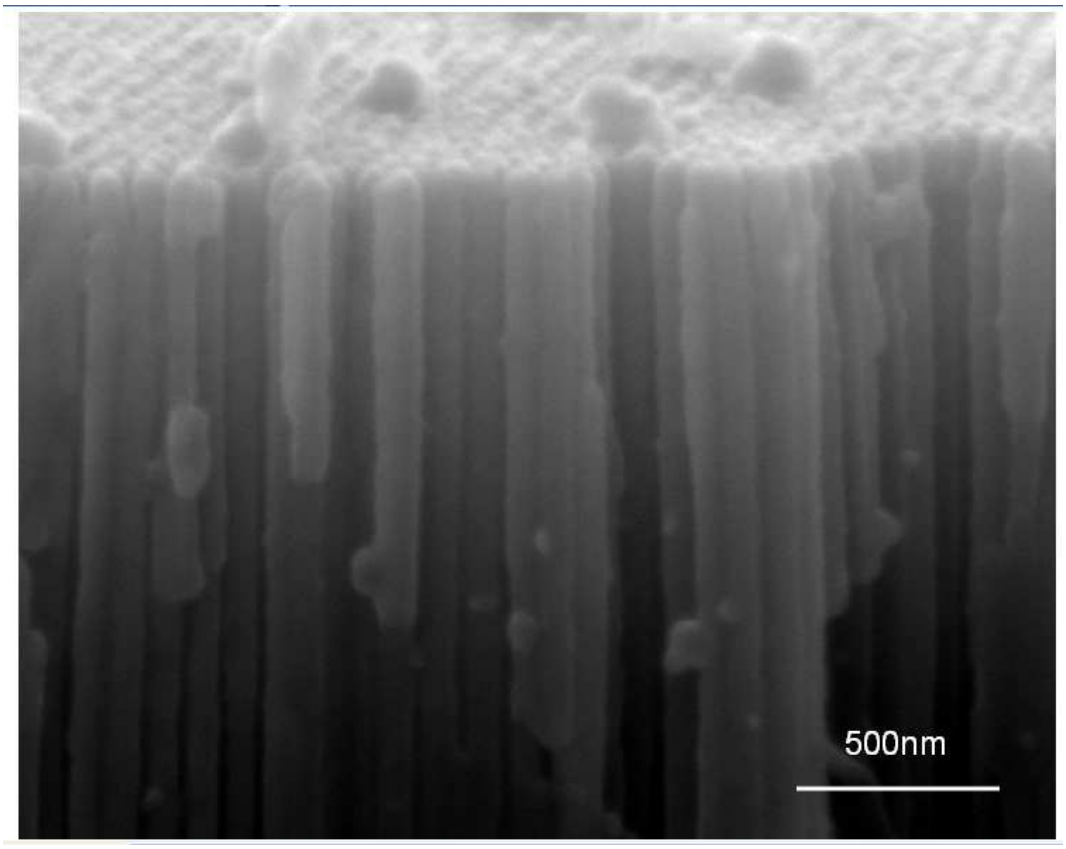

Figure 4.8 *SEM image of the cross session of porous anodic film formed by the second step anodizing in 0.3 M oxalic acid at 40 V at room temperature.*

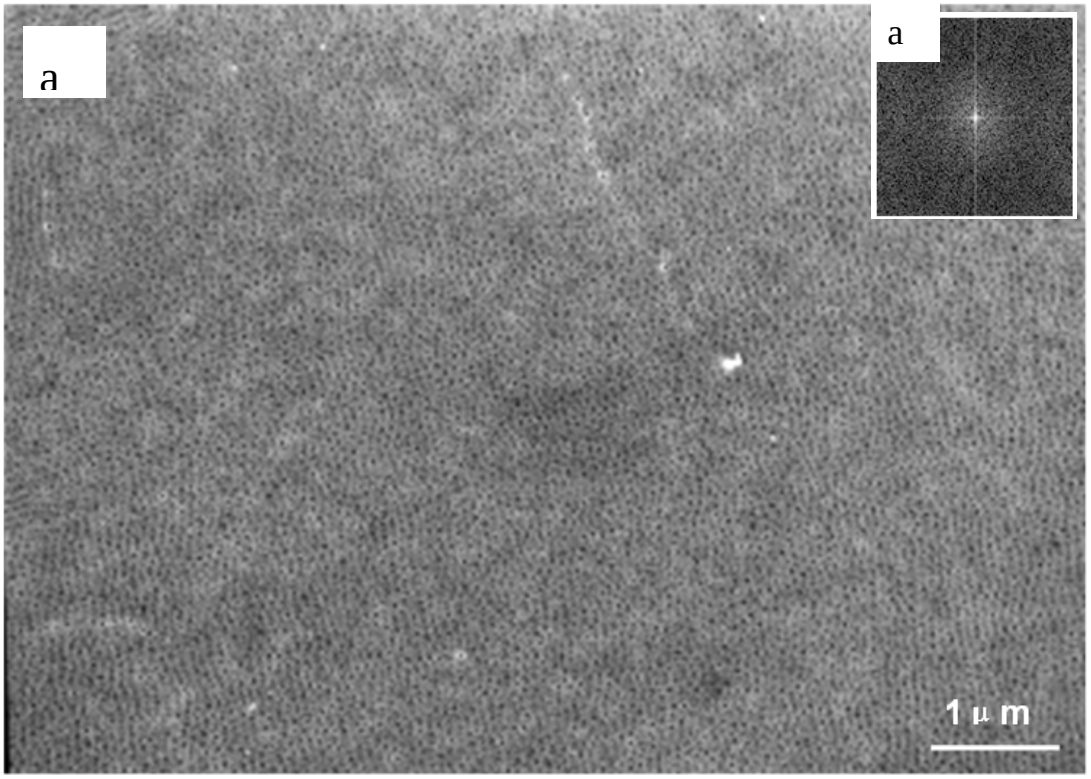
a
a
1 μ m

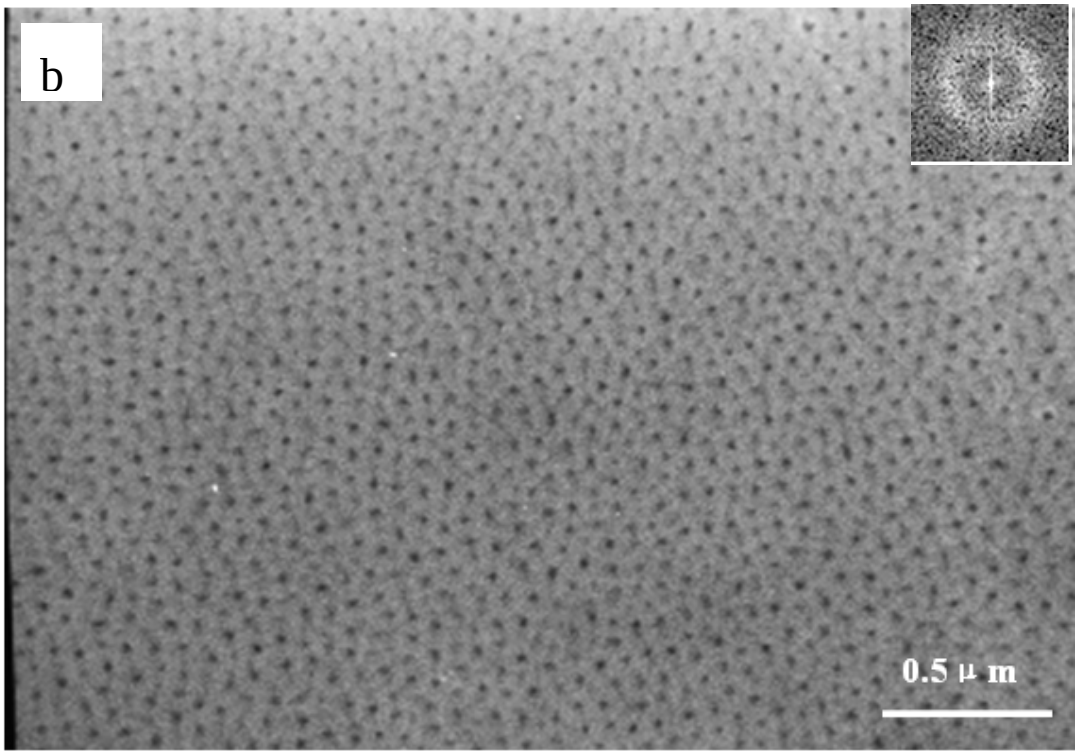
b
0.5 μ m

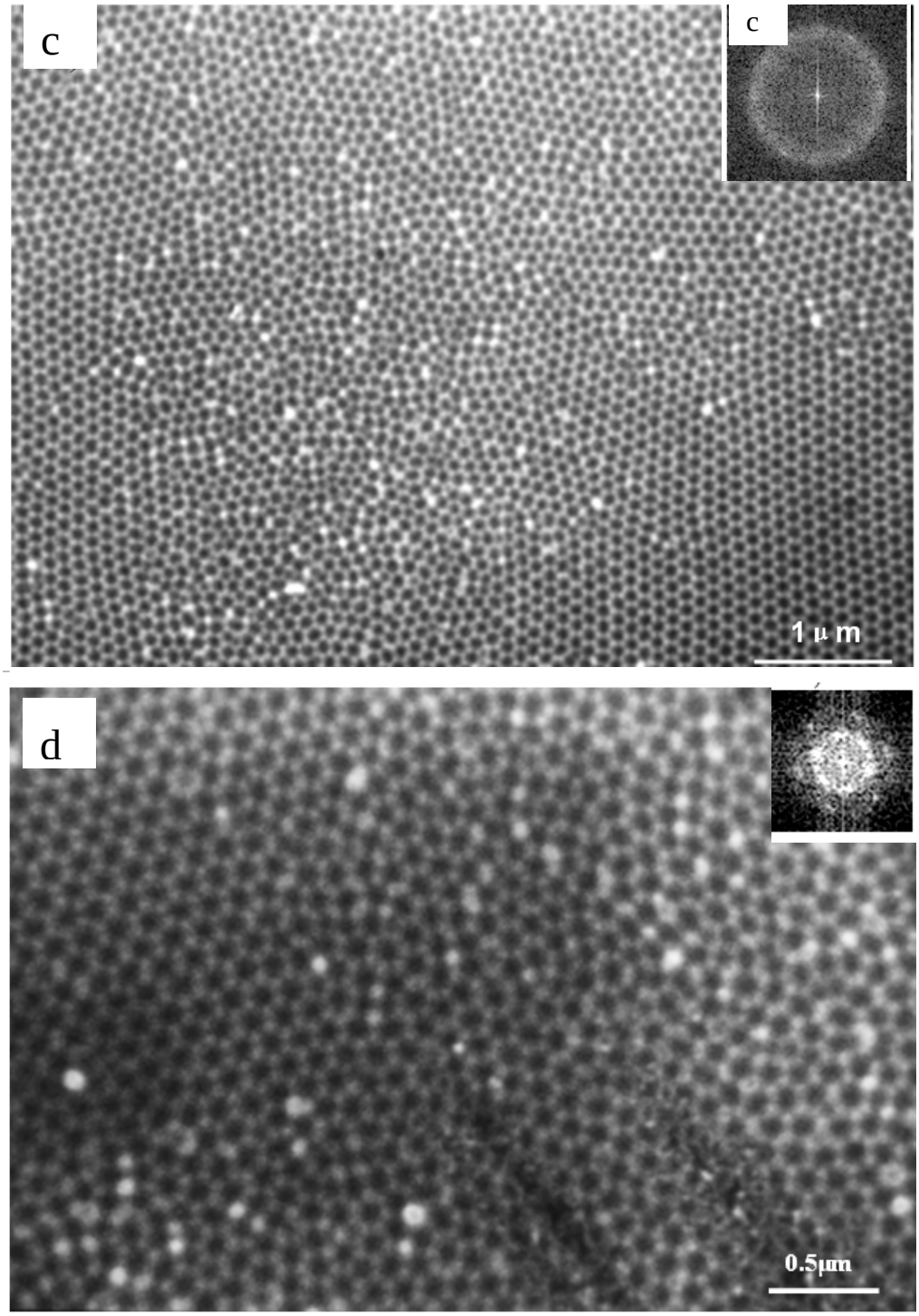
c
c
1 μ m
d
0.5μm

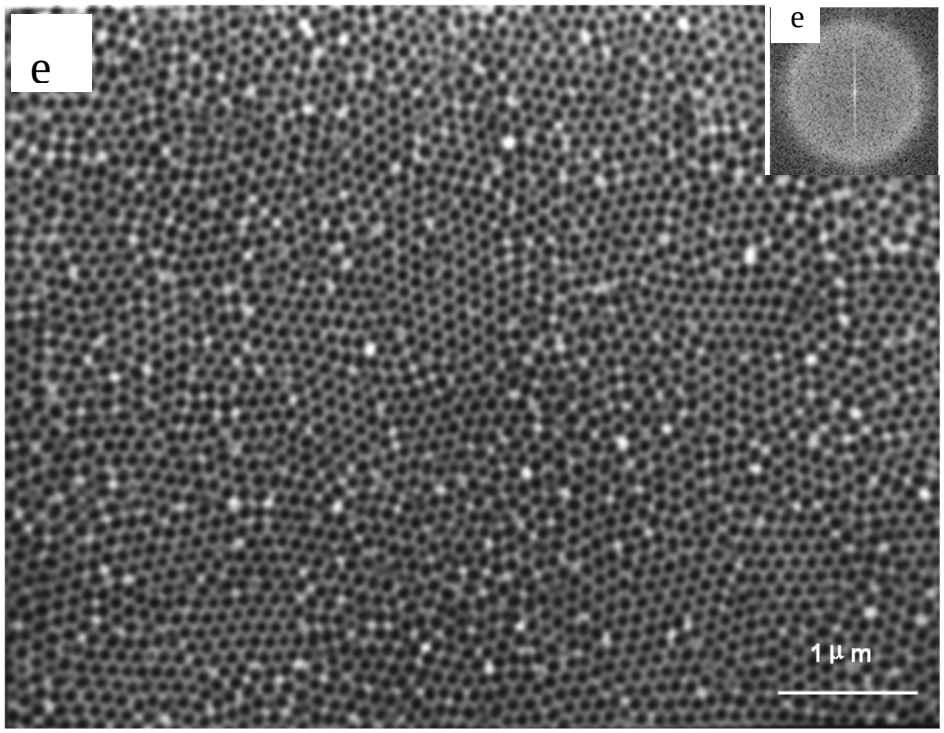
e
e
1 μ m

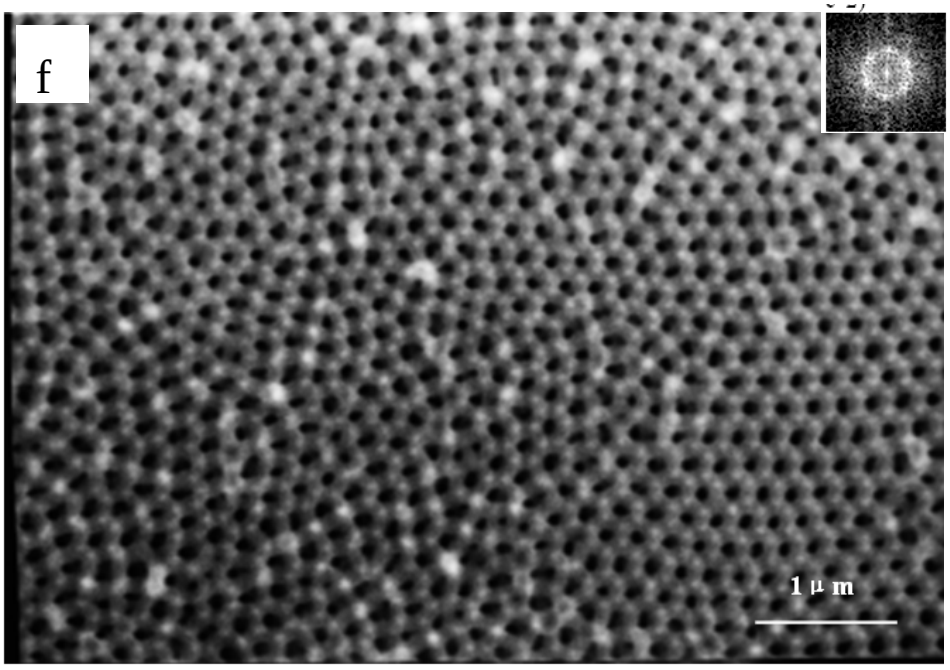
f
1 μ m

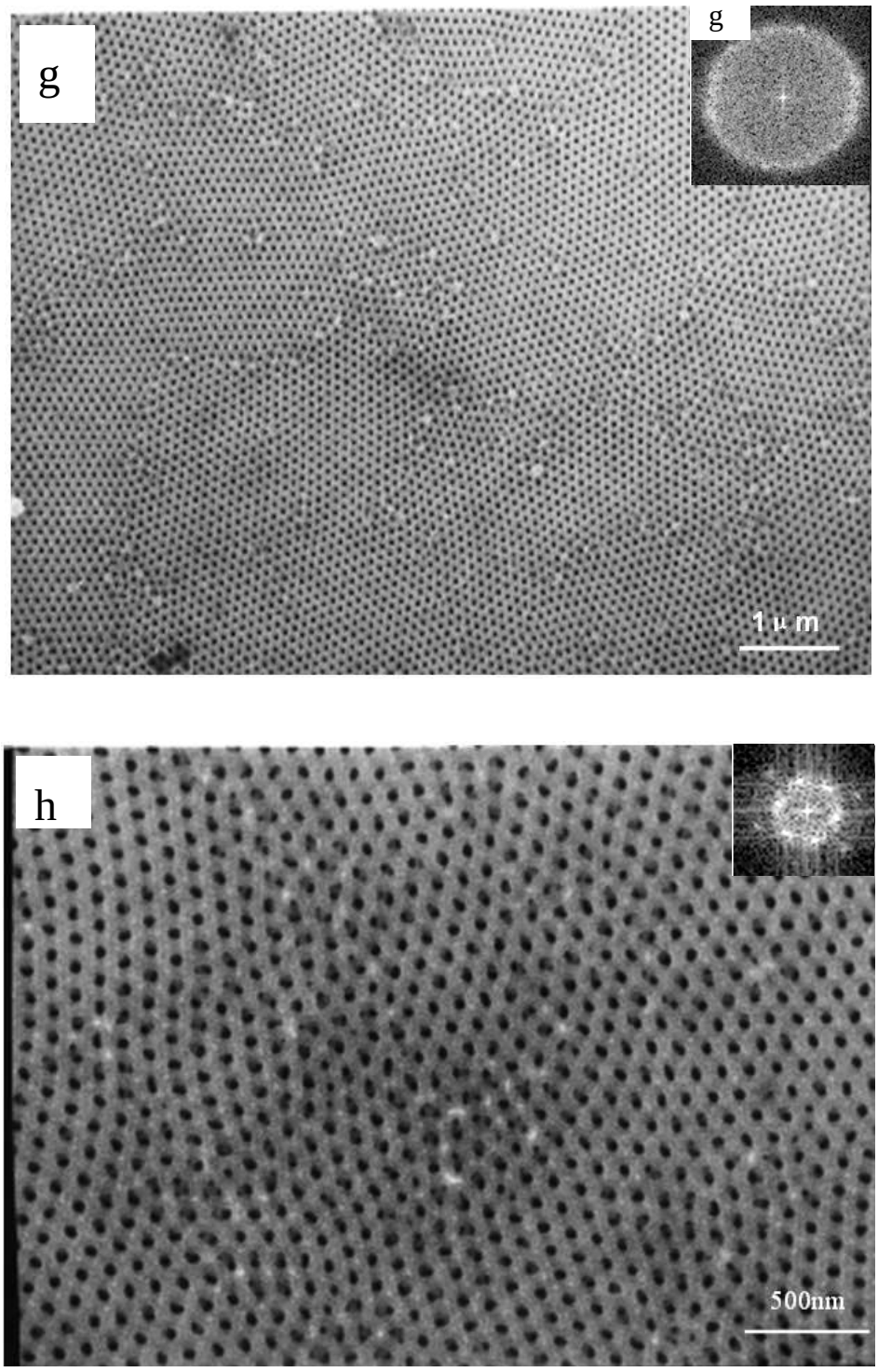

Figure 4.9 *SEM images of the top surfaces of porous anodic films obtained at 40 V in 0.3 M oxalic acid by:*

a) and b) 6 hours one step anodizing;

c) and d) two-steps anodizing with 12h for the first, and 4mins for the second step respectively;

e) and f) two-steps anodizing of 12h for the first, and 30mins for the second step respectively;

g) and h) two-steps anodizing of 12h for the first, and 4h for the second step respectively.

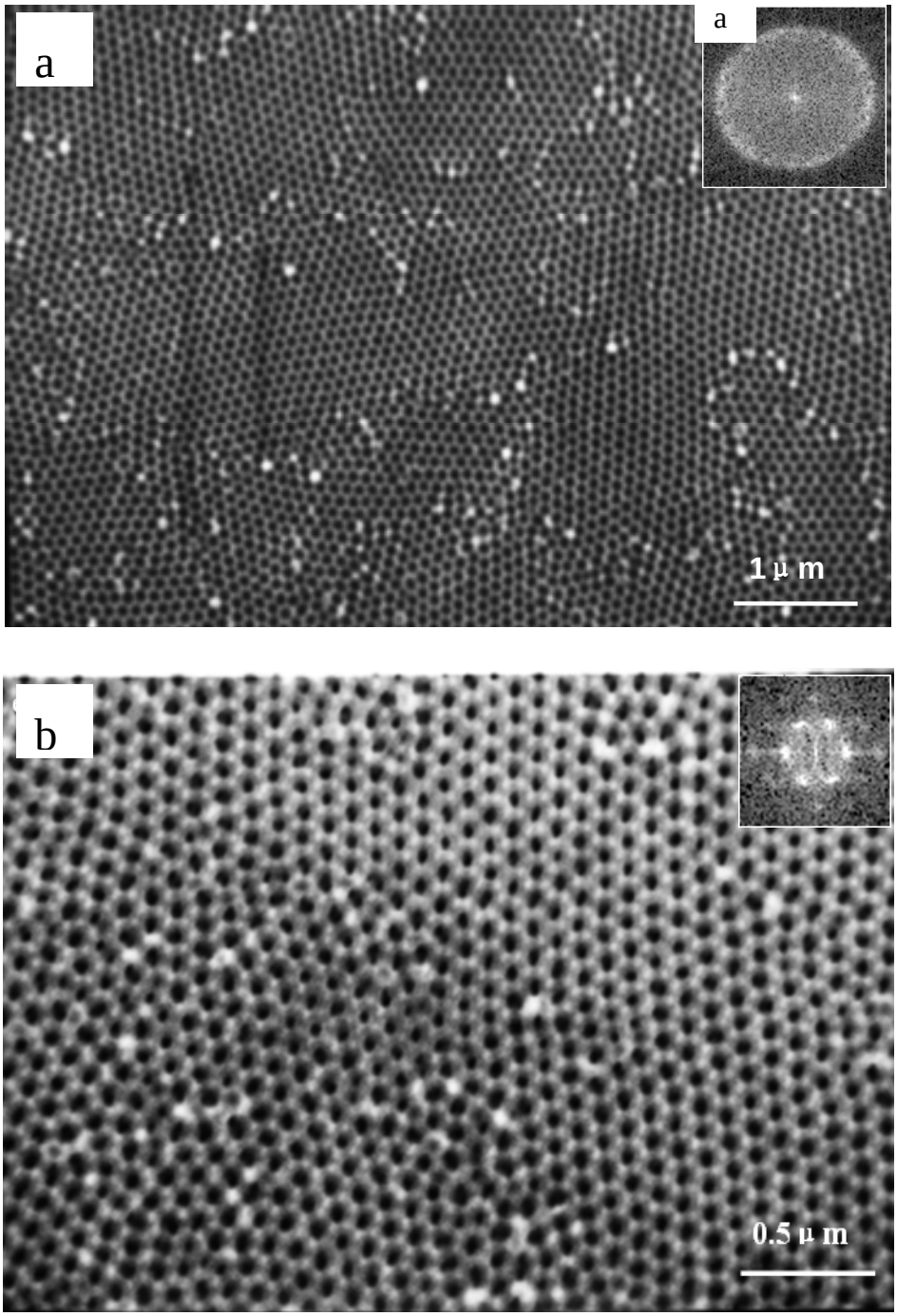

Figure 4.10 *SEM images of the top surfaces of porous anodic oxide films obtained at 40 V in 0.3 M oxalic acid by three-steps anodizing with 12 h for the first step, 4h for the second step and 30mins for the third step respectively.*

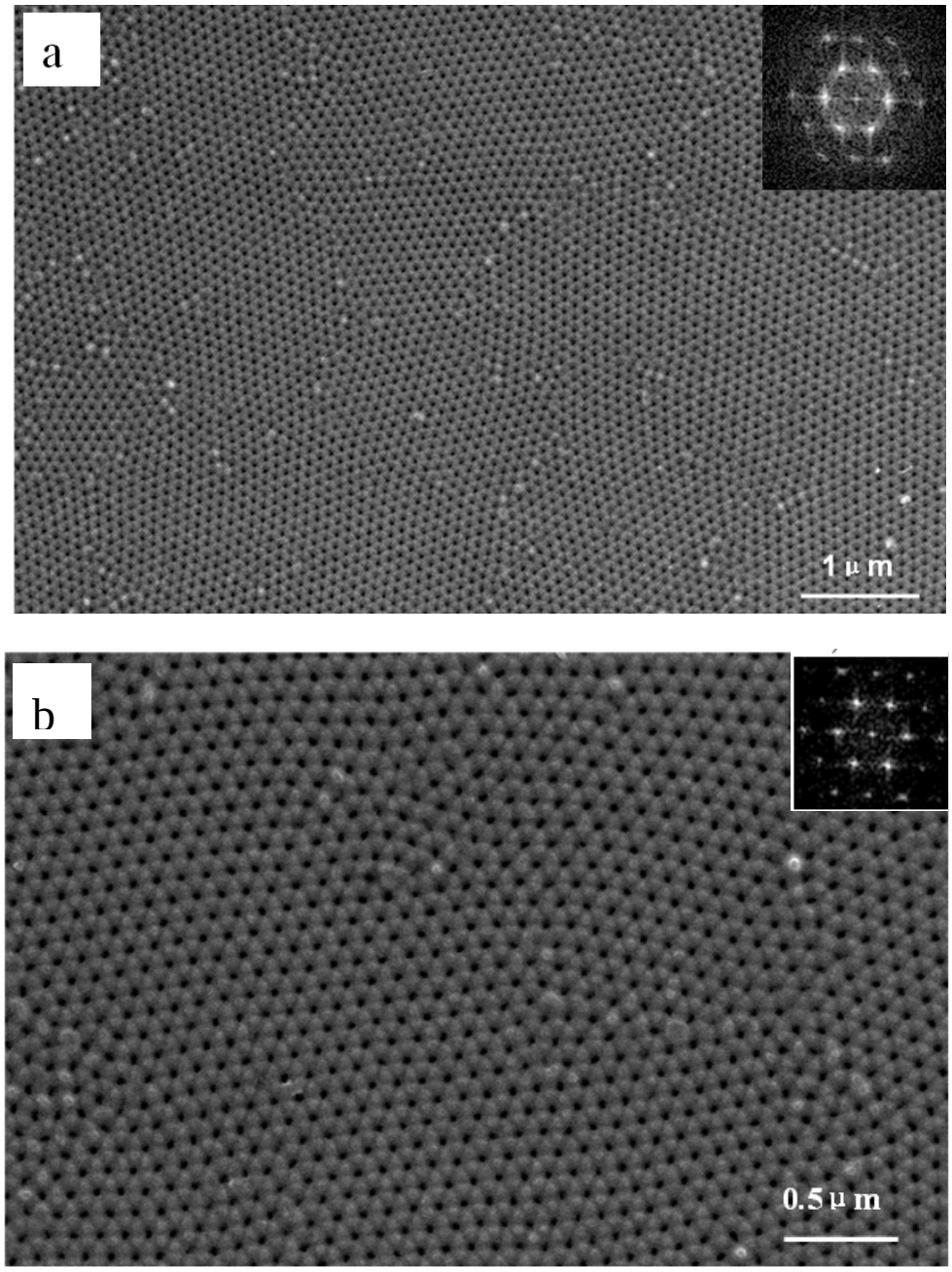

Figure 4.11 *SEM images of the top surfaces of porous anodic films obtained at 40 V in 0.3 M oxalic acid by four steps anodizing of 12 h for the first step, 4h for the second step, 30 mins for the third step and 30mins for the forth steps respectively.*

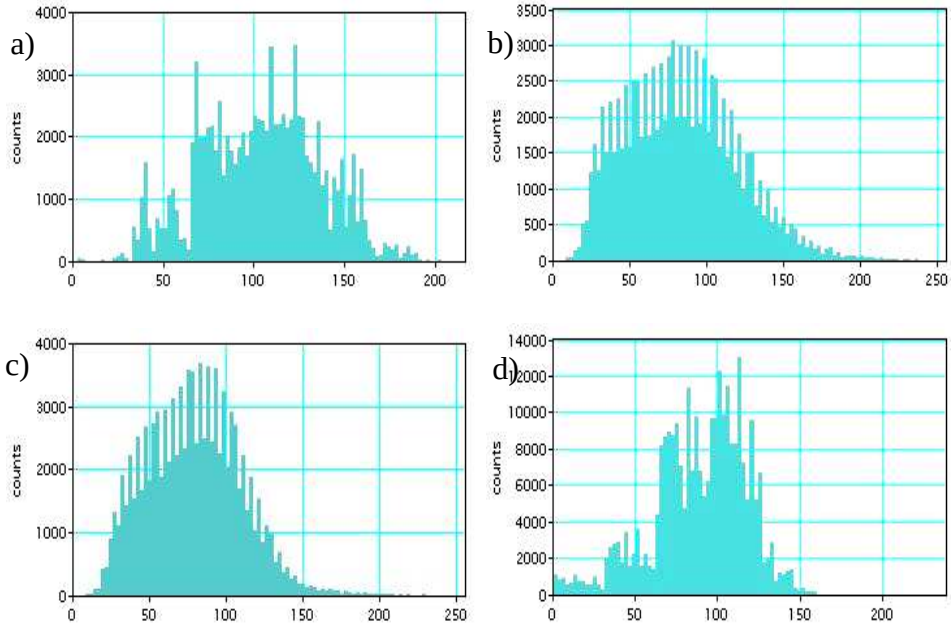

Figure 4.12 *Histograms of anodic cell size distribution of anodic films obtained by multi-steps anodizing (X axis to be interpore distance (nm)):*

a) Two-steps anodizing with 12h for the first and 4mins for the second step respectively;

b) Two-steps anodizing with 12h for the first and 4h for the second step respectively;

c) Three-steps anodizing with 12h for the first step, 4h for the second step and 30mins for the third step respectively;

d) Four-steps anodizing with 12h for the first step, 4h for the second step, 30 minutes for third step and 30 minutes for the forth steps respectively.

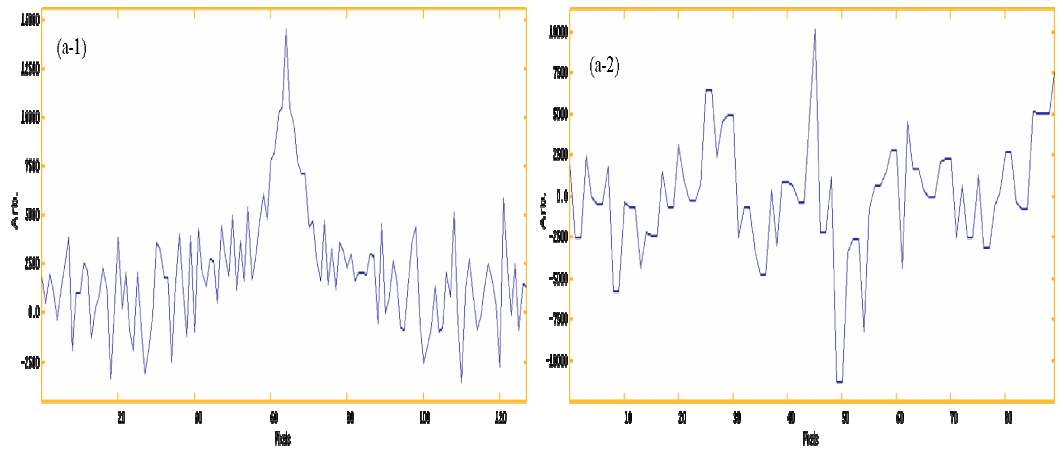

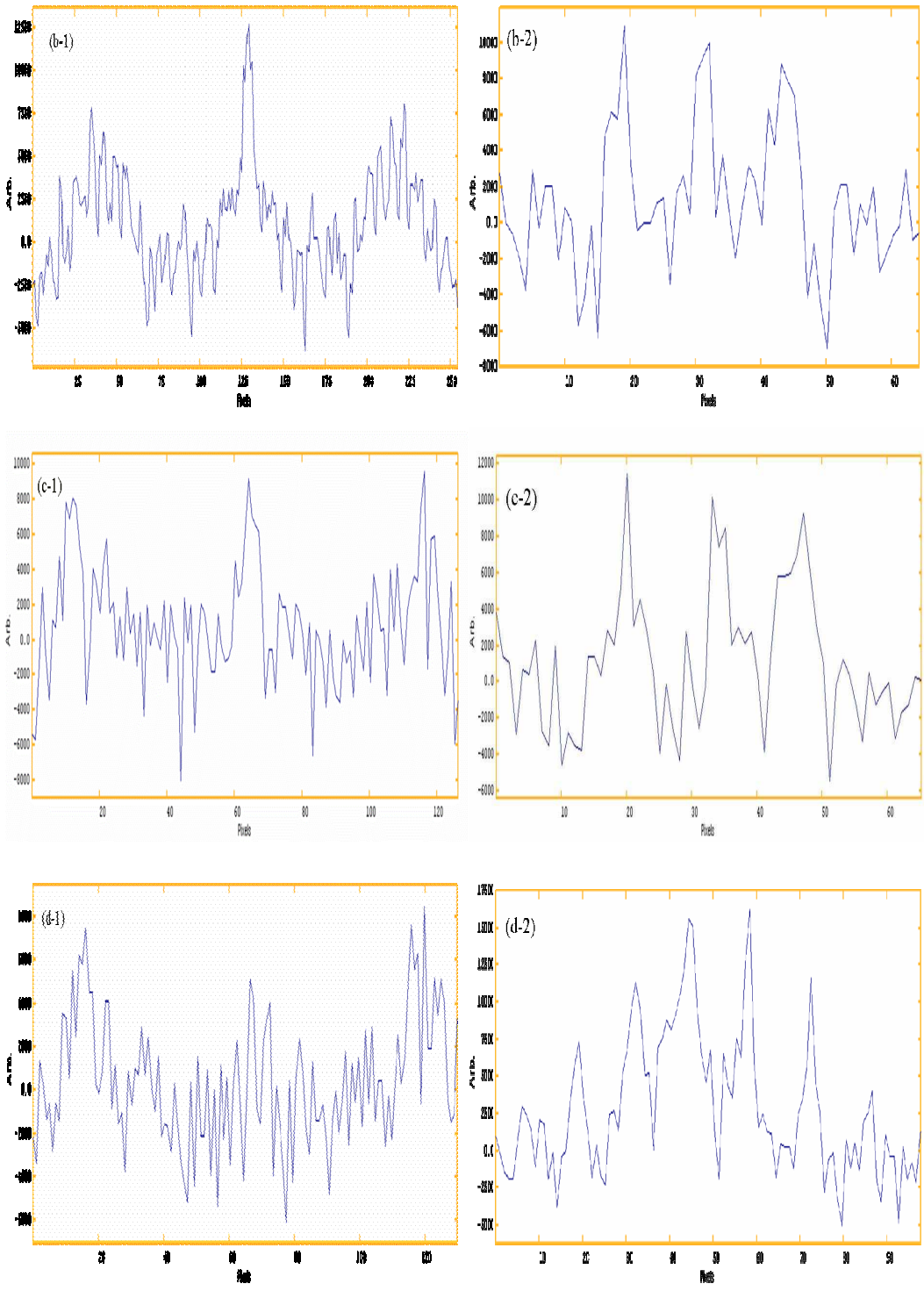
(b-1)
(b-2)
(c-1)
(c-2)
(d-1)
(d-2)

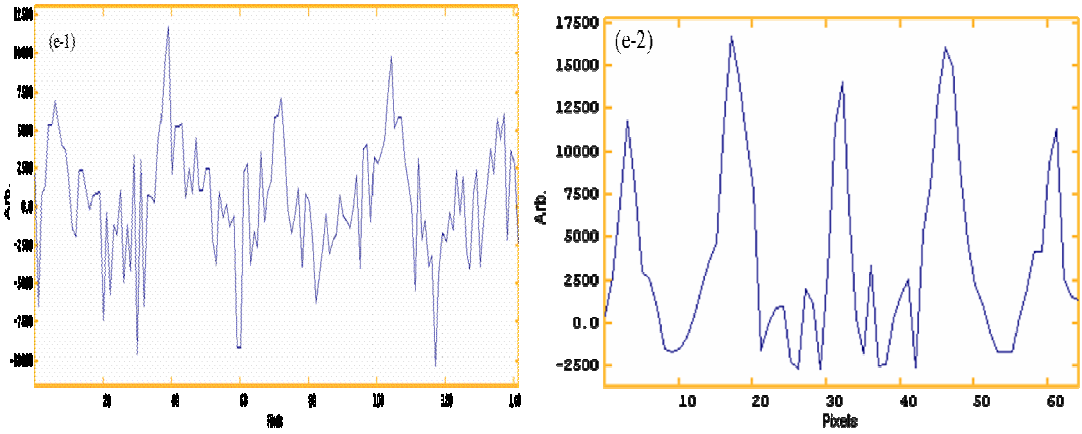

Figure 4.13 *Line scan profiles of FFT images of SEM images of anodic films within an relatively large area (Figure a~e-1) and relatively small area (Figure a~e -2): a) 6 hours one step anodizing; b) two steps anodizing with 12h for the first and 4mins for the second step respectively; c) two steps anodizing with 12h for the first and 4h for the second step respectively; d) three steps anodizing with 12h for the first step, 4h for the second step and 30mins for the third step respectively; e) four steps anodizing with 12h for the first step, 4h for the second step, 30mins for the third step and 30mins for the forth steps respectively.*

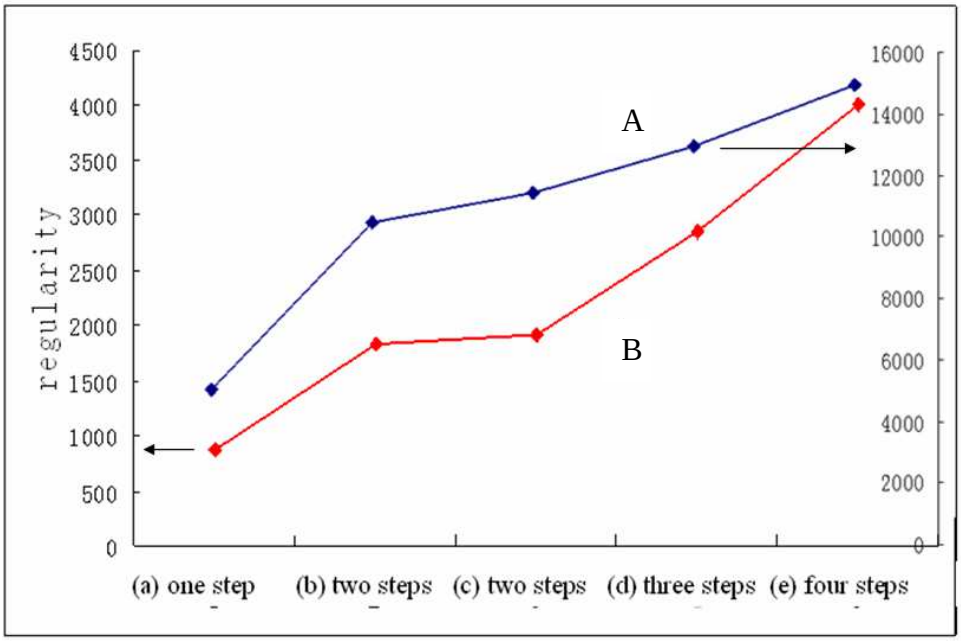

Figure 4.14 *Regularity of the porous structure of the anodic films with multi-steps anodizing a) regularity of anodic oxide films over a relative large area; b) regularity of anodic oxide films over a relative small area.*

.


a)
1μm

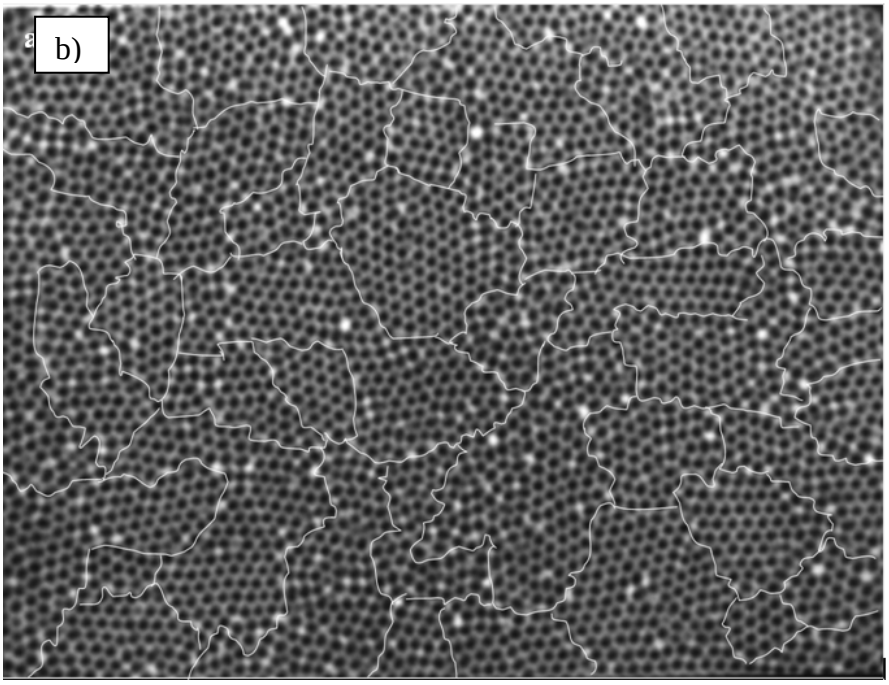
b)

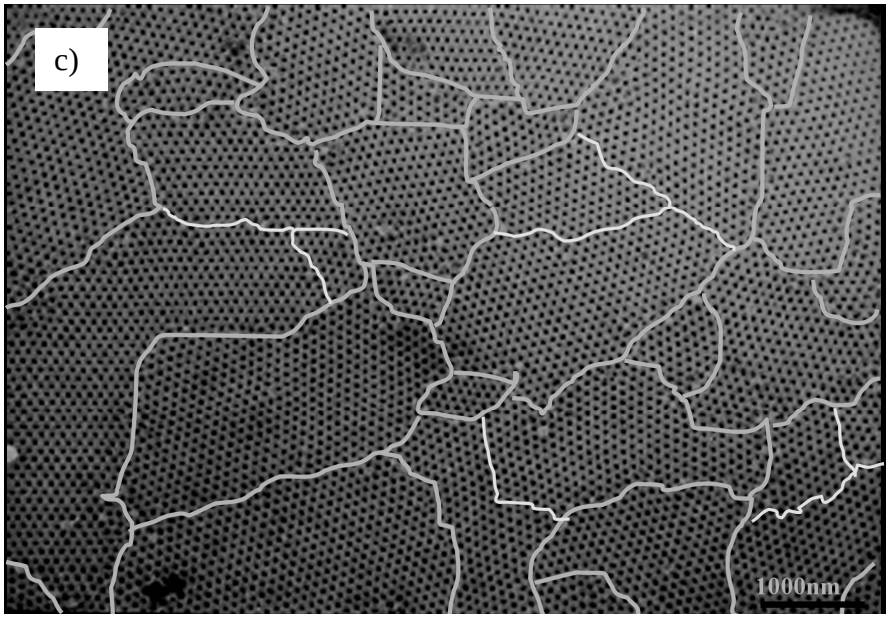
c)
1000nm

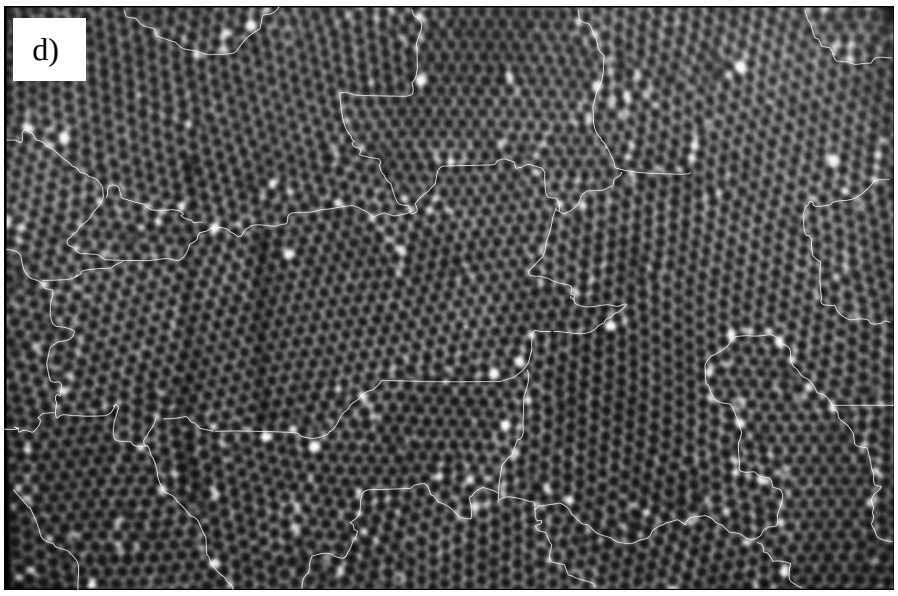
d)

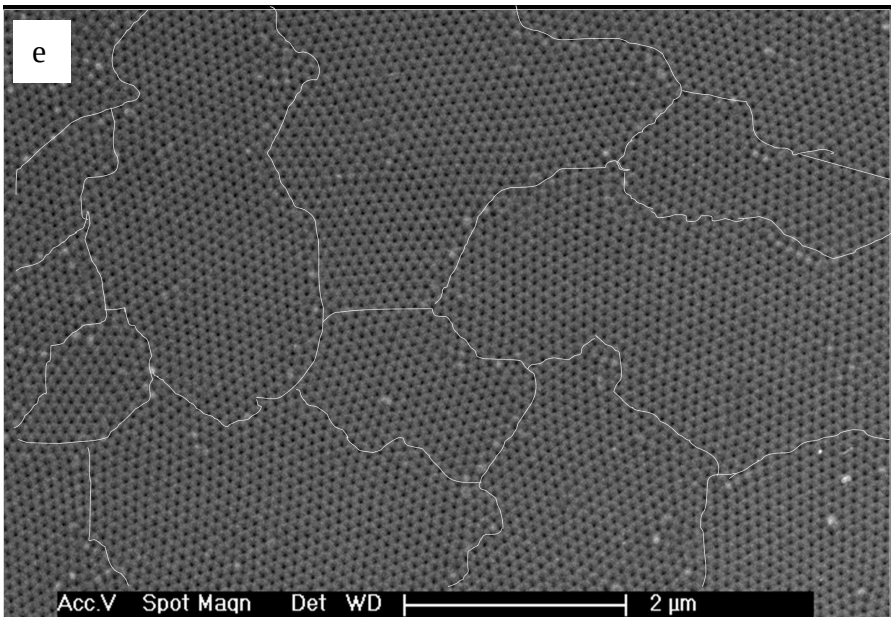

Figure 4.15 *SEM images of anodic oxide films obtained by different conditions with orientation domains outlined:*
a) Two steps anodizing with 12h for the first step ,and 4mins for the second step respectively;
b) Two steps anodizing with 12h for the first step, and 30 minutes for the second step respectively;
c) Two steps anodizing with 12h for the first step, and 4 hours for the second step respectively;
d) Three steps anodizing with 12h for the first step, 4h for the second step and 30mins for the third step respectively;
e) Four steps anodizing with 12h for the first step, 4h for the second step, 30 minutes for third step and 30 minutes for the forth steps respectively.

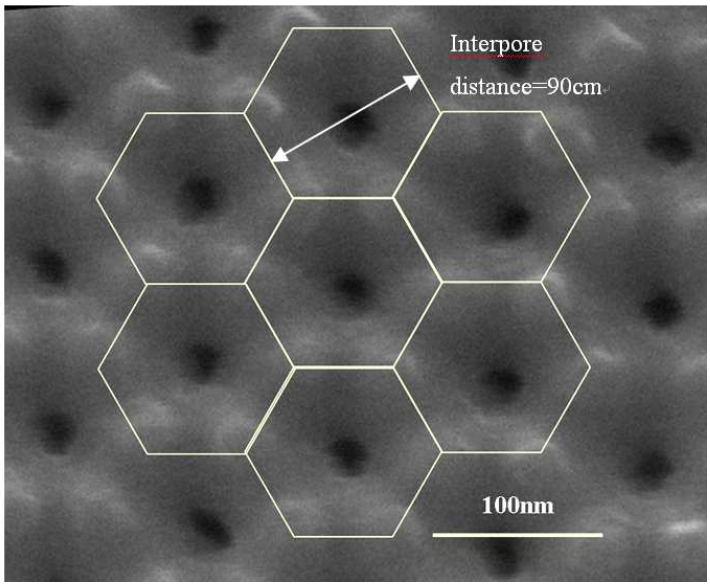

Figure 4.16 *Illustration of pore area calculation.*

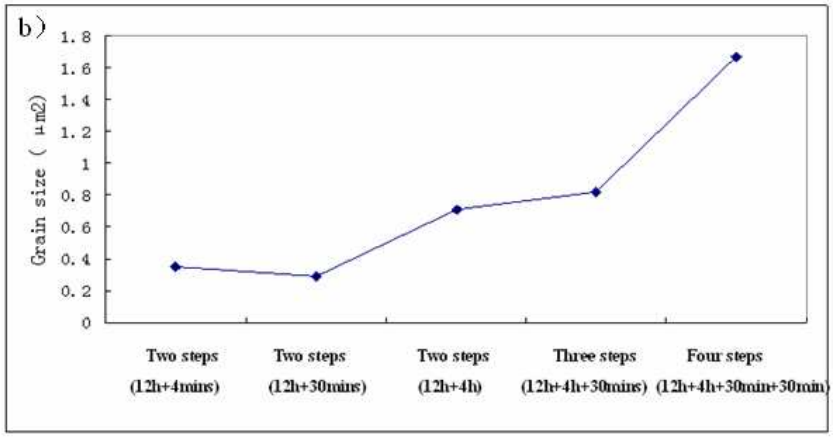

Figure 4.17 *Variation of orientation domain size under different anodizing conditions.*

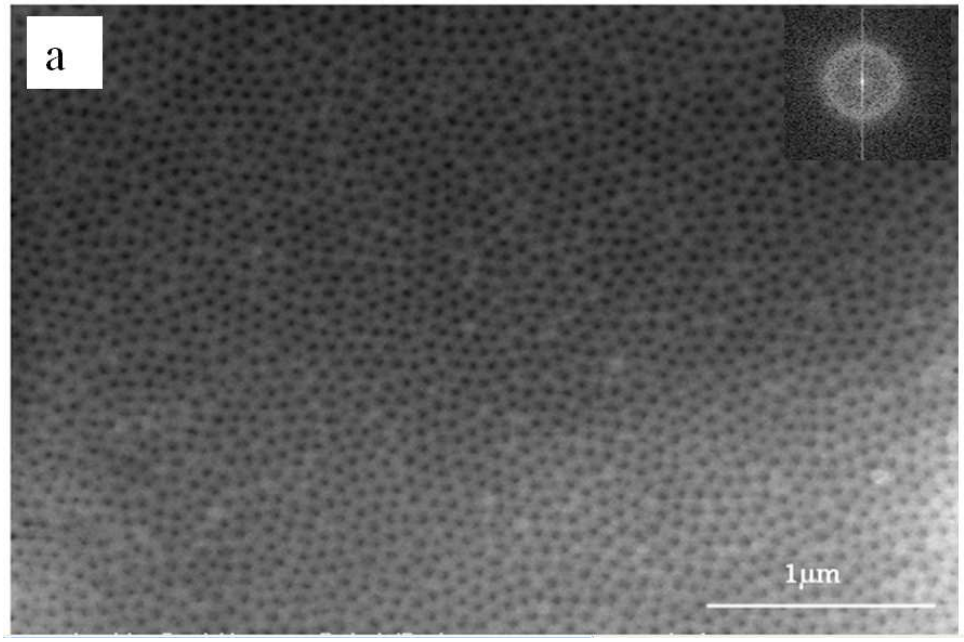
a
1μm

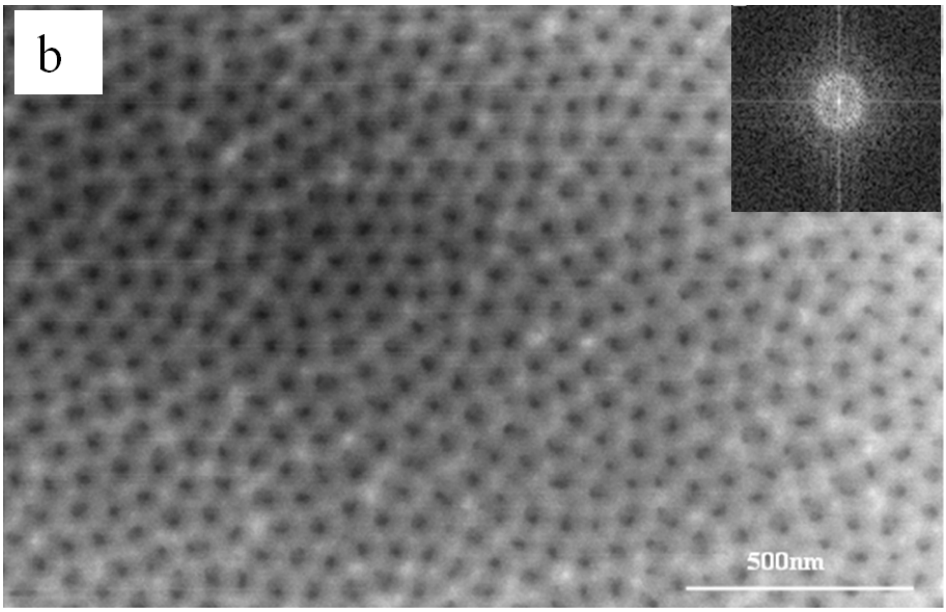
b
500nm

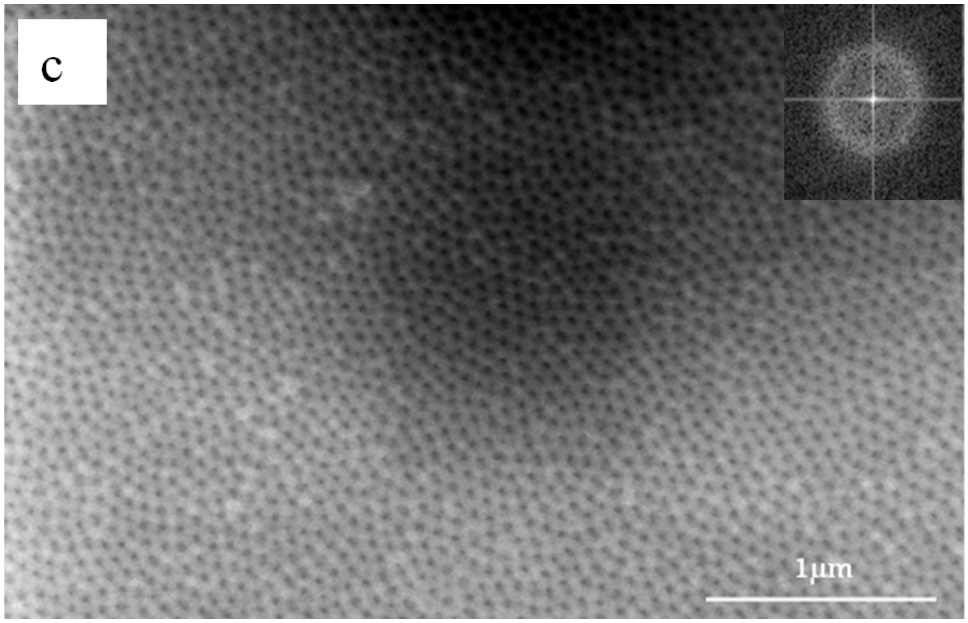

Figure 4.18 *SEM images of top surface and corresponding FFT images of anodic oxide films with following anodizing conditions: a) 30 V voltage and 0.2 M Oxalic acid; b) 30 V voltage and 0.3M oxalic acid; c) 30 V voltage and 0.5 M oxalic acid.*

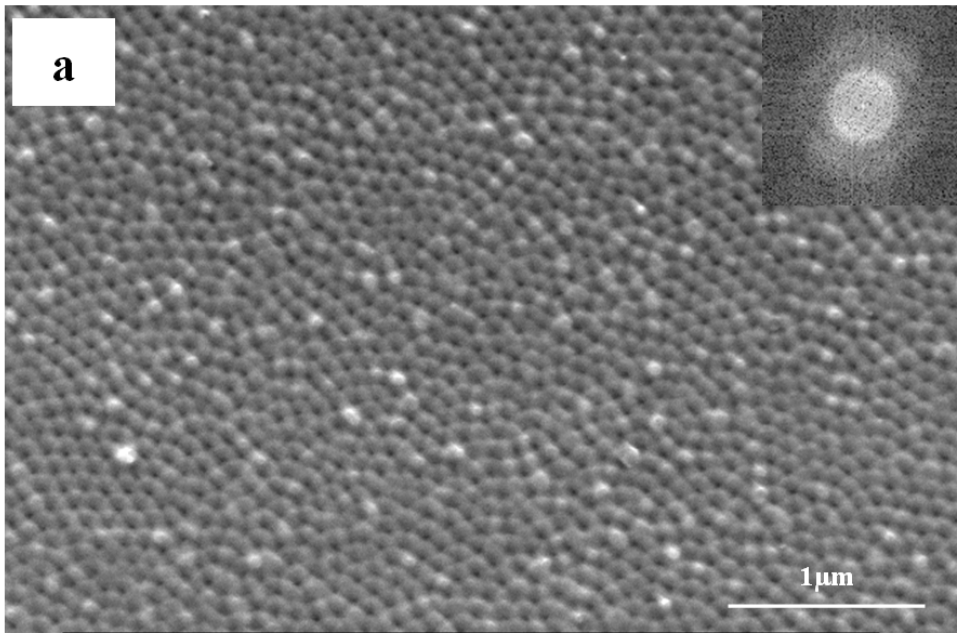

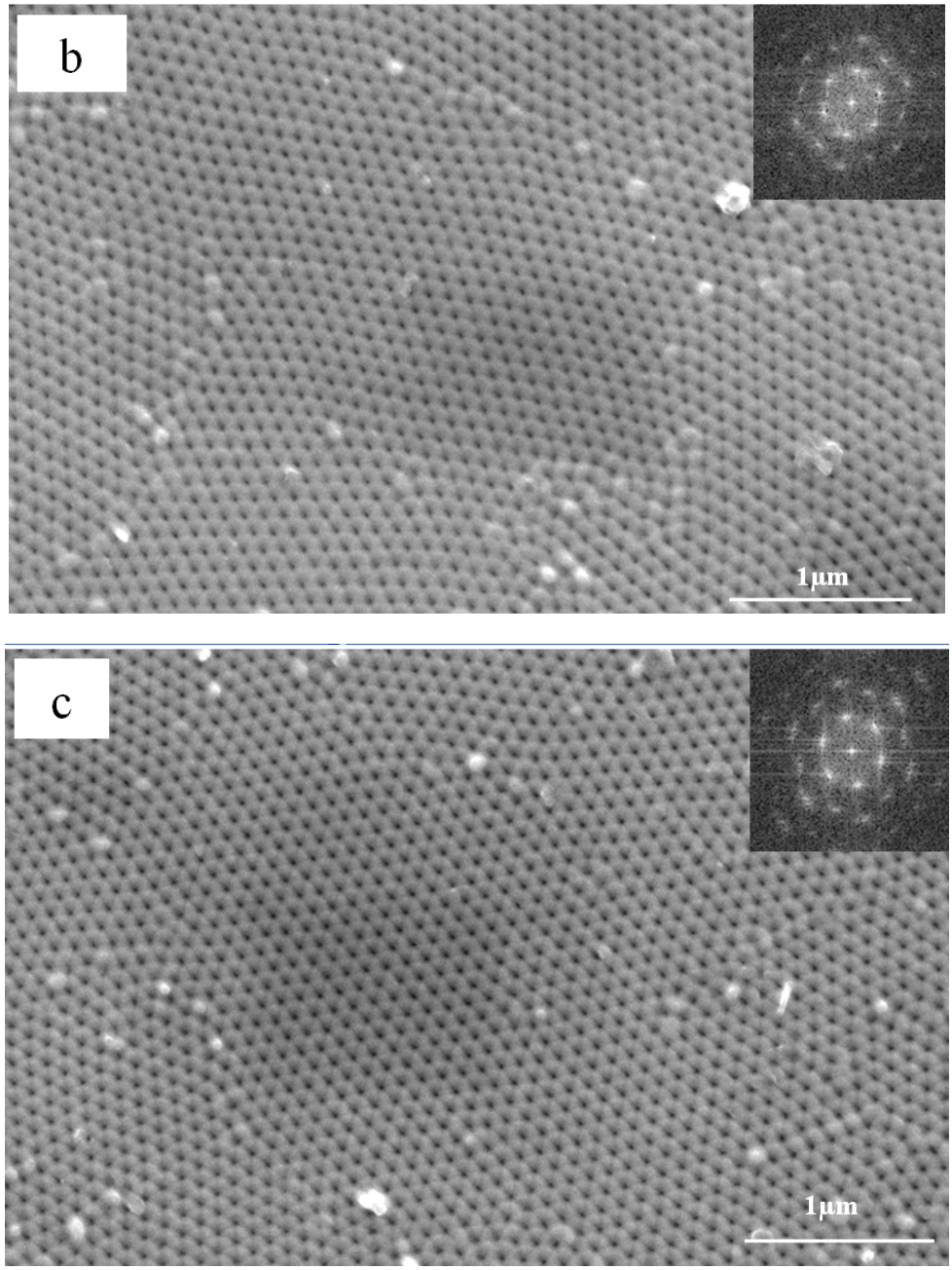

Figure 4.19 *SEM images of top surface and corresponding FFT images of anodic oxide films with following anodizing conditions: a) 40 V voltage and 0.3 M Oxalic acid; b) 40 V voltage and 0.4M oxalic acid; c) 40 V voltage and 0.5 M oxalic acid.*

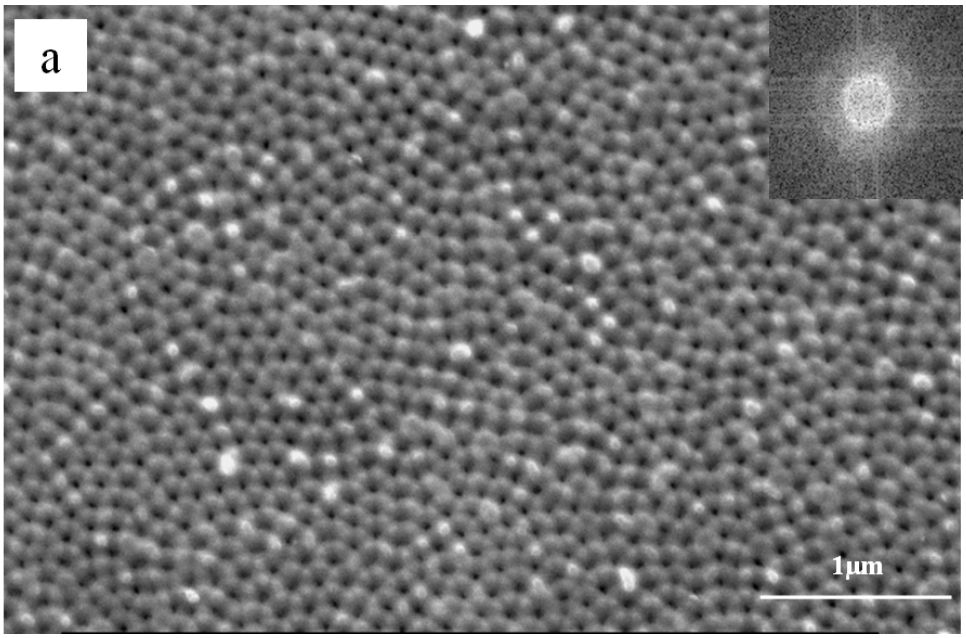
a
1μm

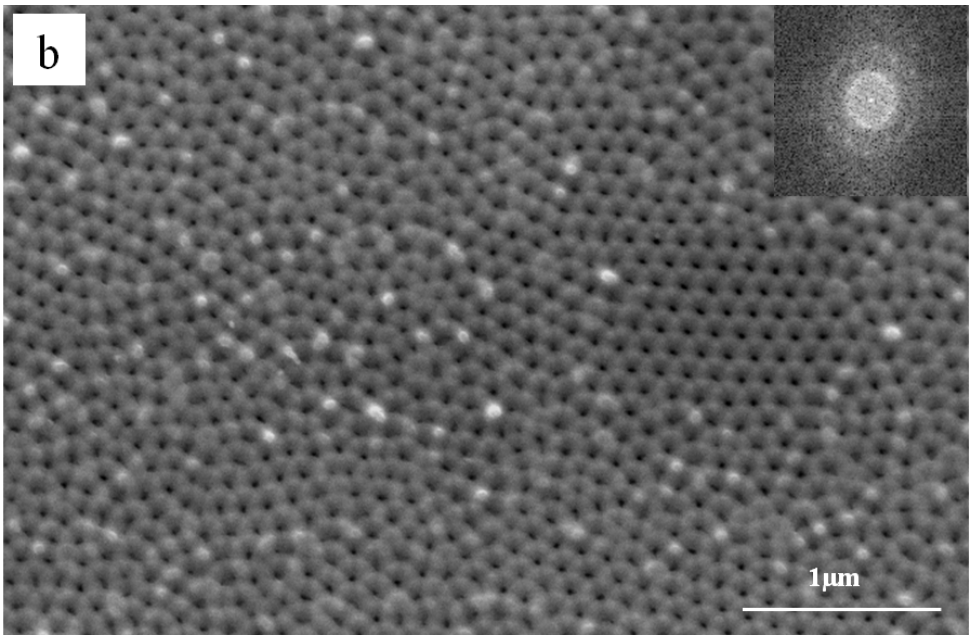
b
1μm

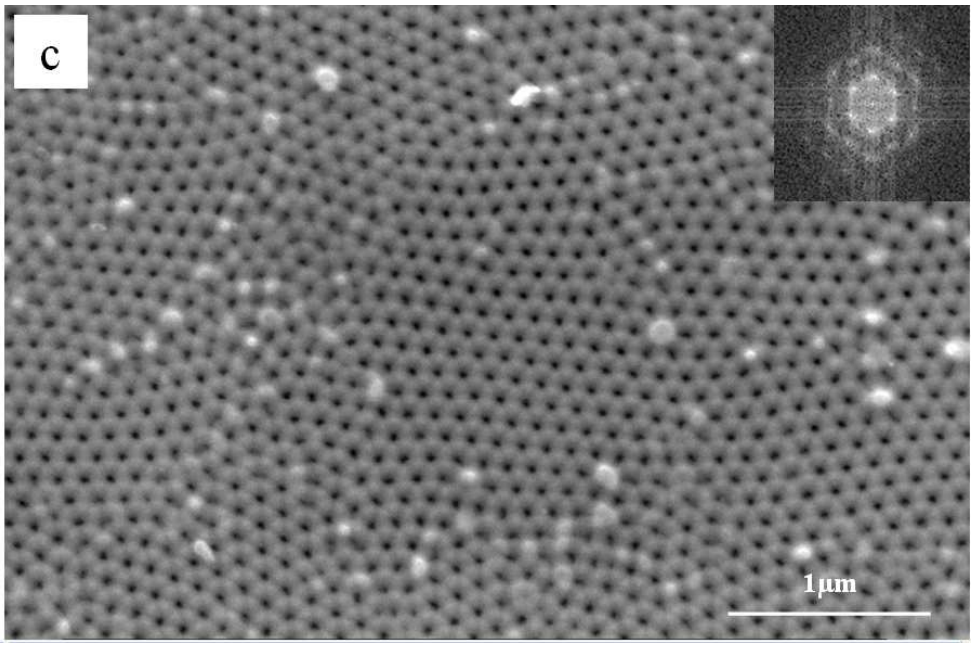

Figure 4.20 *SEM images of top view and corresponding FFT images of anodic oxide films with following anodizing conditions: a) 30 V voltage and 0.3 M Oxalic acid; b) 50 V voltage and 0.4 M oxalic acid; c) 50 V voltage and 0.5 M oxalic acid.*

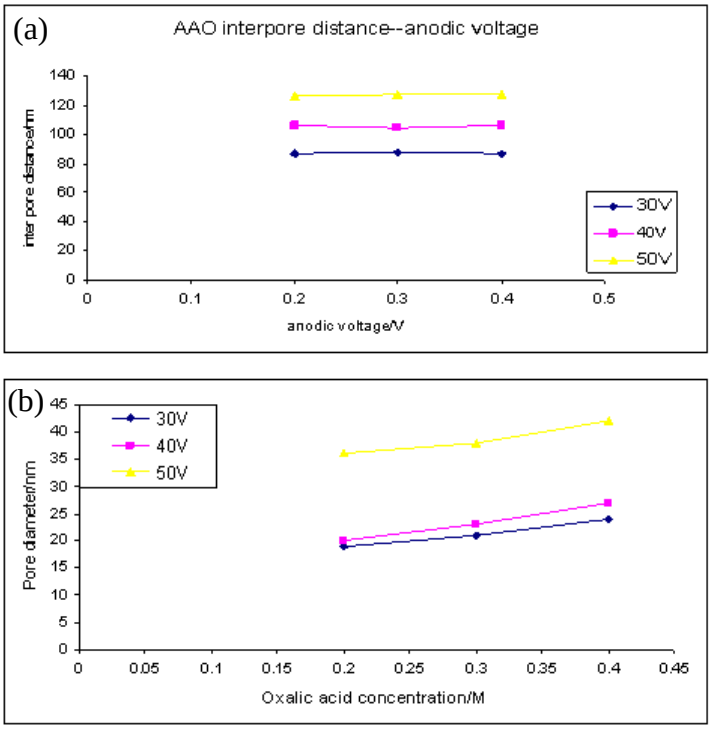

Figure 4.21 *Interpore distance (a) and pore diameter (b) variation as function of anodizing voltage and oxalic acid concentration.*

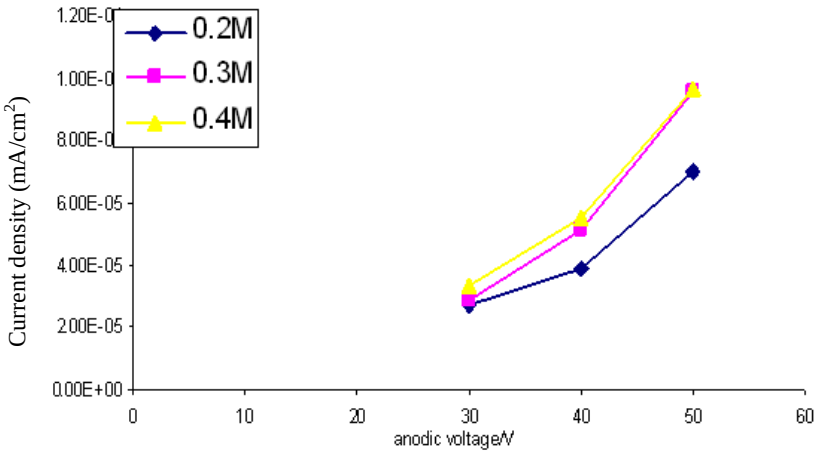

Figure 4.22 *Current density variation via anodizing voltage under various electrolyte concentrations.*

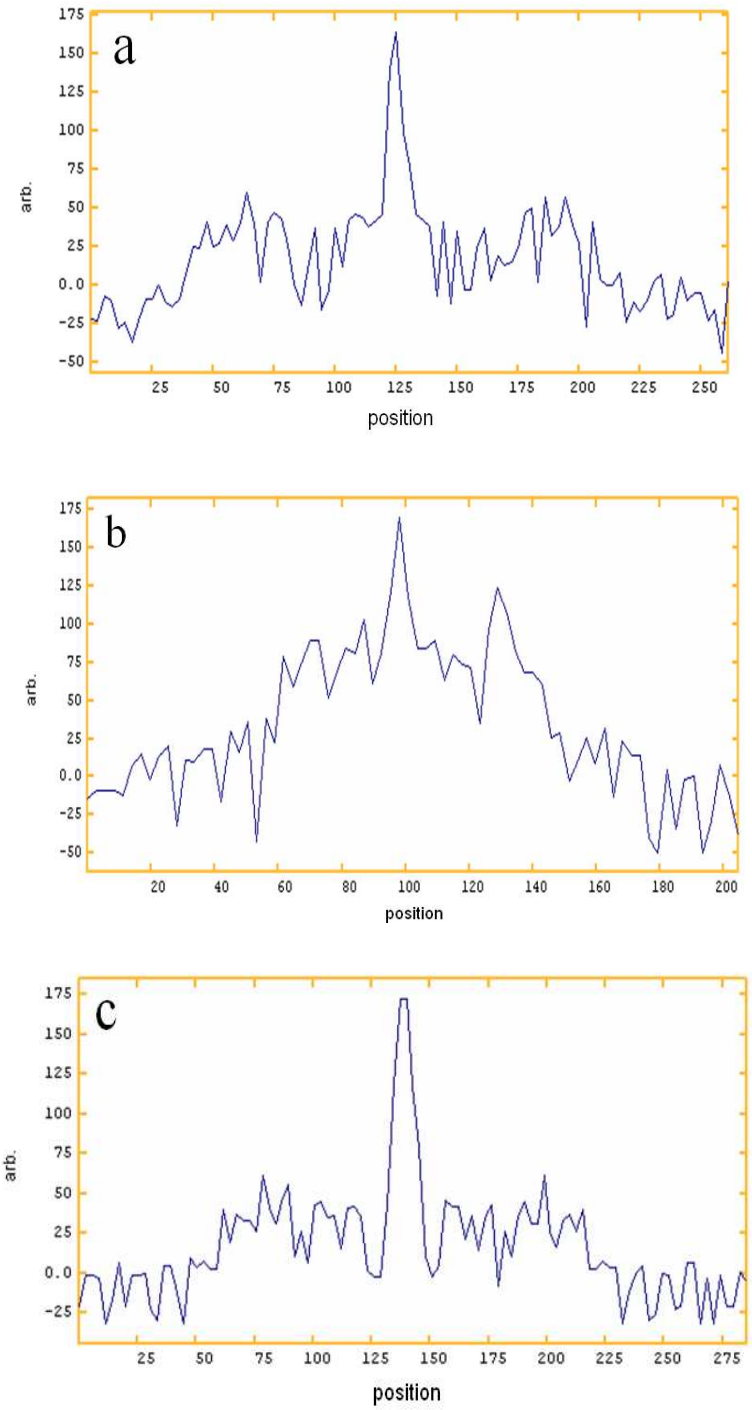
a
b
c
arb.
position

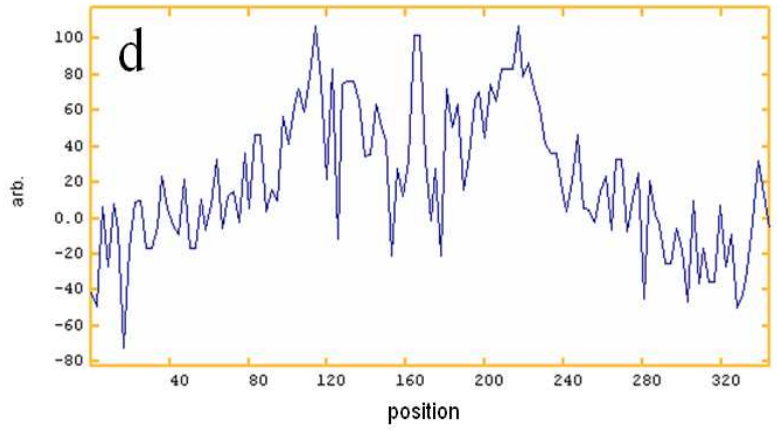
d
arb.
position

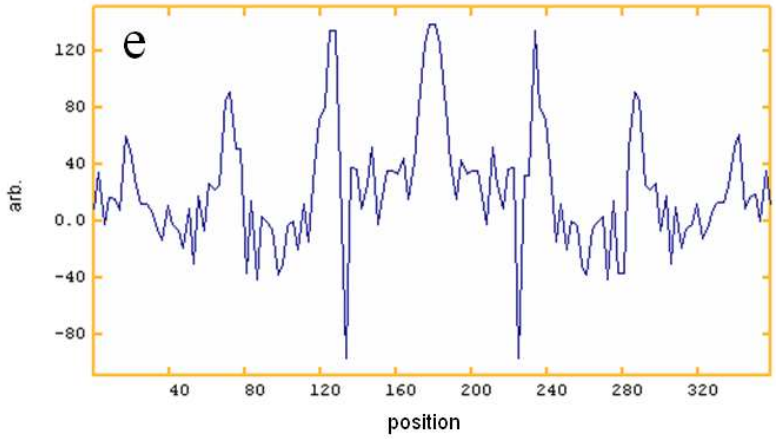
e
arb.
position

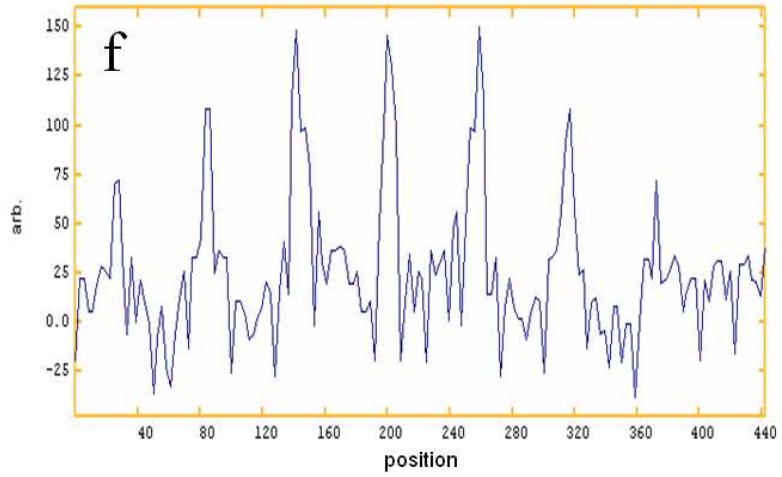
f
arb.
position

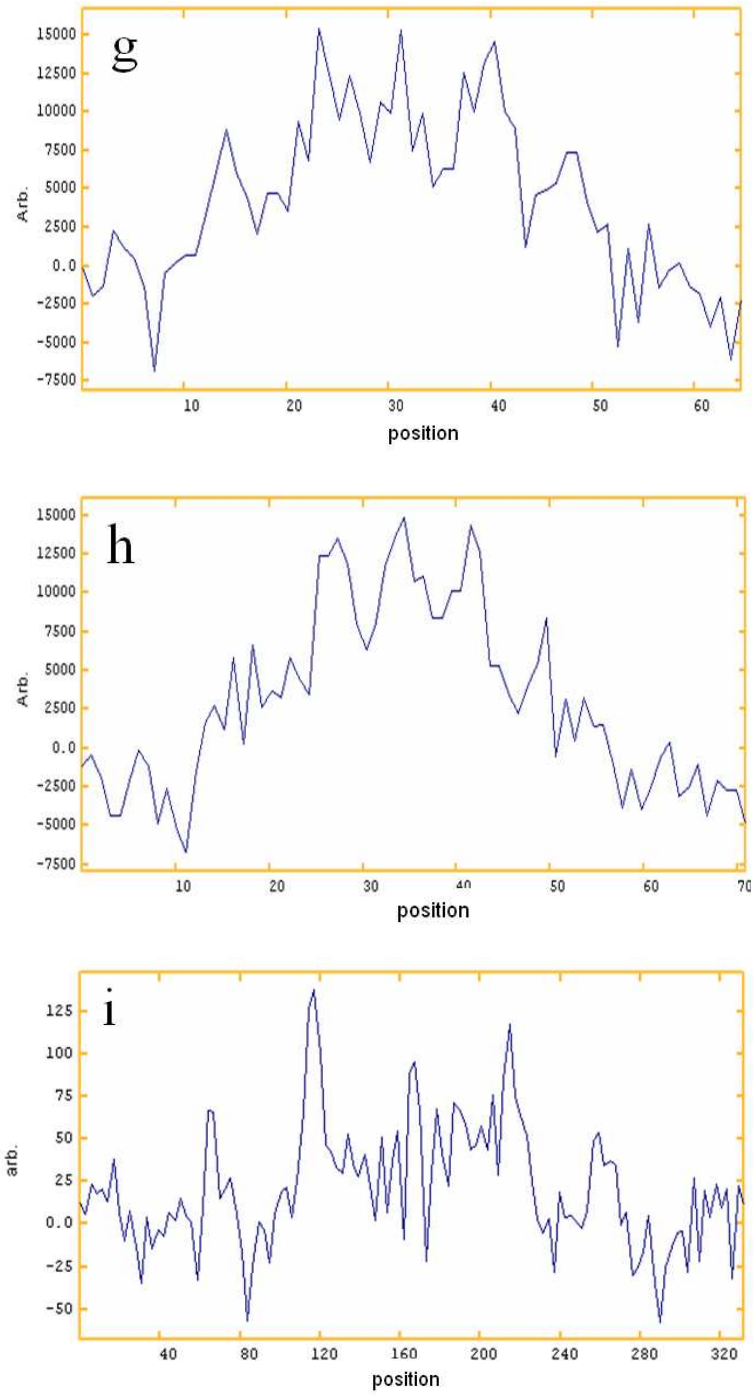

Figure 4.23 *Line scan profile of FFT image of SEM images of films obtained in following conditions: a) 30 V voltage and 0.2 M Oxalic acid; b) 30 V voltage and 0.3M oxalic acid; c) 30 V voltage and 0.5 M oxalic acid; d) 40 V voltage and 0.3 M Oxalic acid; e) 40 V voltage and 0.4M oxalic acid; f) 40 V voltage and 0.5 M oxalic acid; g) 30 V voltage and 0.3 M Oxalic acid; h) 50 V voltage and 0.4 M oxalic acid; i) 50 V voltage and 0.5 M oxalic acid.*

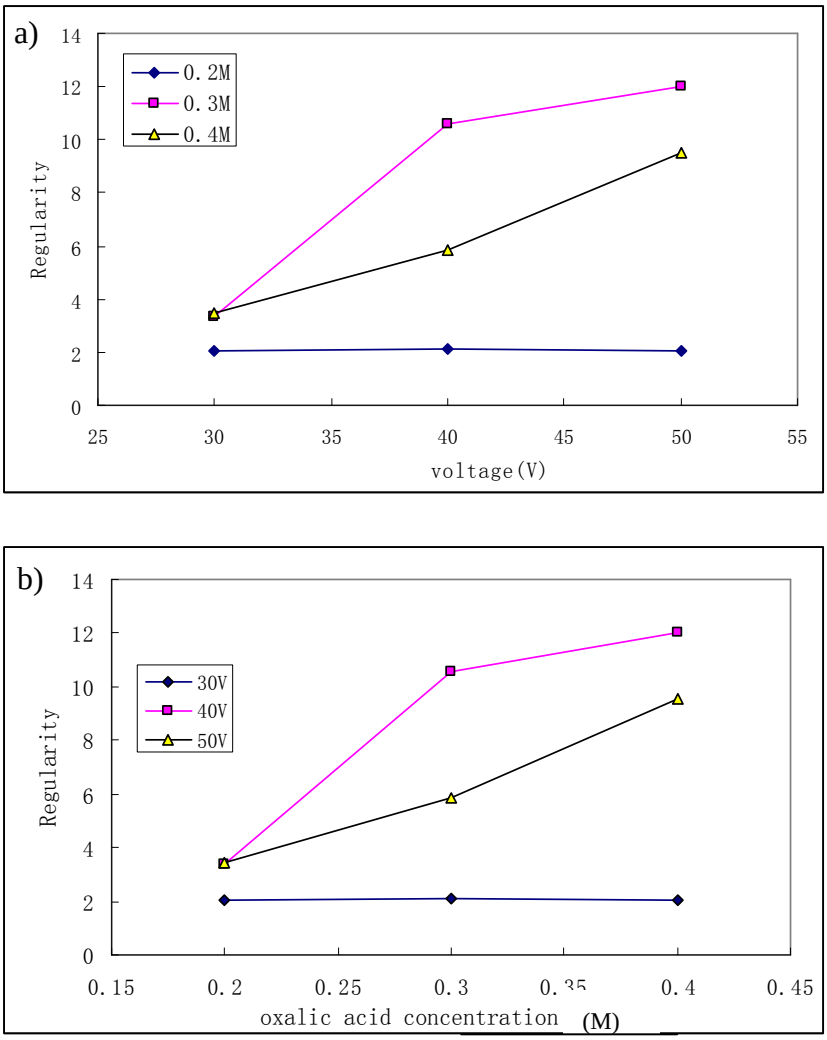

Figure 4.24 *Relationships between the regularity of pore arrays and: (a) the anodizing voltage, (b) oxalic acid concentration.*

Table 4.1 *Comparison of anodizing conditions*

Sample number	Anodizing voltage(V)	Oxalic acid concentration(mol/L)	Steady current density (Amm^{-2})
S1	30	0.2	2.70E-5
S2	30	0.3	2.89E-5
S3	30	0.4	3.35E-5
S4	40	0.2	3.93E-5
S5	40	0.3	5.11E-5
S6	40	0.4	5.56E-5
S7	50	0.2	7.00E-5
S8	50	0.3	9.62E-5
S9	50	0.4	9.64E-5

Chapter 5

Porous Anodic Film Formation on Pre-patterned Substrate

5.1 Introduction

In previous chapters, it was stated that porous anodic films with relatively long-range order can be obtained under selected anodizing conditions. The pores are aligned spontaneously into close-packed hexagonal arrays during film formation. However, the maximum area with pores aligned in the same direction is restricted by the self-organization conditions. The optimum ordering requires long period anodizing and repeated removal of formed films, which is highly time consuming and material costly. Further, the arrangement of pores is limited to hexagonal lattice only. Thus, the feasibility of porous anodic films is limited in many applications, such as optoelectronic devices and optical applications.

One of the approaches employed to overcome such limitations is to employ pre-pattern onto aluminum substrate prior to anodizing, among which imprint and electron-beam lithography are the most commonly used techniques. However, these methods allow only small imprint areas. Typically, an electron-beam writing field is as small as several square micrometers. An easier approach, using a commercial grating, was employed by Mikulskas *et al.* [121], with which significantly larger areas over an area of several tens of square micrometers of anodic film with aligned pores were produced.

In this chapter, aluminum substrates that are pre-patterned using a commercially available optical grating were employed. The surface texture of the grating was transferred to aluminum surface, forming a regular grooved mesh. Subsequent anodizing, under appropriately adjusted conditions in a dilute phosphoric acid solution, generated almost ideal periodicity and size distribution of pores with smaller interpore distance than the pre-patterned lattice constant over relatively large areas of the substrate. Both hexagonally and square arranged pore arrays were fabricated by varying the shape of pre-patterned groove mesh. Further, by adjusting the anodizing voltages, pore arrays with various interpore distances were achieved on pre-patterned aluminum surface with fixed lattice constant.

5.2 Effects of imprinting pressure on pre-patterned substrate

The optical grating was placed onto aluminum substrate and pressing was carried out using a surface micro-cracks testing machine at room temperature on a clean bench. Atomic force micrographs of patterned aluminum substrate with 60° and 90° rotating angles between the first and the second press are shown in Figure 5.1 and 5.2 respectively. Rhombus patterns are evident in Figure 5.1 (a), which was obtained by pressing the aluminum substrate twice by rotating optic grating for 60°. The measured distance between two adjacent grooves is approximately 850 nm. Meanwhile, square patterns are evident in Figure 5.2 (a), which was obtained by pressing the aluminum substrate twice by rotating optic grating for 90°. The measured distance between two adjacent grooves is approximately 850 nm. Three dimensional illustrations are also shown in Figure 5.1 (b) and 5.2 (b).

The appropriate pressure, at which the pattern could be fully transferred to aluminum surface while the grating can still be removed from the patterned aluminum without damaging the substrate and the grating, was determined. Applied loads between 100 N and 250 N, equal to applied pressure of 50 kg cm^{-2} and 125 kg cm^{-2} respectively with the loaded area of 0.2 cm^2, are found to be appropriate. Applied pressure lower

than 50 kg cm^{-2} is not sufficient to produce deep enough grooves on aluminum surface. Pressure higher than 250 kg cm^{-2} causes damage to the optic grating.

Atomic force microscopy of patterned aluminum substrate revealed that the depth of grooves on aluminum is approximately 40 nm for an applied pressure of 50 kg cm^{-2}, and 80 nm for an applied pressure of 125 kg cm^{-2}, as shown in Figure 5.3. Using an optical grating with parallel grooves of right-angle triangular tips, the applied pressure required for stable patterns is about 20 times lower than that of the dot-like master mold used by Masuda *et al* [41].

If the second pressing of optical grating was carried out with the same pressure as that for the first pressing, the depths of two grooves introduced by the two steps would not be identical. This might be because that the effective pressed area on aluminum substrate reduces significantly after first pressing. For the first pressing, the effective pressed area is along the triangular tips as revealed in Figure 5.4 (a). After the first pressing, parallel grooves are formed on aluminum surface. Therefore, during the second pressing, only the ridge areas are touched by triangular tips of optic grating, as shown in Figure 5.4 (b). Therefore, reduction of effective pressing area results in smaller pressing pressure to be required for the same pressing depth.

It is concluded by experiments that the optimum pressing pressures are 125 kg cm^{-2} for the first pressing and 100 kg cm^{-2} for the second pressing for the selected optical grating, so as to ensure that the parallel grooves in both directions have identical depth into aluminum substrate. Figure 5.5 shows SEM images of pressed aluminium substrates with ideal patterns in both 60° and 90° rotating.

5.3 Anodizing of pre-patterned aluminum

It was stated initially by Masuda *et al.* [131] that during anodizing on pre-patterned surface, pores initiate at the position of one missed pore surrounded by six lithographically defined hexagonally ordered pores, when the lattice constant of the

pores introduced by lithography matches with self-ordering conditions such as the applied voltage. For the first time Masuda brought up a self compensation rule for anodizing on pre-patterned substrate. Afterwards, Choi [132] extended the self-compensation rule and assessed how many lithographically defined pores are required to guide anodizing to produce orderly aligned pore arrays with the interpore distance smaller than the lattice constant of the imprint pattern. These previous works give a clue on investigating anodizing behavior of aluminum on pre-patterned surfaces. During anodizing on pre-patterned surfaces, well-ordered pore arrays formation is the result of two competing processes: 1) the self-organization of pores (which is thought to be driven by mechanical stress forces on metal/oxide interface); 2) the initiation of pore at scalloped positions (due to a geometric effect).

The approach employed in the present work was motivated by the idea that if the initiation and development of pores are guided by the appropriate pattern on the substrate surface at the initial stage of anodizing, and an appropriate condition is maintained for the self-ordering, the long range ordered pore arrays can be expected to grow spontaneously.

The interpore distance (D_{int}) of the porous anodic oxide films is proportional to the forming voltage, which could be described as [36]：

$$D_{int} = 2.5\ \text{nm/V} \times U$$

In which D_{int} is the interpore distance measured between the centre points of two adjacent pores, and U is the applied anodizing voltage. It is evident that there is a linear relationship between the interpore distance and anodizing voltage. On pre-patterned surface, if the anodizing voltage is corresponding to the lattice constant, dictated by the relationship between the interpore distance and anodizing voltage, ordered pore growth could be maintained [121]. In the present work, anodizing

voltage was selected based on this linear relationship, which is explained in following paragraphs.

The pre-patterned texture on aluminum has an 850 nm lattice constant, namely, the perpendicular distance between two adjacent parallel grooves. As for the selected anodizing voltage in this work (described in Chapter 3), the corresponding interpore distances in porous anodic oxide films are approximately 500 nm for 200 V, 400 nm for 160 V and 300 nm for 120 V respectively. It was reported that during initial stage of anodizing, the electric field strength focuses on scalloped points of aluminum surface, where pores initiate [133]. In the AFM images of pre-patterned aluminum surface in Figure 5.1 and 5.2, it is obvious that the positions along the parallel grooves, especially the intersection points, are the scalloped positions, thus, are favorable pore initiation locations.

The pore arrangement in the porous anodic oxide film formed on rhomb patterned aluminum at various anodizing voltages was investigated. Figure 5.5 displays the surface morphology of porous anodic oxide film obtained on pre-patterned aluminum by two steps pressing of optical grating with a 60° rotation. The oxide film formed at 200 V exhibits hexagonally arranged pore arrays, as shown in Figure 5.5 (a). The interpore distance between two adjacent pores is measured from the SEM images to be approximately 470 nm. This is near the value of 500 nm, which is the corresponding interpore distance of porous anodic oxide films formed by anodizing at 200 V on non-patterned aluminum substrate.

Similarly, pores in the film formed at 160 V on pre-patterned aluminum by two steps pressing of optical grating with 60° rotation are also arranged in hexagonal pattern, as shown in Figure 5.5 (b). This follows the rhombus pre-patterns on aluminum substrate. The interpore distance is reduced to approximately 320 nm, however. This is also near the value of 400 nm, which is the corresponding interpore distance for films formed by anodizing at 160 V on non-patterned aluminum substrate.

When the anodizing voltage is reduced to 120 V, the formed porous anodic oxide film exhibits random pore distribution (Figure 5.5 c), with an average interpore distance of approximately 300 nm. The pre-pattern with an 850 nm lattice constant shows little influence on the morphology of resultant anodic film.

Figure 5.6 shows porous anodic films formed at various voltages on pre-patterned aluminum with rectangular lattices. For the film formed at 200 V, it is clearly evident that highly ordered pores in square shape arrangement are obtained, as shown in Figure 5.6 (a). The SEM image of Figure 5.6 (b) also exhibits anodic film with highly ordered pore array in rectangular arranged pattern, which was obtained at 160 V on aluminium substrate with the same pre-pattern with square lattices. Measurements based on SEM images reveal that the interpore distance for these two samples is 360 nm for 200 V and 270 nm for 160 V respectively.

Under relatively low anodizing voltage of 120 V, little order of pore distribution could be observed, as shown in Figure 5.6 (c). This is the same situation as the rhomb-like pre-patterned samples shown in Figure 5.5 (c), i.e. the pre-pattern has little influence on the morphology of the resultant anodic films.

For comparison, porous anodic films were formed in a diluted phosphoric acid at the voltages of 200 V and 160 V on aluminum with only one direction optic grating press. The scanning electron micrographs of the resultant films are shown in Figure 5.7. At the anodizing voltage of 200 V, when the corresponding self ordering interpore distance is 500 nm, the pores on resultant porous anodic films are aligned in order only in the direction along the parallel pressing lines, as shown in Figure 5.7 (a). In other directions, however, little order of pore distribution could be observed. The spacing of the parallel pore lines is measured to be approximately 420 nm, which is half the spacing of the grooves on pre-patterned aluminium before anodizing. This suggests that during anodizing, pores were guided to preferably initiate at the

positions along pressed grooves. Further, an additional line of pores developed between the two lines of pores positioned by the pre-pattern, thus making the spacing of parallel pore lines to be 420 nm, which is half value of the grooves.

When the anodizing voltage is reduced to 160 V, parallel lines of pores are evident, as shown in Figure 5.7 (b). The spacing between adjacent parallel lines is measured to be 850 nm, exactly the same value between two adjacent pre-patterned grooves on aluminum substrate before anodizing. This also indicates that pores are initiated on scalloped positions, here the pressed grooves, during anodizing. The pores along the lines are distributed with almost even distance between neighbored pores. However, over the area in between the parallel lines, pores are distributed randomly, and no ordered pore arrays could be observed.

Therefore, two points are confirmed by Figure 5.7. First, pores are preferentially initiated along the grooves, which are the most scalloped positions as illustrated in previous literature [133]. Second, additional pores can initiate, then develop on non-predetermined points due to the self-compensation rules during aluminum anodizing [131].

However, the previous data also brings up one question about the interpore distance for films formed on pre-patterned aluminum under various voltages. The interpore distance in anodic oxide films obtained by anodizing at 200 V on substrate with one direction optic grating press, that is the spacing between parallel lines of pores, is measured to be approximately 420 nm. However, the corresponding interpore distance for the films formed at 200 V on the substrate without pre-pattern is approximately 500 nm. Meanwhile, the interpore distance for the films formed at 160 V on the substrate without pre-pattern is approximately 400 nm. But the interpore distance for the films obtained by anodizing at 160 V on aluminum with one direction optic grating press is roughly measured to be approximately 320 nm, much smaller than 400 nm. Further, the interpore distance of films formed on pre-patterned substrate

with two direction press at all situations are all measured to be smaller than the self-ordering interpore distance under accordant anodizing voltages. Therefore, it is evident that there is a non-neglectable deviation between the values of interpore distance between two types of anodizing under the same anodizing voltage.

It is thought that this difference in the voltage dependence of the ordering between these two growth modes, i.e. the growth with and without pre-pattern, originates in the difference in the initial stage of the ordering of pore configuration. The self-ordering anodizing on non-patterned substrate is presumably strongly dependent on the applied voltage compared to the growth using pre-patterning, because the rearrangement of the cell configuration during growth must take place, in contrast to the ordering with patterning in which the pore can develop orderly in the initial stage of anodizing.

The structure of self-ordered porous anodic films is described as a close packed array of columnar cells, each containing a central pore. The configuration and shape of cells can be defined based on the mathematical expression known as the Voronoi tessellation [134]. In Voronoi diagram, the partitioning of a plane with n points into convex polygons such that each polygon contains exactly one generating point and every point in a given polygon is closer to its generating point than to any other.

In ordered self-organized porous anodic films, the shape of cells takes the hexagon on average in the triangular (hexagonal closely packed) lattice [135], and is a regular hexagon under highly ordered conditions. This is because the triangular lattice has the most possibility to achieve the closest packing of uniformly sized cylindrical pores. Based on the Voronoi tessellation, if the initiation nuclei can be laid out in square or graphite structure lattice patterns, cells with a square shape can be formed other than ordinary hexagonal pores. Therefore, it at least illustrates the possibility of formation of rectangular arranged pores in anodic films on pre-patterned substrate with square pre-patterns. The most important point of considering Voronoi diagram in the present

process is that the arrangement of nuclei in a two dimensional area determines the shape of the obtained structures as a result of the closely packed arranging.

Anodizing voltages control the interpore distance between adjacent pores. Figure 5.8 represents the pore base geometry during formation of self-ordered anodic films. Basically, film formation occurs at a constant rate determined by the electric field. It is balanced by field-assisted dissolution, with the rate being determined by the local field, i.e. by the radius of the pore base and anodizing voltage. Under a certain anodizing voltage, as the radius increases, any enhancement of the field assisting dissolution at the pore base due to convergence of the lines of force there decreases and the field approaches the average field through the barrier layer, which is the same everywhere. A self-adjusting situation predominates, with any tendency for the pore diameter to become too large or too small being checked by a consequent increase or decrease in the radius of the pore base. The constant interpore distance, proportional to cell voltage, is a consequence of the equilibrium barrier-layer thickness and pore base radius established.

During anodizing of pre-patterned surfaces, the self-adjustment of pores should follow basically the same rule as the self-ordered anodizing. However, the existence of pre-patterns on aluminium substrate dominates pore initiations exclusively along grooves. Further, the positions at the intersection of grooves in two directions have the highest priority for pore initiation. The position of these pores is not deviated during the self-adjustment of pores, which could be confirmed by anodizing on pre-patterned substrate with one direction impress. Taking the anodizing on 60° rotating angle under voltage of 160 V for example, the position of pores initiated at the position of intersections remain unchanged, and the distance between them is measured to be 980 nm. Assuming that there is only one additional pore initiated between them, the interpore distance between adjacent pores should be adjusted to 490 nm, i.e. half value of the lattice constant. Meanwhile, the self-ordering interpore distance for anodizing of non-patterned substrate at 160 V is 400 nm. This means that

the electric field is required to form a radius curvature of pore base corresponding to an interpore distance of 490 nm. However, the electric field generated at 160 V is only sufficient to maintain a pore base with a radius of 400 nm. Thus, an extra pore should be initiating at a certain position between the existed pores. After self-adjustment during anodizing, the obtained interpore distance of pores in films formed by anodizing on pre-patterned substrate should be 1/3 of the lattice constant, i.e. 320 nm. This value is basically consistent with the experimental results. Therefore, this explains that the interpore distance of pores in films formed on pre-patterned substrate is only possible to be smaller than self-ordering distance, but never larger than it.

In Figure 5.9, the position arrangements of pore initiation in each situation are illustrated. The schematics explain the experimentally obtained interpore distance and pores arrangements when anodizing parameters such as anodizing voltages and pre-patterns were varied. In all cases, it is assumed that pores nucleate preferentially at the scalloped locations, which is firstly the intersection points of grooves in two directions, noted with largest size spots in number 1 in Figure 5.9. Further, the locations along the grooves in two directions are also the points that favorite pore initiation. This has been confirmed by anodizing aluminum substrate with one direction pressing as shown in Figure 5.7.

Additional pores nucleate over the large non-patterned area between grooves. These pore nuclei points are represented with smallest spots in Figure 5.9. Under constant voltage anodizing, the interpore distance was adjusted by the electric field as described precisely. Finally, porous anodic film with ordered hexagonal or rectangular pore arrangements in various pore sizes could be obtained over a relatively large area.

The calculated interpore distances of porous anodic film obtained in Figure 5.9 in all cases, i.e. 200 V anodizing voltage with 60° pressing angle, 160 V anodizing voltage with 60° pressing angle, 200 V anodizing voltage with 90° pressing angle and 160 V

anodizing voltage with 90° pressing angle, are all consistent with the measured data. Choi [132] summarized on anodizing of aluminium with an interpore distance smaller than lattice constant of pre-patterned substrate. He made a reasonable assumption that new pores can be guided by three pre-patterned points but not by two pre-patterned points. Further, if there are more than three guiding points on the surface by pre-patterning methods, perfectly self ordered porous anodic oxide in the center of the guiding points can be obtained without the imprint pattern having a reduced lattice constant. In the present work, the patterns in Figure 5.9 were arranged following this rule. The theoretical interpore distances are consistent with the measured data, confirming that three guiding points are necessary for additional pore initiation in an ordered arrangement.

Figure 5.10 gives a large scale SEM image of porous anodic film obtained by anodizing on pre-patterned aluminum by optic grating press. The area of almost perfect hexagonal pattern is in several tens of micrometer scale. There is a great improvement of ordering area than porous anodic films obtained by self-organized anodizing. Further, compared to electron lithography pre-patterning method, the pre-patterning method by optic grating pressing employed in this work showed great potential on low cost, large area and commercial feasible applications.

Figure 5.11 is the current density-time responses of anodizing aluminum in phosphoric acid at various voltages. The three curves are almost identical, except for that higher anodizing voltage led to higher peak value at the initial stage of anodizing. With the progress of anodizing, the current became stable at a low value until the end of the process, indicating a stable, but slow growth rate of anodic film formation.

5.4 Conclusion

With the method of optic grating pressing, highly ordered porous anodic oxide films with both hexagonal and square cell arrangement in a large area of up to 20 μm^2 were obtained.

Pressing pressure has influence on the resultant texture over aluminum substrate surface. Pressing pressure between 50 kg cm^{-2} and 125 kg cm^{-2} is suitable to produce texture on aluminium surface, leading to an appropriate depth of pressed grooves around 40 to 100 nm, which is sufficient to generate uniformly arranged porous structures.

Pores nucleate preferentially at the intersections of grooves formed by optical grating presses, and also at positions along grooves, with additional pores initiating over the area between grooves due to self-compensation rule during aluminum anodizing. Anodizing voltage controls the interpore distance between adjacent pores along grooves according to linear relationship between the anodizing voltage and the interpore distance determined by self-ordering. However, the interpore distance is not only decided by anodizing voltage, but also greatly affected by the texture introduced by optic grating. When the anodizing voltage is not deviated far away from the lattice constant of the pre-pattern, aligned pores on anodic oxide film could be obtained. The interpore distance is smaller than that formed by anodizing on non-patterned substrate under same anodizing voltage. If the anodizing voltage deviated far away from the voltage, little ordering was achieved. It is concluded that the pre-pattern on aluminum substrate surface could influence pore initiation. In other words, the interpore distance of porous anodic oxide is decide by both the anodizing voltage and pre-patterns together.

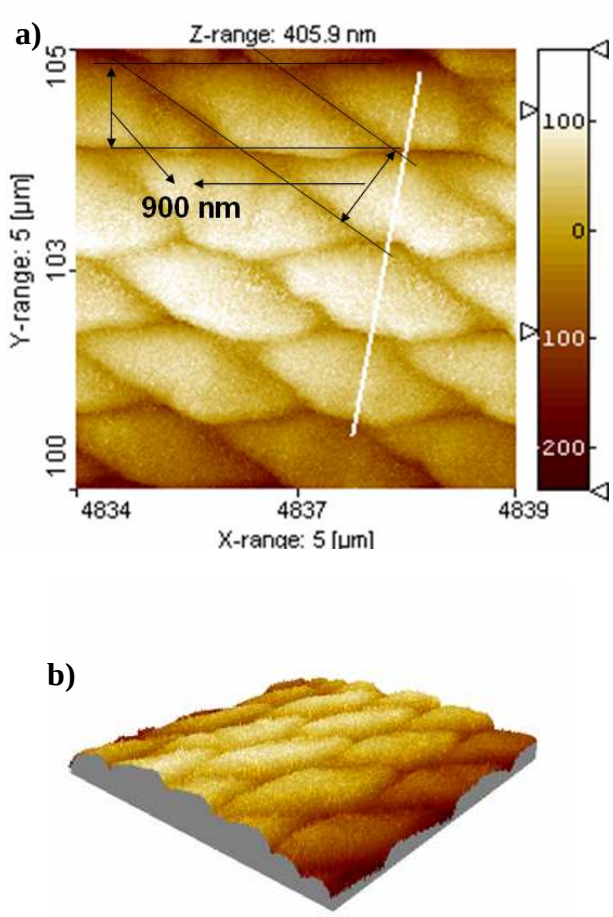

Figure 5.1 *AFM images of the aluminium surface after 60° pressing with a pressure of 125 kg. cm^{-2}: a) Top view of the pre-patterned aluminium surface; b) 3D view of the pre-patterned aluminium surface.*

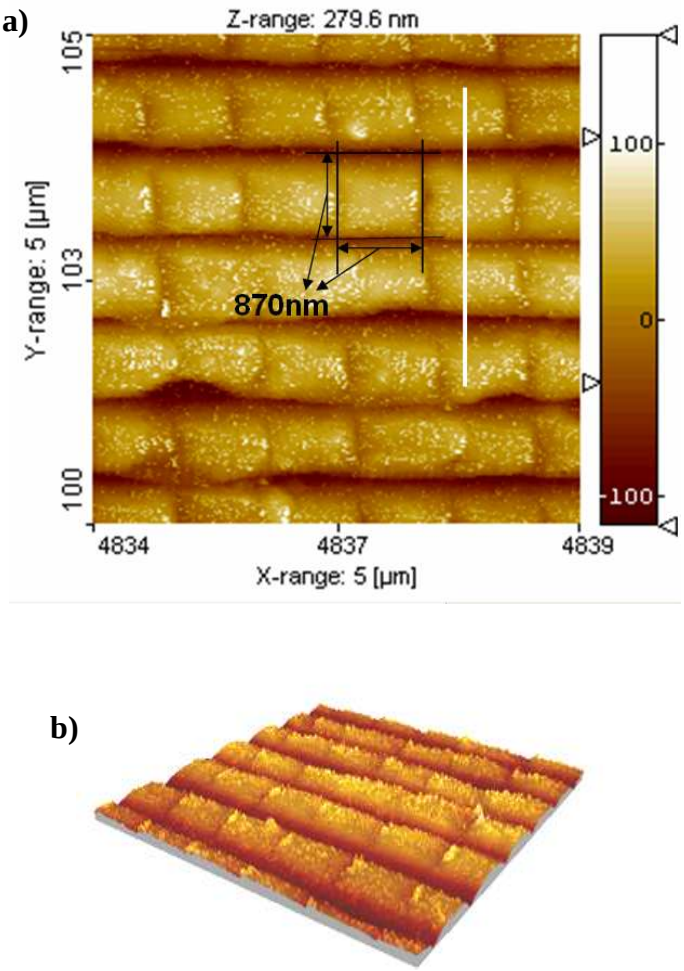

Figure 5.2 *AFM images of the aluminium surface after 90° pressing with a pressure of 125 kg. cm^{-2}: a) Top view of the pre-patterned aluminium surface; b) 3D view of the pre-patterned aluminium surface.*

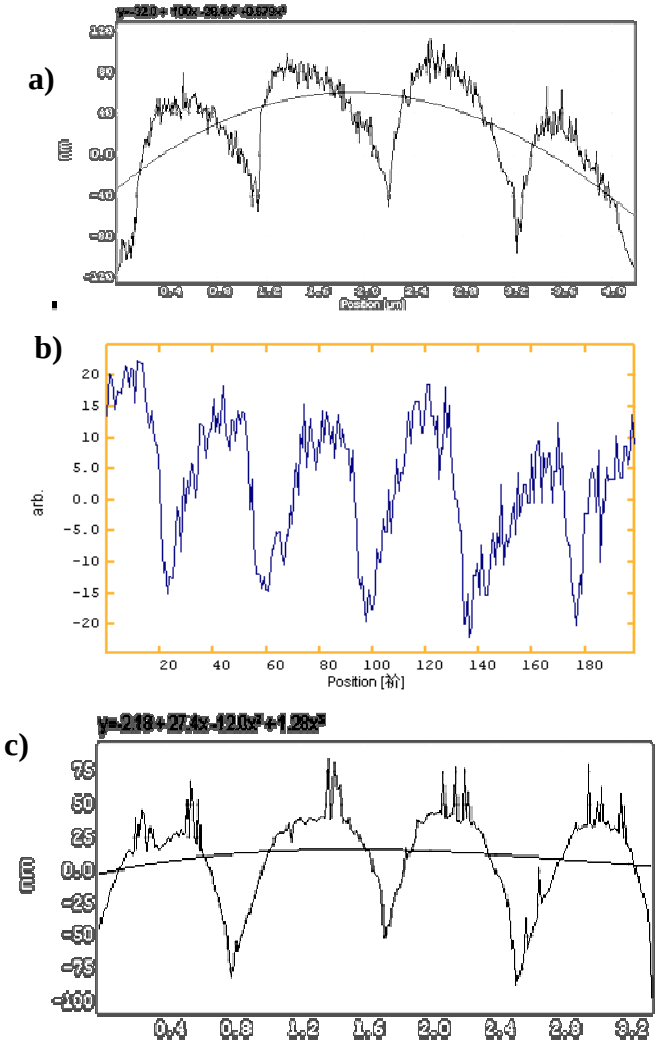

Figure.5.3 *Line profile of the patterned aluminium surface showing the depth of pressed grooves: a) Aluminium surface after 60° pressing with a pressure of 125 kg. cm^{-2}; b) Aluminium surface after 60° pressing with a pressure of 50 kg. cm^{-2}; c) Aluminium surface after 90° pressing with a pressure of 125 kg. cm^{-2}.*

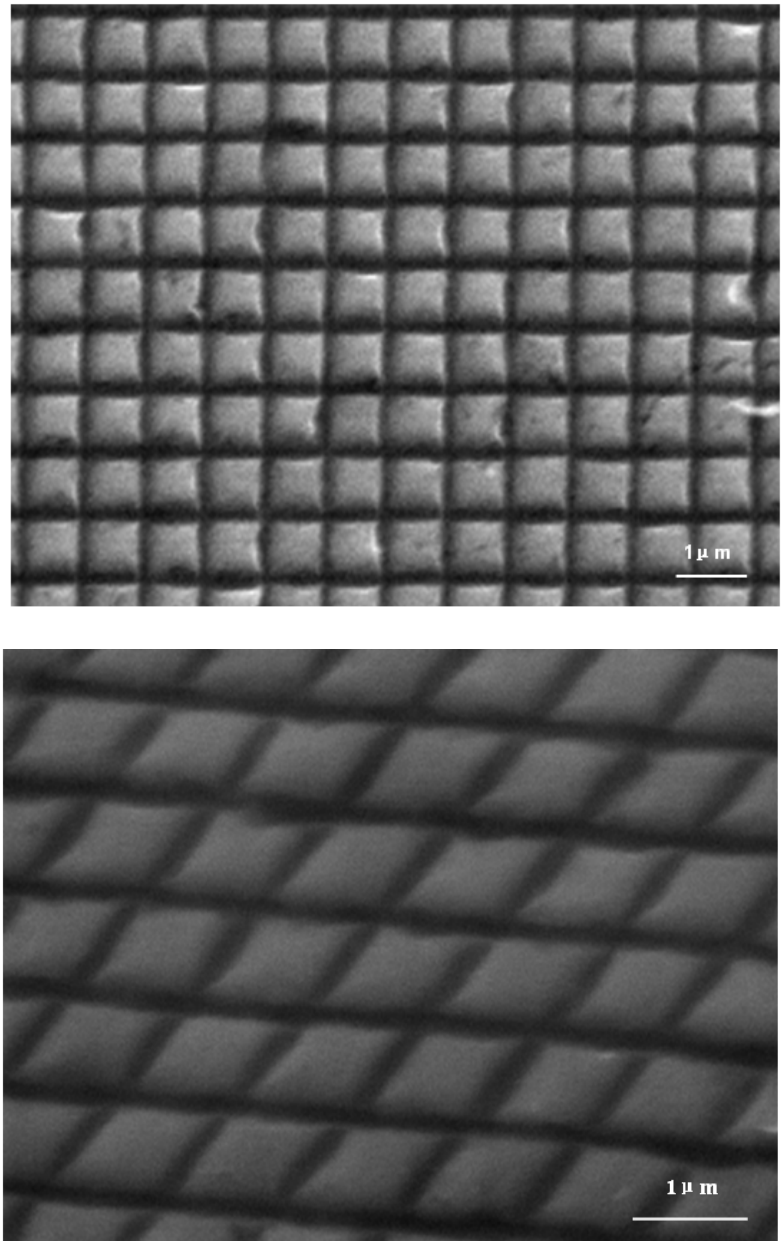

Figure 5.4 *SEM images of the aluminium surface obtained by 60° and 90° pressing with pressures of 125 kg cm^{-2} for the first and 100 kg cm^{-2} for the second pressing steps respectively.*

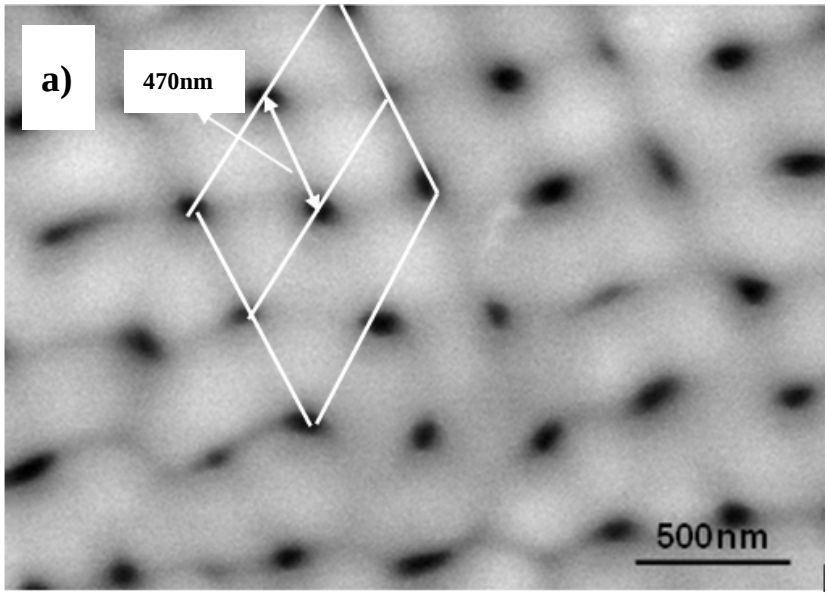
a)
470nm
500nm

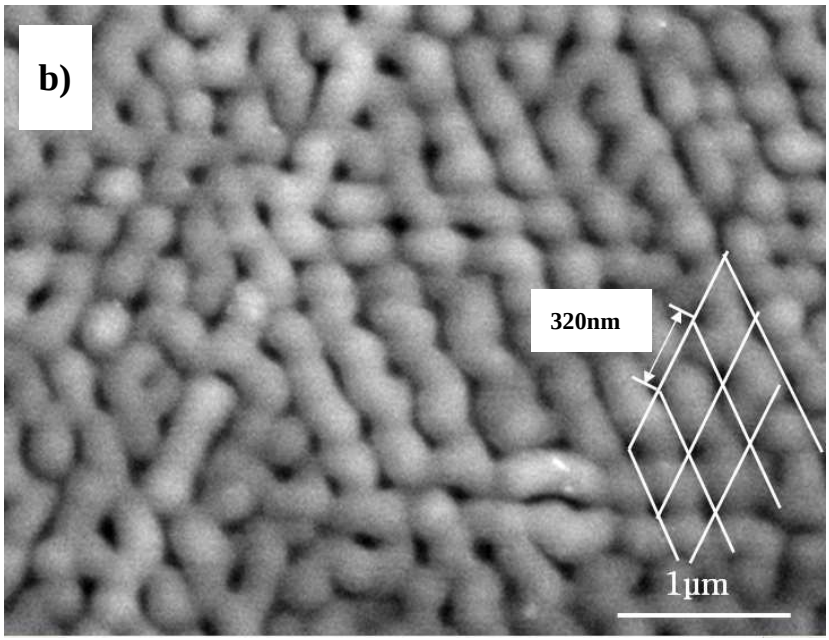
b)
320nm
1μm

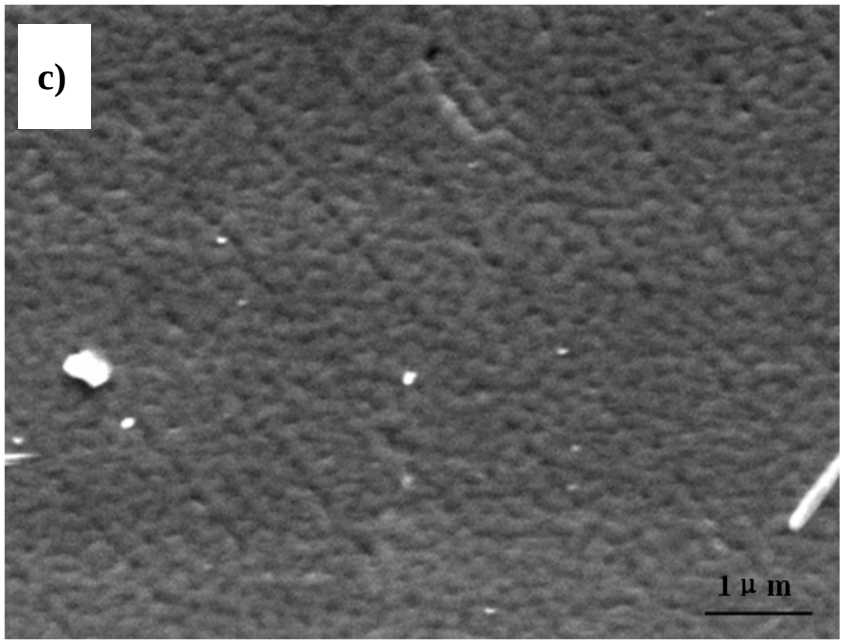

Figure 5.5 *SEM images of specimens with two presses at an angle of 60° and anodized at a) 200 V; ） b) 160 V; c) 120 V.*

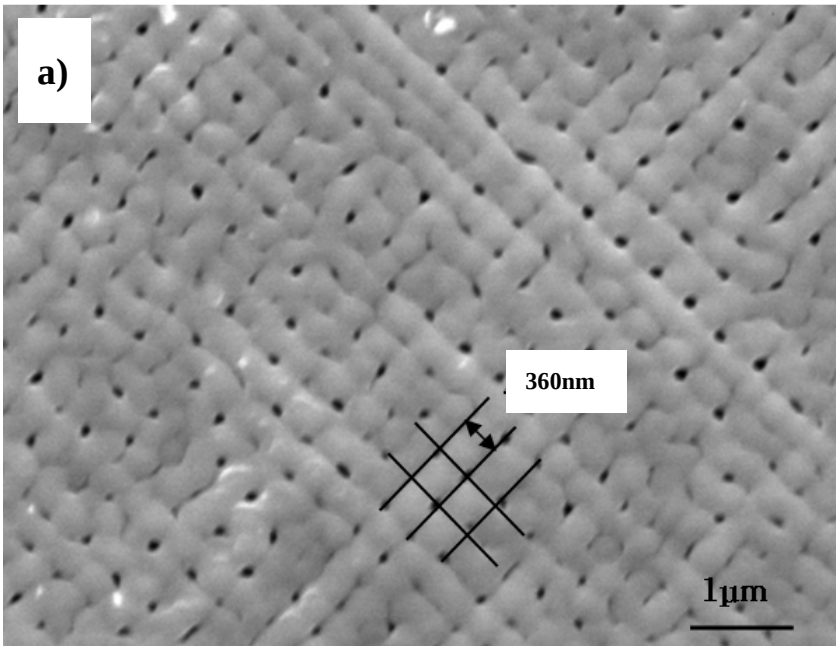

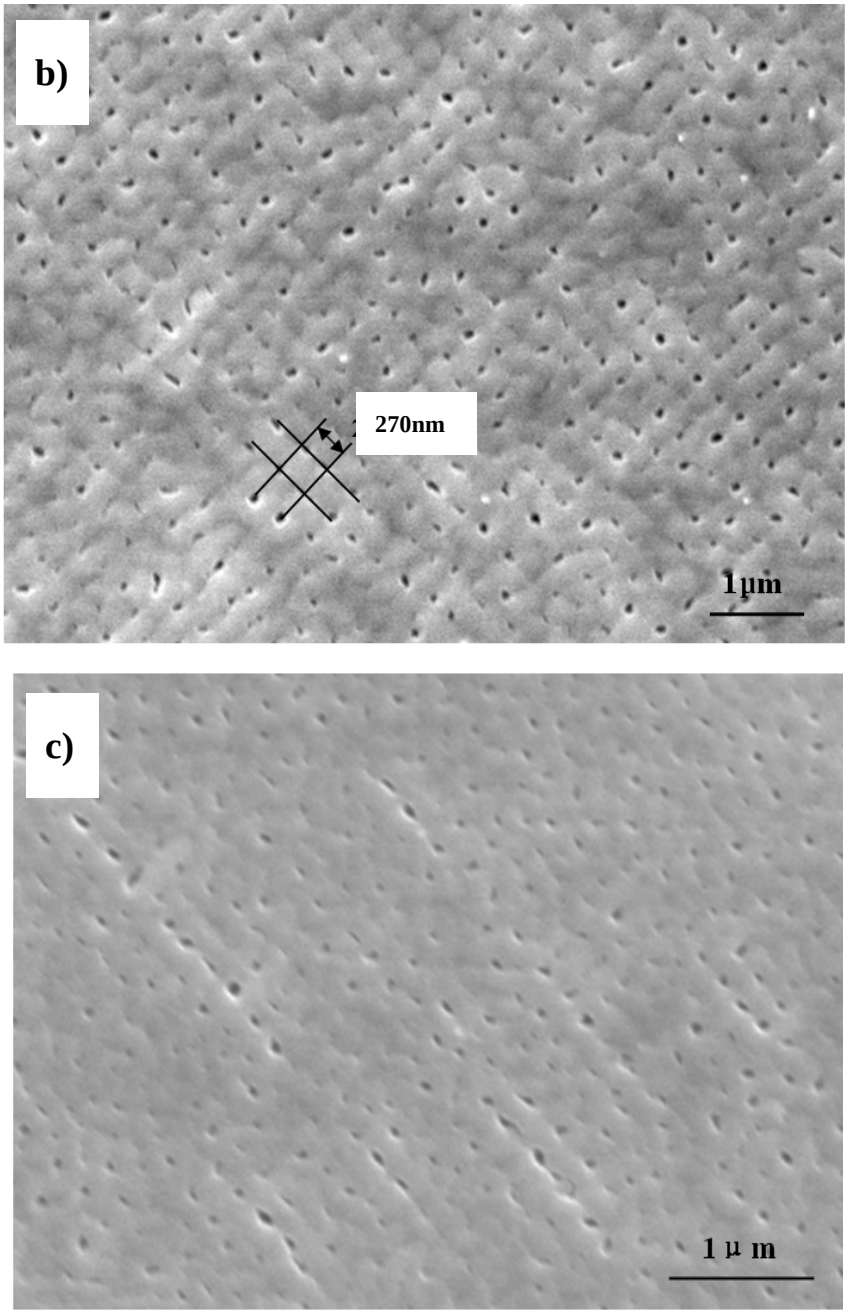

Figure 5.6 *SEM images of specimens with two presses at an angle of 90° and anodized at a) 200 V;) b) 160 V; c) 120 V.*

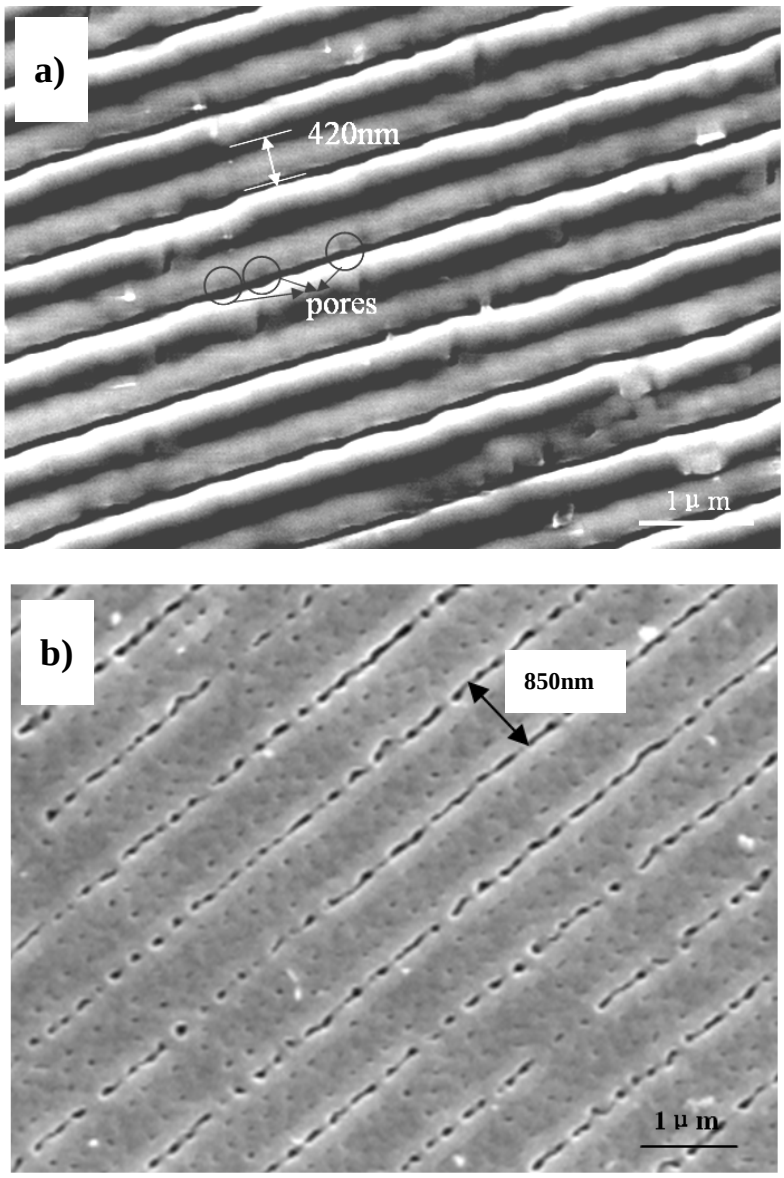

Figure 5.7 *SEM images of specimens with single presses and anodized at a) 200 V; b) 160 V.*

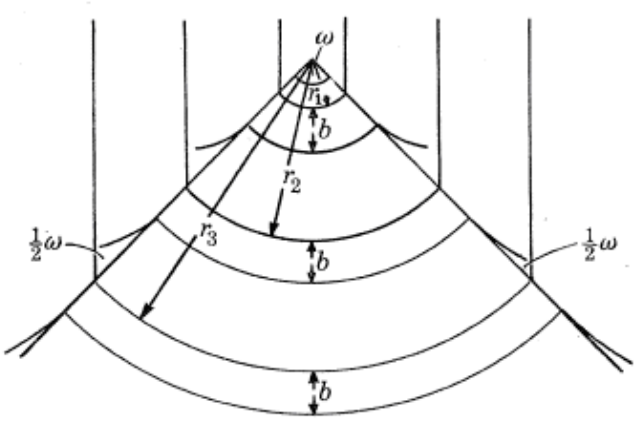

Figure 5.8 *Schematic representation of pore base size self-adjustment, r1,r2 and r3 representing the radii of the pore bases and w the solid angle subtended from the centre of curvature to pore bases. r2 is the steady-state radius under the prevailing anodizing conditions.*

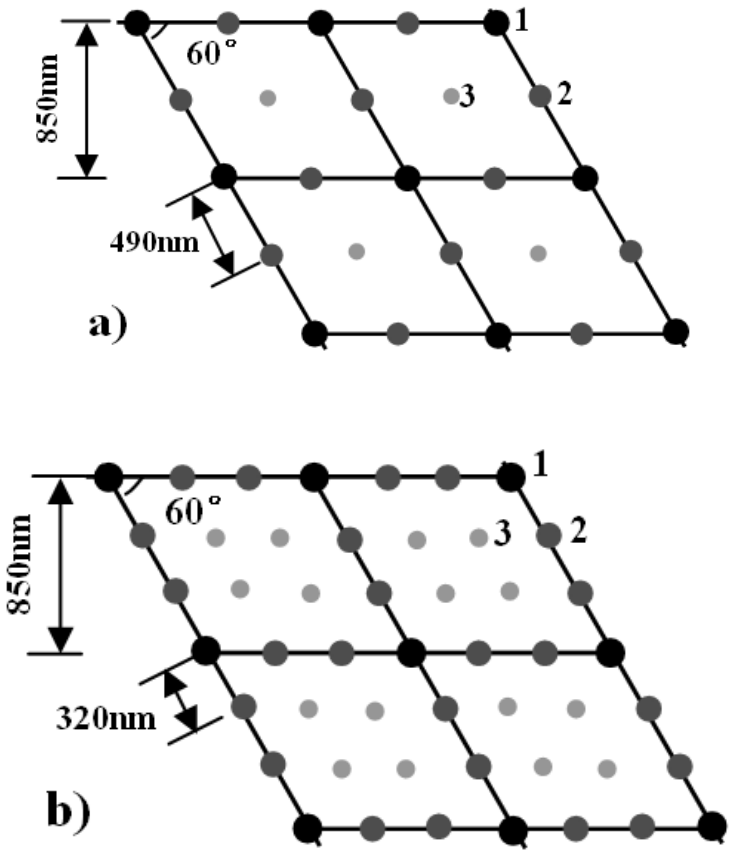

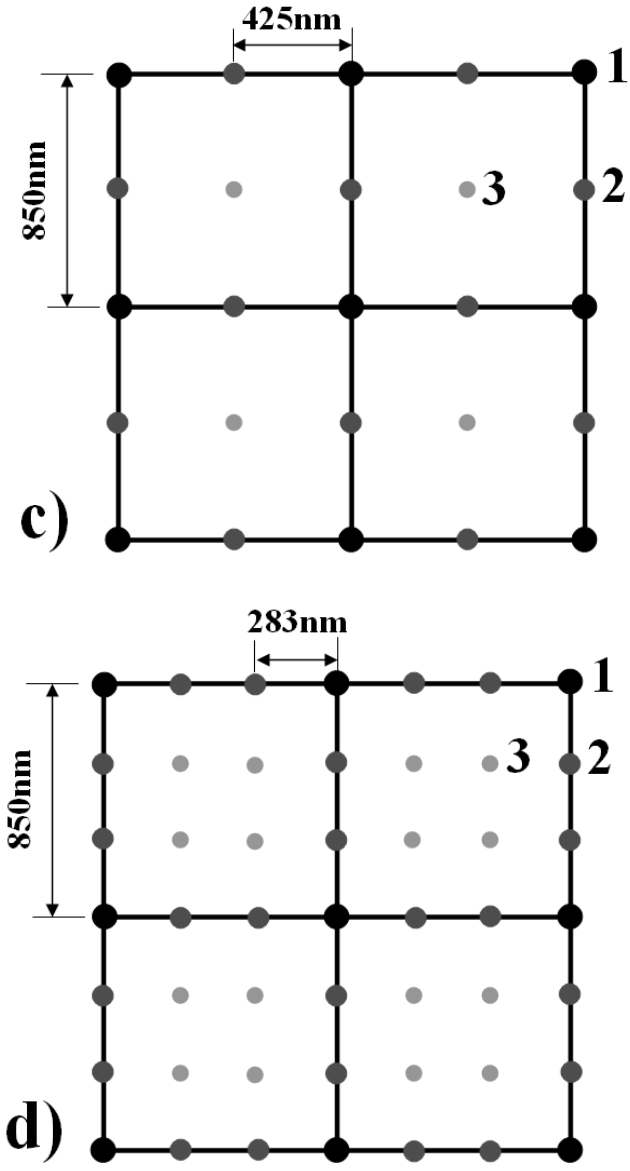

Figure 5.9 *Illustration of pore initiation positions under various anodizing conditions: a) 60° presses and anodized at 200 V; b) 60° presses and anodized at 160 V; c) 90 °presses and anodized at 200 V; d) 90° presses and anodized at 160 V.*

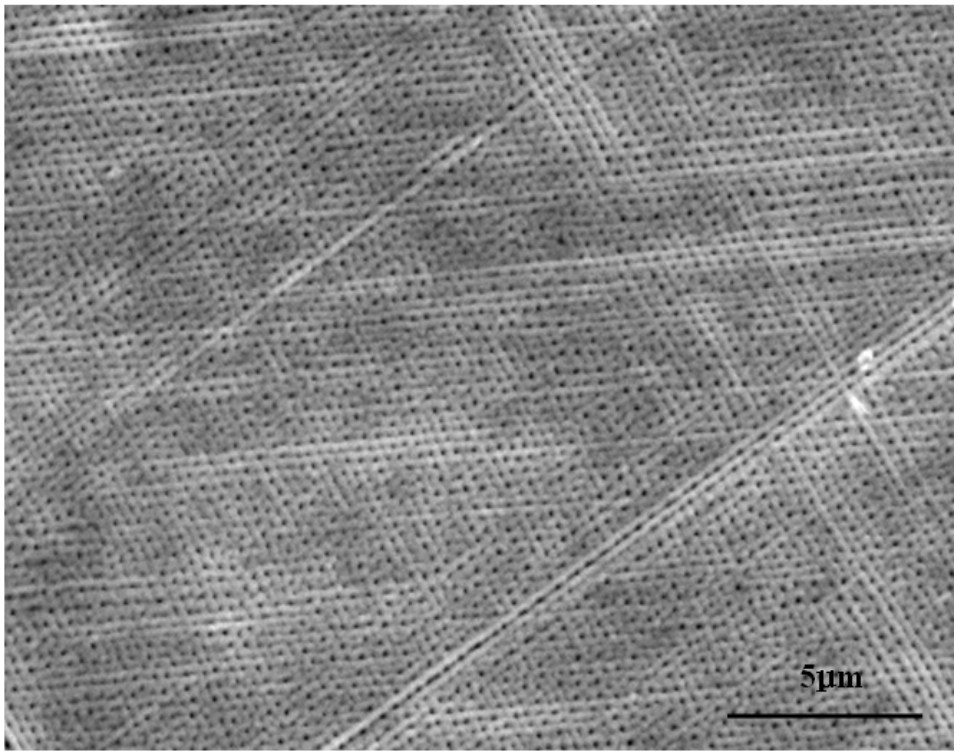

Figure 5.10 *SEM image of specimens with two presses of an angle of 90°, anodized at 200 V.*

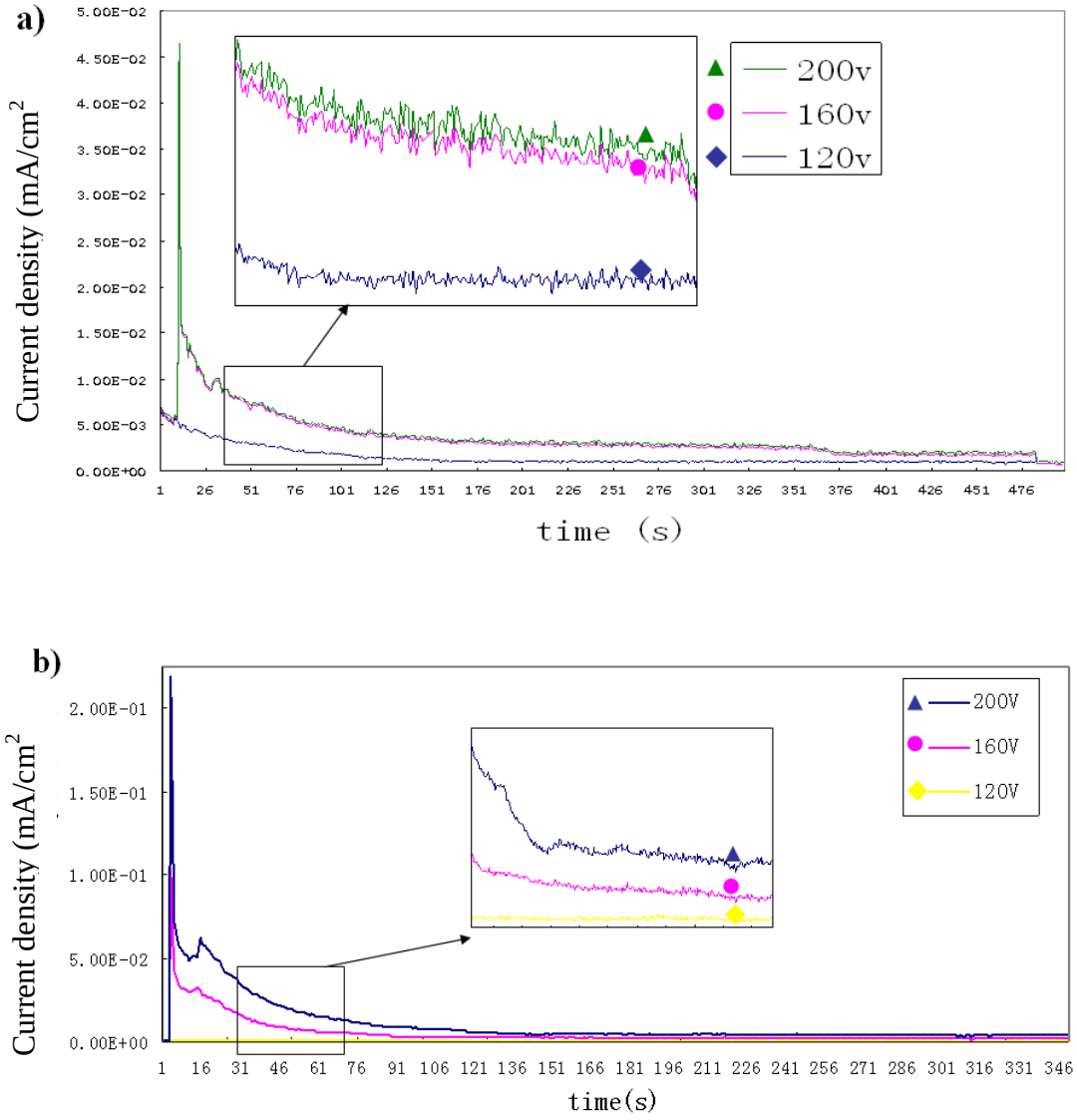

Figure 5.11 *Current density – time response during anodizing of aluminium with two presses: a) at an angle of 60°; b) at an angle of 90°.*

Chapter 6

Electrodeposition of Nickel Nanowires

6.1 Introduction

One-dimensional metallic nanowires have attracted great interest because of their unique properties and potential practical applications in the areas such as magnetic data storage [136], cell separation [137], non-biofouling surfaces [138] and magnetic field or acoustic sensors [139].

A promising method for preparing nanowires is template-mediated growth, including polycarbonate membranes created by chemical etching and alumina membranes produced by anodic oxidation of aluminum foil [1]. The advantage of anodic oxide template over other templates is that the pore population density is high, the pore distribution is uniform, pore diameter is adjustable and the channels are parallel and highly straight [4, 5].

For the template-mediated growth of nanowires, electrodeposition is considered as one of the most effective methods among many processes adopted to fabricate one dimensional metallic nanowires, such as chemical vapor deposition (CVD) [94], chemical polymerization [95], electroless deposition [140] and sol–gel chemistry [96]. The growth of nanowires by electrodeposition is electric field-assisted and usually selectively occurs at the conductive area of the template, which makes it possible to avoid electrodeposition in unwanted area, therefore, to avoid the closure of the pore mouth and to increase the filling efficiency. The cost of the equipments for electrodeposition is relatively low compared to other nanostructure fabrication processes.

In this work, electrodeposition of nickel nanowires using anodic film templates is

investigated. The influence of temperature and electrodeposition voltage on the growth of nickel nanowires is accessed. Current efficiency is monitored with the aim of better understanding the electrodeposition process. The composition and morphology of nickel nanowires obtained under various electrodeposition conditions are characterized.

6.2 Electrodeposition of nickel nanowires

6.2.1 Growth of nickel nanowires

Figure 6.1 shows the current density (*i)* - time (*t)* response obtained during electrodeposition of nickel nanowires at a constant voltage of -1.35 V at 37 °C. The variation of *i-t* response could be divided into three stages. At the initial stage (marked with A), the current density exhibits a relatively low value. The current density increases smoothly in a moderate rate as electrodeposition processes. After approximately 2500 s of electrodeposition progress, the current density starts to increase significantly from the point marked with X in Figure 6.1, where stage B starts. This stage lasts for a relatively short period of approximately 400 s, after which the current density reaches a stable state again (from the point marked with Y), but at a much higher value, which is labeled stage C. Current density remains at this value until the electrodeposition was terminated.

SEM images of nickel nanowires formed at different growth stages are shown in Figure 6.2. In Figure 6.2 a), the electrodeposition was terminated at stage A. It is evident that nanowires are closely packed. The wires appear uniform in diameter, measured to be approximately 90 nm with slightly varied lengths. The difference in nanowire length could be caused by inhomogeneous growth in each pore. For the pores that were initially poorly wetted, nickel electroposition at these locations was delayed compared to those well wetted pores. Therefore, the length of nanowires within the initially poorly wetted pores could be slightly short compared to others.

In Figure 6.2 b), a top view of nickel nanowires embedded in oxide templates is

displayed. In this case, electrodeposition was conducted until the pores were filled up to the top when the current started to increase sharply at point X in Figure 6.1, which is the starting point of stage B. It is evident that approximately 70% of the pores have nanowires embedded inside. The empty pores do not necessarily mean that no nanowire has been deposited inside. It might also be due to inhomogeneous growth within individual pores. When some of the nanowires reach the top surface of template, those nanowires of relatively short lengths are still not visible, because their top ends have not reached the surface of template yet.

SEM image of nickel nanowire arrays formed with the process being terminated at the same stage as that in Figure 6.2 (b) after removal of the template is shown in Figure 6.2 (c). It is evident that nanowires exactly replicate the shape of pores in anodic film template. The diameters of the nanowires are highly uniform. The relative bright nanowires are those with relative long lengths, and the relative dark nanowires have relative short lengths. There exist approximately ten black voids as indicated by arrows in Figure 6.2 (c). They might be pores where no nickel nanowire was formed. This image confirms that the pore filling rate of nickel is almost 99%.

Figure 6.2 (d) corresponds to stage C when the template surface was mostly covered. On some of the wires small hemispherical caps were formed. A large area top view of the specimens in the same situation is presented in Figure 6.2 (e). Particles of relative large size are distributed on the template surface. Particles are distributed close to each other, or overlapped. The empty area (circled in Figure 6.2 (e)) is the oxide template surface, where nickel nanowires might not have reached the surface of template due to the inhomogeneous rate of electrodeposition at different locations.

By summarizing information from SEM images of the resultant nickel nanowires obtained by electrodeposition terminated at different stages, three schematic diagrams are presented in Figure 6.1, indicating different growth stages corresponding to *i-t* response. During the first stage (left schematics labeled with A), nickel nanowires was

growing within the pores while the current remained at a stable value of 0.1~0.2 mA/cm^2, indicating that nickel was continuously deposited into pores of anodic film template at a stable rate.

Growth proceeds in the pores until they are filled up to the top surface of the template (middle schematics marked with B). Beyond this point, growth continues in three dimensions. Hemispherical caps form on top of nanowires which grow in uniform size until coalescence on the template surface occurs. This is stage B as shown in Figure 6.1. The current is now related to the effective electrode area. Before the pores were filled up, only the areas of pores were electrodeposited. After that the whole three dimensional surface area of hemispherical caps are effective. Therefore, the effective electrodeposition area increases rapidly during this stage, thus, resulting in the current density to increase sharply during this period. Further, the sharply increasing slope of *i-t* response in this stage is an indication for homogeneous growth within all the pores in anodic film template. A sharp transition indicates a sudden increase of effective electrodeposition area, thus represents that nanowires in most pores reach the top of template surface at the same time.

Once growth proceeds over the whole template surface (right schematics labeled with C), the current approaches an asymptotic value. This value is corresponding to the current on a metallic electrode of the same overall area and for the same applied voltage.

6.2.2 Current efficiency

The total charge needed to fill the pores to form nanowires to a length of L is calculated as bellows. The total electrodeposited area of a sample is represented as S', thus:

$$S' = S \times P \qquad (1)$$

Where S represents the area of the templates, and *P* is the porosity of anodic oxide templates, since the effective electrodeposition area is only the pore areas in middle of each cell. Thus the porosity *P* could be described as:

$$P = S_{pores}/S_{cells}$$

$$P = \pi/2\sqrt{3}\,(d_{pore}/I_{cell})^2$$

$$P = 0.90(d_{pore}/I_{cell})^2 \qquad (2)$$

Where d_{pore} and I_{cell} are measured from SEM images of porous anodic film template. Figure 6.3 schematically illustrates d_{pore} and I_{cell} in hexagonally ordered porous film. The volume V_{ED} of electrodeposited metal into pores with a pore diameter of d_{pore}, is given by:

$$V_{ED} = L\times S' = L\times S \times P \qquad (3)$$

$$= L\times S\times 0.90\,(d_{pore}/I_{cell})^2$$

Where *L* is the length of deposited nickel nanowires.

Using the molar volume V_M of Ni, the total charge needed to fill the pores to a length of *L* is:

$$Q = zFV_{ED}/VM$$

where z =2 for the divalent Ni^{2+} ions and *F* is the Faraday constant. Thus

$$Q = zF\times Porosity\times S\times L/VM$$

$$Q = 0.90\ zFS\times(d_{pore}/I_{cell})^2\times L\times\rho_{Ni}/M_{Ni} \qquad (4)$$

By measuring the average length of as-formed nanowires, d_{pore} and I_{cell} as well as the whole area of electrodeposited templates, the effective quantity of electricity during electrodeposition is obtained.

During the electrodeposition process, the total transfer of charge is obtained by calculating based on current density-time curve:

$$Q = \int I dt \tag{5}$$

By comparing the effective value with the actual transfer of charge, the current efficiency for electrodeposition of nickel nanowires could be obtained.

Several factors can affect the calculation of current efficiency. First, different pore densities from samples to samples can be present. Second, defects in the anodic oxide template, which may block or limit solution penetration into the very narrow pores. Third, the presence of small cracks in the fragile anodic oxide template, where due to the greater accessibility of cations, deposition would lead to preferential deposition. Finally, but most importantly, the presence of simultaneous side reactions must be considered, that is hydrogen evolution ($2H_2O+2e^- \rightarrow 2OH^- + H_2$), which can compete with and/or block the metal nanowire growth. Hydrogen evolution takes place along with nickel deposition. The adsorption of hydrogen atoms is an essential intermediate step in the evolution of hydrogen gas. Hydrogen evolution could be a main factor for the current efficiency reduction. The current efficiency in the present work is approximately 70% to 95%, close to that reported in literatures for electrodeposition of nanowires into polycarbonate or anodic film templates [141]. However, the 100% current efficiency is still a challenge.

6.2.3 Effects of voltage on the electrodeposition of nickel nanowires

Figure 6.4 shows the current density (*i*) – time (*t*) responses for different applied voltages during the electrodeposition of nickel nanowires into anodic film template with pores of 90 nm diameter at 37°C. It is evident that with increased electrodeposition voltage, the current density during electrodeposition increases. A surge of current density at the initial stage of i-t response of nickel electrodeposition is

observed. This should be attributed to an establishment of diffusion path of ions within the pore channels[142]. It should be noted that at the initial stage of *i-t* response in Figure 6.1, such abrupt decrease also exist, but was missed in the figure due to the delayed switching on of monitoring software during the experiment.

In Figure 6.5, SEM images of the nickel nanowires, with varied aspect ratio, formed by electrodeposition at -1.0 V under room temperature for different time periods, are displayed. All nanowires with different aspect ratio exhibit uniform diameters, smooth surface and even diameter from top to end.

Figure 6.6 shows the dependence of nickel nanowires length on electrodeposition time at -0.8 V, -1.0 V and -1.35 V respectively. The length of nanowires increases lineally with the increase of electrodeposition time, indicating that the growth rate of electrodeposition is stable and almost constant. This is consistent with the *i-t* response in which the current density is constant and stable.

With the increase of applied voltage, the growth rate of nickel nanowires increases, as shown by the nanowire length-time curve in Figure 6.6. It is interesting that once the applied voltage is lower than 1.0 V (represented here as 0.8 V), the growth rate of nickel nanowire dramatically decreases to a significantly low value.

The current efficiency at various applied voltages is calculated by the method described in section 6.2.2 and presented in Table 6.1. When increasing the applied electrodeposition voltage, the current efficiency decreases, with a maximum as high as 91% at $\eta = -0.8$ V. This implies that hydrogen evolution reaction increases as the electrodeposition voltage increases, leading to reduced current efficiency.

6.2.4 Effects of pore diameter of anodic film templates on electrodeposition of nickel nanowires

SEM images of nanowires with different diameter of approximately 60 nm, 90 nm and 280 nm respectively are presented in Figure 6.7. The diameter of nanowires is determined by the pore diameter of template. Among them, oxide templates with pore diameter of 60 nm and 90 nm were formed by anodizing in 0.3 M oxalic acid at 40 V. The oxide templates with pore diameter of 280 nm were formed by anodizing in 0.01 M phosphoric acid at 195 V. The pore diameter was adjusted by controlling the time of chemical pore widening process in warm 5wt% phosphoric acid solution. In all cases nickel was electrodeposited at voltage of -1.0 V (SCE) at 17°C.

As revealed by the SEM images, the nanowires exhibit uniform cylindrical structures, confirming that nickel could be successfully electrodeposited into anodic oxide templates of various pore sizes. Thus, the size of nanowires could be precisely tailored by varying the pore size of anodic film templates.

Figure 6.8 illustrates the current density-time responses during electrodeposition of nickel nanowires of various diameters. In the *i-t* responses, current density varies with the pore diameters. The electrodeposition current density is relatively high in the case of oxide template with pores of 90 nm pore diameter. Lower current densities were recorded in other two cases of template with the smallest pores of 60 nm diameter and the largest pores of 280 nm diameter.

The current density is determined by applied voltage, but also influenced by the effective electrodeposition area. When calculating the current density, area of template surface is normally used. However, the effective deposition area is not the same as the area of template surface, since only within pores that metal is possible for metal to be electrodeposited.

The porosity of the templates with different pore diameters is 29.4%, 66.1% and 31.4% for 60 nm, 90 nm and 280 nm pore diameters respectively. The calculation was based on the hexagonal cells as illustrated in Figure 6.3. It is evident that the template

with pores of 90 nm diameter has the highest porosity. Effective deposition area increases with the increase of porosity over oxide template surface, thus the resultant current is higher. This is consistent with recorded current density (*i*)-time (*t*) in Figure 6.7.

The current efficiency and corresponding electrodeposition conditions are listed in Table 6.2. The current efficiency increases from 76% to 88% when the pore diameter of oxide templates increases from 60 nm to 280 nm. It was reported that the ability of mass transport of metal ions in pores decreases with decreasing pore size [141]. Hydrogen absorption tends to block the pores when pore size decreases. This could be the main reason for the variation of current efficiency with the change of pore size in anodic films.

6.2.5 Effects of temperature on the electrodeposition of nickel nanowires

The current density-time responses obtained during electrodeposition of nickel nanowires at a constant voltage of -1.0 V (SCE) at various temperatures are illustrated in Figure 6.9.. It is clearly evident that the current density during stable stage of electrodeposition increases with the rise of temperature. The current density at 37°C is in the range of 1.5 ~ 1.8 mA/cm^2, with an increasing tendency as electrodeposition proceeds. The irregular peaks of the *i-t* response at 37°C should be due to equipment interrupt during electrodeposition. For electrodeposition at 17°C and 3°C, the current densities are approximately 0.5 and 0.3 mA/cm^2 respectively, which are much lower than the current densities at 37°C. Further, the current densities for electrodeposition at relatively low temperatures of 17°C and 3°C are more stable compared to that at 37°C.

Given a template, the growth rate of nickel in pores of anodic oxide templates is truly represented by the measured current density *i* during electrodeposition. *i* increase with increasing deposition temperature T, as shown in Figure 6.9, suggesting a thermal activation process for the growth of nickel during electrodeposition. Therefore, the

temperature dependence of the reaction rate *I* can give direct kinetic information on the growth of nickel nanowires. According to the Arrhenius equation

$$k = Ae^{-\frac{E_a}{RT}}$$

Thus, $\mathrm{Ln}I = -E_a/R\,\mathrm{T} + \mathrm{LnA}$ (6)

Where E_a is the apparent growth activation energy, *A* is the pre-factor, R is the gas constant and T is the electrodeposition temperature.

There is a linear relationship between growth rate, i.e. current density *i* and 1/T, as shown in Figure 6.10. This is consistent with theoretical equation above. The two lines in Figure 6.10 present *i*-1/T responses obtained at electrodeposition voltage of -1.35 V and -1.0 V for comparison. In equation (6), the slope of *i*-1/T response is determined by E_a, since *R* is a constant value. Linear fits of equation (6) to the data in Figure 6.10 yield the values of Ea = 0.36 and 0.80 eV for the growth of nickel nanowires under electrodeposition voltages of -1.0 V and -1.35 V respectively.

It is observed that the slope of *i*-1/T response was significantly increased under increased applied voltage. Therefore, it is suggested that under higher applied voltage during nickel electrodeposition, growth activation energy E_a is higher. This actually indicates the significant influence of the deposition voltage having more on the growth rate of electrodeposition, which is consistent with the data in 6.2.3.

There was significant change in the current efficiency with the increase of temperature, which decreases from 91% at 3°C to 83% at 17°C and 72% at 37°C. This indicates that at elevated temperature, the hydrogen evolution rate is accelerated.

6.3 Characterization of nickel nanowires

Figure 6.11 shows TEM images of the free standing nickel nanowires formed at -1.0

V within anodic oxide template with pores of 90 nm diameter at various temperatures. It is clearly evident that the nanowires have high aspect ratio and uniform diameter. The nanowires exactly replicate the characteristics of the pores in the templates with an identical wire diameter evenly from bottom to top end, cylindrical shape, indicating that the growth of nanowires was restricted by the pores in anodic oxide films.

The EDX spectrum of the nanowires is shown in Figure 6.12, revealing the existence of nickel metal. The Al and O signals come from the oxide template residues which are not completely removed.

XRD spectrum in Figure 6.13 shows that the deposited nickel nanowires have face centered cubic (fcc) structures. The two spectra are obtained from the nanowires formed at 37°C (Figure 6.13 a) and 3°C (Figure 6.13 b) respectively. The main growth orientation of the nanowire is along [110] at low temperature of 3°C. When temperature was elevated to 37°C, the structure converts to polycrystalline orientation with [111], [110] etc.

Further, the electron diffraction pattern in Figure 6.14 confirmed that the growth orientation of the wire is along the [110] direction at low temperatures. The rings obtained from the nanowire formed at elevated temperature confirm the polycrystalline structure of the nanowires. The TEM and XRD also show that varied voltages and diameters of nickel nanowires have no rational relevance with the crystallographic arrangement of nickel nanowires.

The growth of the nanowires is a complicated process by electrodeposition, which involves the processes listed below:

(1) Mass transport of Ni^{2+} in electrolyte outside nanopores;

(2) Mass transport of Ni^{2+} through electrolyte inside nanopores to the surface of deposited Ni nuclei;

(3) Charge transfer of Ni^{2+} at crystal surface, forming Ni adatoms;

(4) Mass transport of Ni adatoms on crystal surface;

(5) Incorporation of Ni adatoms into crystal structure.

Process (1) would not be the rate-limiting step because the quantity of bulk electrolyte can be considered as infinity compared to the small sample area of approximately 0.2~0.4 cm^2, thus diffusion within the bulk electrolyte solution should not be a limiting step; otherwise the electrodeposition procedure would be highly unstable. Further more, the activation energy for the mass transport of Ni^{2+} in water is 0.2 eV [143], much lower than the measured values (0.36 eV).

Previous studies showed that the ability of mass transport of metal ions in pores decreases with decreasing pore size [141]. However, if mass transport of metal ions in pores is the rate-limiting step, with the proceeding of deposition time, the current density is expected to increase, since diffusion distance within pores decreases as nanowires growing longer. In Figure 6.4, no obvious current increase tendency was observed, suggesting that process (2) is also not the rate-limiting step.

Charge transfer is not believed to be the rate-limiting step for the growth of the nickel crystals in pores, from the works of Yu[141], an exchange current density from the similar electrolyte was experimentally determined which is several orders of magnitude larger than the measured in the present work, implying a very fast charge transfer for nickel growth in the pores of anodic films. While the energy barrier for process (4) is expected to be the smallest because no bonds will be broken [144]. Therefore, the mass transport of nickel adatoms on crystal surface is the most likely mechanism to limit the growth of the nickel crystals in the pores.

Nickel nanowires deposited at -1 V at a relative low temperature of 3 °C exhibit single crystal structure. Therefore, a two-dimensional layer growth mechanism is expected and the activation energy of mass diffusion should be close to that of the

intrinsic diffusion on the Ni (110) crystal face. In previous work, the activation energies of intrinsic Ni adatoms self-diffusion on (111), (100), and (110) faces are calculated to be 0.06, 0.68, and 0.39 eV, respectively [145]. A value of Ea ≈ 0.31 eV for Ni adatoms self diffusion on the (110) face was also experimentally determined. The measured value Ea=0.36 eV in the present study is in satisfactory agreement with the intrinsic self-diffusion activation energy on the Ni (110) face. With increased depositing temperature, polycrystalline nickel nanowires were formed. With the increase of the deposition temperature, the diffusivity of nickel adatoms is increased [146]. The nickel adatoms diffuse on crystal surface at a relative high speed when the deposition temperature is elevated, thus resulting in a polycrystalline growth of nickel nanowires. The precise mechanism awaits further investigation.

6.4 Optical limiting property of nickel nanowire arrays

One-dimensional metal nanostructures have attracted much attention because of their potential applications in not only ultra high density magnetic recording, but also ultra fast optical switching and limiting [136, 147, 148]. Materials exhibiting optical limiting properties are necessary for the production of photonic devices that control amplitude gain or extinction, polarization, phase, reflection and refraction of light [149]. Fast response optical limiting materials can be used for eyes and sensors protection from high intensity light source induced damage. Strong optical power limiting properties have been observed in various materials such as carbon nanotubes, carbon-black suspension, metallophtalocyanines, quantum dots, and dendrimer molecules [150-153].

The optical limiting properties of metal nanowires have been studied recently by Pan and colleagues [154] [155] using 7 ns laser pulses. Data obtained indicate broadband optical limiting capabilities for the nanowires. The observed optical limiting is comparable to or better than that of carbon nanotubes. The optical limiting is found to arise mainly from nonlinear scattering. In addition to the scientific interest in mechanisms of nonlinear optical properties in such nanosystems, study of optical

limiting properties of the metal nanowires may lead to cheap and efficient optical limiters.

In the present study, nickel nanowires were electrodeposited into anodic film templates with pores of 90 nm diameter at -1.0 V (SCE) at room temperature for one hour. The optical absorption spectra of the nickel nanowire arrays were firstly measured by a spectrometer (Ocean Optics SD2000) at room temperature. Figure 6.15 shows the optical absorption spectra of the nickel nanowire/oxide template composite, and the blank oxide template for comparison. It is obvious that the spectrum obtained from the nickel nanowire/oxide template composite is different from that of the blank anodic oxide template. The optical absorption in the range between 300 and 800 nm is higher for nickel nanowire/oxide template than that of the blank anodic oxide template.

The optical limiting properties of nickel nanowires were then characterized by fluence-dependent transmittance measurements using a Spectron SL402 Nd:YAG laser, at the wavelengths of 532 and 1064 nm, respectively. The laser pulse width (FWHM) was approximately 15 ns. The laser beam, which is spatially Gaussian, was focused using a plano-convex lens. The nanowires specimen was mounted on a stepper motor controlled linear translation stage. The transmitted energy was measured using a pyroelectric laser energy detector (Gentec DUO_2). Another detector was placed at a vertical angle to the beam axis to measure the reflected light by the beam splitter as reference energy, as shown in Figure 6.16. The interval between two laser pulses was kept sufficiently large (typically more than 1 s), to enable the complete thermal relaxation of the sample before the arrival of the following pulse. The input laser fluence (reference) vs. sample transmittance fluence (measurement) was plotted in Figure 6.17.

The energy transmittance at the light fluences less than 5.2×10^3 J /m^2 is constant for both the wavelength of 532 and 1064 nm. However, in excess of 5.2×10^3 J/m^2, the

transmittance decreases as the incident fluence increases a typical property for the optical limiters. The limiting threshold, defined as the incident fluence at which the transmittance falls to 50% of the normalized linear transmittance [151]. The limiting threshold at 532 nm is 2.4 x 10^4 J/m^2; while the limiting threshold at 1064 nm radiation is approximately 5 x 10^4 J/m^2 for nickel nanowires. Obviously, the nonlinear optical limiting is much weaker at 1064 nm compared to that at 532 nm.

There are several mechanisms proposed for optical limiting, including two-photon absorption, free-carrier absorption associated with two-photon absorption, reverse-saturable absorption, self-focusing/defocusing, thermal blooming, and nonlinear scattering [156, 157] . The observation of nonlinear limiting for the nanowires with laser incidence in this work shows that nonlinear scattering is the main mechanism responsible for the nonlinear limiting of the nickel nanowires, since the energy of the laser light is too low (2.32 eV for 532 nm and 1.16 eV for 1064 nm laser) [158] for single-photon excitation which generally requires much higher photon energy (5 eV for Ni) [11]. In non-linear scattering, the key mechanism is the photon-induced ionization and excitation of the metal atoms in metal nanowires. This leads to the formation of rapidly expanding micro-plasmas, which strongly scatter the incident light and results in the limiting behavior. The response of the optical limiting induced by the nonlinear scattering is related to the ability of the photo-ionization of the atoms and the subsequent expansion of the micro-plasmas [159, 160].

In summary, with the observation of optical limiting both at 532 and 1064 nm, non-linear scattering is believed to make a dominant contribution to the limiting performance of nickel nanowire arrays.

6.5 Conclusion

1. Nickel nanowire arrays were successfully fabricated by electrodeposition using highly ordered porous anodic film as templates. The *i-t* response exhibit three different stages corresponding to three growth stages of nickel nanowires during

electrodeposition. The growth rate of nickel nanowires during electrodeposition increases with the increase of electrodeposition voltage and the increase of temperatures.

2. Current efficiency could be influenced by electrodeposition conditions mainly due to affecting the hydrogen evolution rate during the nickel electrodeposition. Increased voltage, higher porosity and lowered temperature improve the current efficiency. However, it is difficult to achieve 100% current efficiency due to the hydrogen evolution as well as template defects.

3. Single crystal nanowires could be obtained at relative low temperature of 3°C. At relatively high temperature of 37°C, nickel nanowires with polycrystalline structure is formed. Mass diffusion on the crystal surface is considered to be the rate-limiting step during nickel electrodeposition at -1 V at 3°C. This explains the formation of single crystal nanowires in the direction of [110]. However, at elevated temperature, the nickel adatoms diffusion rate increases significantly, which is suggested as the reason for the formation of polycrystalline structure.

4. Optical limiting property of the as prepared nickel nanowires/oxide template composite is obtained using a Spectron SL402 Nd:YAG laser. In excess of 5.2 x 10^3 J/m^2 for 1064 nm and 2.4 x 10^3 J/m^2 for 532 nm, the transmittance decreases as the incident fluence increases a typical property for the optical limiters. With the observation of optical limiting both at 532 and 1064 nm, non-linear scattering is believed to make a dominant contribution to the limiting performance of nickel nanowires. This property indicates the highly potential applications of nickel nanowires in ultrahigh-density magnetic recording, ultrafast optical switching, and microwave devices.

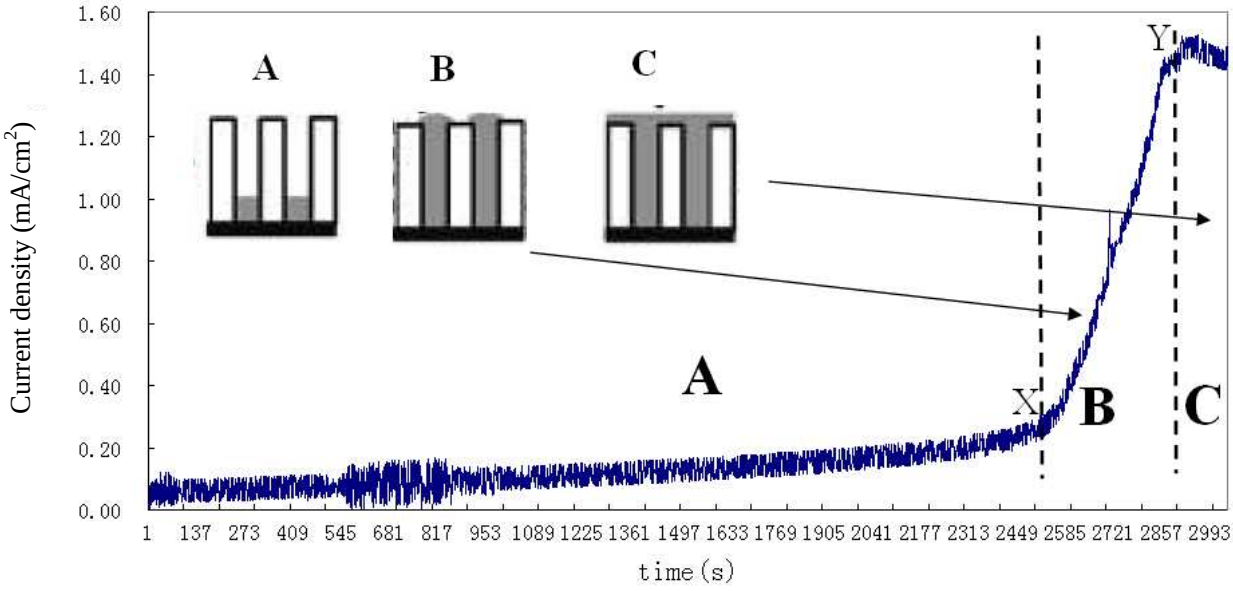

Figure 6.1 *i-t response during nickel electrodeposition, illustrating three growth stages.*

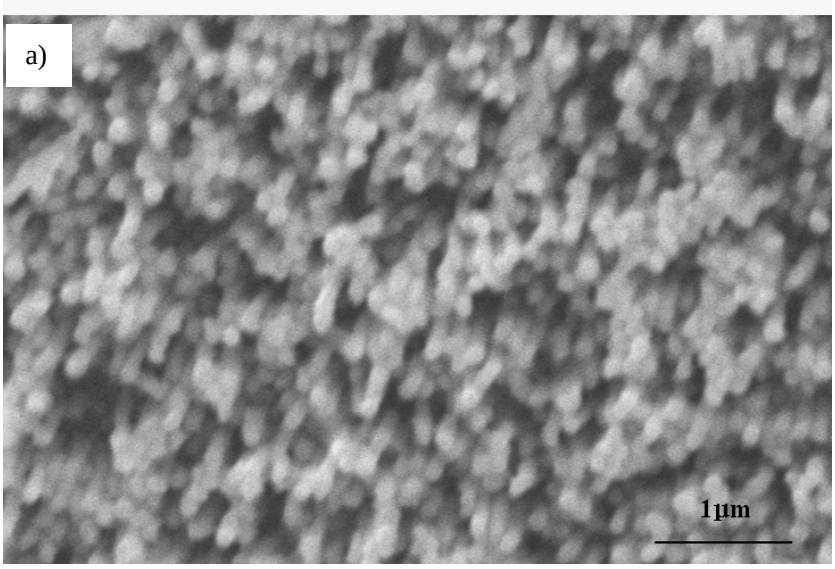

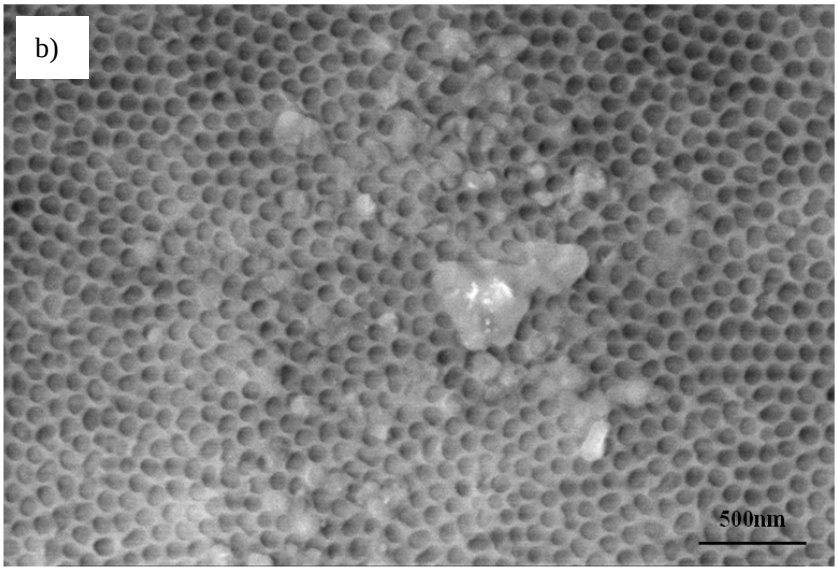
b)
500nm

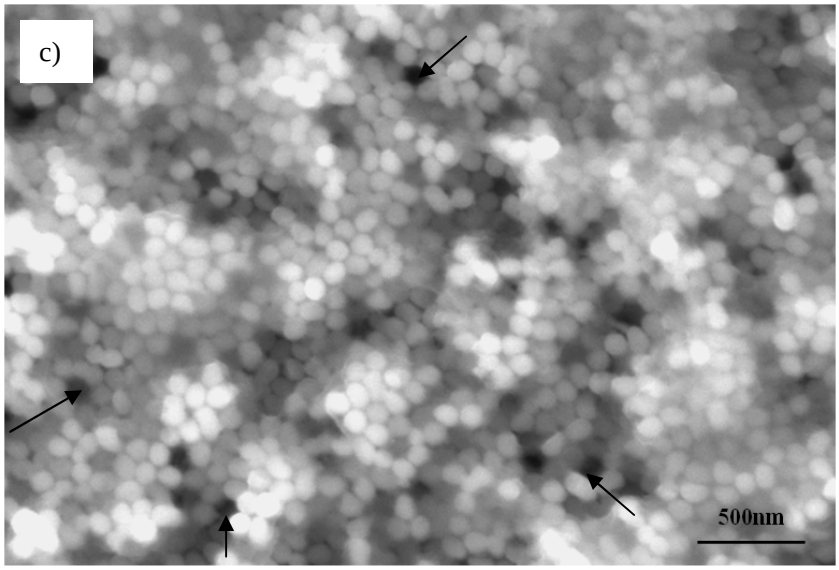
c)
500nm

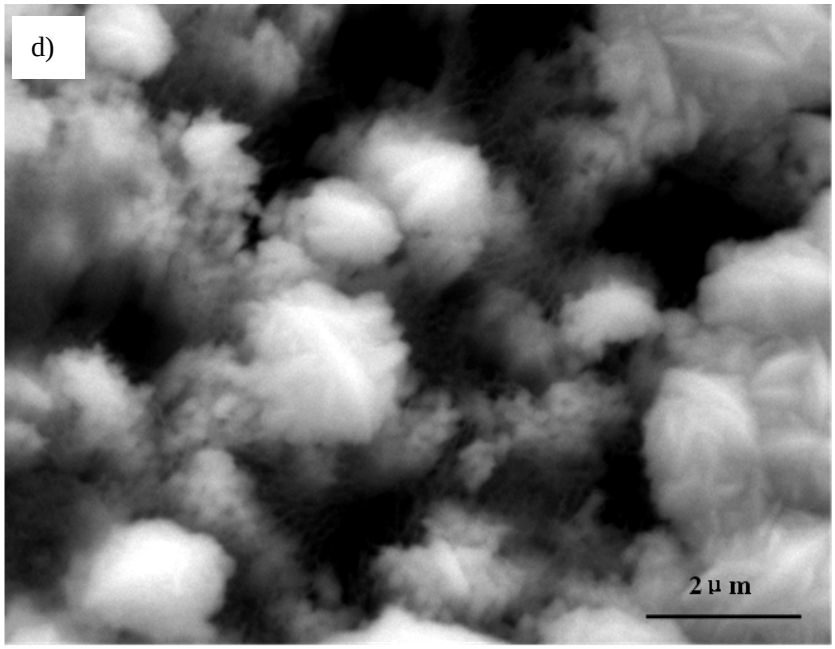

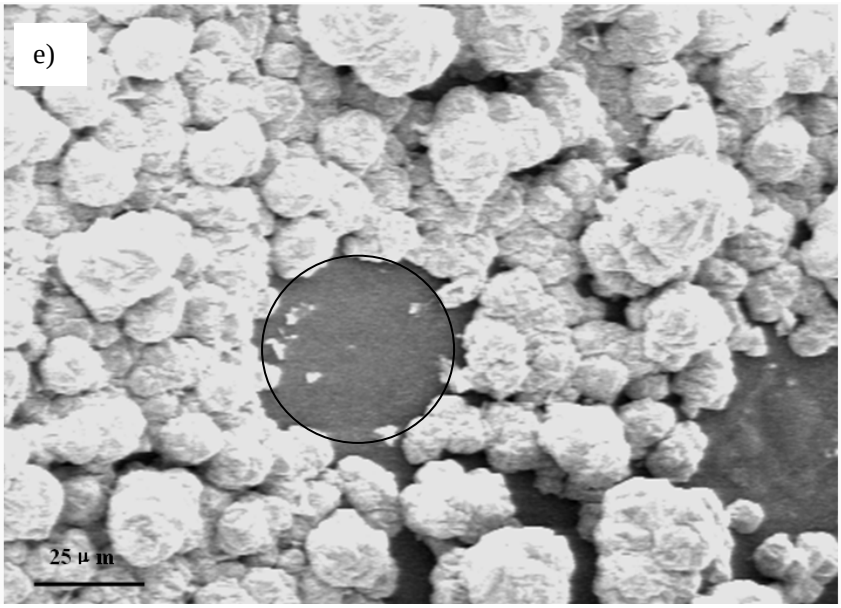

Figure 6.2 *SEM images of top view of deposited nickel nanowires terminated at different stages:*

a) free standing nickel nanowire arrays stopped at stage A;

b) nickel nanowires embedded in oxide template stopped at beginning of stage B;;

c) free standing nickel nanowires stopped at beginning of stage B;

d) nickel nanowires stopped at stage C with hemispherical caps formed on top tips of nanowires, with anodic oxide partly removed;

e) large area top view of nickel nanowires embedded in oxide template stopped at stage C, with extra deposits formed over surface of template.

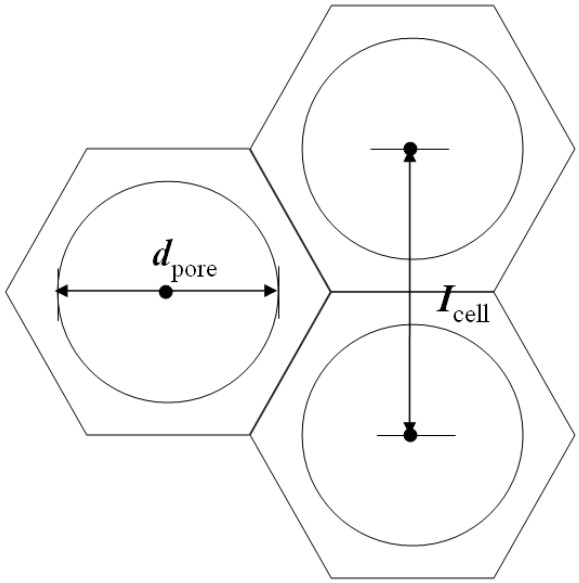

Figure 6.3 *Schematic pore structure of anodic oxide film*

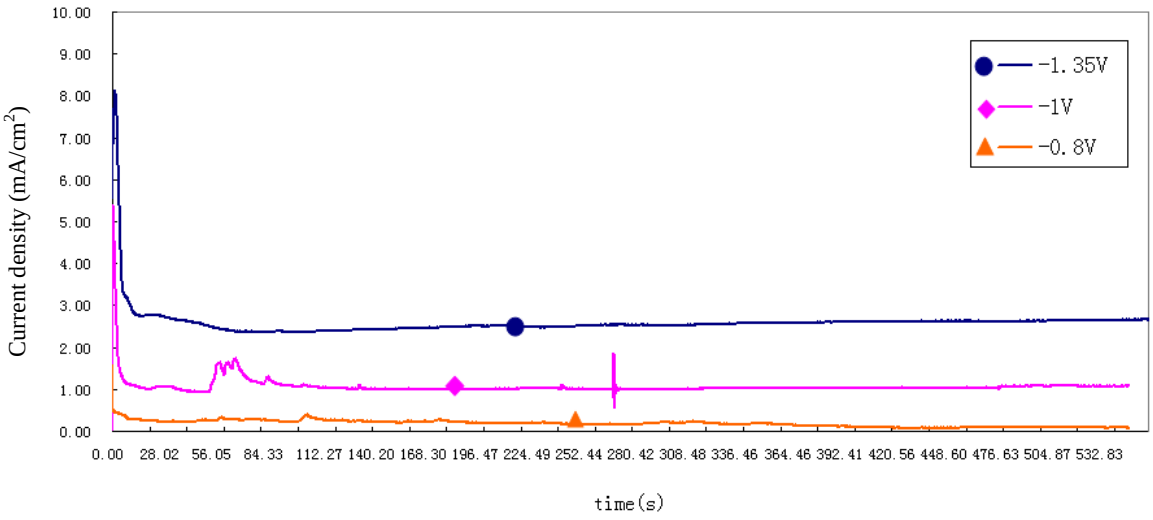

Figure 6.4 *i-t response of nickel electrodeposition at different voltages*

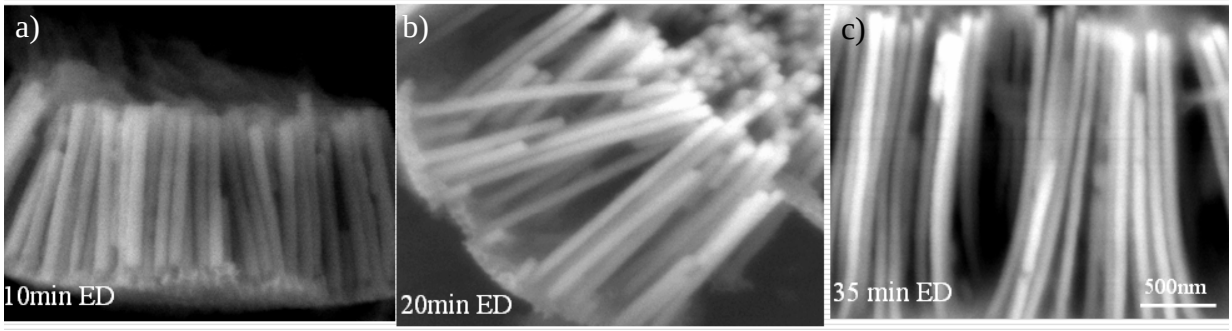

Figure 6.5 *SEM images of: a) Free standing nickel nanowire arrays deposited in oxide template with 90 nm diameters at -1V for 10 mins; b) Free standing nickel nanowire arrays deposited in oxide template with 90 nm diameters at -1 V for 20 mins; c) Free standing nickel nanowire arrays deposited in oxide template with 90 nm diameters at -1 V for 30=5 mins.*

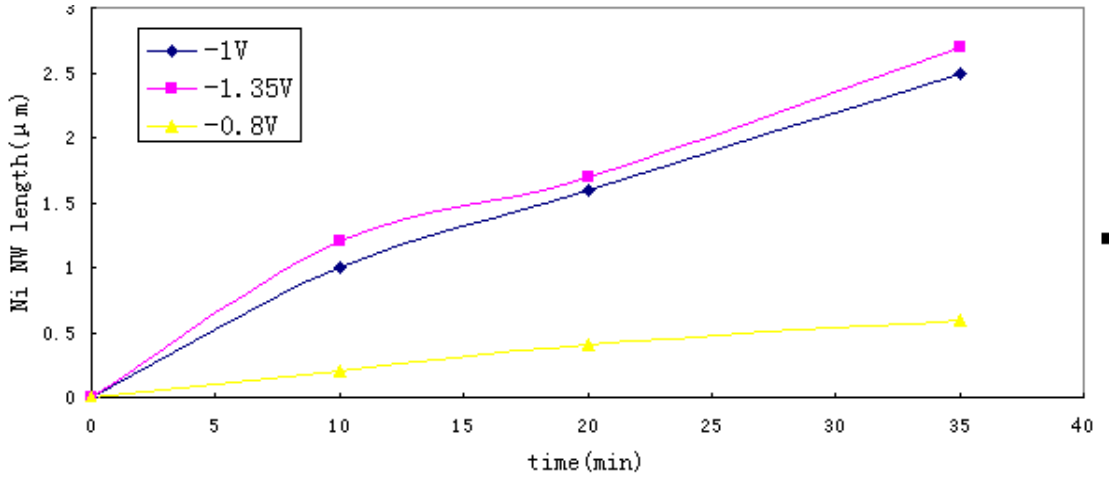

Figure 6.6 *The length of nanowires vs electrodeposition time curve at different voltages.*

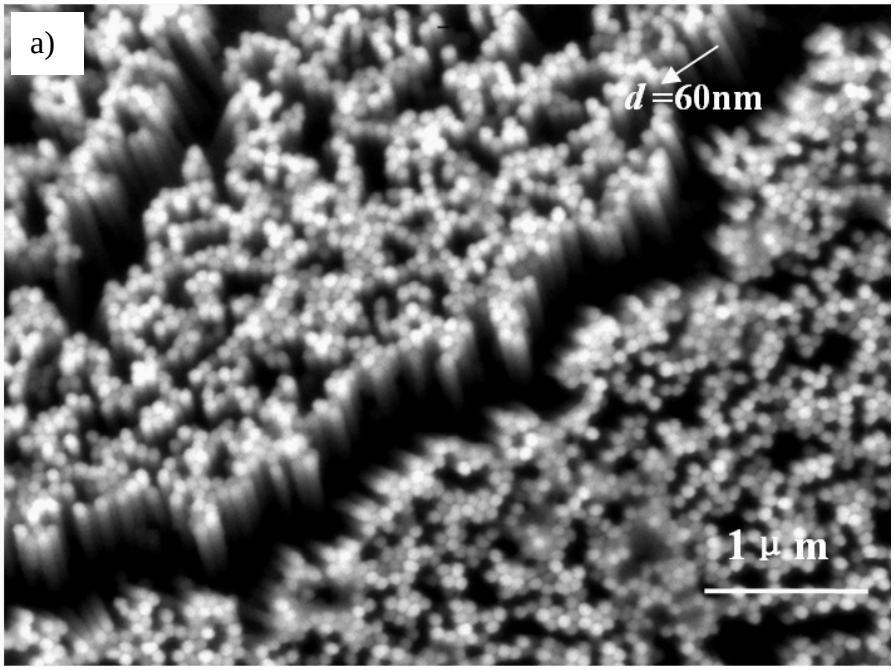
a)
d =60nm
1 μ m

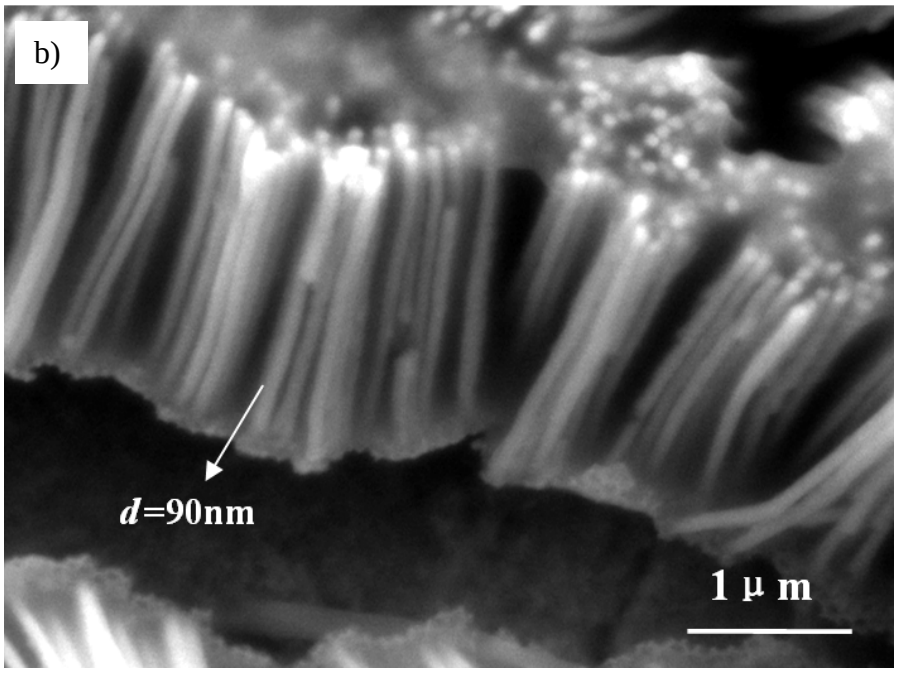
b)
d=90nm
1 μ m

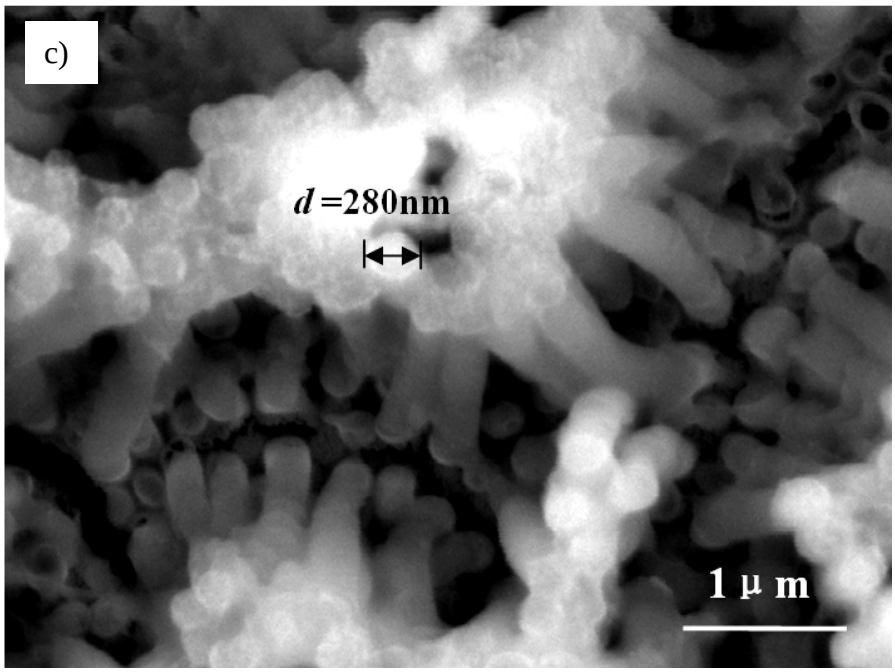

Figure 6.7 *SEM images of nickel nanowire arrays with different diameters*

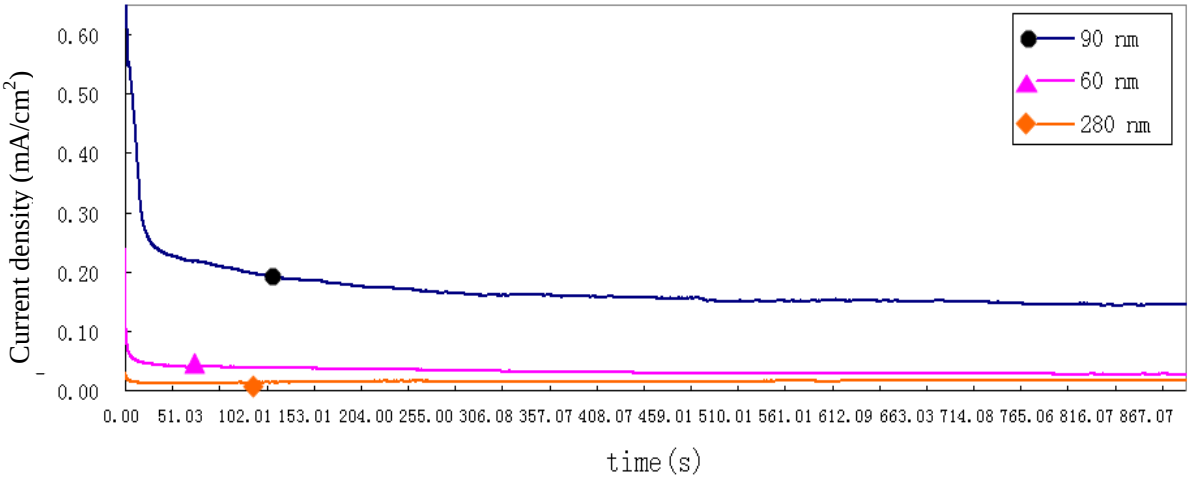

Figure 6.8 *I-t response of nickel electrodeposition at -1 V using oxide template with different pore diameters.*

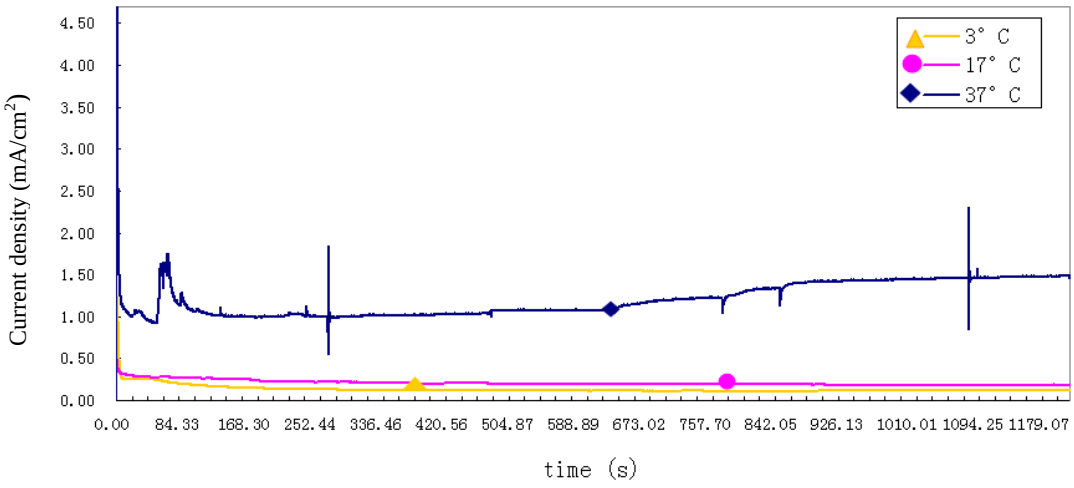

Figure 6.9 *I-t response of nickel electrodeposition at -1 V under various temperatures.*

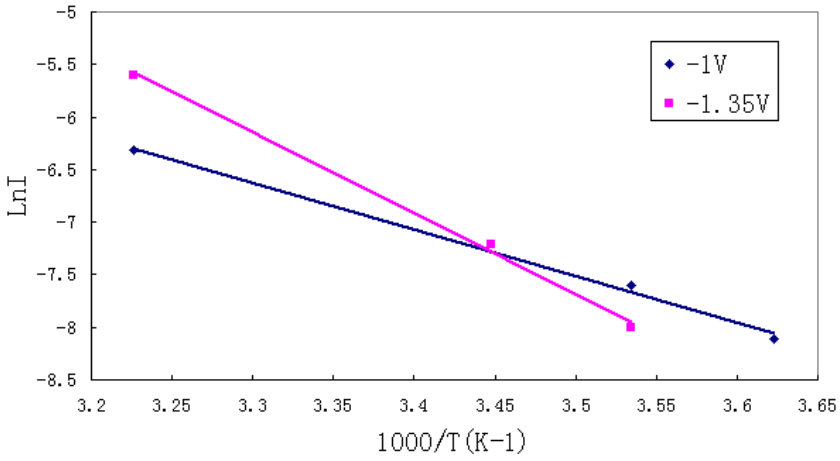

Figure 6.10 *Temperature dependence of the growth rate I of Ni electrodeposition at varied voltages*

a)

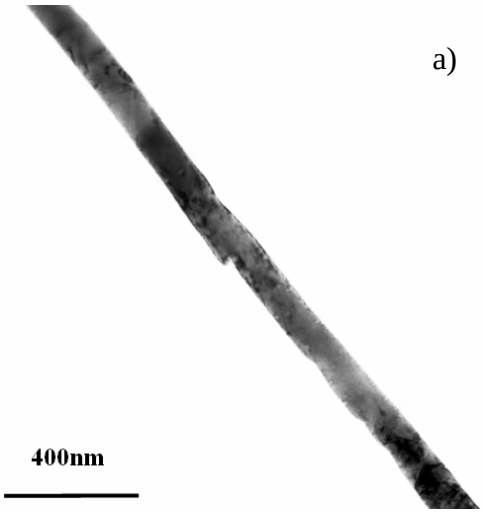

b)

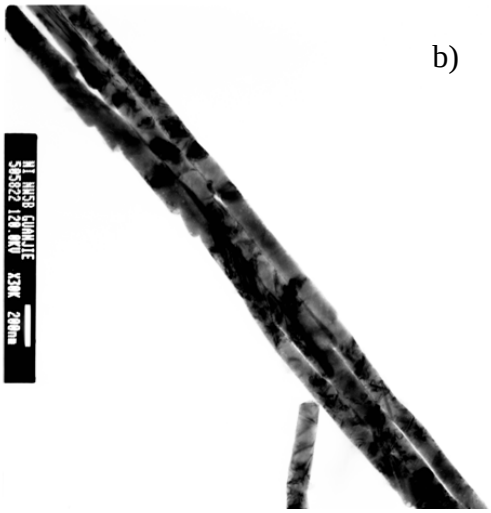

c)

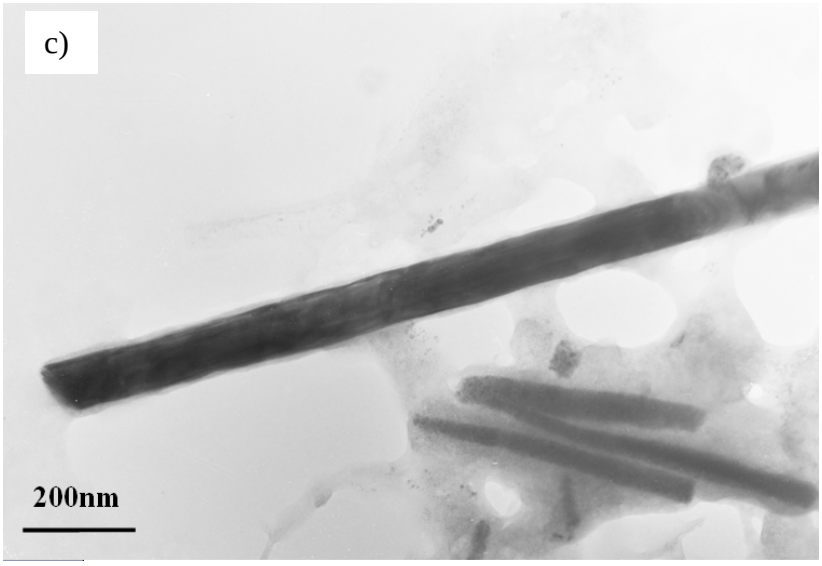

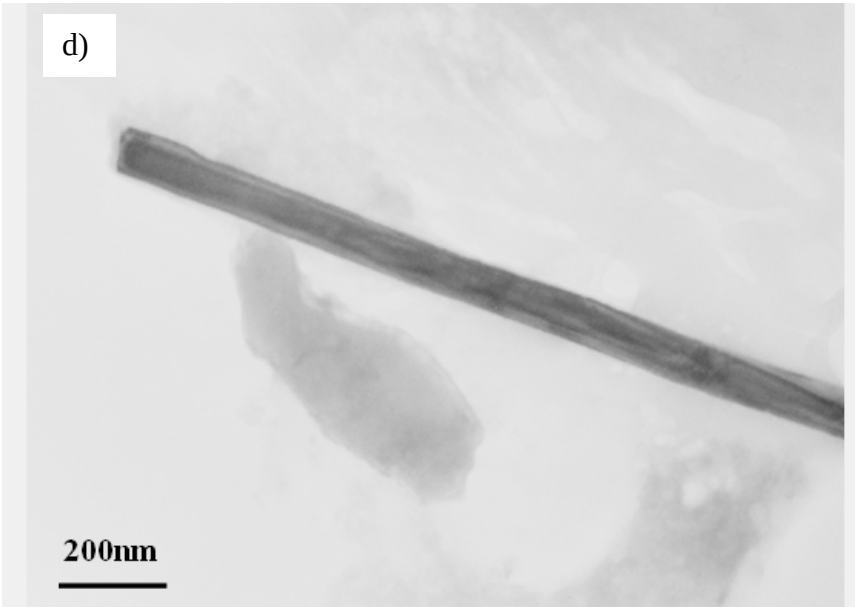

Figure 6.11 *TEM images of free nickel nanowires obtained by electrodeposition at varied temperatures: a) single nickel nanowire obtained under -1 V at 37°C; b) a bunch of nickel nanowires deposited under -1 V at 37°C; c) single nickel nanowire deposited under -1 V at 17°C; d) single nickel nanowire deposited under -1 V at 3°C.*

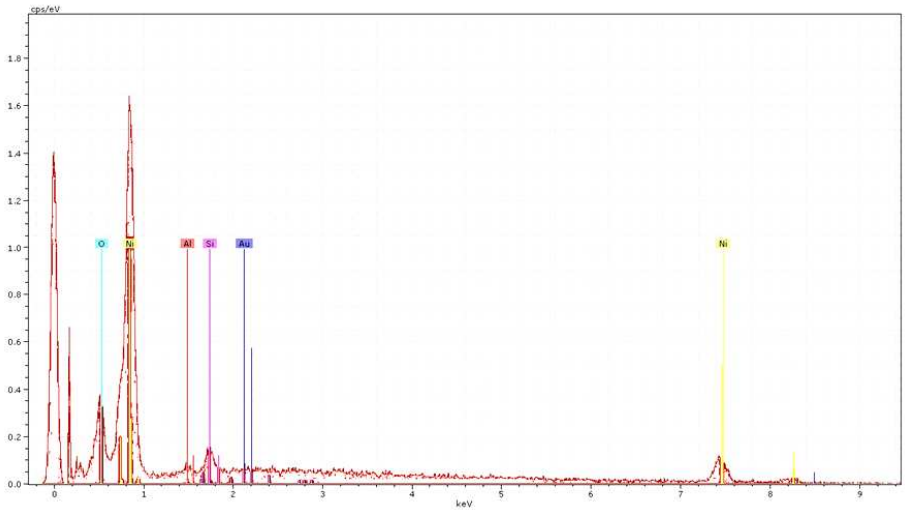

Figure 6.12 *EDX spectrum of free standing nickel nanowire arrays.*

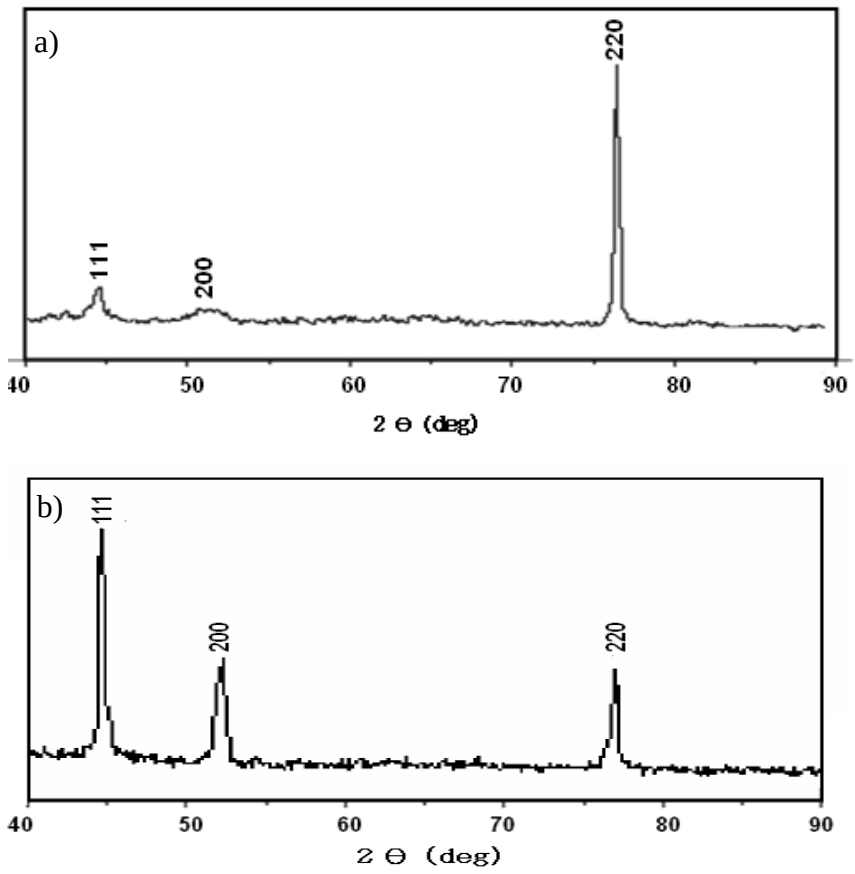

Figure 6.13 *XRD spectra of nickel nanowires deposited under a) 3°C; b) 37°C.*

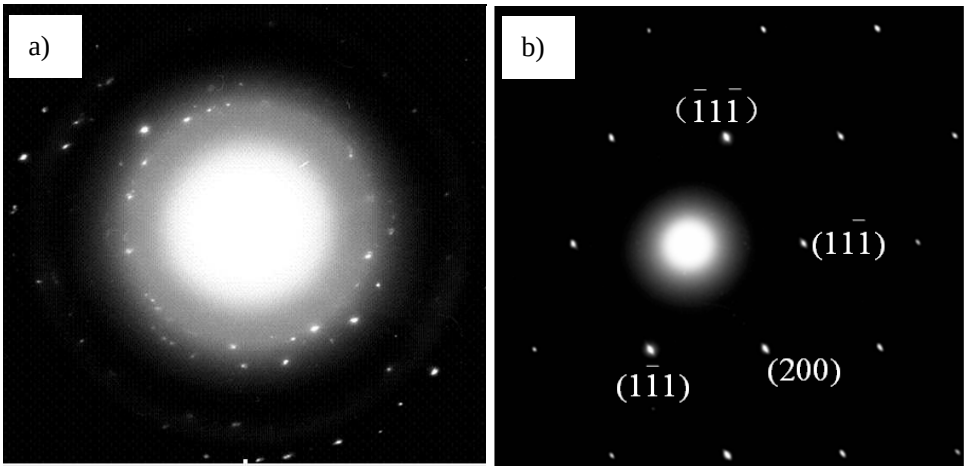

Figure 6.14 *Electron diffraction patterns of nickel nanowires deposited under: a) 37°C; b) 3°C.*

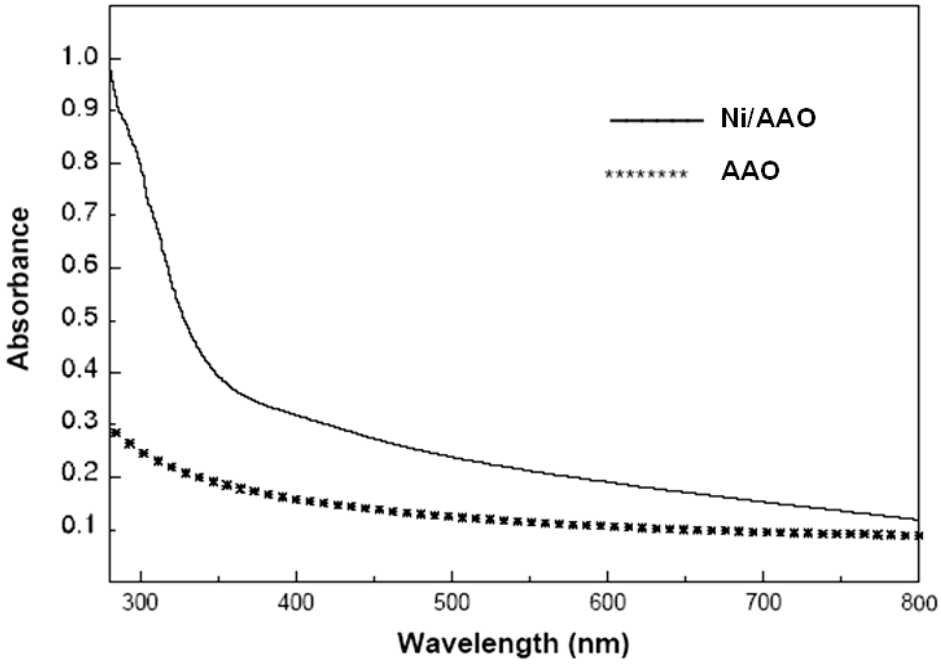

Figure 6.15 *Optical absorption spectra of nickel nanowire arrays and blank oxide template*

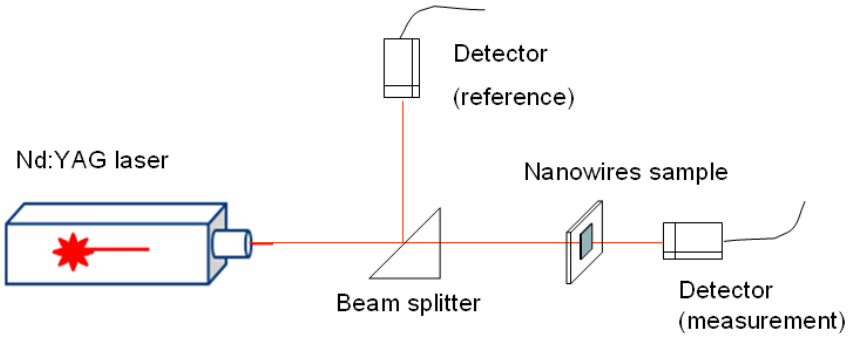

Figure 6.16 *Schematic diagram of the experimental setup for fluence-dependent transmittance measurements of nickel nanowires*

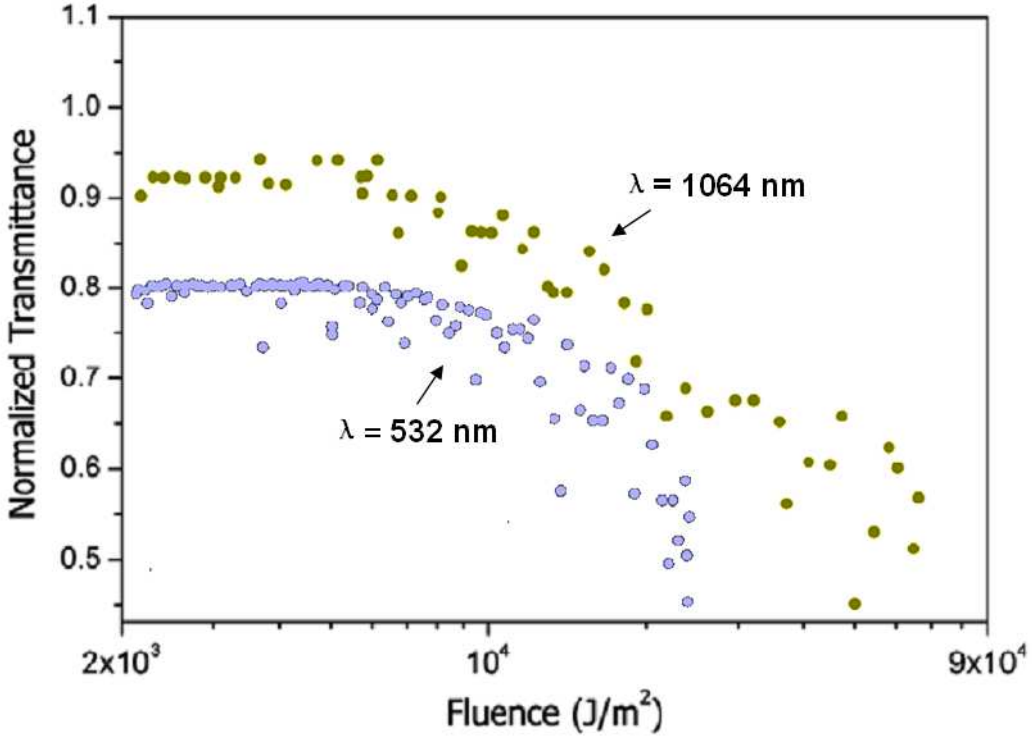

Figure 6.17 *Optical limiting response of the nickel nanowires obtained with laser pulses at a wavelength of 532 nm and 1064 nm*

Table.6.1 *Current efficiency of nickel electrodeposition under selected voltages*

Voltage (V)	Deposition time (s)	Diameter	*Current Efficiency (%)*
-0.8	2100	90 nm	83
-1.0	2100	90 nm	85
-1.35	2100	90 nm	91

Table 6.2 *Current efficiency of nickel electro deposition with alumina template of different pore diameters*

diameter	Voltage (SCE)	Current efficiency (%)
60 nm	-1.0	76
90 nm	-1.0	85
280 nm	-1.0	88

Chapter 7

Fabrication of Manganese Oxide Nanowire Arrays

7.1 Introduction

Supercapacitors are charge-storage devices of high power and energy density that exhibit excellent reversibility and a long cycle life. Such supercapacitors have recently become the subjects of increasing research interest due to their potential applications in several fields including load leveling for batteries in electric vehicles during starting, acceleration, and regenerative braking [161], as well as burst power generation in electronic devices such as mobile phones, photodiode array, camcorders, and navigational devices. Supercapacitors are considered to be a potential device in several future applications, such as an energy manager and tuner in electric systems.

Two types of electrochemical capacitors, the electric double layer capacitor and the electrochemical pseudocapacitor, have been intensively investigated. The electric double layer capacitor typically consists of electrodes such as active carbon with very high surface areas [162]. The non-faradic separation of charges at the interface between a solid electrode and an electrolyte governs the capacitance of such device [163]. On the other hand, the pseudocapacitance arises from fast, reversible faradic redox reactions that occur at electrode surface over an appropriate range of potentials [164]. The difference between the charge storage mechanisms and the fact that carbon has been found to suffer from deterioration by oxidation and from high internal resistance [163] have caused the electrochemical pseudocapacitor to have attracted significant attention for its potential supercapacitor applications. For electrochemical

pseudocapacitors, their capacitive performance is mainly determined by the factors that influence electrochemical kinetics, e.g. reversibility, stability, and power property.

Although amorphous hydrous ruthenium oxide prepared by sol-gel process exhibits ideal pseudocapacitive behavior, very large specific capacitance (over 700 F/g) and excellent reversibility, the high cost of the material limits its commercial use. Therefore, the search for a cheaper oxide with equivalent characteristics is attracting attention. The natural abundance of manganese oxide and its environmental compatibility make it a promising electrode material for use in various energy-storage technologies. A Mn^{4+}/Mn^{3+} redox system involving single-electron transfer is responsible for MnO_2 pseudocapacitive behavior. Manganese oxide stores electrochemical energy by simultaneous injection of electrons and charge-compensating cations, as with other electroactive transition metal oxides, which makes it potentially useful for charge storage applications. Amorphous/crystalline manganese oxide shows high specific capacitance due to the utilization of both electric double layer and redox effects.

Recently, several researchers began to develop an effective method for preparing manganese oxide with favorable pseudocapacitive characteristics. In order to synthesize manganese oxide electrodes, several chemical techniques such as sol–gel deposition from colloidal suspensions and electrochemical deposition have been adopted. The preparations of powder manganese oxides by thermal decomposition and co-precipitation processes have been studied previously. The processes of using such oxide powders for the fabrication of electrodes, including synthesizing the powder, mixing the power with a conducting agent and a binder, and making electrodes, are, however, complicated and inconvenient. A more effective preparation process for manganese oxide electrodes for application in capacitors is being sought. Hu and Tsou [165] reported that hydrous manganese oxide with ideal pseudocapacitive behavior could be prepared by anodic deposition in $MnSO_4$ solution

on a carbon substrate. However, the physical and chemical nature of the oxide and the effects of the process conditions on the electrochemical characteristics of the oxide have not been well established. Furthermore, the deposition rate in such media was low. So, anodic deposition of manganese oxide in other electrolytes with a relatively high deposition rate is of interest.

In the present study, the deposition of manganese oxide nanowires in anodic oxide template in 0.1 M manganese acetate and 0.1 M Na_2SO_4 mixed solution is investigated. The deposited manganese oxide nanowires are characterized by X-ray diffraction (XRD), scanning electron microscopy (SEM), conventional and high resolution transmission electron microscopy (TEM). The electrochemical characteristics of the manganese oxide deposited at various potentials are also evaluated by cyclic voltammetry (CV).

7.2 Deposition kinetics

The deposition of manganese oxide takes place through a number of intermediate steps, as follows [166]:

$$\text{Anode: } Mn^{2+} + 2H_2O \longrightarrow MnO_2 + 4H^+ + 2e- \quad (1)$$

$$\text{Cathode: } 2H^+ + 2e \longrightarrow H_2 \quad (2)$$

$$\text{Overall: } Mn^{2+} + 2H_2O \longrightarrow MnO_2 + H_2 + 2H^+ \quad (3)$$

The mechanism of the electrodepositing reaction at the anode is:

$$2Mn^{2+} \longrightarrow 2Mn^{3+} + 2e^- \quad (5)$$

$$2Mn^{3+} \longrightarrow Mn^{2+} + Mn^{4+} \quad (6)$$

$$Mn^{4+} + 4H_2O \longrightarrow Mn(OH)_4 + 4H^+ \quad (7)$$

$$Mn(OH)_4 \longrightarrow MnO_2 + 2H_2O \quad (8)$$

In Elsemongy‘s work [167], it was stated that the first step is the oxidation of Mn^{2+} to form the Mn^{3+} compound $Mn[(CH_3COO)_2]^-$. After the hydrolysis of the Mn^{3+} ion,

resulting from the dissociation of the complex in the presence of acetate, the deposition of manganese oxides including MnO, Mn_2O_3 and MnO_2 etc. proceed due to the instability of Mn^{3+}. Acetate acts as complexing agent, which has an important role in supporting the presence of small metal ion concentration at the anode, so that their concentration may be high enough for the deposition of oxides. From the above reactions, it is obvious that both the concentration of manganese ions near the anode and the current density (available electrons) have an influence on the deposition process.

7.3 Anodic deposition of manganese oxides

7.3.1 Electrolyte composition

The effect of manganese acetate concentration, in the range of 0.1 to 0.5 M, on the formation of manganese oxide nanowires under constant current was investigated. 0.1 M sodium sulphate was added in the electrolyte in all cases. The current density was 10 mA/cm^2 in both cases. The deposition process lasted for 250 s.

Figure 7.1 displays the SEM micrographs of the manganese oxide nanowires produced in 0.1 M and 0.5 M manganese acetate solution respectively. Figure 7.1 (a) shows the manganese oxide nanowires after the removal of anodic film template. Bundles of nanowires could be observed with nanosized dots present at the tips of nanowires, as indicated by arrows in Figure 7.1 (a).

In Figure 7.1 (b), the anodic film template was not removed. A compact manganese oxide film was formed all over the surface of the anodic film template. The manganese oxide film seems to be composed of granules in the size of approximately 100 nm to 300 nm.

Therefore, the manganese acetate concentration influences the morphology of the formed manganese oxide. When the electrolyte concentration is at a relatively lower

value of 0.1 M, manganese oxide was successfully deposited into pores of anodic film template to form nanowires.

EDX analysis of the deposited manganese oxide is shown in Figure 7.2. The aluminium peak is due to the residual anodic oxide template. Sodium and sulphur are due to species incorporated from deposition electrolyte. EDX analysis revealed that the deposited oxide in 0.5 M manganese acetate solution had an O/Mn content ratio that is about 30% higher than that of the oxide deposited in 0.1 M manganese acetate solution. It should be noted that the influence of Al_2O_3 is excluded by determining the amount of aluminium element, calculating the accordant oxygen content in Al_2O_3, and then subtract from the measured oxygen yields. Chang [168] investigated the manganese oxide obtained in electrolyte of different concentrations using XPS. It was found that the water contents were almost constant in the oxide deposited in solutions with different manganese acetate concentration. Therefore, the O/Mn ratio determined by EDX analysis is reliable, since the influence of water content induced by hydrous oxides is also excluded. This implies that the oxide deposited in an electrolyte of higher concentration may have a higher oxidation state of manganese ions compared to that formed in electrolyte of lower concentration. However, 0.5 M solution is not suitable for nanowires fabrication. Thus, the relatively moderate electrolyte concentration is suitable for the formation of manganese oxide nanowires.

7.3.2 Constant current deposition

The effect of current density on the formation of manganese oxide nanowires was investigated. The applied current densities are 0.1 mA/cm^2 and 10 mA/cm^2. Electrodeposition was carried out in a mixed solution of 0.1 M manganese acetate and 0.1 sodium sulphate for 250 s.

Figure 7.3 shows the SEM micrographs of the manganese oxide nanowires formed at various current densities after the removal of anodic film template. Nanowire arrays

are clearly observed in both cases. For the nanowires shown in Figure 7.1 (a), nanosized nodules exist at the top tips of nanowires in both cases. EDX analysis of the samples is shown in Figure 7.4. Both manganese and oxygen peaks are present in each spectrum, indicating the successful formation of manganese oxide nanowires by deposition.

7.3.3 Constant voltage deposition

Constant voltage deposition was conducted in a mixed solution of 0.1 M manganese acetate and 0.1 M sodium sulphate. Figure 7.5 displays the current density-time response when the applied voltage is 0.6 V (SCE). The current density decreases with time at the start of the process, and finally reached a stable value after approximately 100 s. In literatures [168, 169], similar current density-time response during constant voltage deposition of manganese oxides was reported.

SEM images of manganese oxide nanowires formed by constant voltage deposition process after the removal of anodic film template are displayed in Figure 7.6. The deposition process was conducted for 300 s. Nanowire arrays are clearly evident, exhibiting relatively short length. Neighboring individual nanowires conglomerate together to form bundles. This is commonly observed in previous works [169], and in Figure 7.1 and 7.3 of the present work. Nevertheless, there are no nodules as that observed in Figure 7.4, indicating that manganese oxides are successfully filled into pores without any unwanted deposits on the template surface. EDX analysis confirmed the existence of manganese and oxygen, as shown in Figure 7.7.

7.3.4 Pulse voltage deposition

Pulse constant voltage deposition refers to deposition process with the potential being alternated rapidly between two different values. This is accomplished with a series of

pulses of equal amplitude, duration and polarity, separated by periods of zero voltage. Each pulse consists of an 'on' period during which a potential is applied, and an 'off' period during which the open-circuit potential is applied.

During the period when the voltage is off, metal ions migration from the bulk solution into the layer next to the anode continues. Several pulsing scheme with one segment 'on' at an applied potential of 0.6 V (SCE) is shown in Figure 7.8 (a) and (b). The 'on' period is set at two levels: 5 s and 10 s, and the 'off' period remain at 10 s in both cases. The corresponding current density-time responses are shown in Figure 7.8 (c) and (d). It is evident that for each 'on' period, the current exhibits an instantaneous high peaks, and then decreases significantly but smoothly until reaching stable values. A current density-time response on one segment of 'on' period is the same as the current density-time response of constant current deposition. In the case of 5 s 'on' period, when the applied potential was stopped, a significant reversal current was observed. This might be due to the precipitation of the hydroxide in neutral electrolyte (employed here), thus opposing the process of deposition [167].

Figure 7.9 shows the SEM images of the manganese oxide nanowires deposited using pulse voltage with the 'on' period of 5 s (Figure 7.9 a) and 10 s (Figure 7.9 b and c) of pulsed deposition after removal of anodic oxide template. It is observed that manganese oxide nanowires could be obtained in both cases.

In the present work, when the deposition was performed on porous anodic oxide template, pulsed voltage deposition does not exhibit obvious advantages. By comparing the SEM images of manganese oxides nanowires obtained in both conditions (Figure 7.6 and Figure 7.9), no improvements of morphology could be observed. Therefore, pulsed voltage deposition was not employed in the following works.

7.4 Effects of the process parameters on the formation of manganese oxide nanowires

7.4.1 Morphology

The morphology of the manganese oxide nanowires produced at various potentials was examined using SEM. All manganese oxide nanowires were formed in a mixed solution of 0.1 M manganese acetate and 0.1 M sodium sulphate at room temperature. The scanning electron micrographs of Fig 7.12 shows the manganese oxide nanowires formed with the deposition potentials of 0.4 V, 0.6 V and 1.0 V. It is evident that manganese oxide nanowires can be successfully deposited into pores of anodic film template in the selected range of deposition potentials. The nanowires exhibit great uniformity of thickness with almost the same length, as shown in Figure 7.10 (a), after the removal of anodic film template. The nanowires exactly replicate the inner-shape of the pores with the diameter of approximately 90 nm. Figure 7.10 (c) shows the cross section view of the nanowires with manganese oxide nanowires being still embedded within the pores of anodic film template. It is evident that in most of the pores, manganese oxides were successfully deposited in, indicating a high pore filling rate.

The TEM micrographs of manganese oxide nanowires formed from various deposition voltages are shown in Figure 7.13. Individual nanowires produced by deposition in mixed solution of 0.1 M manganese acetate and 0.1 M sodium sulphate at 0.6 V (SCE) for 600 s are evident. The nanowires have smooth surface and uniform diameter. The inset is a diffraction pattern (ED) of the middle region of the longest nanowire in Figure 7.11 (a). The diffusion ring pattern suggests that the manganese oxide nanowires have an amorphous structure.

Figure 7.11 (b) displays a TEM micrograph of a bunch of nanowires that was obtained with the same condition as for that shown in Figure 7.11 (a). Several nanowires are parallel to each other with almost the same lengths. All nanowires exhibit uniform diameters from top to end. The electron diffraction patterns of the

nanowires suggest amorphous structures.

7.4.2 Composition

High resolution transmission electron microscopy was used to further investigate the composition and crystallographic structure of the as-prepared manganese oxide nanowires.

High angle anular dark field images of the manganese oxide nanowire formed by deposition at voltages of 0.4 V, 0.6 V and 0.8 V respectively are shown in Figure 7.12. It is evident that the nanowires formed in all three conditions possess cylindrical shape with even diameter of approximately 65 nm. The surface of nanowires is smooth. Fine bright spots are randomly dispersed all over nanowires in all three cases. The composition of these spots awaits further investigation.

The bright tips at the end of nanowires, as shown in Figure 7.12 (b) and (c)，are silver, which has been confirmed by EDX line scan analysis along the nanowire length, as shown in Figure 7.13. An silver-paste was employed to adhere the anodic film template onto copper substrate, which could be the reason that silver is detected in EDX analysis. The other two detected elements are Mn and O. The percentages of these two elements increase simultaneously when EDX line scanned over nanowire. The analysis provides convincing evidence that the composition of nanowires is Mn and O, i.e. manganese oxides.

Diffraction patterns of the nanowires are exhibited in Figure 7.14. In all three cases diffusion rings are observed, suggesting amorphous structures of the deposited materials. In Figure 7.14 (c) which is the specimen deposited at 0.8 V，scattered spots are observed, indicating the existence of crystallites. This might be due to the existence of silver.

Energy dispersive X-ray spectra are shown in Figure 7.15. Compared to EDX analysis with SEM, the one with Tecnai F30 HRTEM provides more precise statistics, since the analysis was restricted within specific fine area over the specimens. The atomic O/Mn ratio was calculated based on quantitative EDX analysis. In each case of the three different voltages, EDX data over two different areas was employed to ensure accuracy. As seen in EDX spectra, Si peak is present, which should be from silicone paste that was used to seal samples during the template fabrication process. The formula of silicone is –(Si-O)n-, therefore the amount of oxygen in silicone is excluded by reducing the atomic amount of Si. Further, the amount of oxygen in anodic film was calculated with the atomic ratio of 3:2 as in Al_2O_3 and then excluded. The resultant O/Mn ratios are 3.05 for 0.4 V, 2.45 for the nanowires formed at 0.6 V and 1.42 for 0.8 V. Therefore, in the deposited manganese oxide nanowires, manganese oxide at different valances could be present. However, due to the possible existence of hydrous oxides, the measured O/Mn ratio does not indicate the actual Mn valance. It is the variation of O/Mn ratio that could be useful to provide information on the valance of manganese in manganese oxide nanowires deposited at different voltage. The average O/Mn ratio increases as the electrodeposition voltage decreases from 0.8 V to 0.4 V. Under higher deposition voltage, the resultant manganese oxides have a higher percentage of higher valence manganese.

In order to further investigate the difference in the structures between the nanowires obtained by deposition under varied voltages, high resolution TEM of the nanowires were carried out, as shown in Figure 7.16. It could be seen that although the diffraction pattern shows amorphous rings, there are short range order of the microstrucutre. As mentioned in previous paragraph, fine bright spots are dispersed all over the nanowires. By high resolution TEM, as shown in Figure 9.17, these bright spots are confirmed to be crystalline particles.

Fast fourier transform (FFT) of the lattice images of the fine crystalline particles was

carried out using digitalmicrograph software to determine the crystalline structure. In Figure 7.16 (d), the d-spacings are 2.17 A, 2.45 A and 2.27 A respectively, and the angle in between are measured to be approximately 60°. By comparing these results with relevant material crystal data sheet, the d-spacings and the angle are consistent with that of MnO_2 with a hexagonal structure. i.e. ε-MnO_2, in which a=b=0.28 nm, c=4.45 nm and α=β=90°, γ=120°. The three crystal faces are indexed to be (100), (002) and (101) corresponding to the measured d-spacings of 2.45 A, 2.27 A and 2.17 A respectively.

As shown in Figure 7.16, calculation from these HRTEM images reveals that high population of fine crystalline particles with an average diameter of approximately 2 nm to 5 nm exist within the manganese oxide nanowires. Crystalline particles with the smallest average size are observed in manganese oxide nanowires deposited at 0.4 V with diameters of approximately 2 to 3 nm, while the average sizes of crystalline particles in nanowires deposited at 0.6 V and 0.8 V appears no difference. Previously manganese oxides formed with anodic deposition were reported to be amorphous, since in diffraction patterns, only amorphous rings are evident. However, the high resolution TEM images in the present work explored the existence of fine crystalline particles embedded within the amorphous matrix for the first time. Further, the properties of manganese oxide nanowires could be influenced by this microstructure, which is illustrated below.

7.5 Electrochemical behavior

Figure 7.17 shows the cyclic voltammograms of manganese oxides electrodes in 0.1 M Na_2SO_4 solution at 25°C. A potential scanning rate of 5 mV s^{-1} was employed.

Within the potential range 0 V–1.0 V (SCE), the capacitive-like and symmetric i=E responses of the CV curves indicated that the oxides formed at different voltages possess electrochemical characteristics suitable for pseudocapacitor application.

Further, since the voltammetric charge on the positive and negative sweeps were approximately equal, the reversibility of the redox transitions in each deposited manganese oxide was very high. However, the specific voltammetric charge (voltammetric charge per gram of the deposited manganese oxide), which was integrated from positive to negative sweeps, varied with the deposition voltage. The size of the rectangular loop, which reveals the capability of charge storage, decreased with increasing deposition voltage. The specific capacitance (C) of the manganese oxide could be evaluated from Equation (9):

$$C = \text{specific voltammetric charge} / \text{potential range} \quad (9)$$

The calculated specific capacitance values of the manganese oxide, measured in 0.1 M Na_2SO_4 solution with a potential scanning rate of 5 mV s^{-1}, are 220, 210 and 195F g^{-1} for the manganese oxides deposited at 0.4 V, 0.6 V and 0.8 V, respectively. The high specific capacitance of the manganese oxide deposited at the relatively low voltage might be attributed to the change of manganese oxide microstructures. A fine crystalline microstructure might be beneficial in increasing the specific capacitance of the oxide electrode for the supercapacitor [170, 171]. The fine crystalline particles within the amorphous matrix of the manganese oxide nanowires could favorite the higher capacitance.

7.6 Conclusion

Manganese oxide nanowires were fabricated by anodic deposition under constant current, pulse voltage and constant voltage mode respectively. A mixed solution of 0.1 M manganese acetate and 0.1 M sodium sulphate was selected as the deposition electrolyte.

Uniform manganese oxide nanowires were fabricated at constant voltage in the range of 0.4 V to 1.0 V (SCE). Manganese oxide nanowires formed under different

deposition voltage exhibit amorphous structure with short range order. Fine crystalline particles with average diameter of 2 to 5 nm in high population were revealed. The crystalline particles were determined to be ε-MnO_2 with hexagonal structure. The average O/Mn ratio of manganese oxide nanowires decreases with the increase of deposition voltage, indicating that higher percentage of high valence manganese are present in the oxides formed at higher deposition voltage.

EDX analysis provides the average O/Mn ratio of deposited manganese oxide nanowires. The ratio decreases with the increase of deposition voltage, indicating that an increased percentage of higher valence manganese species is present in the oxide formed at lower deposition voltage.

The electrochemical performance of manganese oxide nanowires array is investigated by cyclic voltammograms at a scan rate of 5 mV s-1 from 0 to 1 V (SCE) in 0.1 M Na2SO4 solution at 25°C. High capacitance of 220, 210 and 195 F g^{-1} for those deposited at 0.4 V, 0.6 V and 0.8 V, respectively were obtained, indicating excellent capacitive property.

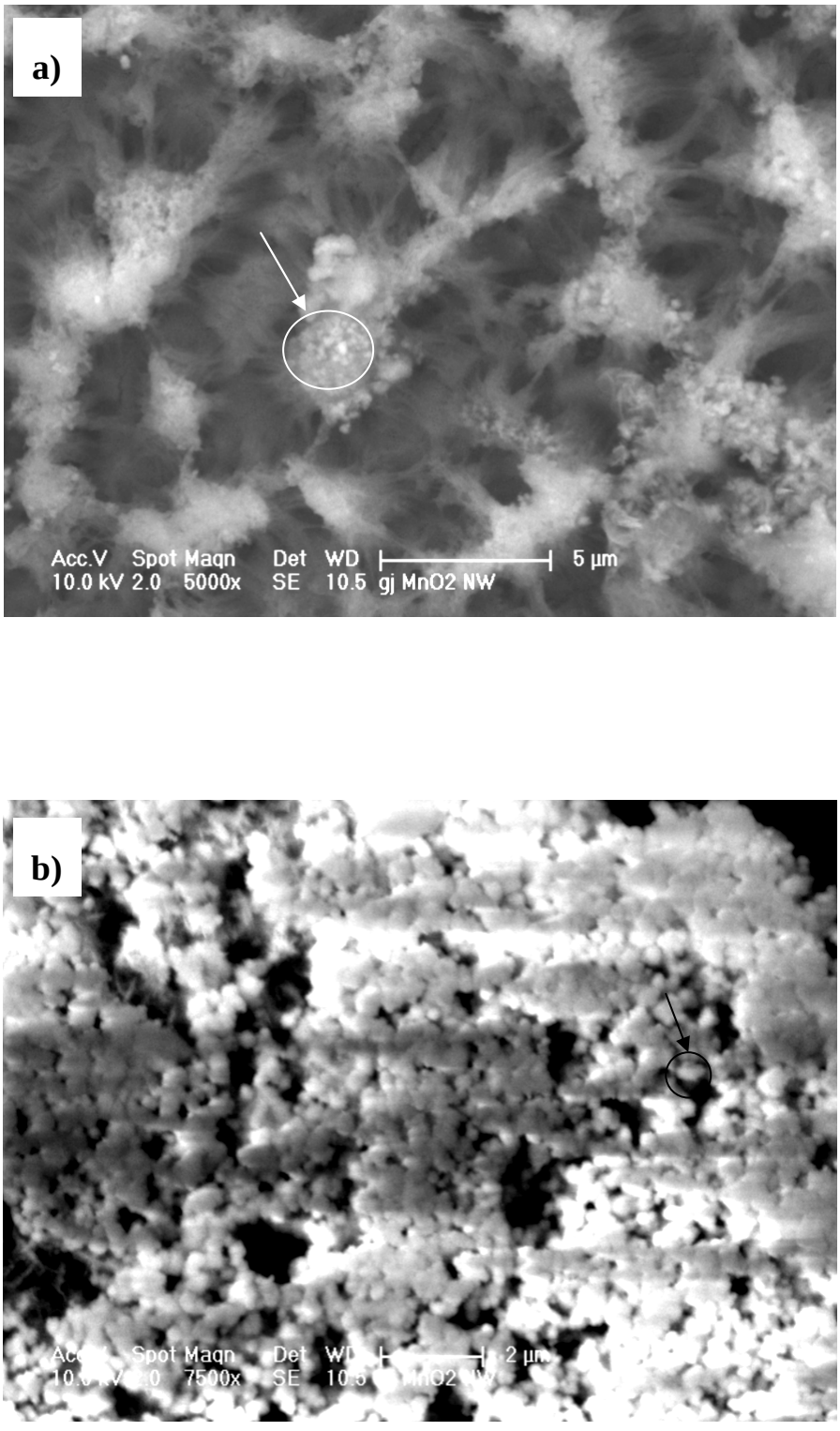

Figure 7.1 *SEM images of manganese oxides formed under constant current density of 10 mA/cm^{2}in: a) 0.1 M manganese acetate; b) 0.5 M manganese acetate*

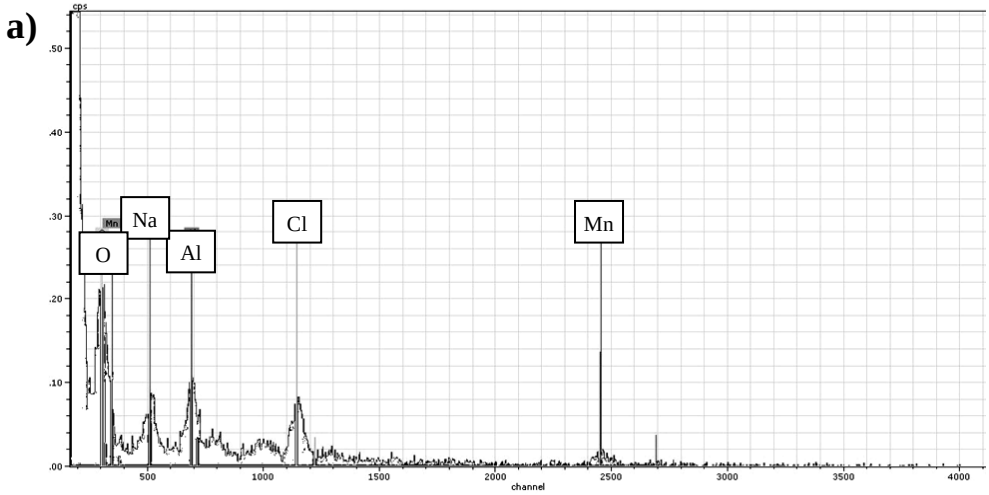

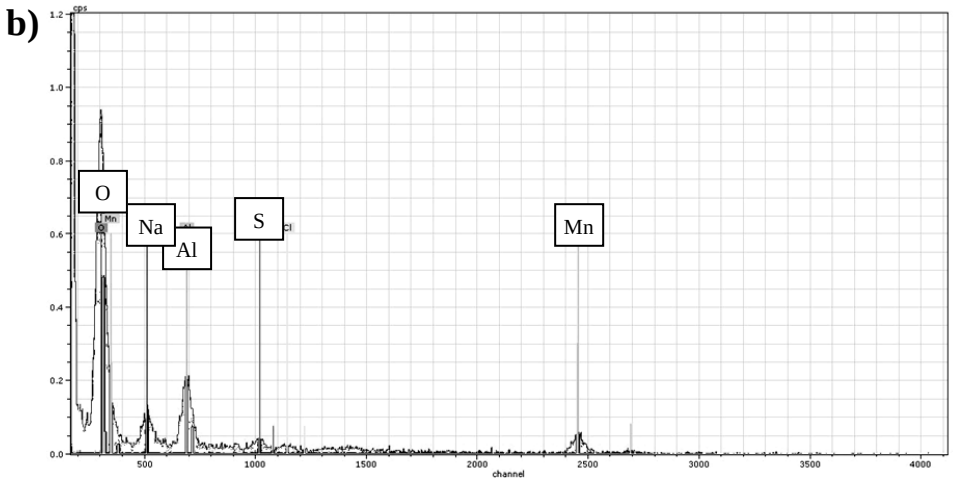

Figure 7.2 *EDX spectra of manganese oxide nanowires formed under constant current density10 mA/cm^2 in: a) 0.1 M manganese acetate; b) 0.5 M manganese acetate.*

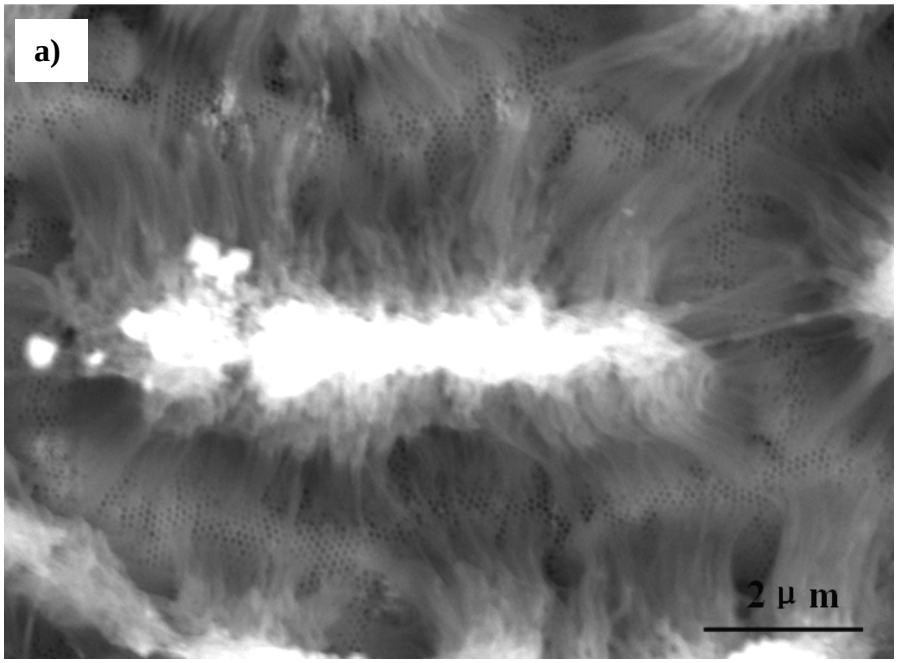

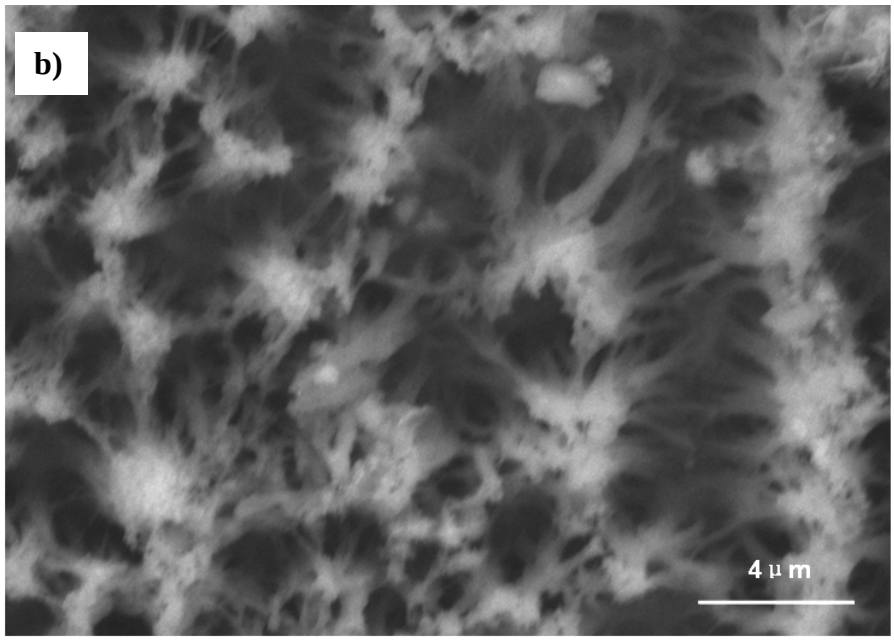

Figure 7.3 *SEM images of manganese oxide nanowires obtained by constant current density deposition: a) 0.1 mA/cm^2 and b) 10 mA/cm^2.*

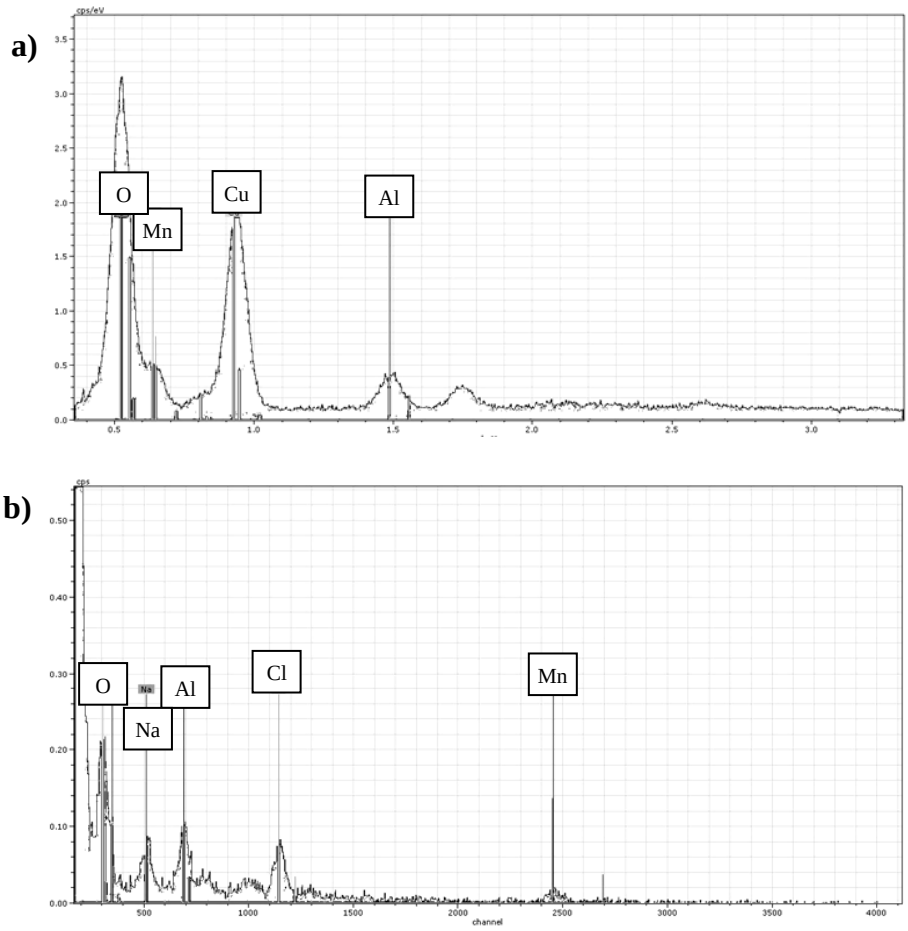

Figure 7.4 *EDX spectra obtained from manganese oxide nanowires produced by constant current density deposition: a) 0.1 mA/cm^2 and b) 10mA/cm^2.*

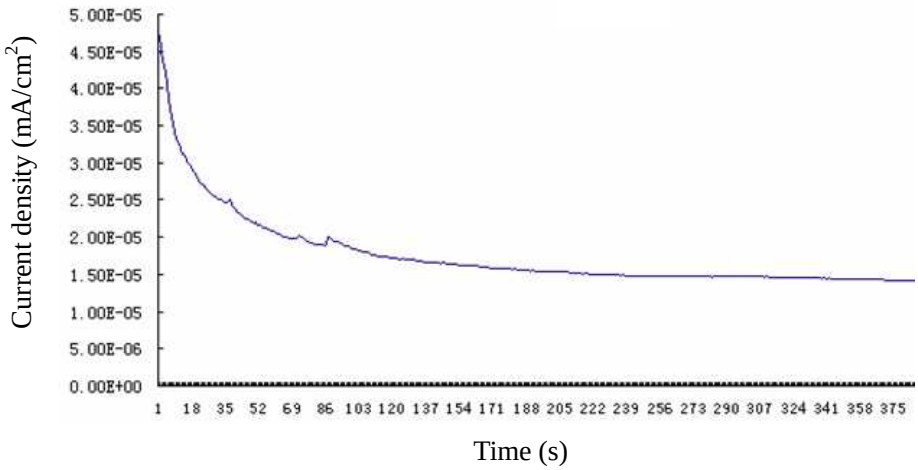

Figure 7.5 *Current-time responses during deposition of manganese oxide nanowires at constant voltage of 0.6 V (SCE).*

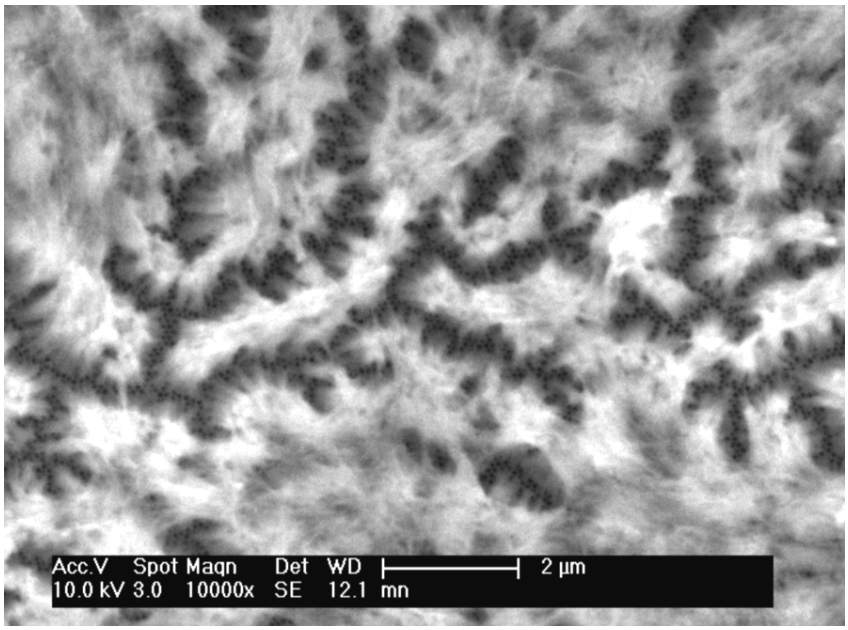

Figure 7.6 *SEM image of manganese oxide nanowires produced by constant voltage deposition at 0.6 V (SCE).*

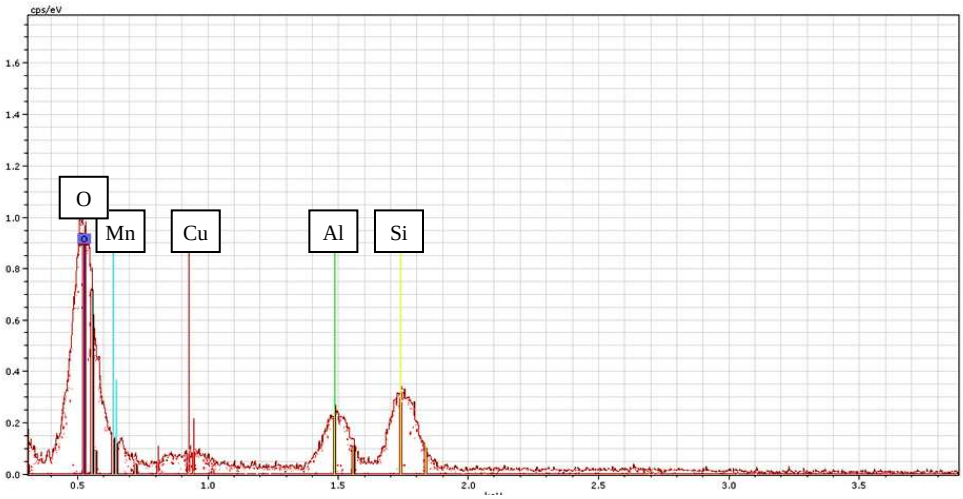

Figure 7.7 *EDX spectrum of manganese oxide nanowires produced by deposition at constant voltage under 0.6 V (SCE).*

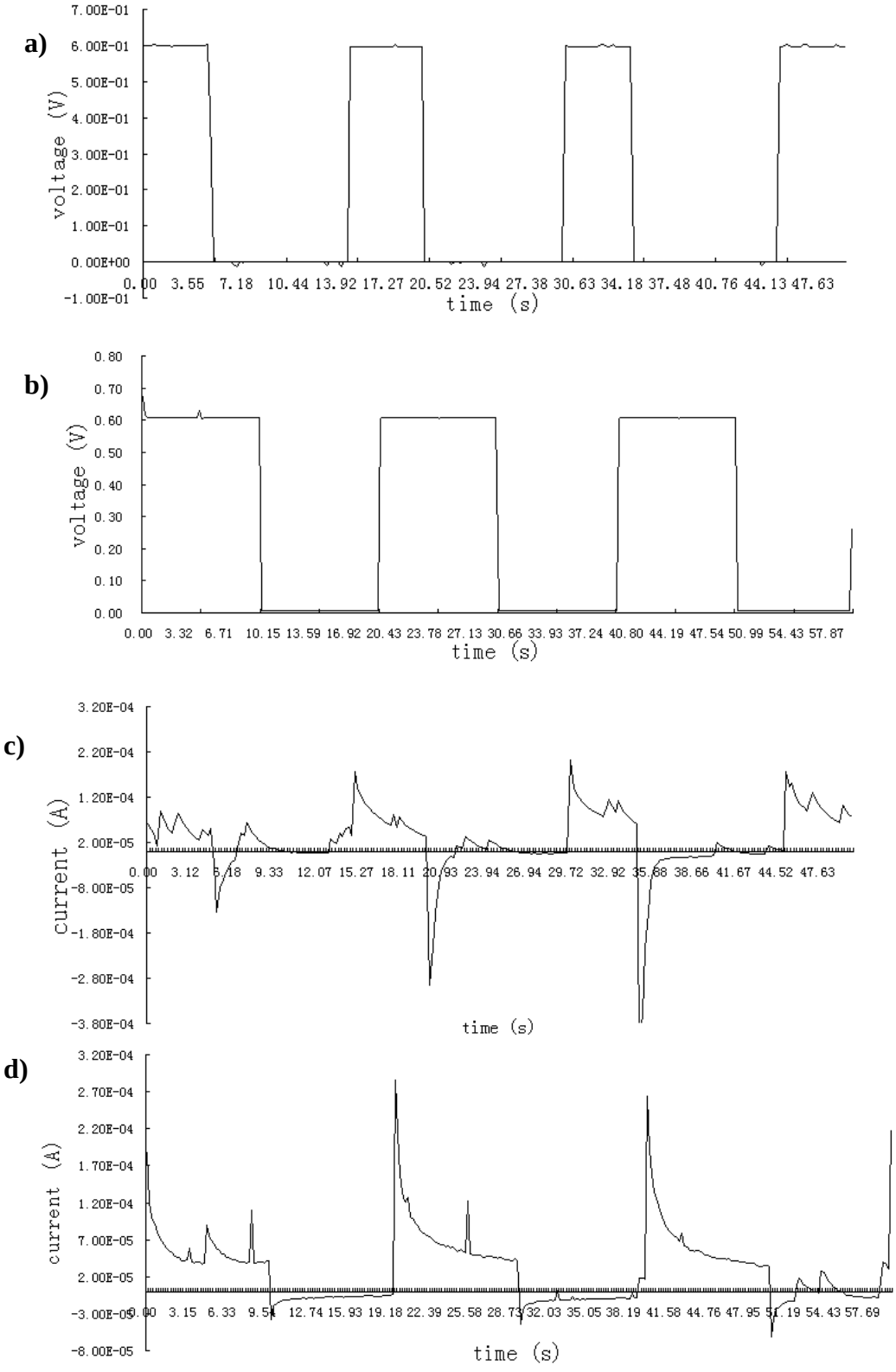

Figure 7.8 *(a) and (b) potential pulsing scheme for deposition; (c) and (d) corresponding current-time responses under four pulsed potentials*

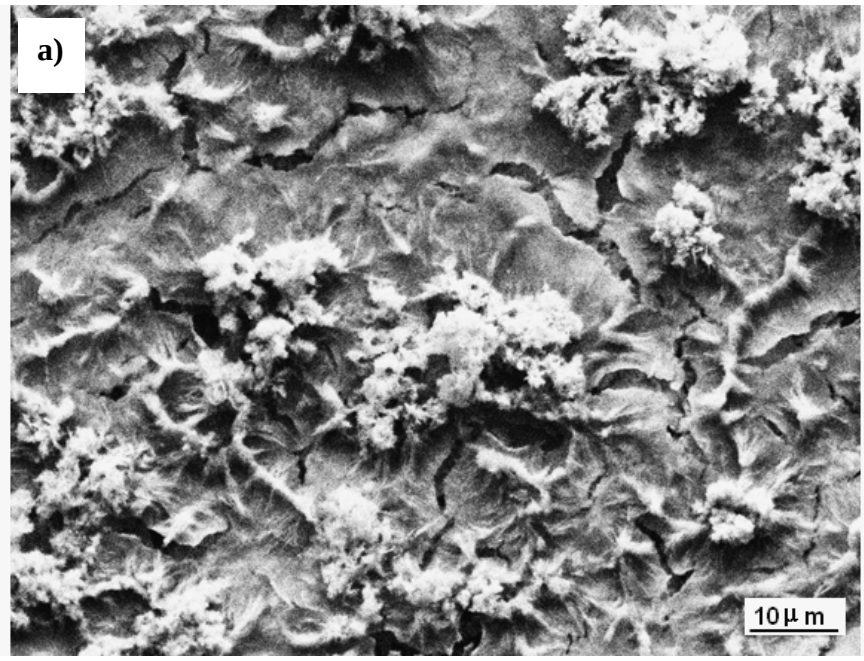
a)
10 μ m

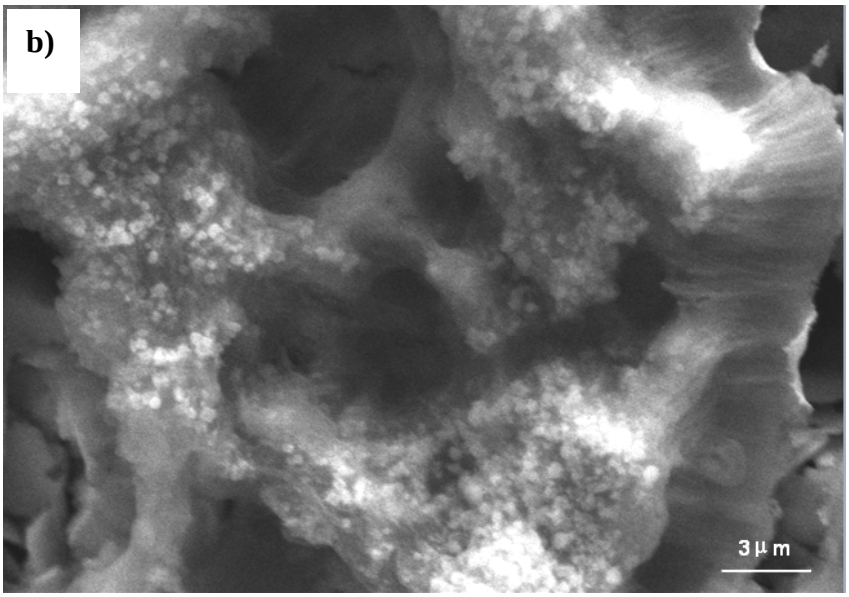
b)
3 μ m

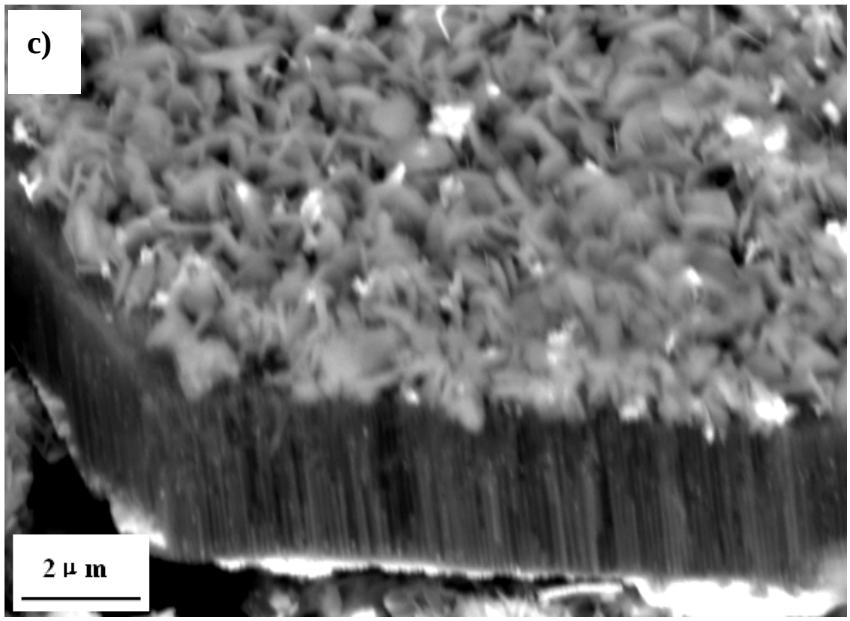

Figure.7.9 *SEM images of manganese oxide nanowires obtained by pulse deposition: a) 0.6 V; 5 s (on) + 10 s (off); b) 0.6 V, 10 s (on) + 10 s (off).*

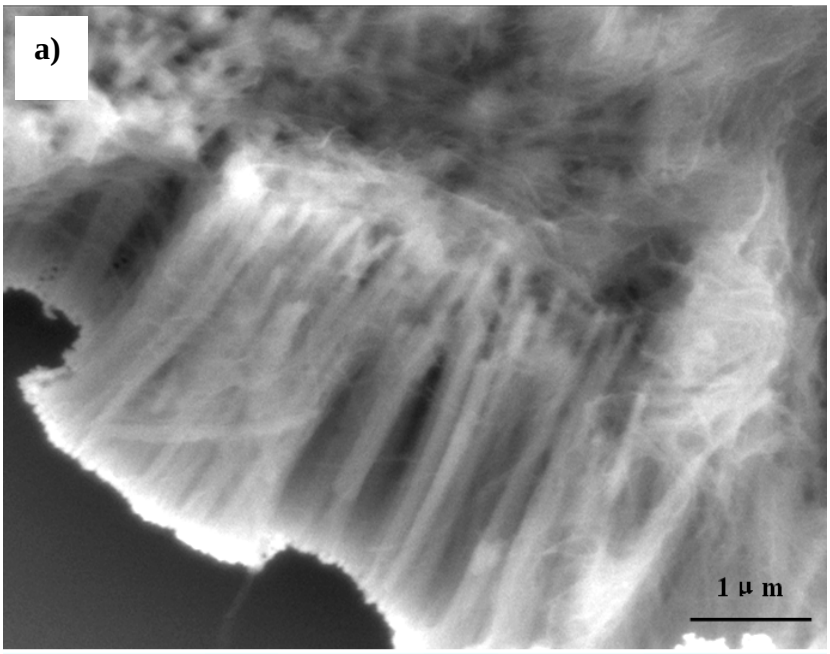
a)
1 μ m

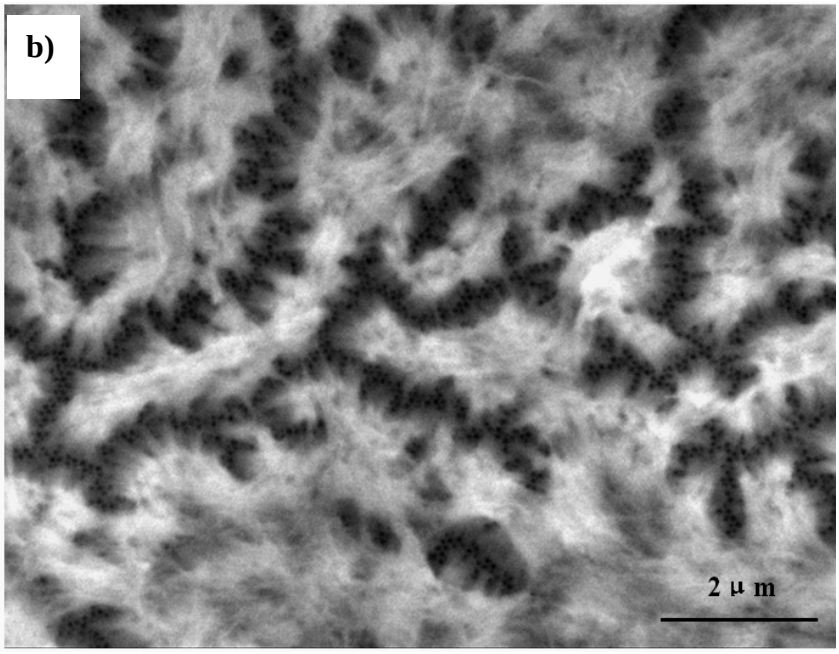
b)
2 μ m

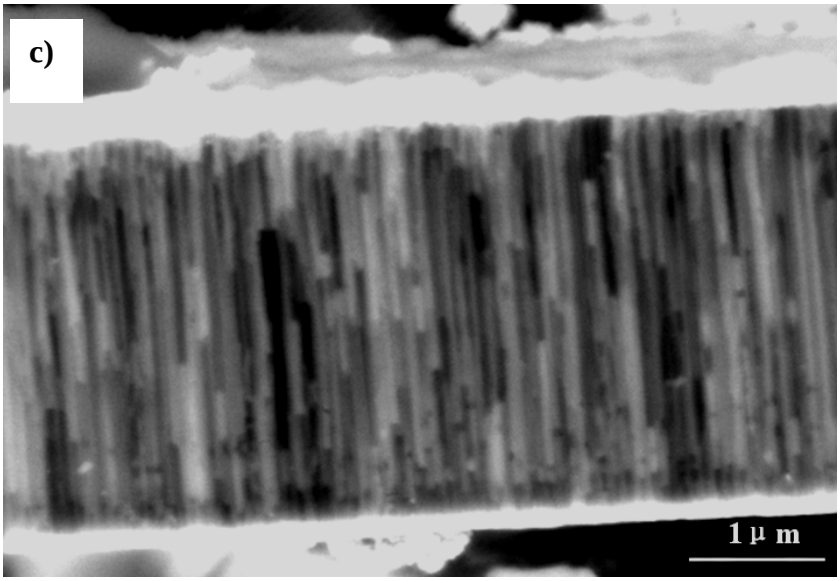

Figure 7.10 *SEM images of manganese oxide nanowires deposited at a): 0.4 V, side view of free-standing nanowires after removal of oxide template; b) 0.6 V, top view of free standing nanowires after removal of oxide template; c) 1.0 V, side view of nanowires embedded within oxide templates.*

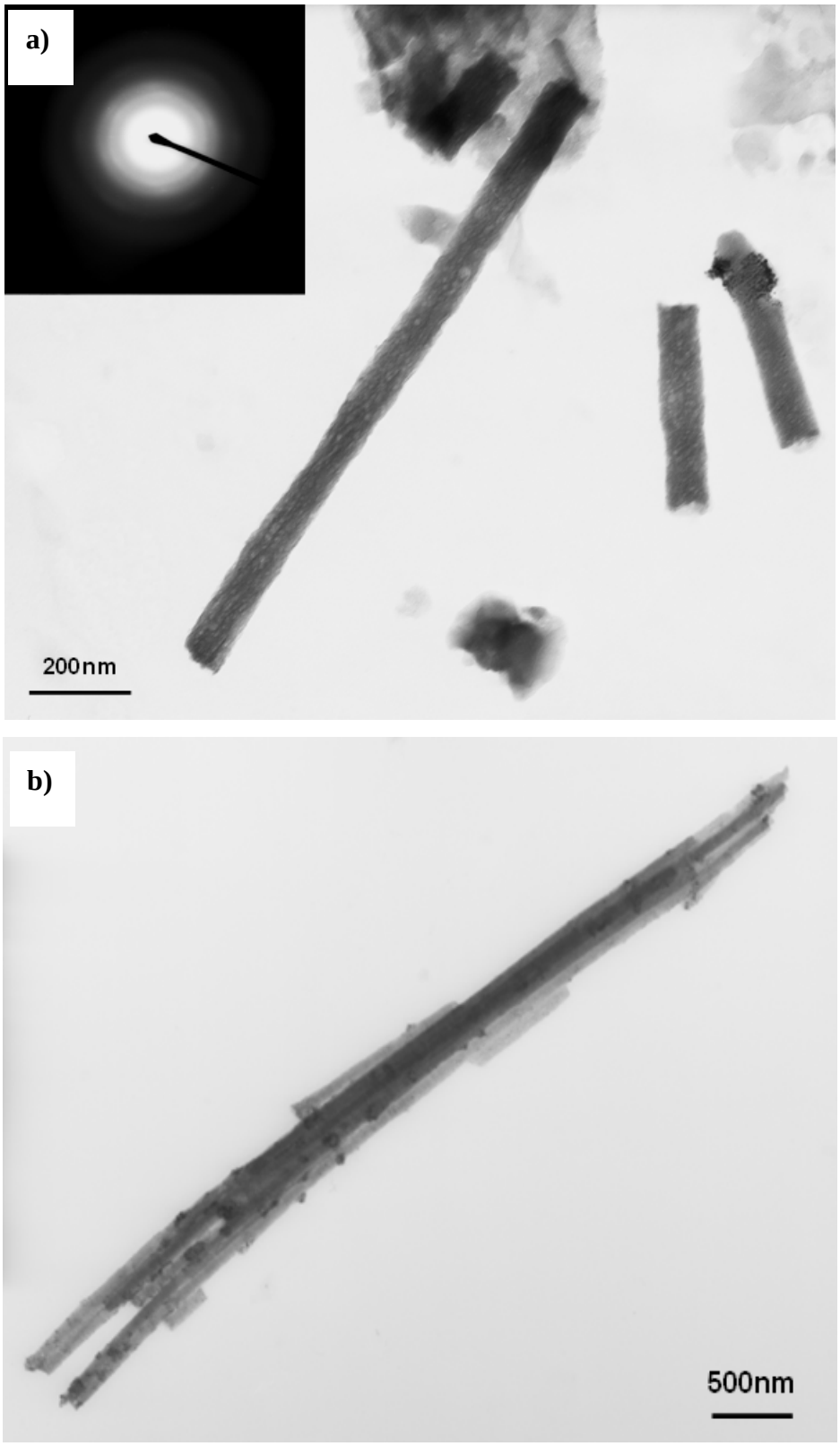

Figure 7.11 *TEM images of free standing nanowires obtained by deposition at 0.6 V.*

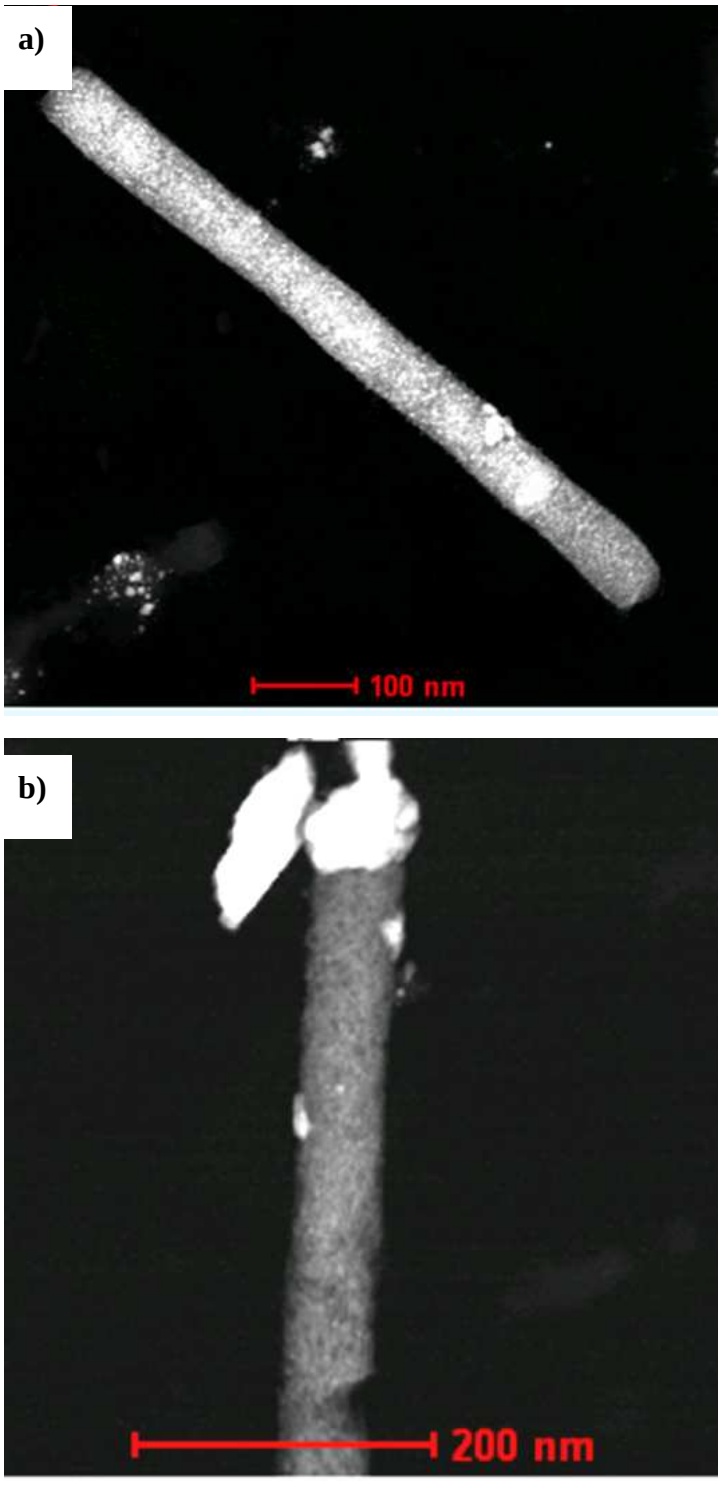
a)
100 nm
b)
200 nm

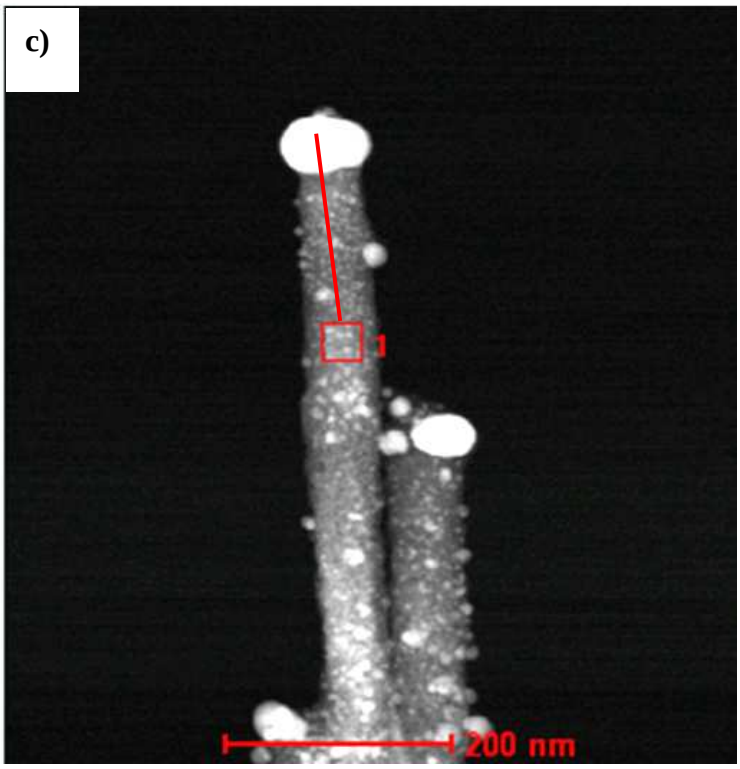

Figure 7.12 *High angle anular dark field images of manganese oxide nanowires obtained at voltages of: a) 0.4 V; b) 0.6 V; c) 0.8 V*

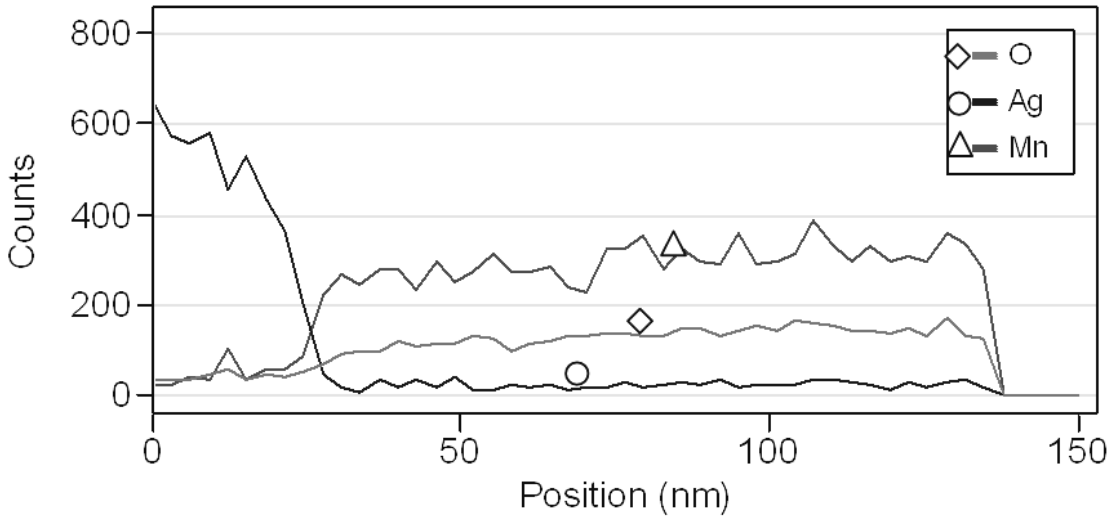

Figure 7.13 *EDX line scan, revealing the compositional profile along the line indicated in Figure 7.12.*

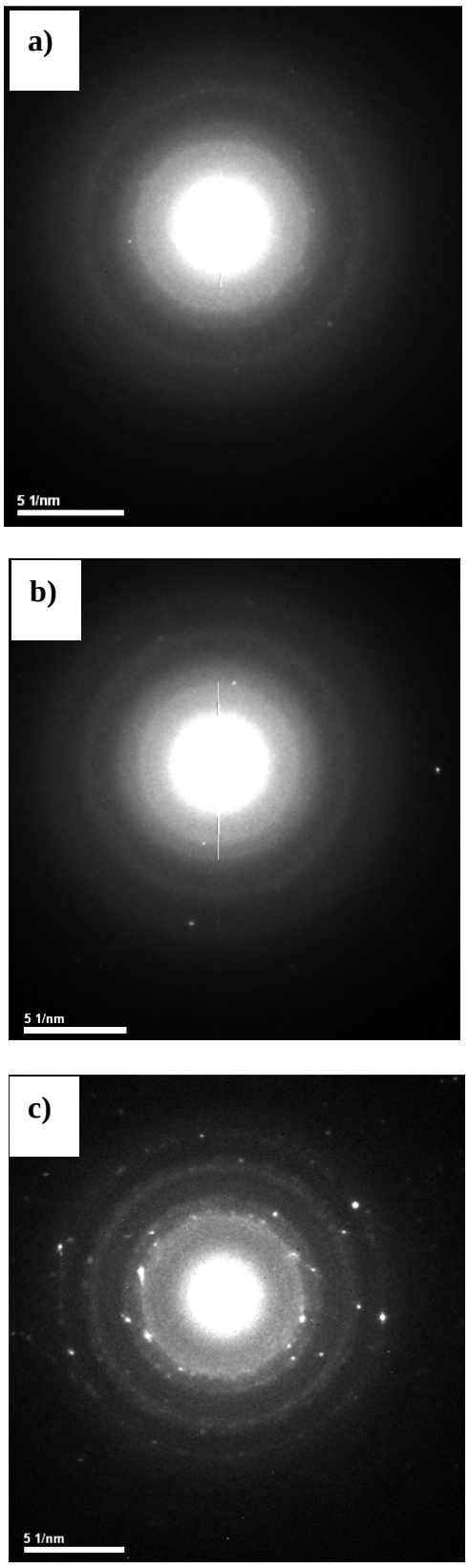

Figure 7.14 *Electron diffraction patterns of manganese oxide nanowires obtained at voltages of a) 0.4 V; b) 0.6V; c) 0.8 V.*

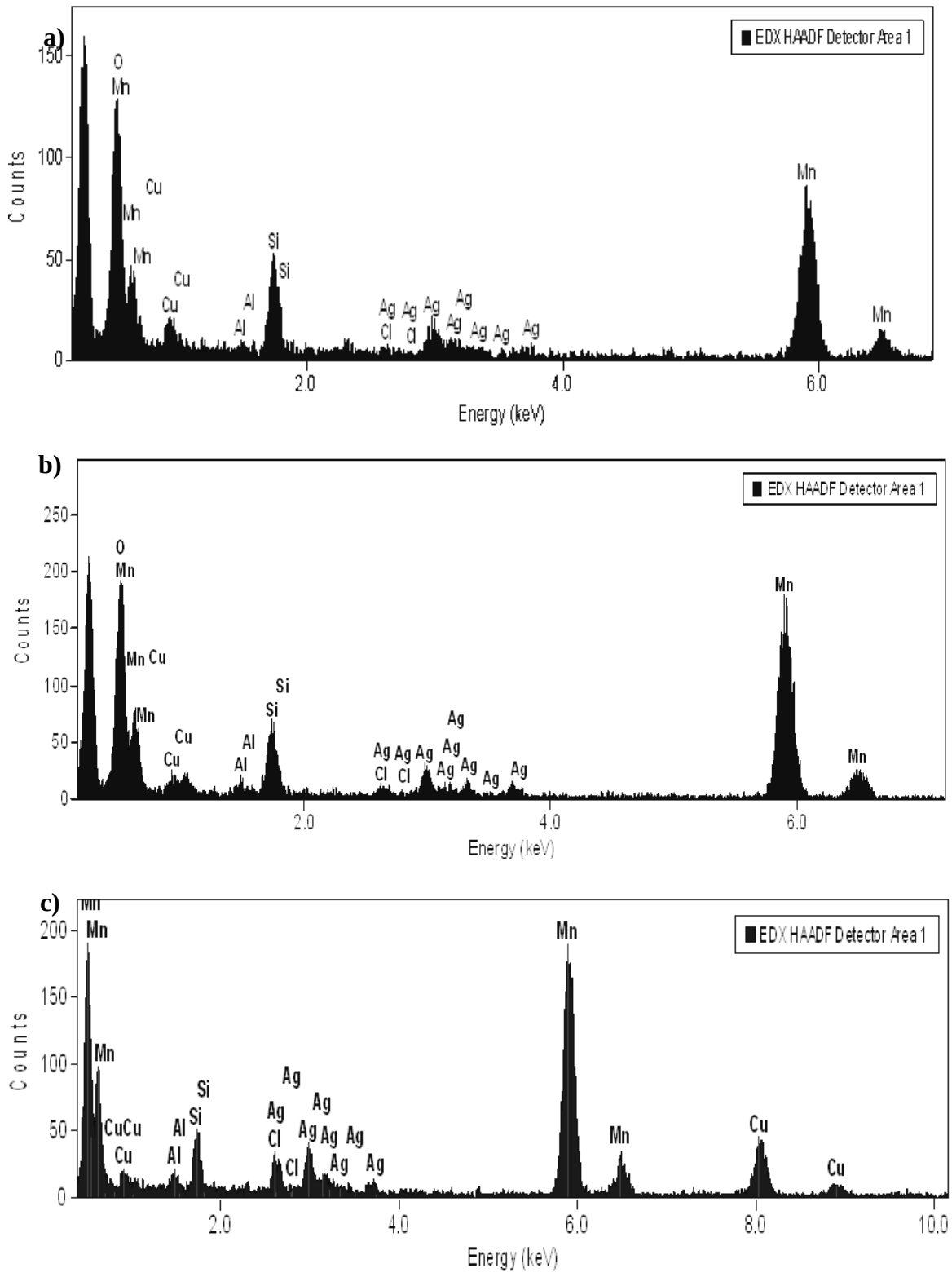

Figure 7.15 *EDX spectra of manganese oxide nanowires obtained at voltages of a) 0.4 V; b) 0.6 V; c) 0.8 V.*

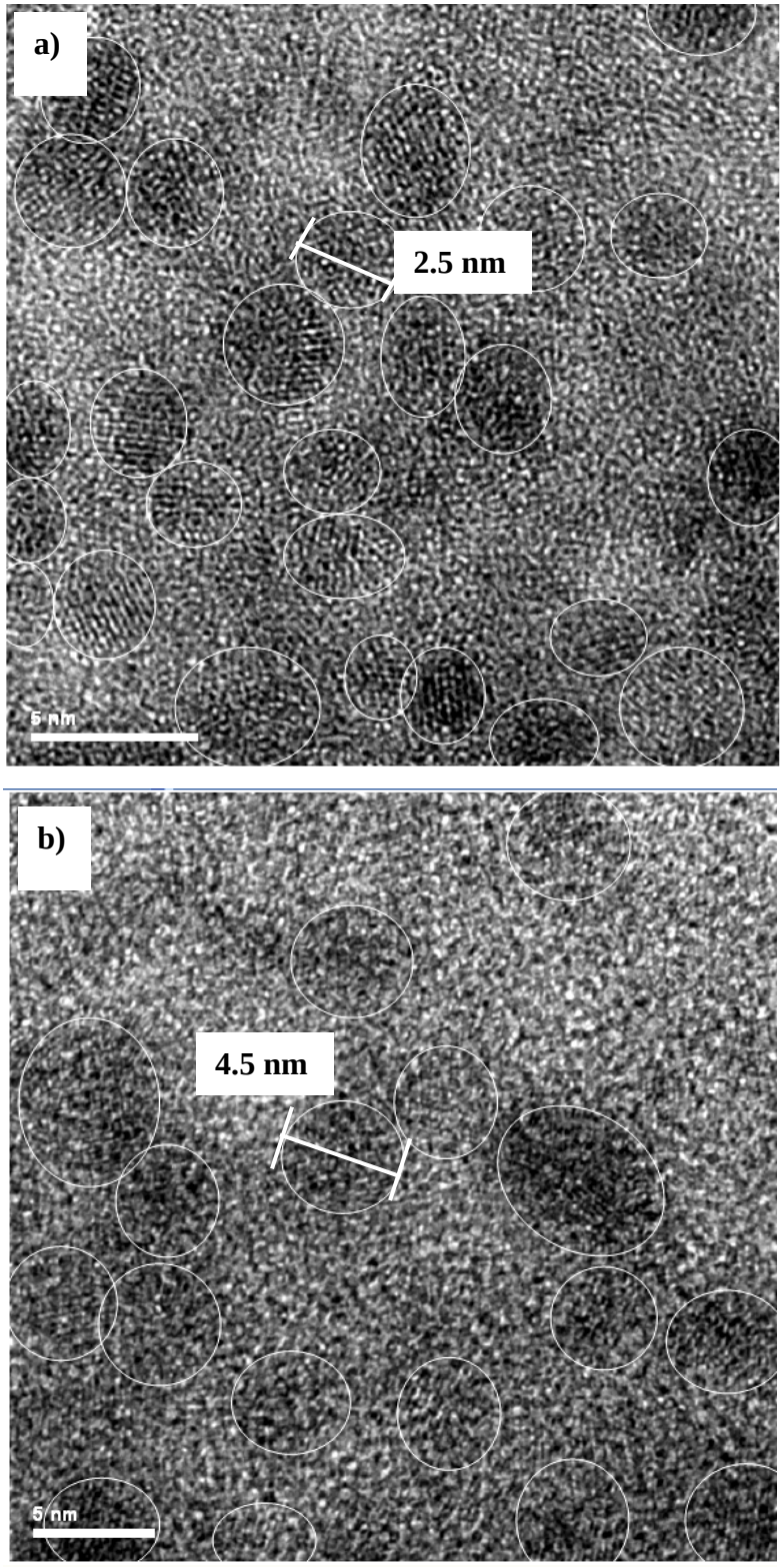
a)
2.5 nm
5 nm
b)
4.5 nm
5 nm

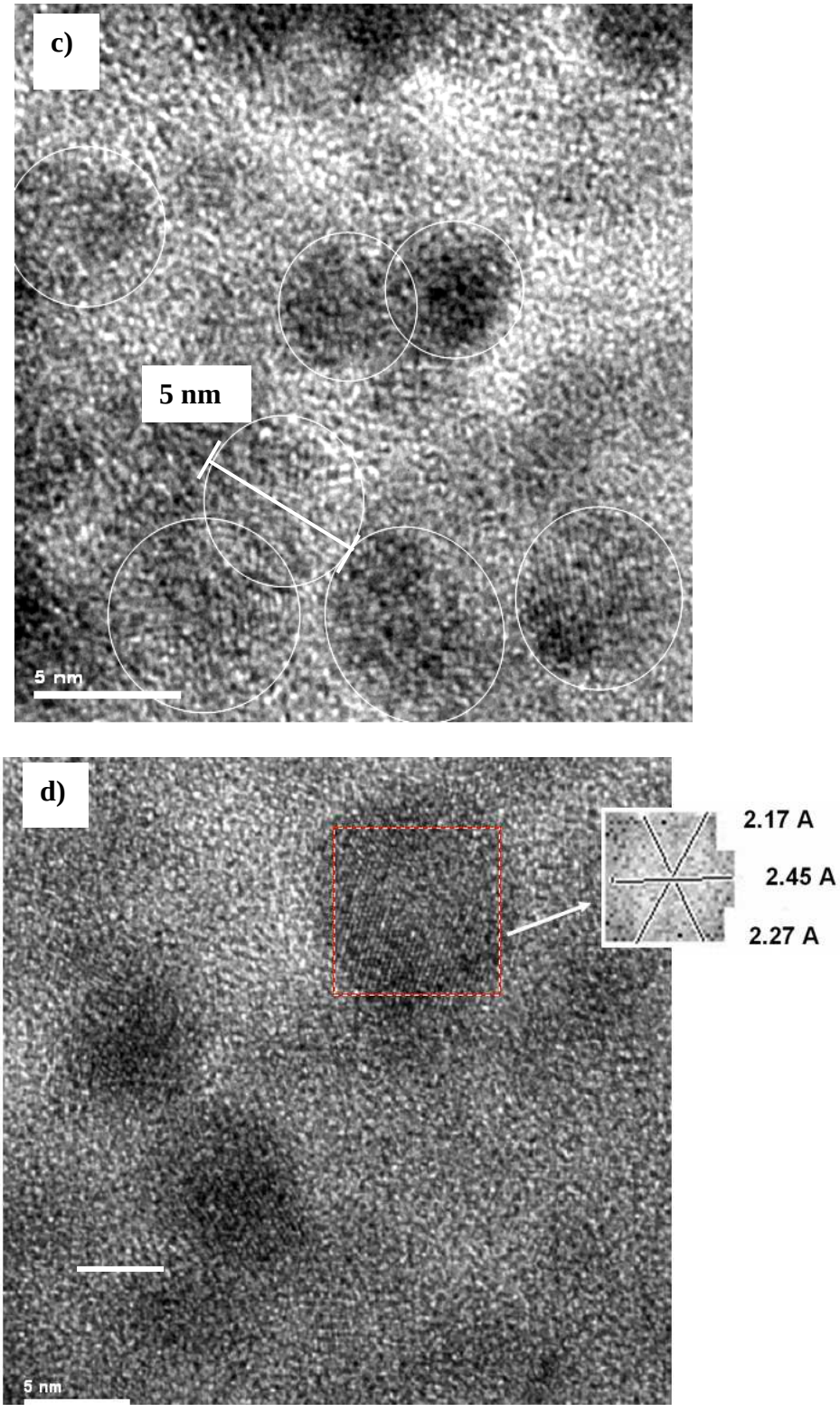

Figure 7.16 *HRTEM images of manganese oxide nanowires produced by deposition at voltages of a) 0.4 V; b) 0.6 V; c) 0.8 V; d) FFT of crystalline particles.*

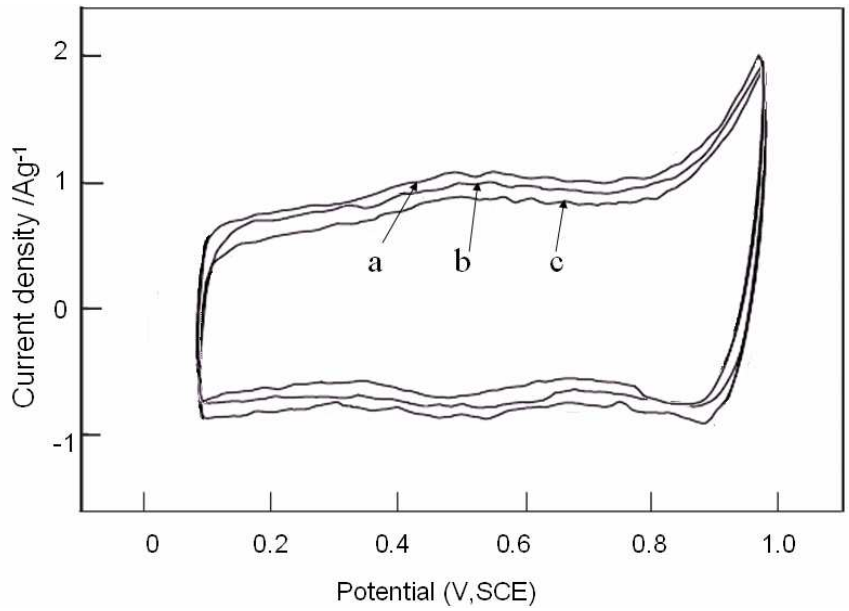

Figure 7.17 *Cyclic voltammograms of manganese oxide nanowire array electrodes formed at voltages of: a) 0.4V; b) 0.6 V; c) 0.8 V in 0.1 M Na_2SO_4 solution at 25°C.*

Chapter 8

Conclusions and Suggested Future Work

8.1 Fabrication of anodic film template with highly ordered pores

Porous anodic films with highly ordered pores of approximately 90 nm cell diameter were obtained in 0.3 M oxalic acid electrolyte at the voltage of 40 V. Each pore is surrounded by six hexagonally arranged columns. The minimum current density in current density-time responses indicates the start of pore initiation, which occurs earlier during the second step anodizing compared to that in the first step anodizing, suggesting that the pore initiation during the second step anodizing was accelerated by the scalloped texture on the aluminum substrate introduced by the previous step. The steady current density during constant voltage anodizing increases nearly exponentially with the increase of anodizing voltage in the range of 30 V to 50 V in oxalic acid electrolyte.

Anodizing conditions, e.g. anodizing voltage and the electrolyte concentration, are found to have significant effects on pore ordering. At relatively low anodizing voltages (i.e. 30 V) and low oxalic acid electrolyte concentration (i.e. 0.2 M), little order in the pore distribution and interpore distances could be observed. The steady current density needs to exceed a critical current density value of approximately $4E^{-5}$ mA/cm^2 for the formation of anodic films with ordered pores. This is consistent with the mechanical stress theory. A sufficient value of the repulsive interactions between the pores, which are associated with volume expansion during anodizing, is needed for the self adjustment for pore ordering. The best regularity of pores in anodic oxide film was achieved in 0.3 M oxalic acid with an anodizing voltage of 40 V and in 0.4 M oxalic acid with an anodizing voltage of 50 V.

The interpore distance in anodic films varies linearly with anodizing voltage, regardless of electrolyte concentration. For a given anodizing voltage, the interpore distances remain constant, while the pore diameter increases nearly lineailly with

electrolyte concentration. Significantly increased regularity of pore distribution and uniformity of interpore distances were achieved with increased number of anodizing steps. Multi-step anodizing, especially with more than two-steps, can significantly improve the regularity of pores over a long range. It is the combination of prolonged anodizing time and repeated anodizing steps that leads to sufficient self-adjustment and self-ordering, thus, resulting in ordered pore arrays.

Anodic oxide films with pores arranged in hexagonal or square patterns were obtained by anodizing of aluminium with corresponding pre-patterns induced by optic grating impress under selected anodizing voltages. The pressing pressure between 50 kg cm^{-2} and 125 kg cm^{-2} was found to be critical to form grooves on the aluminium substrate with a depth of 40 to 100 nm that are suitable for the selected anodizing conditions. Pores nucleate preferentially at the intersections of grooves formed by the optical grating impressions, and also at positions along grooves, with additional pores initiating over the area between grooves due to self-compensation rules during anodizing of aluminum. Following the linear relationship between the anodizing voltage and the interpore distance determined by self-ordering mechanism, when the anodizing voltage is near the value for interpore distance that is equal to the lattice constant of the pre-pattern, an anodic oxide film with ordered pores could be obtained. However, the interpore distance in films formed on the pre-patterned substrate is generally smaller than that formed by anodizing on non-patterned substrates under the same anodizing voltage. If the anodizing voltage is significantly different from the value for interpore distance that is equal to the lattice constant of the pre-pattern, little ordering was achieved.

8.2 Electrodeposition of nickel nanowires

Nickel nanowire arrays were successfully fabricated by electrodeposition using porous anodic film templates. The current density-time responses reveal three growth stages of nickel nanowires during electrodeposition. The growth rate of nickel nanowires during electrodeposition increases with increased electrodeposition voltages and temperatures.

The electrodeposition current efficiency is influenced by electrodeposition conditions mainly by affecting the side reaction, i.e. hydrogen evolution. Increased voltage, high porosity in the anodic film template and low process temperature improve the current efficiency.

Single crystal nanowires grew preferentially along the [110] direction at a relatively low temperature of 3°C. This is because mass diffusion on the crystal surface is considered to be the rate-limiting step during nickel electrodeposition at 3°C under the selected voltage. However, polycrystalline nanowires were obtained at the increased temperature of 37°C due to the increased surface diffusion rate of nickel adatoms. Therefore, the crystal texture of the resultant nickel nanowires can be controlled by justifying the fabrication parameters.

Further, the optical limiting property of nickel nanowires/oxide template composite was assessed. The transmittance decreases as the incident fluence increases, in excess of 5.2×10^3 J/m^2 for 1064 nm and 2.4×10^3 J/m^2 for 532 nm. This is a typical property for the optical limiters. The limiting performance of nickel nanowires is mainly due to non-linear scattering. This suggests potential applications in the fields of ultrahigh-density magnetic recording, ultrafast optical switching and microwave devices.

8.3 Fabrication of manganese oxide nanowires

Manganese oxide nanowires were fabricated by anodic deposition under constant current, pulse voltage and constant voltage mode respectively. A mixed solution of 0.1 M manganese acetate and 0.1 M sodium sulphate was selected as the deposition electrolyte.

Uniform manganese oxide nanowires were fabricated at constant voltages in the range of 0.4 V to 1.0 V (SCE). Manganese oxide nanowires formed under different deposition voltages exhibit an amorphous structure with short range order. A high population of fine crystalline particles with an average diameter of 2 to 5 nm, was revealed in the manganese oxide nanowires. The crystalline particles were determined to be ε-MnO_2 with a hexagonal structure. The average O/Mn ratio of the

manganese oxide nanowires decreases with increase of deposition voltage, indicating that an increased percentage of higher valence manganese species is present in the oxides formed at lower deposition voltage.

In cyclic voltammetry measurement, at a scan rate of 5 mV s^{-1} from 0 to 1 V (SCE) in 0.1 M Na_2SO_4 solution at 25°C, high specific capacitances of 220, 210 and 195 F g^{-1} were recorded on the electrode fabricated from the manganese oxide nanowire array formed at 0.4 V, 0.6 V and 0.8 V respectively, indicating an excellent capacitive property.

8.4 Suggestions for future work

In the present work, increased regularity of pore distribution in self-ordered anodic oxide films were observed with the increased anodizing steps. However, the misorientation between the orientation domains of the aluminium substrate might be responsible for the existence of orientation domains. Electron backscatter diffraction data (EBSD) could be employed to determine the effect of grain orientation of aluminium substrate on pore ordering and the formation of orientation domains.

During the anodizing process on pre-patterned substrate, the pre-pattern have been proven to be able to influence the pore distribution and cell size in the resultant anodic films. Improved insight on the ordered pore formation mechanism could be gain by investigating the initial stages of pore development. Cross-sections of the film formed for a short period at different anodizing voltages on the substrates with hexagonal and square patterns is suggested to be examined using TEM to determine precisely the pore initiation location on the pre-patterned surfaces.

The manganese oxide nanowires formed in the present work exhibit increased capacitive property than the bulk manganese oxide films. Further work is suggested to explore the effects of deposition conditions on the capacitive variation of manganese oxide nanowires; since the pseudocapacitance of electrochemical supercapacitors was stored by means of the redox reactions of electroactive materials with several oxidation states. X-ray photoelectron spectroscopy (XPS) could be employed to determine the precise composition of the formed manganese oxides.

The effects of size and distribution of the fine crystalline particles on the capacitance of manganese oxide nanowires could be further investigated. Further, composite nanowire arrays composed of manganese oxide and metal particles or dots is suggested to be fabricated to further improve the capacitive property, since the metal component could provide better conductivity, thus facilitating the electron transport within manganese oxides.

References

1. Martin, C.R., Membrane-based synthesis of nanomaterials. Chemistry of Materials, 1996. **8**(8): p. 1739-1746.
2. Masuda, H. and K. Fukuda, Ordered Metal Nanohole Arrays Made by a two-Step Replication of Honeycomb Structures of Anodic Alumina. Science, 1995. **268**(5216): p. 1466-1468.
3. Ono, S., et al., Controlling factor of self-ordering of anodic porous alumina. Journal of the Electrochemical Society, 2004. **151**(8): p. B473-A478.
4. Li, A.P., et al., Hexagonal pore arrays with a 50-420 nm interpore distance formed by self-organization in anodic alumina. Journal of Applied Physics, 1998. **84**(11): p. 6023-6026.
5. Jessensky, O., F. Muller, and U. Gosele, Self-organized formation of hexagonal pore structures in anodic alumina. Journal of the Electrochemical Society, 1998. **145**(11): p. 3735-3740.
6. Fournier-Bidoz, S., et al., Highly ordered nanosphere imprinted nanochannel alumina (NINA). Advanced Materials, 2004. **16**(23-24): p. 2193-+.
7. Choi, J.S., R.B. Wehrspohn, and U. Gosele, Moire pattern formation on porous alumina arrays using nanoimprint lithography. Advanced Materials, 2003. **15**(18): p. 1531-+.
8. Chang, J.K. and W.T. Tsai, Material Characterization and Electrochemical Performance of Hydrous Manganese Oxide Electrodes for Use in Electrochemical Pseudocapacitors. Journal of the Electrochemical Society, 2003. **150**(10): p. A1333-A1338.
9. Wilsdorf, H.G.F., Structure of amorphous aluminium oxide films. Nature, 1951. **168**(4275): p. 600-601.
10. Thompson, G.E. and G.C. Wood, Porous anodic film formation on aluminium.Nature, 1981. **290**(5803): p. 230-232.
11. Wood, G.C. and Osulliva.Jp, Electron-optical examination of sealed anodic

alumina films-surface and interior effects. Journal of the Electrochemical Society, 1969. **116**(10): p. 1351-&.

12. Peng, Y., et al., Magneto-optical characteristics of magnetic nanowire arrays in anodic aluminum oxide templates. Applied Physics Letters, 2003. **83**(2): p. 362-364.
13. Zhao, J., et al., Quantum transport properties of ultrathin silver nanowires. Nanotechnology, 2003. **14**(5): p. 501-504.
14. Kodama, K. and K. Wagatsuma, Excitation mechanism for nickel and argon lines emitted by radio-frequency glow discharge plasma associated with bias current introduction. Spectrochimica Acta - Part B Atomic Spectroscopy, 2004. **59**(4): p. 429-434.
15. Thompson, G.E., Porous anodic alumina: Fabrication, characterization and applications. Thin Solid Films, 1997. **297**(1-2): p. 192-201.
16. Verwey, E.J.W., Incomplete atomic arrangement in crystals. The Journal of Chemical Physics, 1935. **3**(9): p. 592-593.
17. Taylor, C.S., C.M. Tucker, and J.D. Edwards, Anodic Coatings with Crystalline Structure on Aluminum. Transactions of the Electrochemical Society, 1945. **88**: p. 325-333.
18. Stirland, D.J. and R.W. Bicknell, Studies of the structure of anodic oxide films on aluminium.1. Journal of the Electrochemical Society, 1959. **106**(6): p. 481-485.
19. Franklin, R.W., Structure of non-porous anodic films on aluminium. Nature, 1957. **180**(4600): p. 1470-1471.
20. Keller, F., M.S. Hunter, and D.L. Robinson, Structural features of oxide coating on aluminium. Journal of the Electrochemical Society, 1953. **100**(9): p. 411-419.
21. Wood, G.C. and Osulliva.Jp, Anodizing of aluminium in sulphate solutions. Electrochimica Acta, 1970. **15**(12): p. 1865-&.
22. Wood, G.C., Osulliva.Jp, and B. Vaszko, Direct observation of barrier layers in porous and anodic oxide films. Journal of the Electrochemical Society, 1968.

115(6): p. 618-&.

23. Wada, K., et al., Microstructure of porous anodic oxide films on aluminium. Journal of Materials Science, 1986. **21**(11): p. 3810-3816.
24. Xu, Y., et al., Anion incorporation and migration during barrier film formation on aluminum. Corrosion Science, 1987. **27**(1): p. 83-&.
25. Su, Z.X., G. Hahner, and W.Z. Zhou, Investigation of the pore formation in anodic aluminium oxide. Journal of Materials Chemistry, 2008. **18**(47): p. 5787-5795.
26. Martin, T. and K.R. Hebert, Atomic Force Microscopy Study of Anodic Etching of Aluminum: Etching Morphology Development and Caustic Pretreatment. Journal of the Electrochemical Society, 2001. **148**(2).
27. Caicedo-Martinez, C.E., G.E. Thompson, and E.V. Koroleva, Nanoscale engineering of aluminium surfaces. Surface Engineering, 2002. **18**(2): p. 145-150.
28. Hoar, T.P. and N.F. Mott, A mechanism for the formation of porous anodic oxide films on aluminium. Journal of Physics and Chemistry of Solids, 1959. **9**(2): p. 97-99.
29. Parkhutik, V.P. and V.I. Shershulsky, THEORETICAL MODELING OF POROUS OXIDE-GROWTH ON ALUMINUM. Journal of Physics D-Applied Physics, 1992. **25**(8): p. 1258-1263.
30. Shingubara, S., et al., Self-Organization of a Porous Alumina Nanohole Array Using a Sulfuric/Oxalic Acid Mixture as Electrolyte. Electrochemical and Solid-State Letters, 2004. **7**(3).
31. Pavlovic, T. and A. Ignatiev, Optical and microstructural properties of anodically oxidized aluminum. Thin Solid Films, 1986. **138**(1): p. 97-109.
32. Hou, K., J.P. Tu, and X.B. Zhang, Preparation of porous alumina film on aluminum substrate by anodization in oxalic acid. Chinese Chemical Letters, 2002. **13**(7): p. 689-692.
33. Masuda, H., F. Hasegwa, and S. Ono, Self-ordering of cell arrangement of anodic porous alumina formed in sulfuric acid solution. Journal of the

Electrochemical Society, 1997. **144**(5).

34. Masuda, H., K. Yada, and A. Osaka, Self-ordering of cell configuration of anodic porous alumina with large-size pores in phosphoric acid solution. Japanese Journal of Applied Physics, Part 2: Letters, 1998. **37**(11 PART A): p. L1340-L1342.
35. Nielsch, K., et al., Self-ordering regimes of porous alumina: The 10% porosity rule. Nano Letters, 2002. **2**(7): p. 677-680.
36. Jessensky, O., F. Muller, and U. Gosele, Self-organized formation of hexagonal pore arrays in anodic alumina. Applied Physics Letters, 1998. **72**(10): p. 1173-1175.
37. Li, A.P., et al., Hexagonal pore arrays with a 50-420 nm interpore distance formed by self-organization in anodic alumina. Journal of Applied Physics, 1998. **84**(11): p. 6023-6026.
38. Ono, S., et al., Controlling factor of self-ordering of anodic porous alumina. Journal of the Electrochemical Society, 2004. **151**(8): p. B473-B478.
39. Shingubara, S., et al., Ordered two-dimensional nanowire array formation using self-organized nanoholes of anodically oxidized aluminum. Japanese Journal of Applied Physics, Part 1: Regular Papers and Short Notes and Review Papers, 1997. **36**(12 SUPPL. B): p. 7791-7795.
40. Masuda, H., et al., Square and triangular nanohole array architectures in anodic alumina. Advanced Materials, 2001. **13**(3): p. 189-192.
41. Choi, J.S., et al., Monodisperse metal nanowire arrays on Si by integration of template synthesis with silicon technology. Journal of Materials Chemistry, 2003. **13**(5): p. 1100-1103.
42. Rabin, O., et al., Formation of thick porous anodic alumina films and nanowire arrays on silicon wafers and glass. Advanced Functional Materials, 2003. **13**(8): p. 631-638.
43. Masuda, H., et al., Highly ordered nanochannel-array architecture in anodic alumina. Applied Physics Letters, 1997. **71**(19): p. 2770-2772.
44. Mikulskas, I., et al., Aluminum oxide photonic crystals grown by a new hybrid

method. Advanced Materials, 2001. **13**(20): p. 1574-+.

45. Masuda, H., K. Kanezawa, and K. Nishio, Fabrication of ideally ordered nanohole arrays in anodic porous alumina based on nanoindentation using scanning probe microscope. Chemistry Letters, 2002(12): p. 1218-1219.
46. Shingubara, S., et al., Formation of aluminum nanodot array by combination of nanoindentation and anodic oxidation of aluminum. Surface Science, 2003. **532-535**: p. 317-323.
47. Matsui, Y., K. Nishio, and H. Masuda, Highly ordered anodic porous alumina with 13-nm hole intervals using a 2D array of monodisperse nanoparticles as a template. Small, 2006. **2**(4): p. 522-525.
48. Rajendra, A., et al., Hard anodisation of aluminium and its application to sensorics. Surface Engineering, 2005. **21**(3): p. 193-197.
49. Shingubara, S., et al., Self-Organization of a Porous Alumina Nanohole Array Using a Sulfuric/Oxalic Acid Mixture as Electrolyte. Electrochemical and Solid-State Letters, 2004. **7**(3): p. E15-E17.
50. Chu, S.Z., et al., Fabrication of ideally ordered nanoporous alumina films and integrated alumina nanotubule arrays by high-field anodization. Advanced Materials, 2005. **17**(17): p. 2115-2119.
51. Ono, S., M. Saito, and H. Asoh, Self-ordering of anodic porous alumina formed in organic acid electrolytes. Electrochimica Acta, 2005. **51**(5): p. 827-833.
52. Lee, W., et al., Fast fabrication of long-range ordered porous alumina membranes by hard anodization. Nature Materials, 2006. **5**(9): p. 741-747.
53. Iijima, S., Helical microtubules of graphitic carbon. Nature, 1991. **354**(6348): p. 56-58.
54. Ferrer R, et al., Magnetization processes in nickel and cobalt electrodeposited nanowires. Physical Review B - Condensed Matter and Materials Physics, 1997. **56**(21): p. 14066-14075.
55. Wang, J.B., et al., Magnetic texture in iron nanowire arrays. Nanotechnology, 2004. **15**(5): p. 485-489.

56. Wang, Y.W., et al., Fabrication of ordered ferromagnetic-nonmagnetic alloy nanowire arrays and their magnetic property dependence on annealing temperature. Journal of Physical Chemistry B, 2002. **106**(10): p. 2502-2507.
57. Zhang, Z., et al., High-yield solvothermal formation of magnetic CoPt alloy nanowires. Journal of the American Chemical Society, 2003. **125**(25): p. 7528-7529.
58. Shiomi, S., T. Nishii, and H. Kohama, Effect of Pt seed on magnetic properties of Co-Pt alloy deposited into aluminum oxide pores. IEEE Transactions on Magnetics, 2002. **38**(5 I): p. 2568-2570.
59. Henry, Y., et al., Magnetic anisotropy and domain patterns in electrodeposited cobalt nanowires. European Physical Journal B, 2001. **20**(1): p. 35-54.
60. Chen, W., et al., The magnetic properties and reversal of Fe-Co nanowire arrays. Journal of Physics Condensed Matter, 2003. **15**(26): p. 4623-4630.
61. Martin, J.I., et al., Ordered magnetic nanostructures: Fabrication and properties. Journal of Magnetism and Magnetic Materials, 2003. **256**(1-3): p. 449-501.
62. Chien, C.L., Granular magnetic solids (invited). Journal of Applied Physics, 1991. **69**(8): p. 5267-5272.
63. Zeng, H., et al., Magnetic properties of self-assembled Co nanowires of varying length and diameter. Journal of Applied Physics, 2000. **87**(9 II): p. 4718-4720.
64. Cowburn, R.P., et al., Lateral interface anisotropy in nanomagnets. Journal of Applied Physics, 2000. **87**(9): p. 7067-7069.
65. deHaan, S. and J.C. Lodder, Magnetisation reversal mechanism in Co-Cr media for perpendicular magnetic recording. Journal of Magnetism and Magnetic Materials, 1997. **168**(3): p. 321-335.
66. Muller, C.J., J.M. Van Ruitenbeek, and L.J. De Jongh, Conductance and supercurrent discontinuities in atomic-scale metallic constrictions of variable width. Physical Review Letters, 1992. **69**(1): p. 140-143.
67. Muller, C.J., et al., Quantization effects in the conductance of metallic contacts

at room temperature. Physical Review B - Condensed Matter and Materials Physics, 1996. **53**(3): p. 1022-1025.

68. Van Wees, B.J., et al., Quantized conductance of point contacts in a two-dimensional electron gas. Physical Review Letters, 1988. **60**(9): p. 848-850.
69. Costa-Krimer, J.L., N. Garcoa, and H. Olin, Conductance quantization in bismuth nanowires at 4 K. Physical Review Letters, 1997. **78**(26): p. 4990-4993.
70. Gudiksen, M.S., et al., Growth of nanowire superlattice structures for nanoscale photonics and electronics. Nature, 2002. **415**(6872): p. 617-620.
71. Huang, H.H., et al., Photochemical formation of silver nanoparticles in poly(N-vinylpyrrolidone). Langmuir, 1996. **12**(4): p. 909-912.
72. Kim, J.R., et al., Schottky diodes based on a single GaN nanowire. Nanotechnology, 2002. **13**(5): p. 701-704.
73. Duan, X., et al., Indium phosphide nanowires as building blocks for nanoscale electronic and optoelectronic devices. Nature, 2001. **409**(6816): p. 66-69.
74. Duan, X., Y. Huang, and C.M. Lieber, Nonvolatile Memory and Programmable Logic from Molecule-Gated Nanowires. Nano Letters, 2002. **2**(5): p. 487-490.
75. Derycke, V., et al., Carbon Nanotube Inter- and Intramolecular Logic Gates. Nano Letters, 2001. **1**(9): p. 453-456.
76. Majumdar, A., Thermoelectricity in Semiconductor Nanostructures. Science, 2004. **303**(5659): p. 777-778.
77. Lin, Y.M., X. Sun, and M.S. Dresselhaus, Theoretical investigation of thermoelectric transport properties of cylindrical Bi nanowires. Physical Review B - Condensed Matter and Materials Physics, 2000. **62**(7): p. 4610-4623.
78. Cronin, S.B., et al., Transport measurements of individual Bi nanowires. Materials Research Society Symposium - Proceedings, 2000. **582**.
79. Mingo, N., Thermoelectric figure of merit and maximum power factor in III-V

semiconductor nanowires. Applied Physics Letters, 2004. **84**(14): p. 2652-2654.

80. Hicks, L.D. and M.S. Dresselhaus, Thermoelectric figure of merit of a one-dimensional conductor. Physical Review B, 1993. **47**(24): p. 16631-16634.
81. Chen, G., et al., Recent developments in thermoelectric materials. International Materials Reviews, 2003. **48**(1): p. 45-66.
82. Heremans, J.P., et al., Thermoelectric power of bismuth nanocomposites. Physical Review Letters, 2002. **88**(21): p. 2168011-2168014.
83. Heremans, J., et al., Bismuth nanowire arrays: Synthesis and galvanomagnetic properties. Physical Review B - Condensed Matter and Materials Physics, 2000. **61**(4): p. 2921-2930.
84. Zhou, X.T., et al., Silicon nanowires as chemical sensors. Chemical Physics Letters, 2003. **369**(1-2): p. 220-224.
85. Aspnes, D.E., Optical properties of thin films. Thin Solid Films, 1982. **89**(3): p. 249-262.
86. Foss Jr, C.A., et al., Template-synthesized nanoscopic gold particles: Optical spectra and the effects of particle size and shape. Journal of Physical Chemistry, 1994. **98**(11): p. 2963-2971.
87. Schider, G., et al., Plasmon dispersion relation of Au and Ag nanowires. Physical Review B - Condensed Matter and Materials Physics, 2003. **68**(15): p. 1554271-1554274.
88. Van Vugt, L.K., et al., Increase of the photoluminescence intensity of InP nanowires by photoassisted surface passivation. Journal of the American Chemical Society, 2005. **127**(35): p. 12357-12362.
89. Lee, M.W., et al., Optical characterization of wurtzite gallium nitride nanowires. Applied Physics Letters, 2001. **79**(22): p. 3693-3695.
90. Blom, S., et al., Magneto-optics of electronic transport in nanowires. Physical Review B - Condensed Matter and Materials Physics, 1998. **58**(24): p. 16305-16314.

91. Johnson, J.C., et al., Single gallium nitride nanowire lasers. Nature Materials, 2002. **1**(2): p. 106-110.
92. Haghiri-Gosnet, A.M., et al., Nanofabrication at a 10 nm length scale: limits of lift-off and electroplating transfer processes. Journal De Physique. IV : JP, 1999. **9**(2).
93. Marrian, C.R.K. and D.M. Tennant, Nanofabrication. Journal of Vacuum Science and Technology A: Vacuum, Surfaces and Films, 2003. **21**(5).
94. Hanrath, T. and B.A. Korgel, Nucleation and growth of germanium nanowires seeded by organic monolayer-coated gold nanocrystals. Journal of the American Chemical Society, 2002. **124**(7): p. 1424-1429.
95. Chik, H., et al., Periodic array of uniform ZnO nanorods by second-order self-assembly. Applied Physics Letters, 2004. **84**(17): p. 3376-3378.
96. Che, G., et al., Chemical Vapor Deposition Based Synthesis of Carbon Nanotubes and Nanofibers Using a Template Method. Chemistry of Materials, 1998. **10**(1): p. 260-267.
97. Parthasarathy, R.V. and C.R. Martin, Synthesis of polymeric microcapsule arrays and their use for enzyme immobilization. Nature, 1994. **369**(6478): p. 298-301.
98. Lakshmi, B.B., C.J. Patrissi, and C.R. Martin, Sol-Gel Template Synthesis of Semiconductor Oxide Micro- and Nanostructures. Chemistry of Materials, 1997. **9**(11): p. 2544-2550.
99. Huber, C.A., et al., Nanowire array composites. Science, 1994. **263**(5148): p. 800-802.
100. Zhang, Z., J.Y. Ying, and M.S. Dresselhaus, Bismuth quantum-wire arrays fabricated by a vacuum melting and pressure injection process. Journal of Materials Research, 1998. **13**(7): p. 1745-1748.
101. Cheng, G.S., et al., Large-scale synthesis of single crystalline gallium nitride nanowires. Applied Physics Letters, 1999. **75**(16): p. 2455-2457.
102. Lew, K.K., et al., Template-directed vapor-liquid-solid growth of silicon nanowires. Journal of Vacuum Science and Technology B: Microelectronics

and Nanometer Structures, 2002. **20**(1): p. 389-392.

103. Holmes, J.D., et al., Control of thickness and orientation of solution-grown silicon nanowires. Science, 2000. **287**(5457): p. 1471-1473.

104. Bae, C.H., et al., Array of ultraviolet luminescent ZnO nanodots fabricated by pulsed laser deposition using an anodic aluminium oxide template. Nanotechnology, 2006. **17**(2): p. 381-384.

105. Ma, X.D., et al., Preparation and characterization of polyvinyl alcohol-selenide nanocomposites at room temperature. Journal of Materials Chemistry, 2002. **12**(3): p. 663-666.

106. Li, Y., G.S. Cheng, and L.D. Zhang, Fabrication of highly ordered ZnO nanowire arrays in anodic alumina membranes. Journal of Materials Research, 2000. **15**(11): p. 2305-2308.

107. Zelenski, C.M. and P.K. Dorhout, Template synthesis of near-monodisperse microscale nanofibers and nanotubules of MoS_2. Journal of the American Chemical Society, 1998. **120**(4): p. 734-742.

108. Mikhaylova, M., et al. Nanowire formation by electrodeposition in modified nanoporous polycrystalline anodic alumina templates. in Materials Research Society Symposium - Proceedings. 2002.

109. Blondel, A., et al., Giant magnetoresistance of nanowires of multilayers. Applied Physics Letters, 1994. **65**(23): p. 3019-3021.

110. Bhattacharrya, S., S.K. Saha, and D. Chakravorty, Nanowire formation in a polymeric film. Applied Physics Letters, 2000. **76**(26): p. 3896-3898.

111. Zhang, X.Y., et al., Fabrication and characterization of highly ordered Au nanowire arrays. Journal of Materials Chemistry, 2001. **11**(6): p. 1732-1734.

112. AlMawlawi, D., N. Coombs, and M. Moskovits, Magnetic properties of Fe deposited into anodic aluminum oxide pores as a function of particle size. Journal of Applied Physics, 1991. **70**(8): p. 4421-4425.

113. Peng, Y., et al., Magnetic properties and magnetization reversal of 伪-Fe nanowires deposited in alumina film. Journal of Applied Physics, 2000. **87**(10): p. 7405-7408.

114. Sun, L., P.C. Searson, and C.L. Chien, Electrochemical deposition of nickel nanowire arrays in single-crystal mica films. Applied Physics Letters, 1999. **74**(19): p. 2803-2805.

115. Yi, G. and W. Schwarzacher, Single crystal superconductor nanowires by electrodeposition. Applied Physics Letters, 1999. **74**(12): p. 1746-1748.

116. Rahman, I.Z., et al., Fabrication and characterization of nickel nanowires deposited on metal substrate. Journal of Magnetism and Magnetic Materials, 2003. **262**(1): p. 166-169.

117. Nielsch, K., et al., Uniform nickel deposition into ordered alumina pores by pulsed electrodeposition. Advanced Materials, 2000. **12**(8): p. 582-586.

118. Schider, G., et al., Optical properties of Ag and Au nanowire gratings. Journal of Applied Physics, 2001. **90**(8): p. 3825-3830.

119. Routkevitch, D., et al., Electrochemical fabrication of CdS nanowire arrays in porous anodic aluminum oxide templates. Journal of Physical Chemistry, 1996. **100**(33): p. 14037-14047.

120. Xu, D., et al., Preparation of CdS single-crystal nanowires by electrochemically induced deposition. Advanced Materials, 2000. **12**(7): p. 520-522.

121. Xu, T.T., R.D. Piner, and R.S. Ruoff, An improved method to strip aluminum from porous anodic alumina films. Langmuir, 2003. **19**(4): p. 1443-1445.

122. Chakkingal, U., A.B. Suriadi, and P.F. Thomson, Microstructure development during equal channel angular drawing of Al at room temperature. Scripta Materialia, 1998. **39**(6): p. 677-684.

123. Mikulskas, I., et al., Aluminum oxide photonic crystals grown by a new hybrid method. Advanced Materials, 2001. **13**(20): p. 1574-1577.

124. Jessensky, O., F. Muller, and U. Gosele, Self-organized formation of hexagonal pore arrays in anodic alumina. Applied Physics Letters, 1998. **72**(10): p. 1173-1175.

125. Ono, S., M. Saito, and H. Asoh, Self-ordering of anodic porous alumina induced by local current concentration: Burning. Electrochemical and

Solid-State Letters, 2004. **7**(7).

126. Patermarakis, G. and N. Papandreadis, Study on the kinetics of growth of porous anodic Al2O3 films on Al metal. Electrochimica Acta, 1993. **38**(15): p. 2351-2361.
127. Diggle, J.W., T.C. Downie, and C.W. Goulding, Anodic Oxide Films on Aluminum. Chemical Reviews, 1969. **69**(3): p. 365-&.
128. Thompson, G.E., et al., NUCLEATION AND GROWTH OF POROUS ANODIC FILMS ON ALUMINUM. Nature, 1978. **272**(5652): p. 433-435.
129. Fiemings, M.C., Solidification Processing, 1974: p. 58.
130. Patermarakis, G. and K. Moussoutzanis, Mathematical models for the anodization conditions and structural features of porous anodic Al2O3 films on aluminum. Journal of the Electrochemical Society, 1995. **142**(3): p. 737-743.
131. Li, F., L. Zhang, and R.M. Metzger, On the Growth of Highly Ordered Pores in Anodized Aluminum Oxide. Chemistry of Materials, 1998. **10**(9): p. 2470-2480.
132. Nielsch, K., et al., Self-ordering Regimes of Porous Alumina: The 10% Porosity Rule. Nano Letters, 2002. **2**(7): p. X-680.
133. Masuda, H., et al., Self-repair of ordered pattern of nanometer dimensions based on self-compensation properties of anodic porous alumina. Applied Physics Letters, 2001. **78**(6): p. 826-828.
134. Choi, J., et al., Fabrication of monodomain alumina pore arrays with an interpore distance smaller than the lattice constant of the imprint stamp. Journal of Vacuum Science and Technology B: Microelectronics and Nanometer Structures, 2003. **21**(2): p. 763-766.
135. Masuda, H. and M. Satoh, Fabrication of gold nanodot array using anodic porous alumina as an evaporation mask. Japanese Journal of Applied Physics, Part 2: Letters, 1996. **35**(1 B).
136. Voronoi, Nouvelles applications des paramètres continus à la théorie des formes quadratiques. J. reine angew. Math. , 1907. **133**(97): p. 178.

137. Broughton, J. and G.A. Davies, Porous cellular ceramic membranes: A stochastic model to describe the structure of an anodic oxide membrane. Journal of Membrane Science, 1995. **106**(1-2): p. 89-101.

138. Chou, S.Y., et al., Single-domain magnetic pillar array of 35 nm diameter and 65 Gbits/in. 2 density for ultrahigh density quantum magnetic storage. Journal of Applied Physics, 1994. **76**(10): p. 6673-6675.

139. Hultgren, A., et al., Cell manipulation using magnetic nanowires. Journal of Applied Physics, 2003. **93**(10 2): p. 7554-7556.

140. Ainslie, K.M., et al., Attenuation of protein adsorption on static and oscillating magnetostrictive nanowires. Nano Letters, 2005. **5**(9): p. 1852-1856.

141. Citrin, D.S., Magnetic bloch oscillations in nanowire superlattice rings. Physical Review Letters, 2004. **92**(19): p. 196803-1.

142. Wirtz, M., et al., Template-synthesized nanotubes for chemical separations and analysis. Chemistry - A European Journal, 2002. **8**(16): p. 3572-3578.

143. Sch 枚 nenberger, C., et al., Template synthesis of nanowires in porous polycarbonate membranes: Electrochemistry and morphology. Journal of Physical Chemistry B, 1997. **101**(28): p. 5497-5505.

144. Riveros, G., et al., Crystallographically-oriented single-crystalline copper nanowire arrays electrochemically grown into nanoporous anodic alumina templates. Applied Physics A: Materials Science and Processing, 2005. **81**(1): p. 17-24.

145. Sato, H., M. Yui, and H. Yoshikawa, Ionic diffusion coefficients of Cs^{+}, Pb^{2+}, Sm^{3+}, Ni^{2+}, $SeO2^{-4}$ and TcO^{-4} in free water determined from conductivity measurements. Journal of Nuclear Science and Technology, 1996. **33**(12): p. 950-955.

146. Hofmann, S., et al., Surface diffusion: The low activation energy path for nanotube growth. Physical Review Letters, 2005. **95**(3): p. 1-4.

147. Kurpick, U., Self-diffusion on (100), (110), and (111) surfaces of Ni and Cu: A detailed study of prefactors and activation energies. Physical Review B, 2001. **64**(7).

148. Njau, K.N. and L.J.J. Janssen, Electrochemical reduction of nickel ions from dilute solutions. Journal of Applied Electrochemistry, 1995. **25**(10): p. 982-986.

149. Nielsch, K., et al., Hexagonally ordered 100 nm period nickel nanowire arrays. Applied Physics Letters, 2001. **79**(9): p. 1360-1362.

150. Whitney, T.M., et al., Fabrication and magnetic properties of arrays of metallic nanowires. Science, 1993. **261**(5126): p. 1316-1319.

151. O'Flaherty, S.M., et al., Material investigation and optical limiting properties of carbon nanotube and nanoparticle dispersions. Journal of Physical Chemistry B, 2003. **107**(4): p. 958-964.

152. Jia, W., et al., Optical limiting of semiconductor nanoparticles for nanosecond laser pulses. Applied Physics Letters, 2004. **85**(26): p. 6326-6328.

153. Sun, X., et al., Investigation of an optical limiting mechanism in multiwalled carbon nanotubes. Applied Optics, 2000. **39**(12): p. 1998-2001.

154. Goedert, R., et al., Time-resolved shadowgraphic imaging of the response of dilute suspensions to laser pulses. Journal of the Optical Society of America B: Optical Physics, 1998. **15**(5): p. 1442-1462.

155. Banfi, G.P., et al., Third-order nonlinearity of semiconductor doped glasses at frequencies below band gap. Applied Physics Letters, 1995. **67**(1): p. 13-15.

156. Pan, H., et al., Optical limiting properties of metal nanowires. Applied Physics Letters, 2006. **88**(22).

157. Polavarapu, L., et al., Optical limiting properties of silver nanoprisms. Applied Physics Letters, 2008. **92**(26).

158. Tutt, L.W. and T.F. Boggess, A review of optical limiting mechanisms and devices using organics, fullerenes, semiconductors and other materials. Progress in Quantum Electronics, 1993. **17**(4): p. 299-338.

159. El-Sayed, M.A., Some interesting properties of metals confined in time and nanometer space of different shapes. Accounts of Chemical Research, 2001. **34**(4): p. 257-264.

160. Boyd, G.T., Z.H. Yu, and Y.R. Shen, Photoinduced luminescence from the

noble metals and its enhancement on roughened surfaces. Physical Review B, 1986. **33**(12): p. 7923-7936.

161. Chen, P., et al., Electronic structure and optical limiting behavior of carbon nanotubes. Physical Review Letters, 1999. **82**(12): p. 2548-2551.

162. Sutherland, R.L., et al., Nonlinear absorption study of a C60 - toluene solution. Optics Letters, 1993. **18**(11): p. 858-860.

163. Burke, A.F. and T.C. Murphy. Material characteristics and the performance of electrochemical capacitors for electric/hybrid vehicle applications. in Materials Research Society Symposium - Proceedings. 1995.

164. Ishikawa, M., et al., Electric double-layer capacitor composed of activated carbon fiber cloth electrodes and solid polymer electrolytes containing alkylammonium salts. Journal of the Electrochemical Society, 1994. **141**(7): p. 1730-1734.

165. Sarangapani, S., B.V. Tilak, and C.P. Chen, Materials for electrochemical capacitors theoretical and experimental constraints. Journal of the Electrochemical Society, 1996. **143**(11): p. 3791-3799.

166. Zheng, J.P. and T.R. Jow, New charge storage mechanism for electrochemical capacitors. Journal of the Electrochemical Society, 1995. **142**(1).

167. Hu, C.C. and T.W. Tsou, Ideal capacitive behavior of hydrous manganese oxide prepared by anodic deposition. Electrochemistry Communications, 2002. **4**(2): p. 105-109.

168. preisler, E. in Proceedings of the second Symposium on Battery Materials. 1985.

169. Elsemongy, M.M., Y.A. Elewady, and M.M. Gouda, Anodic deposition of manganese and cobalt oxides. Journal of Electroanalytical Chemistry, 1977. **81**(1): p. 113-121.

171. Zheng, J.P., P.J. Cygan, and T.R. Jow, Hydrous ruthenium oxide as an electrode material for electrochemical capacitors. Journal of the Electrochemical Society, 1995. **142**(8): p. 2699-2703.

172. Zheng, J.P., et al., Proton insertion into ruthenium oxide film prepared by

pulsed laser deposition. Journal of the Electrochemical Society, 1996. **143**(3): p. 1068-1070.

173. Chang, J.Y. and A. Shan, Intermediate annealing of pure aluminum during cyclic equal channel angular pressings. Journal of Materials Science, 2003. **38**(12): p. 2613-2617.